

**IMPAIRED SIGNALING IN SENESCING T CELLS:  
INVESTIGATION OF THE ROLE OF REACTIVE OXYGEN  
SPECIES USING MICROFLUIDIC PLATFORMS AND  
COMPUTATIONAL MODELING**

A Dissertation  
Presented to  
The Academic Faculty

by

Catherine-Aur lie RIVET

In Partial Fulfillment  
of the Requirements for the Degree  
Doctor of Philosophy in the  
School of Electrical & Computer Engineering

Georgia Institute of Technology  
August, 2012

**IMPAIRED SIGNALING IN SENESCING T CELLS:  
INVESTIGATION OF THE ROLE OF REACTIVE OXYGEN  
SPECIES USING MICROFLUIDIC PLATFORMS AND  
COMPUTATIONAL MODELING**

Approved by:

Dr. Melissa L.Kemp, Co-Advisor  
School of Biomedical Engineering  
*Georgia Institute of Technology/Emory  
University*

Dr. Hang Lu, Co-Advisor  
School of Chemical & Biomolecular  
Engineering  
*Georgia Institute of Technology*

Dr. Harry Asada  
School of Mechanical Engineering  
*Massachusetts Institute of Technology*

Dr. Robert Butera  
School of Electrical & Computer  
Engineering  
*Georgia Institute of Technology/Emory  
University*

Dr. Niren Murthy  
School of Bioengineering  
*UC Berkeley*

Dr. Cheng Zhu  
School of Mechanical Engineering  
*Georgia Institute of Technology*

Date Approved: June 21<sup>st</sup>, 2012

*To my parents*

## ACKNOWLEDGEMENTS

First and foremost, I would like to thank my co-advisors, Dr. Melissa L. Kemp and Dr. Hang Lu who have been wonderful mentors. They have both created an open and nurturing lab environment and this work could not have been completed without their advice, patience, optimism and constant support. I also would like to thank all my committee members, Dr. Harry Asada, Dr. Robert Butera, Dr. Niren Murthy and Dr. Cheng Zhu for their expertise, constructive criticism and guidance through this process.

I also would like to thank the technical and administrative staff in IBB and in the biomedical engineering department, in particular Steve Woodard and Nadia Boguslavsky for their patience and expertise concerning core equipment.

I would like to thank all the members of the Kemp and Lu Lab, as well as all the students and post-docs in Wing 1D for their camaraderie and the delightful work atmosphere. I would like to mention in particular Dr. Kwanghun Chung and Dr Alison Paul who taught me all I know today about microfluidics. In the Kemp Lab, I would like to thank especially Linda Kippner for being an awesome friend and lab manager and Gaurav Dwivedi for the fruitful discussions and keeping the same late hours. I worked closely with Abby Hill and Anish Potnis for this thesis. I would like to thank them for their eagerness to learn and to help as well as their scientific contribution.

Finally, and most importantly, I thank my family for their constant support and love.

## TABLE OF CONTENTS

|                                                                                              | Page |
|----------------------------------------------------------------------------------------------|------|
| ACKNOWLEDGEMENTS                                                                             | iv   |
| LIST OF TABLES                                                                               | ix   |
| LIST OF FIGURES                                                                              | x    |
| SUMMARY                                                                                      | xiii |
| <br><u>CHAPTER</u>                                                                           |      |
| 1 INTRODUCTION                                                                               | 1    |
| 1.1 Research objectives                                                                      | 2    |
| 1.2 Significance of results                                                                  | 3    |
| 2 LITERATURE REVIEW                                                                          | 6    |
| 2.1 The aging of the immune system or immunosenescence                                       | 6    |
| 2.2 Adoptive T cell transfer and immunosenescence                                            | 7    |
| 2.3 CD8+ T cell signaling in aging                                                           | 7    |
| 2.4 Quantifying and predicting senescence                                                    | 8    |
| 2.5 ROS as a signaling molecule in lymphocytes                                               | 9    |
| 2.5 ROS in lymphocyte aging                                                                  | 10   |
| 2.7 Ca <sup>2+</sup> as a signaling molecule in lymphocytes                                  | 11   |
| 2.8 Known interactions between ROS and Ca <sup>2+</sup> signaling                            | 12   |
| 2.9 Microfluidics as an excellent tool for biological experiments                            | 13   |
| 2.10 Using computational modeling tools to extract dominant signaling features and processes | 14   |

|        |                                                                                                                                                       |    |
|--------|-------------------------------------------------------------------------------------------------------------------------------------------------------|----|
| 3      | PHENOTYPICAL AND SIGNALING BIOMARKERS OF SENESCENCE IN<br>IN VITRO LONG-TERM CULTURE OF CYTOTOXIC T CELLS                                             | 16 |
| 3.1    | Introduction                                                                                                                                          | 16 |
| 3.2    | Results                                                                                                                                               | 19 |
| 3.2.1. | Parallel multi-time point cell stimulation and lysis on-chip for<br>studying early signaling events                                                   | 19 |
| 3.2.2. | Multi-time point cell stimulation and simultaneous lysis and fixation<br>on-chip. Device design and operation                                         | 21 |
| 3.2.3. | Global characteristics of age-associated protein expression and<br>activation changes in human CD8+ T cells                                           | 25 |
| 3.2.4. | A combination of dynamic signaling and expression metrics (Lck,<br>ERK, CD28 and CD27) are the most informative markers in predicting<br>cellular age | 32 |
| 3.3    | Discussion                                                                                                                                            | 39 |
| 3.4    | Conclusion                                                                                                                                            | 45 |
| 3.5    | Material & Methods                                                                                                                                    | 45 |
| 4      | REDOX-RELATED MARKERS OF SENESCENCE ARE ALTERED BY <i>IN</i><br><i>VITRO</i> LONG-TERM CULTURE OF CD8+ T CELLS                                        | 52 |
| 4.1    | Introduction                                                                                                                                          | 52 |
| 4.2    | Results                                                                                                                                               | 54 |
| 4.2.1  | RT-qPCR gene expression profile of young CD8+ T cells                                                                                                 | 54 |
| 4.2.2. | Age-related modifications in gene expression of redox-related<br>proteins                                                                             | 56 |
| 4.2.3. | Age-related modifications in total amounts of the redox-related<br>proteins Prx2, Grx1, Duox1                                                         | 57 |
| 4.2.4. | Age-related modifications in overall cellular redox status                                                                                            | 59 |
| 4.3    | Discussion                                                                                                                                            | 61 |
| 4.4    | Conclusion                                                                                                                                            | 65 |
| 4.5    | Materials & Methods                                                                                                                                   | 66 |

|        |                                                                                                                                               |     |
|--------|-----------------------------------------------------------------------------------------------------------------------------------------------|-----|
| 5      | CALCIUM SIGNALING IS ALTERED IN <i>IN VITRO</i> LONG-TERM CULTURED CD8+ T CELLS                                                               | 70  |
| 5.1.   | Introduction                                                                                                                                  | 70  |
| 5.2.   | Computational model of calcium dynamics in T lymphocytes                                                                                      | 72  |
| 5.2.1. | Model description                                                                                                                             | 72  |
| 5.2.2. | Model optimization and simulation                                                                                                             | 80  |
| 5.3.   | Results                                                                                                                                       | 82  |
| 5.3.1. | Parameter and species fitting                                                                                                                 | 82  |
| 5.3.2. | Calcium signaling of <i>in vitro</i> aging T cells                                                                                            | 87  |
| 5.3.3. | Changes in mRNA levels of plasma membrane channels are not sufficient to explain age-related changes in cytoplasmic Ca <sup>2+</sup> dynamics | 88  |
| 5.3.4. | Model predictions                                                                                                                             | 90  |
| 5.4.   | Discussion                                                                                                                                    | 92  |
| 5.5.   | Conclusion                                                                                                                                    | 97  |
| 5.6.   | Materials & Methods                                                                                                                           | 98  |
| 6      | IMAGING SINGLE-CELL SIGNALING DYNAMICS WITH A DETERMINISTIC HIGH-DENSITY SINGLE-CELL TRAP ARRAY                                               | 101 |
| 6.1.   | Introduction                                                                                                                                  | 101 |
| 6.2.   | Author's contribution                                                                                                                         | 104 |
| 6.3.   | Results                                                                                                                                       | 104 |
| 6.3.1. | Design of an efficient microfluidic single-cell trap array                                                                                    | 104 |
| 6.3.2. | Optimization of single cell loading efficiency                                                                                                | 107 |
| 6.3.3. | On-chip microscopy and cell study                                                                                                             | 108 |
| 6.4.   | Discussion                                                                                                                                    | 113 |
| 6.5.   | Conclusion                                                                                                                                    | 117 |
| 6.6.   | Materials & Methods                                                                                                                           | 118 |

|             |                                                                                                       |     |
|-------------|-------------------------------------------------------------------------------------------------------|-----|
| 7           | FREQUENCY RESPONSE ANALYSIS OF CROSS-TALK BETWEEN ROS AND $\text{Ca}^{2+}$                            | 122 |
| 7.1.        | Introduction                                                                                          | 122 |
| 7.2.        | Computational model of $\text{Ca}^{2+}$ -ROS cross-talk in T lymphocytes                              | 124 |
| 7.2.1.      | Model description                                                                                     | 124 |
| 7.2.2.      | Module 1                                                                                              | 126 |
| 7.2.3.      | Module 2                                                                                              | 132 |
| 7.2.4.      | Model optimization and simulation in the time domain                                                  | 138 |
| 7.2.5.      | Frequency response analysis                                                                           | 142 |
| 7.3.        | Results                                                                                               | 146 |
| 7.3.1.      | Cellular redox status affects $\text{Ca}^{2+}$ response to $\text{H}_2\text{O}_2$ and TCR stimulation | 146 |
| 7.3.2.      | Computational model of $\text{Ca}^{2+}$ /ROS cross-talk                                               | 148 |
| 7.3.3.      | $\text{Ca}^{2+}$ /ROS cross-talk model frequency response                                             | 150 |
| 7.3.4.      | Generation and delivery of chemical pulses to Jurkat cells                                            | 156 |
| 7.3.5.      | Cell response to a periodic input of $\text{H}_2\text{O}_2$                                           | 158 |
| 7.4.        | Conclusion                                                                                            | 162 |
| 7.5.        | Materials & Methods                                                                                   | 165 |
| 8           | Conclusion                                                                                            | 170 |
| 8.1.        | Impact in the field                                                                                   | 170 |
| 8.2.        | Future research directions                                                                            | 175 |
| APPENDIX A: | APPENDIX CHAPTER 3                                                                                    | 180 |
| APPENDIX B: | APPENDIX CHAPTER 4                                                                                    | 192 |
| APPENDIX C: | APPENDIX CHAPTER 5                                                                                    | 197 |
| APPENDIX D: | APPENDIX CHAPTER 6                                                                                    | 199 |
| APPENDIX E: | APPENDIX CHAPTER 7                                                                                    | 205 |



|                                                         |     |
|---------------------------------------------------------|-----|
| APPENDIX F: $\text{CA}^{2+}$ SIGNALING MODEL            | 216 |
| APPENDIX G: $\text{ROS}/\text{CA}^{2+}$ SIGNALING MODEL | 226 |
| APPENDIX H: MATLAB SCRIPT SINGLE CELL ANALYSIS          | 234 |
| REFERENCES                                              | 242 |

## LIST OF TABLES

|                                                                                                                                             | Page |
|---------------------------------------------------------------------------------------------------------------------------------------------|------|
| Table 3-1: Day in culture when assayed and corresponding PD for each donor. ....                                                            | 47   |
| Table 4-1: Normalized mRNA levels of individual genes expressed in young CD8+ T cells, ranked in descending order of expression (n=6). .... | 55   |
| Table 5-1: Initial conditions.....                                                                                                          | 80   |
| Table 5-2: Model parameters bounds for optimization.....                                                                                    | 81   |
| Table 5-3: Optimized parameter values for the Jurkat cell model and the "young" CD8+ T cell model.....                                      | 85   |
| Table 6-1: Calcium response to various ionomycin concentrations .....                                                                       | 113  |
| Table 7-1: Initial conditions.....                                                                                                          | 138  |
| Table 7-2: Model parameter values .....                                                                                                     | 140  |

## LIST OF FIGURES

|                                                                                                                                       |     |
|---------------------------------------------------------------------------------------------------------------------------------------|-----|
| Figure 3-1: Microfluidic chip for multi-time point cell stimulation and lysis .....                                                   | 20  |
| Figure 3-2: Microfluidic device for cell stimulation and simultaneous fixing or lysing..                                              | 23  |
| Figure 3-3: Dynamics of ERK phosphorylation measured by flow cytometry on fixed samples and bead-based immunoassay on lysates.. ..... | 24  |
| Figure 3-4: Complete aging dataset.. .....                                                                                            | 26  |
| Figure 3-5: Time course of population doublings for each donor. ....                                                                  | 27  |
| Figure 3-6: Cell cycle, surface marker expression and signaling trends over time in culture. ....                                     | 30  |
| Figure 3-7: Cellular age prediction with signaling measurements and phenotypic markers using a multivariate regression model.. .....  | 35  |
| Figure 3-8: Cellular age prediction from signaling data only.....                                                                     | 37  |
| Figure 3-9: Surface marker prediction from signaling information.....                                                                 | 38  |
|                                                                                                                                       |     |
| Figure 4-1: Fold changes in gene expression of redox related proteins .....                                                           | 57  |
| Figure 4-2: Duox1 protein levels.. .....                                                                                              | 58  |
| Figure 4-3: Relative fold changes in Grx1 and Prx2 protein expression.....                                                            | 59  |
| Figure 4-4: Total glutathione levels and corresponding GSH/GSSG redox potential.....                                                  | 60  |
| Figure 4-5: Trx levels.....                                                                                                           | 61  |
|                                                                                                                                       |     |
| Figure 5-1: Schematic of the $\text{Ca}^{2+}$ signaling model .....                                                                   | 74  |
| Figure 5-2: PLC- $\gamma$ phosphorylation dynamics following TCR stimulation.....                                                     | 82  |
| Figure 5-3: Time course of $\text{IP}_3$ and $\text{Ca}^{2+}$ in Jurkat cells.. .....                                                 | 84  |
| Figure 5-4: Model predictions of $\text{IP}_3$ and $\text{Ca}^{2+}$ dynamics in CD8+ T cells. ....                                    | 85  |
| Figure 5-5: Age related $\text{Ca}^{2+}$ changes in CD8+ T cells.....                                                                 | 88  |
| Figure 5-6: Changes in mRNA levels of $\text{Ca}^{2+}$ channels and pumps with age. ....                                              | 89  |
| Figure 5-7: Model sensitivity analysis.....                                                                                           | 91  |
| Figure 5-8: Model predictions of $\text{Ca}^{2+}$ dynamics in old T cells.....                                                        | 92  |
|                                                                                                                                       |     |
| Figure 6-1: Design and principle of single-cell trapping array.....                                                                   | 106 |
| Figure 6-2: Characterizing trapping efficiency. ....                                                                                  | 108 |
| Figure 6-3: High-resolution imaging of cellular features and activities. ....                                                         | 110 |
| Figure 6-4: Calcium dynamics in response to ionomycin stimulation of multiple cells tracked on chip.....                              | 112 |
|                                                                                                                                       |     |
| Figure 7-1: Schematic of the $\text{Ca}^{2+}$ /ROS cross-talk model in T cells.. .....                                                | 126 |
| Figure 7-2: Average traces of $\text{Ca}^{2+}$ dynamics following TCR stimulation in the presence of antioxidants.....                | 146 |
| Figure 7-3: Cell response to 5 min perfusion with DTT and bolus of 100 $\mu\text{M}$ $\text{H}_2\text{O}_2$ .....                     | 149 |
| Figure 7-4: ER ROS levels after $\text{Ca}^{2+}$ release from the ER intracellular stores.....                                        | 150 |
| Figure 7-5: Transient response of cytosolic $\text{Ca}^{2+}$ in response to a 10 min period ROS input. ....                           | 151 |
| Figure 7-6: Cytosolic $\text{Ca}^{2+}$ in response to ROS stimulus input of different periods.....                                    | 152 |
| Figure 7-7: Bode plots of the multiple output system.....                                                                             | 154 |
| Figure 7-8: Fit of a first order transfer function for cytosolic $\text{Ca}^{2+}$ . ....                                              | 155 |

|                                                                                                                                                                                    |     |
|------------------------------------------------------------------------------------------------------------------------------------------------------------------------------------|-----|
| Figure 7-9: Characterization of on-chip chemical pulses. ....                                                                                                                      | 158 |
| Figure 7-10: Single cell analysis of calcium responses to waves of H <sub>2</sub> O <sub>2</sub> (10 min period, 50 $\mu$ M) and quantified for oscillations in fluorescence. .... | 160 |
| Figure 7-11: Impact of stimulus input amplitude on single cell response to a 10 minute period H <sub>2</sub> O <sub>2</sub> treatment.....                                         | 161 |
| Figure 7-12: Effect of the input amplitude on cytosolic Ca <sup>2+</sup> gain and phase. ....                                                                                      | 162 |

## SUMMARY

Immunotherapies are currently investigated as a potential treatment for cancer. Compared to traditional chemotherapies, adoptive T cell transfer therapy has shown promising results in clinical trials for patients with solid tumors. However, the complete remission success rate is still low, around 10%. This treatment relies on the rapid *ex vivo* expansion of CD8<sup>+</sup> cytotoxic tumor-specific T cells and their reintroduction in the patient's body to fight the tumors. Successful treatment requires the reintroduced cells to retain tumor antigen specificity, effector function and to maintain proliferative potential; yet T cells like other somatic cells have a finite replicative potential and multiple rounds of antigenic stimulation required for rapid expansion result in a state of immunosenescence characterized by absence of proliferation, resistance to apoptosis and decreased effector functions. The reintroduction of those non-functional senescent cells has been highlighted as a potential reason for the relatively high failure rate.

The objective of this thesis is to offer two approaches towards an improvement of treatment efficacy. First, a 'senescence metric' can be generated from identification of biomarkers of senescence and could be used in the clinic towards predicting age and responsiveness of T cells prior to transfer. The second approach is to understand at the molecular level the changes that occur during *ex vivo* expansion to devise improved expansion culture conditions. In particular, we focused in this thesis on the shift towards a pro-oxidizing environment and its potential effects on Ca<sup>2+</sup> signaling. Microfluidic tools were extensively developed and used to acquire experimental data of quality and computational models for subsequent data analysis and prediction.

To identify biomarkers of aging and generate our ‘senescence metric’, we reproduced the adoptive T cell transfer culture conditions and characterized signaling dynamics, surface marker expression, cell cycle, cellular morphology and senescence-related protein expression at the single cell and population level at different time in culture. We designed a new microfluidic platform to assay signaling information with excellent time-resolution. This two-module device performs simultaneously multi-time point cell stimulation with chemical stimuli and subsequent lysis and fixation of the same initial stimulated cell population. Followed with a multiplexed phospho-protein assay, a single experiment yields 48 signaling measurements with time points ranging from 30 seconds to 7 minutes, with only 5% of the number of cells that would be needed in a traditional assay which makes this device attractive for clinical use or applications with rare cells. The dataset containing dynamic and static measurements was analyzed using a partial least square regression (PLSR) model. Despite a large donor-to-donor variability the model is able to determine relative contributions of each metric to the phenotype of replicative senescence and predict T cell age with an accuracy of 95%. It highlights the importance of using a combination of metrics rather than a single one to predict age in culture and in particular emphasizes the importance of early signaling dynamics and population noise as a metric to explain and predict T cell age.

In this study, we observed a gradual decrease in protein phosphorylation dynamics with time in culture, which would suggest reduced  $\text{Ca}^{2+}$  dynamics, as it has been observed in T cells from elderly subjects and murine models; yet we did not observe decreased  $\text{Ca}^{2+}$  amplitude or sustained levels with time in culture. Counterintuitively, older T cells displayed overall faster dynamics. Gene expression analysis showed mRNA

overexpression of the plasma membrane  $\text{Ca}^{2+}$  channel and pumps, respectively ORAI1 and PMCA; yet based on our current understanding of the  $\text{Ca}^{2+}$  signaling network, these changes should not result in faster dynamics. To understand this puzzling result we constructed a deterministic ODE-based model of T cell  $\text{Ca}^{2+}$  signaling that can recapitulate main features of  $\text{Ca}^{2+}$  signaling after TCR stimulation in Jurkat cells, a T cell model cell line and young primary CD8+ T cells. The model suggests  $\text{IP}_3\text{R}$ , SERCA and STIM1 as targets of regulation that may be altered by post-translational modifications during *in vitro* aging, possibly oxidation.

Because ROS is a hallmark of aging in many cell types, we investigated whether oxidative damage occurs in long-term cultured cells for ACT. Using quantitative RT-qPCR, HPLC and redox western blots, we show that *in vitro* expanded T cells behold a redox remodeling towards a pro-oxidative environment, similar to what has been observed *in vivo*. This result points towards a possible addition of antioxidants in cell culture or using hypoxic culture conditions to prevent oxidative damage.

Our modeling analysis of  $\text{Ca}^{2+}$  signaling dysregulation during *in vitro* aging pointed to several kinetic parameters associated with purported oxidative modifications on  $\text{Ca}^{2+}$  channels. Several other disease states, such as Alzheimer's or Parkinson's disease, are characterized by a high oxidative environment and improper  $\text{Ca}^{2+}$  signaling. Because regulation of the levels of these two signaling molecules is tightly interconnected, we expanded our  $\text{Ca}^{2+}$  signaling model to incorporate the numerous ROS/ $\text{Ca}^{2+}$  cross-talk and used frequency response analysis to periodical stimuli of oxidative damage to analyze the system. The model predicted cells act like a low-pass filter with a bandwidth dependent on input concentration and cell compartment,

highlighting robustness in the cellular network able to reject high frequency disturbances at low concentration of oxidative stress but taking these signals into account for higher input concentration. To validate this model, an experimental platform able to retain T cells in specific locations while exposing them to periodical stimuli was required. To meet those needs, we designed a new deterministic single-cell trap array for imaging of  $\text{Ca}^{2+}$  dynamics in single T cells and imaged single cell response to periodical  $\text{H}_2\text{O}_2$  stimuli. At the population level, T cells are able to follow the sinusoidal input stimulus; yet a large heterogeneity in responses is observed at the single cell level, in particular in amplitude and phase. Although our experimental data show large non-linearities that are not well captured by the model, this study is an important proof of concept. It highlights the feasibility of experimentally probing the frequency response of non-adherent mammalian cells to extract important features of regulation.



# CHAPTER 1

## INTRODUCTION

The goal of cancer immunotherapies is to boost the immune system's ability to detect tumor antigens and mount an effective anti-tumor immune response. Currently, adoptive T cell transfer therapy (ACT), the administration of *ex vivo* expanded autologous tumor-specific T cells, is one of the most promising immunotherapies to induce durable clinical responses in significant number of cancer patients (1, 2); yet, its efficacy has been limited so far with a mere 10% complete remission rate in the most successful clinical trials (3). The prolonged *ex vivo* culture process is a potential reason for this ineffectiveness because the transfused cells may have reached a state of replicative senescence and immunosenescence and no longer be responsive (4, 5). Although the mechanism leading to immunosenescence is not fully understood, current theories implicate telomere shortening (6) and an oxidative shift in the intracellular environment leading to the cumulative damage in mitochondrial DNA, proteins and lipids by reactive oxygen species (ROS) (7-11). Because ROS are used as second messengers, alteration in ROS regulation can lead to changes in gene expression, replication and in impaired immunity or inflammatory responses. ROS has been postulated as being a key effector inducing cell senescence. However the mechanism by which ROS production and regulation is altering signaling in aging peripheral T cells is poorly understood.

Microfluidic devices are excellent tools to perform biological experiments. Along with reduced reagent consumption and sample handling error, microfluidics

offers the ability to tightly control chemical environments and cellular location (12-15). The combined development and use of microfluidic technologies and computational models will improve our understanding of the phenotypic and dynamic changes occurring in T cells during the course of immunosenescence and promise to have a significant impact on the design of future cancer immunotherapy protocols.

### **1.1. Research objectives**

The objectives of this research are to develop new microfluidic tools and use computational models in order to: (1) Characterize phenotypic and dynamic changes occurring during ACT compatible long-term culture of CD8<sup>+</sup> T cells; (2) Develop a quantifiable measure of T cell quality or degree of senescence prior to adoptive transfer; (3) Assess the redox status of the cell during *in vitro* aging and quantify its impact on cell signaling, more specifically Ca<sup>2+</sup> signaling.

Based on these research objectives, the specific aims of this thesis are as follows:

**Aim 1: Develop a method to quantify and predict responsiveness in senescing T cells cytotoxic T cell using signaling and static biomarkers:** The purpose of this aim was to characterize changes in cell phenotype and signaling during *in vitro* aging under culture conditions consistent with *in vitro* expansion prior to adoptive transfer and use these features to create a metric of cell senescence. We designed a microfluidic platform to sample phosphorylation events occurring in the first few minutes after TCR stimulation by simultaneously fixing and lysing a fraction of stimulated cells. Combined with differentiation surface marker expression, cell cycle and selected senescence-related

protein expression, we built a large dataset of age-related changes in CD8+ T cells. To analyze this dataset we applied a partial least square regression (PLSR) model and extracted the most important metrics of *in vitro* aging. Characterization of signaling dynamics and phenotypic changes during *in vitro* aging as well as extraction of the best biomarkers of senescence are described in Chapter 3.

**Aim 2: Characterize changes in redox status and  $\text{Ca}^{2+}$  signaling in aging**

**CD8+ T cells:** The purpose of this aim was to determine if culture conditions used for T cell expansion prior to adoptive transfer results in reduced  $\text{Ca}^{2+}$  signaling and a pro-oxidizing shift in redox environment as observed *in vivo*. To assess changes in redox status, we measured mRNA levels of a set of 84 genes involved in the oxidative stress and antioxidant pathways, protein levels of a subset of sources of ROS and antioxidants as well as the redox potential of the thioredoxin (Trx-1) and glutathione couple (GSH/GSSG).  $\text{Ca}^{2+}$  dynamics after TCR stimulation were measured and a computational model of  $\text{Ca}^{2+}$  signaling was developed to provide insight into potential targets of age-related modifications resulting in altered  $\text{Ca}^{2+}$  dynamics. The modeling analysis pointed to several kinetic parameters that are likely altered during the aging process; these parameters provide avenues for further investigation by suggesting post-translational modifications of the  $\text{Ca}^{2+}$ -related proteins. Chapter 4 presents results of our characterization of redox-related changes in these culture conditions. Chapter 5 presents changes in  $\text{Ca}^{2+}$  dynamics and the mathematical model used to infer potential perturbation in nodes of the network resulting in these changes.

**Aim 3: Investigate cross-talk between ROS and  $\text{Ca}^{2+}$  as it pertains to signaling and pathologies:** The purpose of this aim was to create a map of interactions between these two signaling molecules and understand how oxidative stress can modulate  $\text{Ca}^{2+}$  signaling. To permit the acquisition of single-cell live imaging data of  $\text{Ca}^{2+}$  signaling under temporally varying conditions of oxidative stress, we designed a deterministic, high-density single-cell trap array microfluidic platform for semi-automated cell trapping, stimulation and imaging. Because of the large degree of cross-talk between ROS and  $\text{Ca}^{2+}$  that are hard to independently examine experimentally, we developed an ODE-based computational model and analyzed it in the frequency domain to discriminate interactions in terms of timescales. Validation of the model was experimentally performed using the single cell trap microfluidic platform and periodic stimulation of T cells. The microfluidic platform used to acquire live single cell experimental data is presented in Chapter 6, while the ROS/ $\text{Ca}^{2+}$  cross-talk computational model and its validation are described in Chapter 7.

### **1.2. Significance of results**

ACT efficacy largely depends on the quality of the transferred cytotoxic tumor-specific lymphocytes in terms of specificity, functionality and further *in vivo* proliferation. Transfusion of cells in a state of senescence would therefore hinder the immunotherapy's effectiveness. Currently, there is no standard method to assess the quality of a mixed CD8<sup>+</sup> T cell population's immune response and its degree of senescence. Loss of CD28 has been associated with senescent CD8<sup>+</sup> T cell population (16); yet its expression can be modulated by inflammatory cytokines (17-19) and CD28<sup>-</sup>

cells have been shown to still be able to proliferate (20). A more robust metric for senescence requires a combination of biomarkers and therefore there is a need for a large scale characterization of the alterations occurring during *in vitro* aging. A reliable ‘senescence metric’ would have a significant impact on the efficacy of the treatment but also on the design of new culture expansion methods.

Because of the role of ROS as both a signaling molecule in normal physiology and a damaging agent during oxidative stress that can lead to acquisition and maintenance of a senescence phenotype (21), the characterization of the cellular redox environment during *in vitro* aging can provide new insight into the potential efficacy of antioxidant treatment or hypoxic culture conditions.

The union of microfluidics and computational modeling is central to acquire and analyze experimental datasets, and then gain a better understanding of the biological system to further generate and test new hypothesis. In particular, the development of new microfluidic platforms for high-throughput analysis of single live cells and robust generation of biochemical samples enables the acquisition of high-quality experimental data at the single cell and population level to study T cell aging. We envision these platforms to be used in a clinical setting, for drug screens or to study other fundamental biological processes.

## CHAPTER 2

### LITERATURE REVIEW

#### **2.1 The aging of the immune system or immunosenescence**

As a result of advances in medicine, the overall life expectancy of an individual has increased, and the US Census Bureau predicts that 25% of the US population will be comprised of individuals over 65. Living longer is good news, but it is also associated with chronic disease, increased susceptibility to infections, cardiovascular diseases, cancers, autoimmune disorders, chronic inflammatory diseases. Although aging affects multiple organs, the impact of aging on the immune system has widespread repercussion, in terms of response to vaccines and infections, as well as cancer (22-24).

Immunosenescence is the name given to the global age-associated immune dysfunctions. Although it is generally accepted that some aspects of innate immunity are well preserved during aging, the existence of age related alterations on the innate system have been reported (25-28). More attention has been paid to age related changes in the adaptive immune system. Thymus involution results in an inability to produce new naïve T cells and T cell repertoire shrinkage (29). Fewer number of CD4<sup>+</sup> T cells express CD28 (30). The number of terminally differentiated cytotoxic CD8<sup>+</sup>/CD28<sup>-</sup> memory T cells increase (31-33). These cells have shortened telomeres, mainly because of the loss of the costimulatory receptor CD28 and are unable to further proliferate.

Pawelec introduced the concept of an “immunological space” filled with unresponsive, non-proliferative and resistant to apoptosis T cells (34). Many of these CD8<sup>+</sup> cells carry receptors for CMV, EBV or HSB (persistent herpes viruses), suggesting immune exhaustion due to chronic antigenic stress (35, 36).

Immunosenescence has very serious clinical consequences. It is partly responsible for the increased incidence of autoimmune diseases, infections or cancers, and subsequently decreased longevity.

## **2.2 Adoptive T cell transfer therapy and immunosenescence**

Adoptive transfer is based on the principle of isolation and infusion of antigen specific or nonspecific lymphocytes with the aim of replacing, repairing or enhancing immune function. In particular, adoptive T cell therapy (ACT) has induced regression of malignant solid tumors in early-stage clinical trials for cancer patients with metastatic melanoma, malignant gliomas, renal carcinoma and ovarian cancer (37). The success of this therapy depends on the ability to optimally select or genetically engineer cells with targeted antigen specificity and then induce the cells to proliferate *in vivo* while preserving their effector function and engraftment and homing abilities. A potential cause of previous unsuccessful ACT clinical trials may have been the reintroduction of a non-functional T cell population that had reached or was near replicative senescence (38). Preservation of replicative potential by telomere engineering or optimized culture condition might improve the engraftment and persistence of adoptively transferred cells.

## **2.3 CD8+ T cell signaling in aging**

In addition to the study of age-related modifications in elderly CD8+ T cells, *in vivo* model of replicative senescence have been developed, replicating characteristics observed in elderly (39). Senescent cells are unable to respond to antigenic cues or IL-2 stimulation, present striking alterations in functions and gene and protein expression

leading to decreased IL-2 production, irreversible cell cycle arrest, and resistance to apoptosis (23). In an earlier study, almost all molecules of the signaling pathways elicited by TCR were found to have decreased activation in human or mouse T cells with aging (40). Loss of CD28 (30), or deficiencies in lipid raft functions, leading to impaired membrane protein motility necessary to form the immune synapse with an antigen presenting cell (APC) (41-43) are possible mechanisms leading to the decreased activation. However, despite these general principles, some debate exists on specific proteins. Depending on the mammalian model and the cell differentiation status, there is no consensus on the alterations of those proteins (44, 45).

#### **2.4 Quantifying and predicting senescence**

The OCTO and NONA longitudinal study had the aim of defining an “immune risk profile”, based on the immunophenotype of elderly populations. Predictive factors extracted from the study comprise high CD8/CD4 ratio, few naïve cells and increased numbers of late differentiated CD8+CD28- T cells but it was found later that the “immune risk profile” characterized previously did not apply to centenarians (46). A similar metric has been developed by Hirokawa *et al.* to assess the extent of the age-related decline of immune functions of individual before and after immunological restoration (47).

Certain immunotherapies utilize solely CD8+ T cells and cannot use the metrics previously described as they rely mainly on the ratios of different cell subpopulations. It has been proposed to use the absence of CD28 (31) or the appearance of late differentiation marker CD57 (48) as markers of T cell senescence. However, univariate,



static assays measuring expression of surface markers alone are not always accurate for prediction of senescence (17-19) and combinations of biomarkers need to be considered to quantitatively predict the level of senescence in a population (49-52). To date, prior proteomic and microarray studies have not attempted to determine the most informative metrics of cellular senescence for the purposes of generating predictive models of T cell function, and relate to functional dynamics of TCR activation.

### **2.5 ROS in lymphocyte aging**

The imbalance between the production of free radicals and antioxidant defenses is a characteristic of the aging process. In other cellular systems, it has been shown that while antioxidant defenses decrease (53, 54), production of ROS from mitochondrial leakage (55, 56) or overexpressed NADPH oxidases (57, 58) lead to an oxidative shift in the cell cytoplasm. A dynamic feedback loop between ROS production and DNA damage response induced senescence has been demonstrated in human fibroblasts to maintain the senescence state (59), as well as a ROS-mediated bystander effect to spread senescence in fibroblasts cell clusters (60).

Lymphocytes are affected by non-specific sequels of the aging process such as oxidative stress or glycation (10, 11, 61, 62). DNA damage and repair increase (63, 64) while proteasomal (11, 65) and methionine sulfoxide reductases A (66) activities decrease leading to the accumulation of oxidized non-functional proteins. Increase in mitochondrial leakage (67-69) and resulting mitochondrial DNA damage (70) has been demonstrated. However, to our knowledge, the alterations in the intracellular antioxidant

and ROS production capacity by NADPH oxidases with *in vitro* aging have not been characterized.

Clinical trials involving antioxidant supplementation have shown mixed results so far. In rodents, overexpression of catalase (71) and thioredoxin (72) or intake of the antioxidant thioproline (73) resulted in increased lymphocyte function and overall lifespan (73). In humans, antioxidant intake was inconclusive (74-76).

## **2.6 ROS as a signaling molecule in lymphocytes**

During T cell receptor engagement, a rapid oxidative burst occurs to regulate and enhance downstream protein activation. The generation of free radicals by the mitochondria has been proposed as a source of early TCR stimulated ROS (77). However, the majority of ROS production has been attributed to non-phagocytic NADPH oxidases, Duox1 and Nox2 (78, 79). The  $\text{Ca}^{2+}$  sensitive Duox1 is responsible for the early phase of  $\text{H}_2\text{O}_2$  generation occurring within 2 to 4 minutes after TCR stimulation (79). Nox2 gets activated 20 minutes later and produces superoxide anions (78, 80). Key regulators of T cell activation can be glutathionylated, leading to an increase (Ras) or decrease in their activity (MEKK1). Protein phosphatases are also known to be regulated by glutathionylation or disulfide formation (81). Intracellular glutathione levels are tightly controlled in lymphocytes (82) and the intracellular redox network tightly controlled to protect against deviations in the redox states (83).

## **2.7 $\text{Ca}^{2+}$ as a signaling molecule in lymphocytes**

$\text{Ca}^{2+}$  is a ubiquitous second messenger regulating signaling in lymphocytes. When a ligand binds to the TCR, tyrosine kinases Lck, LAT and Zap70 are recruited to the TCR/CD3 complex and ultimately activate phospholipase-C  $\gamma$  (PLC- $\gamma$ ). Phosphorylated PLC- $\gamma$  cleaves  $\text{PIP}_2$  to generate  $\text{IP}_3$ .  $\text{IP}_3$  binds to the  $\text{IP}_3$  receptors ( $\text{IP}_3\text{R}$ ) on the ER membrane and activates  $\text{Ca}^{2+}$  release. STIM1, an ER transmembrane protein, can sense  $\text{Ca}^{2+}$  store depletion, by the dissociation of  $\text{Ca}^{2+}$  from a binding site in the luminal portion, triggering a structural change. STIM1 then forms oligomers that migrate to ER-plasma membrane appositions in tens of seconds and recruits ORAI1, a pore subunit of the CRAC ( $\text{Ca}^{2+}$  release activated channel) channels located on the plasma membrane, and opens it possibly by binding to an N-terminal region of ORAI1 (84). To prevent early closure of the CRAC channel, mitochondria migrate to the immunological synapse and buffers local  $\text{Ca}^{2+}$  (85). SERCA on the ER membrane and PMCA pumps on the plasma membrane act as exit channels for  $\text{Ca}^{2+}$ , either by resequestration or release into the extracellular space.

An interesting feature of  $\text{Ca}^{2+}$  signaling is its ability to present oscillatory behaviors. At resting levels, random spontaneous spikes of  $\text{Ca}^{2+}$  release have been reported, probably due to stochastic  $\text{IP}_3$  receptor clustering (86, 87). When challenged with low levels of stimulation or partial depletion of stores, 5-10 mHz  $\text{Ca}^{2+}$  oscillations occur (88).  $\text{Ca}^{2+}$  oscillations enhance the efficiency of signaling to the nucleus and the oscillation frequency contributes to specific activation of transcription factors (89, 90). Evidence suggests that the oscillations are derived from the repetitive and coordinative opening and closing of CRAC channel, rather than from repetitive  $\text{Ca}^{2+}$  release from the ER. Intrinsic

delays might occur when STIM1 senses changes in store content, oligomerizes and migrates before opening the CRAC channel.

## **2.8 Known interactions between ROS and Ca<sup>2+</sup> signaling**

As described in section 5, ROS is a signaling molecule able to modulate strength of signaling. This section will focus on the interactions and cross-talk between ROS and Ca<sup>2+</sup> signaling as it pertains to lymphocyte signaling. Excellent recent general reviews of cross-talk between ROS and Ca<sup>2+</sup> can be found in (91-94).

In B lymphocytes, Ca<sup>2+</sup> and ROS generated upon BCR activation engage in a cooperative interaction that acts in a feedback manner to amplify the early signal generated (95). This cooperativity acts by regulating the concentrations of Ca<sup>2+</sup> and Duox1 produced ROS. The latter inactivates receptor-coupled phosphatases, fine-tuning kinases activity and, as a result, the net strength of the initial signal. In T cells, activation of Duox1, associated with the IP<sub>3</sub>R depends on Ca<sup>2+</sup> release from the ER and potentially phosphorylation of PKC (79).

The influence of Ca<sup>2+</sup> on ROS signaling can be summarized in a first approximation by Ca<sup>2+</sup> binding on Duox1. High concentration of mitochondrial Ca<sup>2+</sup> triggers mitochondrial permeability transition pore opening and enhances ROS production in isolated mitochondria (96-98).

The influence of ROS on Ca<sup>2+</sup> signaling on lymphocytes is more complex. It is believed that oxidation increases activity of IP<sub>3</sub>R (99) and RyR (100, 101). The close proximity of the mitochondria leaking free radicals might be responsible for stochastic modulation of these Ca<sup>2+</sup> release channels and subsequent Ca<sup>2+</sup> spikes. Oxidation also affects STIM1

and ORAI1, suggesting a role for ROS in the time delay in the opening of the CRAC channel. However, the role of ROS in SOCE (store-operated  $\text{Ca}^{2+}$  entry) is not clear yet (102). During oxidative stress in B lymphocytes, Hawkins *et al.* showed that S-glutathionylation of STIM1 leads to a decrease in  $\text{Ca}^{2+}$  binding, mimicking empty  $\text{Ca}^{2+}$  stores, and leading to constitutive activation of the CRAC channels, independently of ER  $\text{Ca}^{2+}$  concentration (103); conversely Prins *et al.* demonstrated binding of STIM1 to the ER oxidoreductase ERp57, inhibiting SOCE, suggesting a negative role of oxidation on STIM1 (104). Orai1 has been reported to be activated in a STIM1-dependent manner after  $\text{H}_2\text{O}_2$  exposure (105); but in another study, in T lymphocytes, ORAI1 was observed to be inhibited by oxidation of Cys195 by  $\text{H}_2\text{O}_2$  (106). Finally evidence on other model systems shows that  $\text{Ca}^{2+}$  uptake channels, such as SERCA on the ER (107-110) or PMCA (111, 112) on the plasma membrane are affected by ROS.

## **2.9 Microfluidics as an excellent tool for biological experiments**

Microfluidics or lab-on-a-chip is an emerging area wherein biological samples are manipulated on the micron length scale, or pico- to nano-liter by volume (113). Microfluidics is particularly suitable for high-throughput analysis and automation; because of the laminar flow conditions attainable on-chip, momentum, energy, and mass transport are deterministic and easily described by a set of well-known equations (114). Microsystems have made possible the study of very complex biological networks (115-121), and single-cell analysis (122) by enhancing uniformity and controllability in sample handling and treatment (12, 123, 124). Microfluidics also allows for generating complex temporal stimuli (125-127). Single cell analysis on non-adherent cells has been enabled

by the design of cell traps (128, 129), however there is an unmet need to balance the fabrication complexity and operational complexity and also enable large-scale high-resolution imaging.

## **2.10 Using computational modeling tools to extract dominant signaling features and processes**

Cells process a multitude of external stimuli through receptor and adaptor proteins that converge on a core set of signal-transduction pathways. The picture gets even more complicated when cross-talk and feedbacks are incorporated. How are such complex inputs converted into robust signaling outputs? Mathematical methods have been developed to identify the dominant molecular signals that contribute to the cell response.

Partial least square (PLS) regression analysis models have been applied previously to understand complex signaling networks involving multiple inputs and multiple outputs, without prior knowledge of the network structure (130-134). This data-driven modeling technique reduces the dimensionality of the dataset, extracts relationships between variables and can generate predictions.

Approaches based on control systems theory have been proposed and applied to determine (1) pathways that dominate observed dynamics; (2) how the network decodes different frequencies; (3) whether it may be blind to specific frequencies. By measuring amplitude and phase responses of *S. cerevisiae* to imposed artificial oscillations of osmotic choc, Mettetal. *et al.* reconstructed an abstract model of the osmotic stress response (135). Bennett *et al.* discovered a previously unknown level of regulation in the galactose-response pathway in *S. cerevisiae* by monitoring metabolic gene regulation to

periodic changes in the external carbon source (136). Chemotactic responses of *E. coli* to time varying stimuli revealed the structure of the feedback transfer function linking the amplification and adaptation modules (137). These studies exemplify an important, emerging niche for biological analysis, involving the union of microfluidics, real-time imaging of biochemical cellular responses, and computational modeling. The essence of this experimental approach is captured through precise, reproducible delivery of well-controlled patterns of stimulation to cells, real-time imaging of cellular responses, and effectively recapitulating these stimulation patterns in a computer model to see how the *in vivo* and *in silico* models compare (138). Studies involving mammalian cells bypassed cell exposure to periodical stimuli by using naturally occurring noise in protein expression as a diagnostic that can excite the system at many frequencies at once (139) or by creating an ODE model fitted to step induced experimental time courses and simulating *in silico* the frequency response of the pathway (140).

Optimization of microfluidic setups for mammalian cells with high-throughput capabilities, and fast-switching, versatile stimulation patterns will enable the validation of models generated with traditional ODE tools but analyzed in the frequency domain.

# CHAPTER 3

## PHENOTYPICAL AND SIGNALING BIOMARKERS OF SENESCENCE IN *IN VITRO* LONG-TERM CULTURE OF CYTOTOXIC T CELLS

### 3.1. Introduction

Immune cell-based therapies hold promise in cancer therapy by harnessing the body's natural defense mechanisms against tumors, while leaving healthy cells unharmed (141, 142). Among those therapies, adoptive transfer of T cells (ACT) has resulted in encouraging clinical trials for treating metastatic melanoma as well as non-Hodgkin's lymphoma, chronic lymphocytic leukemia and neuroblastoma (143-145). Although cancer cells are less immunogenic than pathogens, the adaptive immune system is able to recognize and eliminate tumor cells. Adoptive therapy with cytotoxic CD8<sup>+</sup> cells (CTLs) relies on the isolation of functional and tumor specific T cells and large *in vitro* clonal expansion. Once transferred back in the cancer patient, CTLs need to retain tumor specificity and proliferate further *in vivo* to establish an effective *in vivo* response and tumor shrinkage. *In vivo* persistence is a critical factor for elimination of residual or recurring malignant cells. The encouraging results of adoptive transfer therapy could be improved by enhancing the quality of transferred T cells. Cells derived from aged cancer patients have a skewed immune repertoire towards cells that underwent extensive clonal expansion against persistent antigens, resulting in few tumor-specific CTLs (22, 23, 32).

Adapted from Rivet, C. A., A. S. Hill, et al. (2011). "Predicting cytotoxic T-cell age from multivariate analysis of static and dynamic biomarkers." Mol Cell Proteomics **10**(3): M110 003921.



Once isolated the tumor infiltrating cells go through a prolonged *ex vivo* culture process. T cells, as other somatic cells, have a finite clonal lifespan. Extensive *in vitro* proliferation and clonal expansion result in T cell differentiation and ultimately replicative senescence (146). To obtain sufficient number of cells before transfer, tumor specific CTLs are activated and undergo several rounds of divisions, resulting in the progressive shortening of telomeres. Chronic antigenic stress and critically short telomere length lead CTLs to enter a state of senescence characterized by functional changes. Although extensively cultured CTLs retain antigen specificity for the tumor (147), they present striking alterations in function and gene and protein expressions (23), e.g. they are in an irreversible cell cycle arrest, apoptosis resistant, with short telomeres and unable to respond to antigenic cues or IL-2 stimulation. Once transferred in the cancer patient, these replicative senescent cells will not be able to eliminate tumor cells and further proliferate, thereby hindering the efficacy of these therapies (148, 149).

To ensure success of adoptive transfer therapy, it is desirable to evaluate T cell clones before transfer based upon their specificity or functionality, regardless of diverse *in vivo* priming, selection, or expansion methods. Similarly, evaluation of T cell clones in elderly population, or “immune signature”, can enable the identification of immune risk profiles correlated with increased risk of immune dysfunction and increased mortality (150). Phenotypic markers, such as the loss of expression of co-stimulatory markers CD27 (151) and CD28 (31), have been associated with senescent CD8<sup>+</sup> cell population; however, individual biomarkers are not sufficient to measure the fraction of senescent non-responsive cells. Previous proteomics and microarray studies suggest that clusters of parameters would be more appropriate to quantify age-related alterations (49, 51, 52,

152), and yet to date, prior proteomic and microarray studies have not attempted to determine the most informative metrics of cellular senescence for the purposes of generating predictive models of T cell function. To enable quantification of the “age” of T cells as they expand in culture through combinations of biomarkers, we applied a partial least square regression (PLSR) modeling analysis from data obtained under conditions consistent with *in vitro* expansion prior to adoptive transfer in patients. The multivariate model developed in the present study assesses the quality of T cell function through the use of phenotypic markers and protein signaling dynamics. To acquire signaling dynamics, we adapted a previously developed microfluidic device (12) to sample rapid phosphorylation events by simultaneous lysing and fixing of stimulated cells. This technology takes advantage of the uniformity and controllability in sample handling and treatment to reduce error associated with biochemical assays; at the same time, it requires a small number of cells and performs the assay in a high-throughput and parallel fashion (12, 123, 124). Lysates provide population-averaged measurements compatible with downstream proteomic techniques, while fixed cells analyzed by flow cytometry reveal subpopulations and phenotypic variations within genetically identical cells. The dataset containing signaling dynamics, cellular morphology, and surface expression levels acquired under the uniform, precise conditions of the microfluidic chip allowed the model to determine relative contributions of each metric to the phenotype of replicative senescence despite large donor-to-donor variability. The multivariate analysis highlights the importance of both averaged values and heterogeneity in the cell population for prediction of the replicative senescence within a T cell population.

## **3.2. Results**

### **3.2.1. Parallel multi-time point cell stimulation and lysis on-chip for studying early signaling events**

This microfluidic device has been developed in collaboration with Dr. Alison Paul during my Master's Thesis. It resulted in the following publication (12). The microfluidic chip used in this study is largely inspired by this previous work.

High time resolution acquisition of signaling dynamics is necessary to understand many biological processes related to cancer, immune responses or drug response and to generate quantitative data for accurate computational model generation. We have developed a robust two-module microfluidic platform for simultaneous multi-time point stimulation and lysis of T cells with a resolution down to 20s using only small amounts of cells and reagents (Figure 3.1) (12).

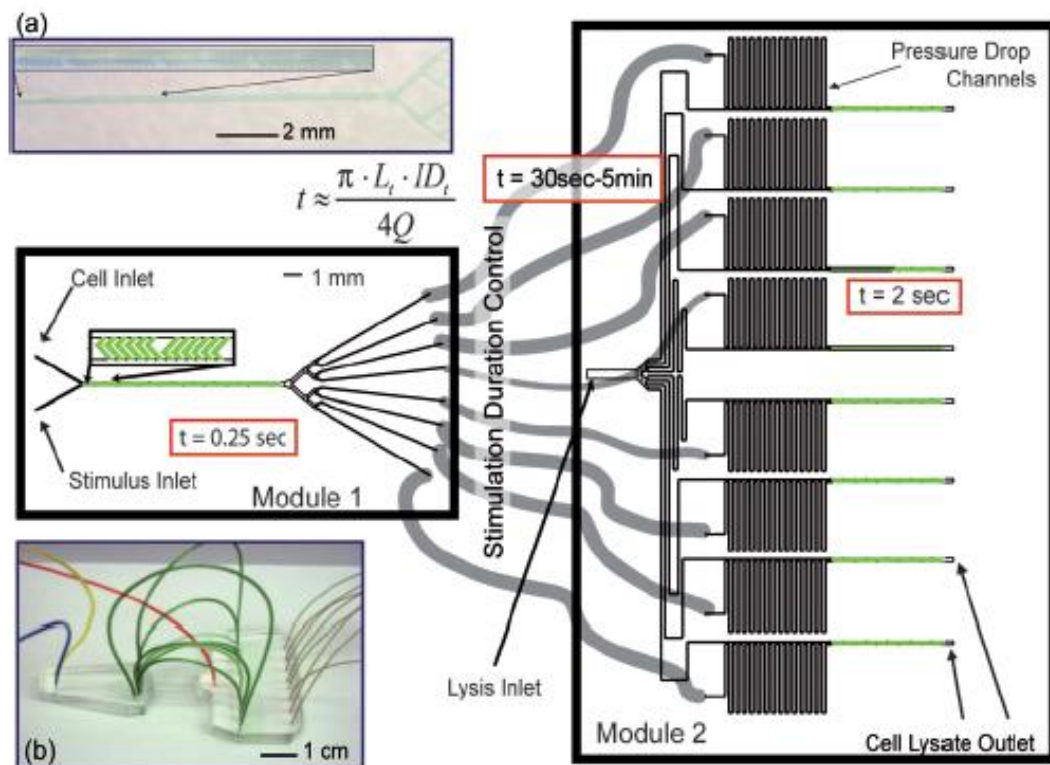


**Figure 3-1:** A schematic of the devices showing inlets, tubing, pressure drop channels and cell lysate outlets for sample collection. The respective residence time  $t$  in each unit is noted in a red box. Inset (a) shows a close-up of Module 1 and (b) the whole device setup. (Adapted from [20])

Fast mixing of reagents (stimulus and lysis buffer) with cells is achieved by chaotic mixing through herringbone structures (153). Parallel and uniform acquisition of eight different stimulation time points from the same initial cell population is enabled by the use of tubings of different lengths and diameters between both microfluidic modules. The flexible nature of this modular design allows easy adjustment of time points without changing the device or operation conditions. Operation of the device does not elicit adverse cellular stress and allowed for the generation of 48 protein measurements from a single experiment and only 10 million Jurkat cells, 5% of the amount that would be required in conventional methods.

### 3.2.2. Multi-time point cell stimulation and simultaneous lysis and fixation on-chip. Device design and operation.

We have adapted the two-module microfluidic chip presented in Figure 3.1 to allow simultaneous lysis and fixation of primary CD8+ T cells (Figure 3.2). This single-layer, modular microfluidic chip is capable of precisely stimulating suspended cells and subsequently lysing and fixing the flowing cells in parallel. In the first module, cells and soluble  $\alpha$ -CD3 and  $\alpha$ -CD28 antibody stimuli are mixed by chaotic mixing using the staggered herringbone mixers (SHM) in the channels (12, 153), and split into 8 different channels, corresponding to 8 different time points sampled (12). Channel height (90 versus 70  $\mu$ m) has been optimized to CD8+ T cell size. We have previously shown that eight cycles of herringbones are sufficient to mix the solutes completely, but we observed that this configuration leads to a predictable cell focusing pattern in specific outlets, insensitive to the additional number of cycles of SHM used or the Reynolds number. To redistribute cells more evenly to facilitate the downstream cell and lysate collection, grooves with randomizer geometries were added after 9 cycles of herringbones, as well as a large splitting area. A flow rate of 44  $\mu$ L/min was chosen as it led to the most uniform cell distribution in the 8 outlets (Figure 3.2b).

The second module receives the cells that have been stimulated for the desired time in the tubings. The length of the tubings was determined using the following formula:

$$L_T = \frac{t * Q}{\pi * R_T^2} \quad (3.1)$$

where  $L_T$  represents the length of a tubing,  $t$  represents time spent in the tubing,  $Q$  is the volumetric flow rate and  $R_T$  corresponds to the radius of a tubing. Time spent in the tubing is defined as:

$$t = t_{desired} - t_r \quad (3.2)$$

where

$$t_r = \frac{L * H * W}{Q} \quad (3.3)$$

represents the time spent in the first module and in the pressure drop channels with rectangular cross sections (L, H and W are respectively the length, height and width of the channels) and  $t_{desired}$  is the total stimulation time desired.

We used *de novo* pressure drop channels to ensure all cells are maintained at the same flow rate (Figure 3.2c) and modified its geometry to minimize shear forces cells are subjected to. These spiral pressure drop channels did not cause measurable inertial focusing or separation of cells. After stimulation, cells are split into two equal populations for lysis or fixation to quench the reaction. Thus, one single experiment yields 8 lysates and 8 fixed cell populations for 8 different time points. Since we were interested in sampling early dynamics after TCR engagement, we chose to look at the first seven minutes of dynamics, the earliest time point being 30 seconds. Each of the eight lysates was analyzed for six proteins; therefore each experiment resulted in 48 dynamic measurements.

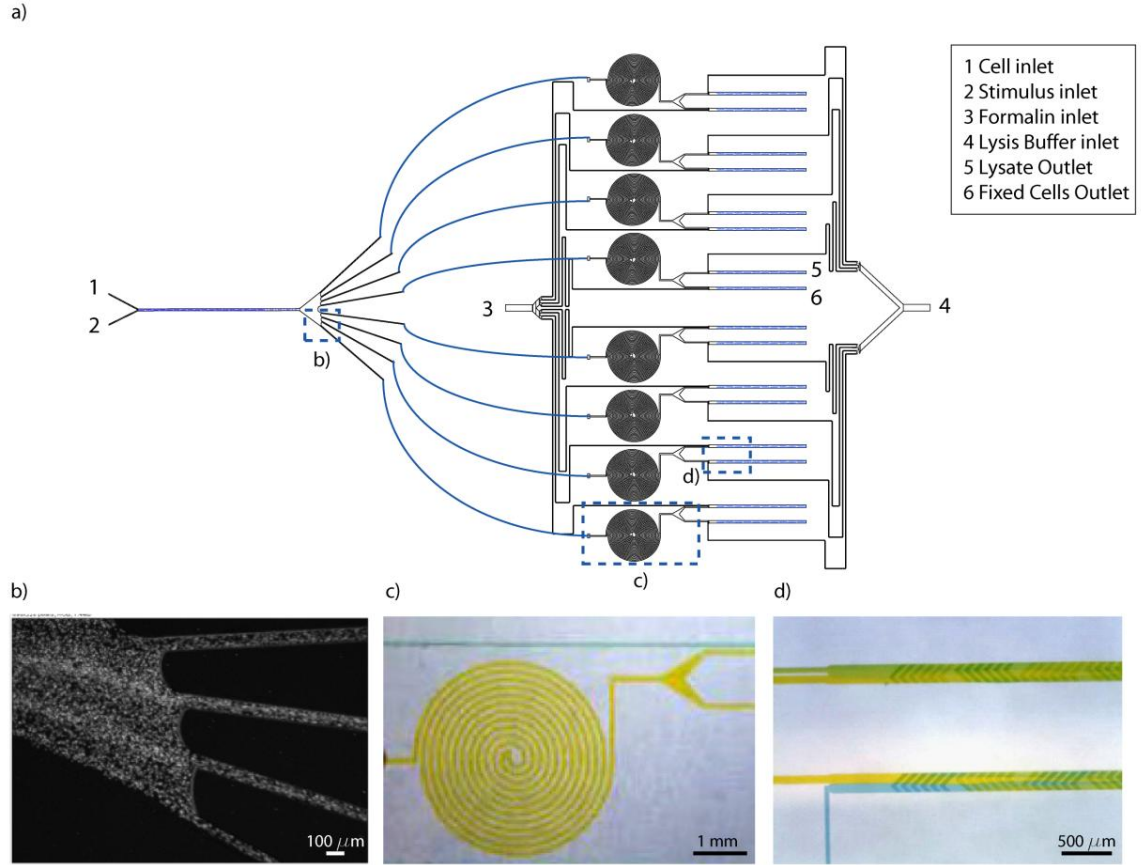


**Figure 3-2:** Microfluidic Device for cell stimulation and simultaneous fixing or lysing.

a) Schematic of the two-module microfluidic chip. Module 1 receives the cells (1) and soluble stimuli (2), mixes these solutions and splits in 8 equals outlets. Module 2 is linked to module 1 by 8 tubings of different lengths and diameters and receives the cells in the circular pressure drop channels. Stimulated cells are mixed either with a fixing solution, here formalin (3) or lysis buffer (4). Lysates (5) and fixed cells (6) can be collected. b) Superposition of inverted bright field images showing cell distribution in the splitting area of module 1 at 44  $\mu\text{L}/\text{min}$ . White dots are individual cells. c) Spiral shaped pressure-drop channel and splitting area for cell fixation or lysis (colors are from food coloring dye solutions that fill the channels). d) Mixing of cells (yellow) with lysis buffer (blue) or formalin (green).

Figure 3.3 compares the dynamics of ERK phosphorylation acquired by flow cytometry and Luminex bead-based assay for different donors and different times in culture. The trends of the signaling dynamics are conserved between both methods with a Pearson's correlation coefficient  $R = 0.61$  (Figure 3.3c). The flow cytometry analysis in general is able to detect higher activation slopes than those achieved with a Luminex

assay, suggesting a higher sensitivity, and/or specificity likely due to the antibody used and the nature of the assay. Furthermore, although phosphatase inhibitors were present in our lysis buffer and most phosphatases are sensitive to fixation (154), a differential inactivation of those phosphatases in the two sample acquisition methods might also explain differences observed in phosphorylation levels between those two assays.

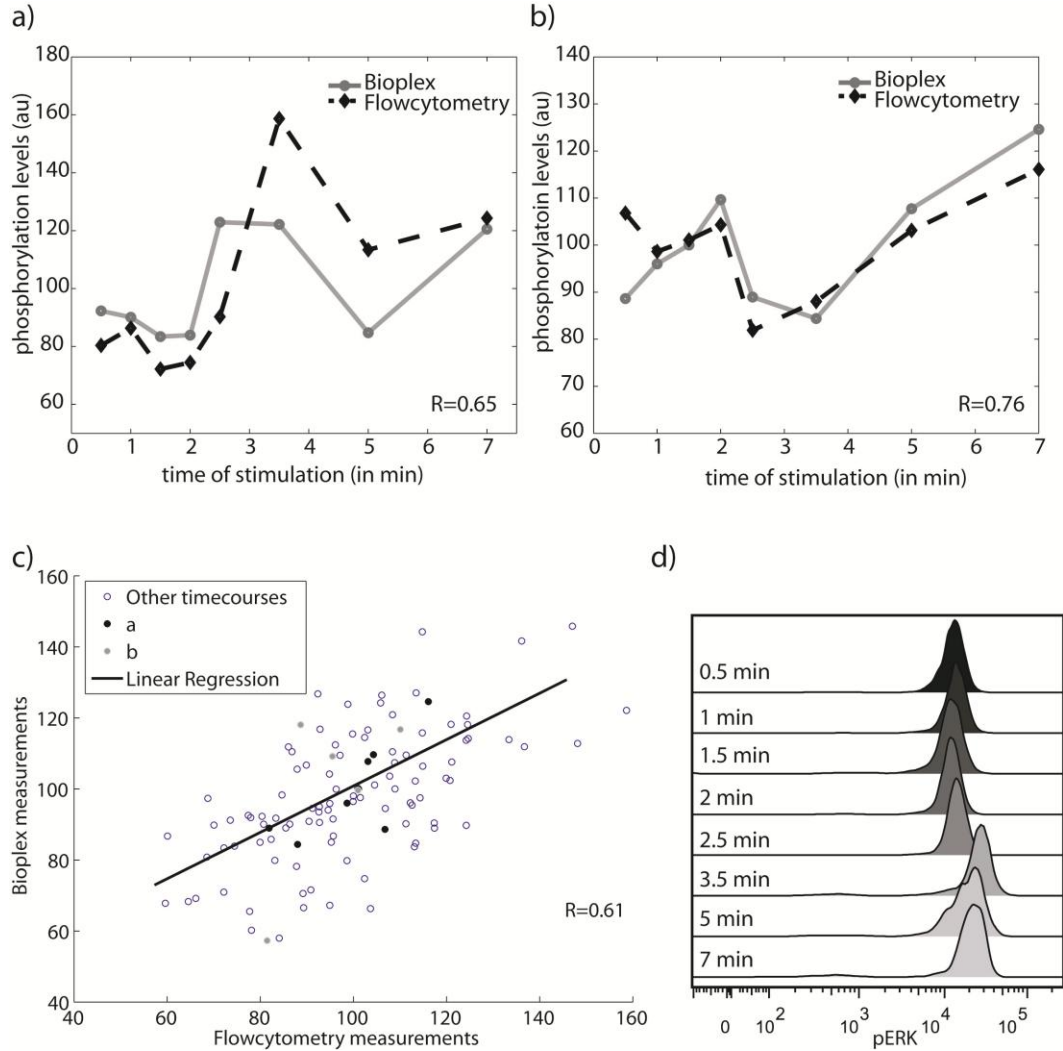


**Figure 3-3:** Dynamics of ERK phosphorylation measured by flow cytometry on fixed samples and bead-based immunoassay on lysates. a-b) Representative traces of ERK phosphorylation for donor 2 at days 11 and 13. Flow cytometry and lysate data are normalized so that the mean value of the time course is equal to 100. c) Linear correlation of ERK phosphorylation between fixed and lysed samples. Data with residuals larger than expected in 90% of the observation were considered as outliers and removed from the regression. d) Representative flow cytometry time course of ERK phosphorylation (also displayed in 3.3a) showing analog activation.



### **3.2.3. Global characteristics of age-associated protein expression and activation changes in human CD8<sup>+</sup> T cells**

Although aging of immune cells has been the focus of intense research, it is difficult to reconcile reports characterizing a variety of biomarkers over a range of culture conditions. By maintaining uniform expansion and sampling conditions, we obtained the data in Figure 3.4 presenting trends across multiple donors for limitations of population doublings, cell growth arrest, surface marker expression, and T cell activation dynamics. The final dataset consists of >2500 measurements generated from 4 donors.

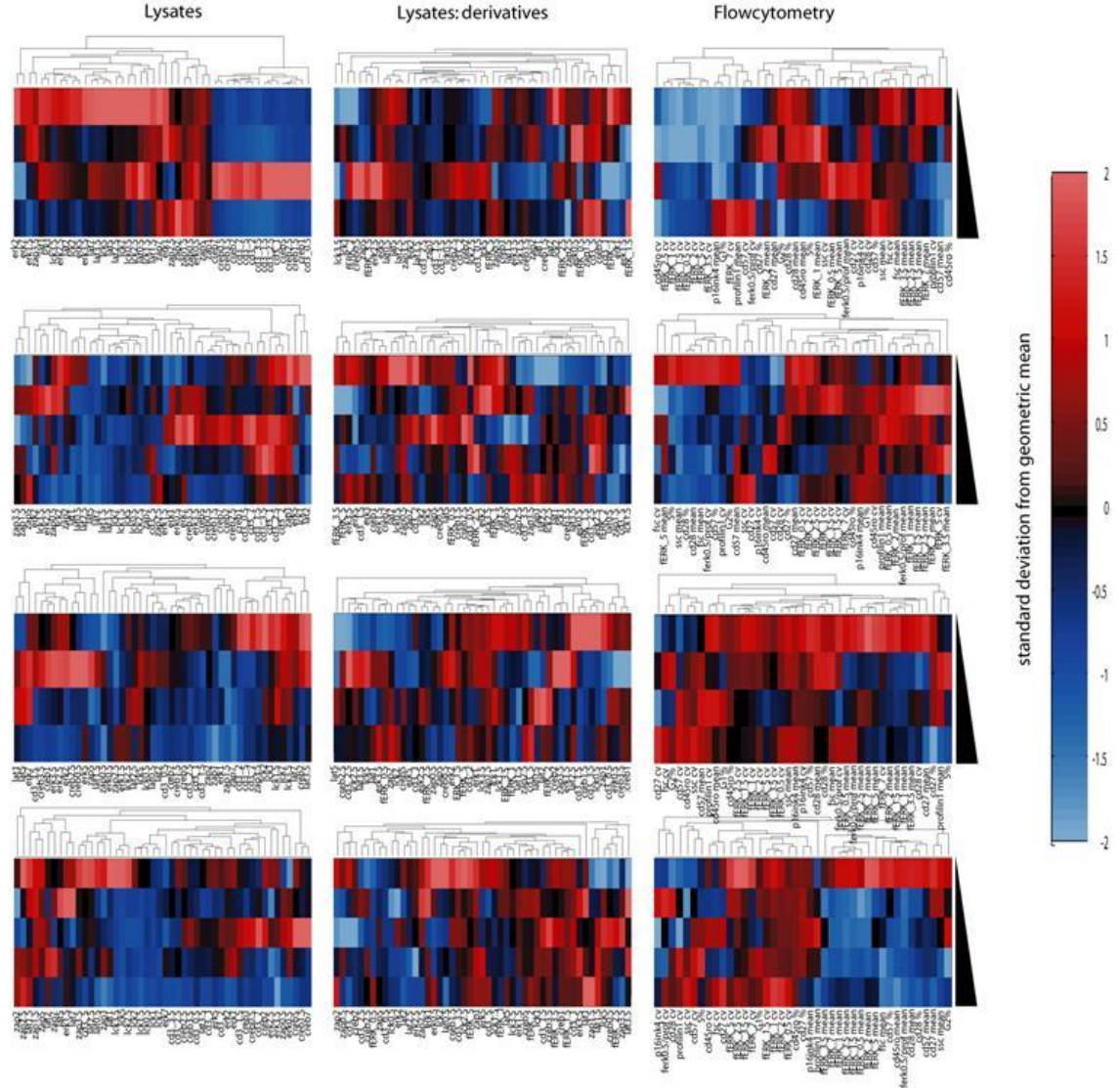


**Figure 3-4:** Complete dataset. For each donor, dendrograms were generated with signaling measurements from lysates (left and middle), protein phosphorylation quantification and instant derivatives of those measurements. Flow cytometry dendrograms (right) contain ERK phosphorylation, cell cycle, cell morphology, surface marker, profilin-1 and p16<sup>ink4</sup> expression. Each row of 3 dendrograms corresponds to a different donor. In each dendrogram, a row corresponds to a sampled time. Each column corresponds to a particular variable measured.

*Human CD8+ T cells cultured with IL-2 and bead-based CD3/CD28 stimulation reach replicative senescence after 12 population doublings:* Primary CD8+ T cells, cultured with chronic bead-based  $\alpha$ -CD3,  $\alpha$ -CD28, and IL-2 stimulation, achieved  $12.2 \pm 0.9$  population doublings, i.e. about 1,000-fold expansion, which is consistent with previous

observations (155, 156). After 12 population doublings, an increase in IL-2 stimulation or in the number of beads did not allow for further growth (Figure 3.5). The cell population could be maintained in culture for several weeks with appropriate culture conditions (IL-2 stimulation and fresh media), suggesting the state of replicative senescence had been reached (157). At different stages in culture, cells were sampled in order to observe changes in cell morphology, cycle, phenotypical markers and signaling as they “aged” in culture.

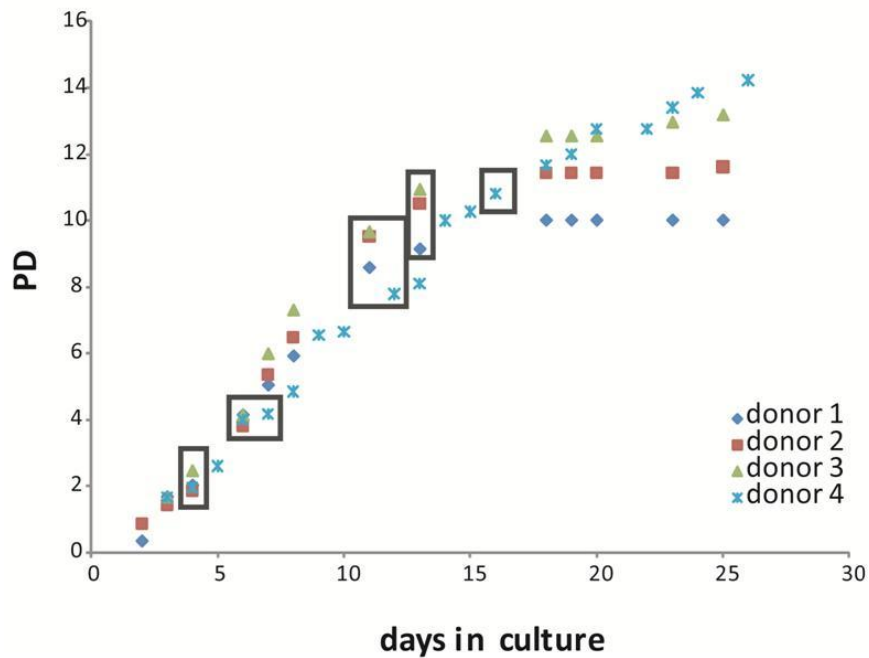


**Figure 3-5:** Time course of population doublings for each donor. The dark grey boxes correspond to times when cells were sampled to assess their phenotype and function through static expression levels and dynamic phosphoprotein dynamics. Donor 4 cells were sampled at different days in culture to correspond with equivalent population doublings.

*Changes in cell morphology and cell growth arrest:* We observed a progressive decrease in cells in S/G2 phase as cells expand in culture, as others have reported (158). At the end of the proliferation phase, cells were found primarily in the G0/G1 phase of cell cycle

(Figure 3.6a). We also observed changes in cell size and shape as cells age through forward and side scatter detection by flow cytometry. Cell size progressively decreased with age and the variance in cellular shape increased (Appendix A.S1). Prior proteomic analysis of *in vitro* cultured CD4+ T cells identified profilin-1 as a potential biomarker for senescence (51); therefore this protein was included in our panel. However, no statistically significant changes in profilin-1 expression were observed in our CD8+ cell population as a function of days in culture (Appendix A.S1). Accumulation of the cell cycle checkpoint p16<sup>ink4</sup> has been observed in senescent T cells (159, 160). However, in our study, the increase in p16<sup>ink4</sup> expression during *in vitro* aging was found to be not significant (Appendix A.S1).

*Changes in surface marker expression with time in culture:* Phenotypic markers of differentiation or co-stimulation have been associated with immunosenescence (151, 161-163). We observe a drop in CD28 expression (Appendix A.S2), from  $84 \pm 4\%$  of CD28+ cells at PD 2 to  $21 \pm 3\%$  at PD 12, consistent with replicative senescence (164). We also observe a decrease in CD27 expression (Figure 3.6b and Appendix A.S2). Although the number of cells expressing the marker remains around 95%, there is a continuous decrease in mean fluorescence intensity, indicating a decrease in the number of costimulatory molecules present on the surface of each cell. After an initial drop in the number of CD57+ cells early in culture, the level of cells expressing CD57 remained constant (Appendix A.S2). We did not observe significant changes in the memory phenotype surface marker CD45RO (Appendix A.S2).

*Overall decrease in protein activation following T cell receptor stimulation:* Along with changes in surface marker expression, it has been proposed that T cell function decline with age could be due to the development of defects in the transduction of mitogenic signals following T cell receptor stimulation (165). From the lysates yielded by the microfluidic chip, we quantified the levels of phosphorylated CD3, Lck, Zap70, LAT, ERK and CREB following T cell receptor ligation using a high-throughput, multiplex bead-based assay (12). We chose to examine early phosphorylation events within 7 minutes of stimulation. T cell receptor stimulation led to an increase in the levels of phosphorylated proteins, with the magnitude and kinetics of activation dependent on the protein, the donor and the age of the cell population (Figure 3.6c and Appendix A.S3). In general, a global decrease in the magnitude of the peak activation levels was observed (Figure 3.6c and Appendix A.S3). Along with those lysates, the microfluidic chip provides fixed cells that have encountered the same stimulation conditions and that can be used for further single cell studies.

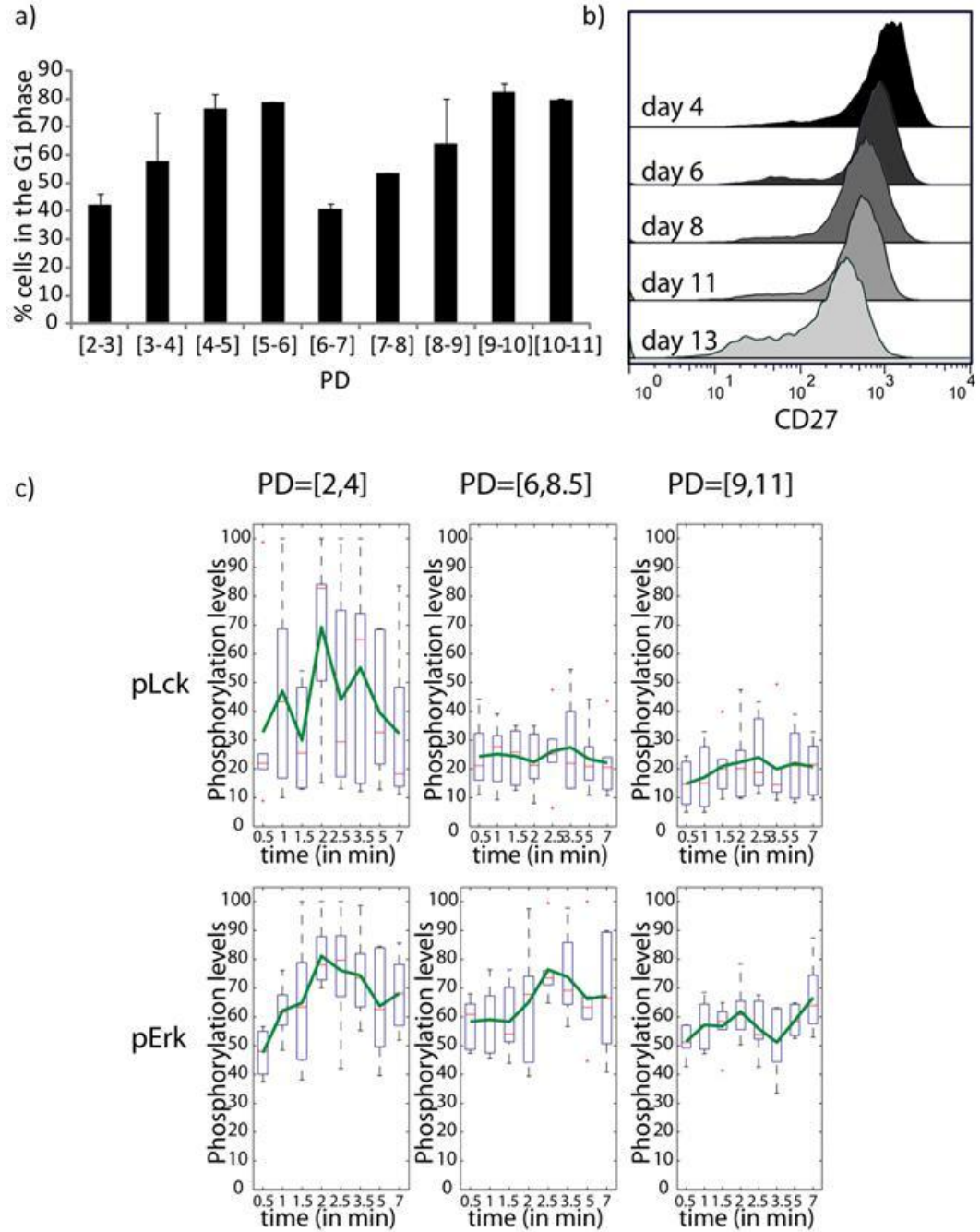


**Figure 3-6:** Cell cycle, surface marker expression and signaling trends over time in culture. a) Percent of cells in the G0/G1 phase determined by the Dean Jett Fox model. Restimulation with  $\alpha$ -CD3,  $\alpha$ -CD28 was performed at passage 6 and 10. b) CD27 expression over time in culture (representative donor data). c) Lck and pErk activation profiles over time in culture. The green line corresponds to the mean of our 4 donors. The box plot represents the median, the 25<sup>th</sup> and 75<sup>th</sup> percentile as well as outliers.

ERK activation has been shown to be essential in mediating proliferation and telomerase activation (166, 167) and displays digital or analog activation patterns depending on the strength and the nature of the stimulus (168-170); thus we investigated this protein by single cell analysis. Analog activation appeared with  $\alpha$ -CD3-CD28 stimulation on our CD8<sup>+</sup> T cell population throughout the duration of culture (Figure 3.3d). This analog activation is consistent with observations by Singh *et al.* who also relied on  $\alpha$ -CD3/CD28 as the means of T cell activation (169). As with the lysate dynamics, an overall decrease in signaling was observed with time in culture. We also measured the heterogeneity in cellular ERK activation within the population, as determined by the coefficient of variation (CV) of the histograms for each time point. Higher coefficients of variations are observed very early and late with respect to culture time (Appendix A.S4). Heterogeneity in the composition of the initial cell population isolated (naïve vs. effector) might result in this high CV observed early in culture.

*Extraction of biomarker combinations of cellular age in culture and prediction of cellular age and quality:* Several biomarkers present modest correlation with time spent in culture; however their rate of change is very donor-specific and therefore individual markers are not sufficient to distinguish non-senescent populations with early-senescent populations. We therefore sought a combination of markers suitable for quantifying age in the cell populations. Hierarchical clustering is a common method used in microarray analysis to extract clusters of genes or proteins having similar response to the same environmental factors (171). Applied to our signaling and flow cytometry data, hierarchical clusterical of the protein phosphorylation time courses suggested higher

phosphorylation values in “young” cells (Figure 3.4). However, the clusters are very donor-specific. Combinations of biomarkers consistent for all donors do not emerge. In addition, this cluster analysis technique, very useful to interpret large dataset and group “like” variables, cannot convey quantitative contributions of markers with predictive power of T cell “age” or quality. Therefore, we applied further analytical methods for extracting markers of aging and their relative contribution to aging that would be universally predictive across donors.

**3.2.4. A combination of dynamic signaling and expression metrics (Lck, ERK, CD28 and CD27) are the most informative markers in predicting cellular age.**

To relate cell age to network activation and phenotypic markers, we constructed a PLSR model. This data-driven modeling approach allows for complexity reduction in multivariate protein expression and signaling data to identify the most informative variables, and has been previously used to predict cellular fate or cytokine production (131, 132). The 140x18 data matrix was parsed by defining the dynamic activation profiles of 6 proteins phosphorylated after T cell receptor ligation (time-course measurements and instantaneous derivatives), cell morphology, cell cycle, costimulatory and differentiation surface markers, and heterogeneity in the population for the flow cytometry data all as independent, predictor variables (i.e. X-block) in our data matrix (Figure 3.4 and Appendix A.T1). The number of days spent in culture or number of population doublings were defined as variables that depend on the X-block (i.e. Y-block) for regression purposes. The principal components derived by the PLSR model contain linear combinations of the predictor variables optimized for maximum covariance with



the dependent outcomes. From this initial optimization, a pruning step was implemented by removing variables with both low importance in the projection and high uncertainty as determined by jack-knifing. The resulting 71x18 data matrix was fitted with a 3-component model with  $R^2Y = 0.96$  (goodness of fit). The model captures variance in the data with a  $Q^2 = 0.78$  (measure of the cumulative fraction of the total X-block variation that can be predicted by all components). Individual observation sets, defined as all measurements for a specific donor for a specific day in culture, were mapped onto the first two principal components via their scores to determine how observations from different experimental conditions influenced the overall age prediction. Samples from late days in culture segregate with positive PC1 loadings, suggesting that the first component can be coarsely defined as an “age” axis (Figure 3.7a). This first component can effectively estimate cell age with a  $R^2Y = 0.667$ ,  $Q^2 = 0.53$ . The second component captures additional 23% of the variance in the data.

Clusters of predictor variables that are highly correlated with outcome variables can be visualized by their proximities to one another on the weight plots in principal component space (Figure 3.7b). Signaling information is mostly anti-correlated to age, consistent with the general understanding of altered signaling dynamics. An analysis of the weight of each variable highlights the importance of the proteins ERK, Lck and LAT for predicting cellular age (Appendix A.T2-3). CD27 and CD28 expression, and number of cells in the G2/M cycle phase appear to be heavily negatively weighted in the first component. Somewhat surprisingly however, the heterogeneity of the cell population in cellular shape, the heterogeneity in CD57 expression, and the basal level in phosphorylated ERK emerged as being highly positively correlated with cellular age

(Figure 3.7c). The heterogeneity in ERK phosphorylation in stimulated cells emerges as important in the second component (Figure 3.7d). P16<sup>ink4</sup> influence was largest in the 3<sup>rd</sup> component (not shown) and was positively correlated to age. This comprehensive model is capable of accurately predicting day in culture and number of divisions with regression coefficients ( $R^2Y$ ) of 0.91 and 0.98 respectively (Figure 3.7e-f). The robustness of the predictions was tested by iteratively omitting one donor set at a time and re-applying the algorithm on the remaining three donor sets. The regression is performed on the mean of four different predictions; errors in the predicted value generated in this manner (Figure 3.7e-f) reflect variation in the ability of the model to be applied to new donor datasets that it has not been previously been trained on.

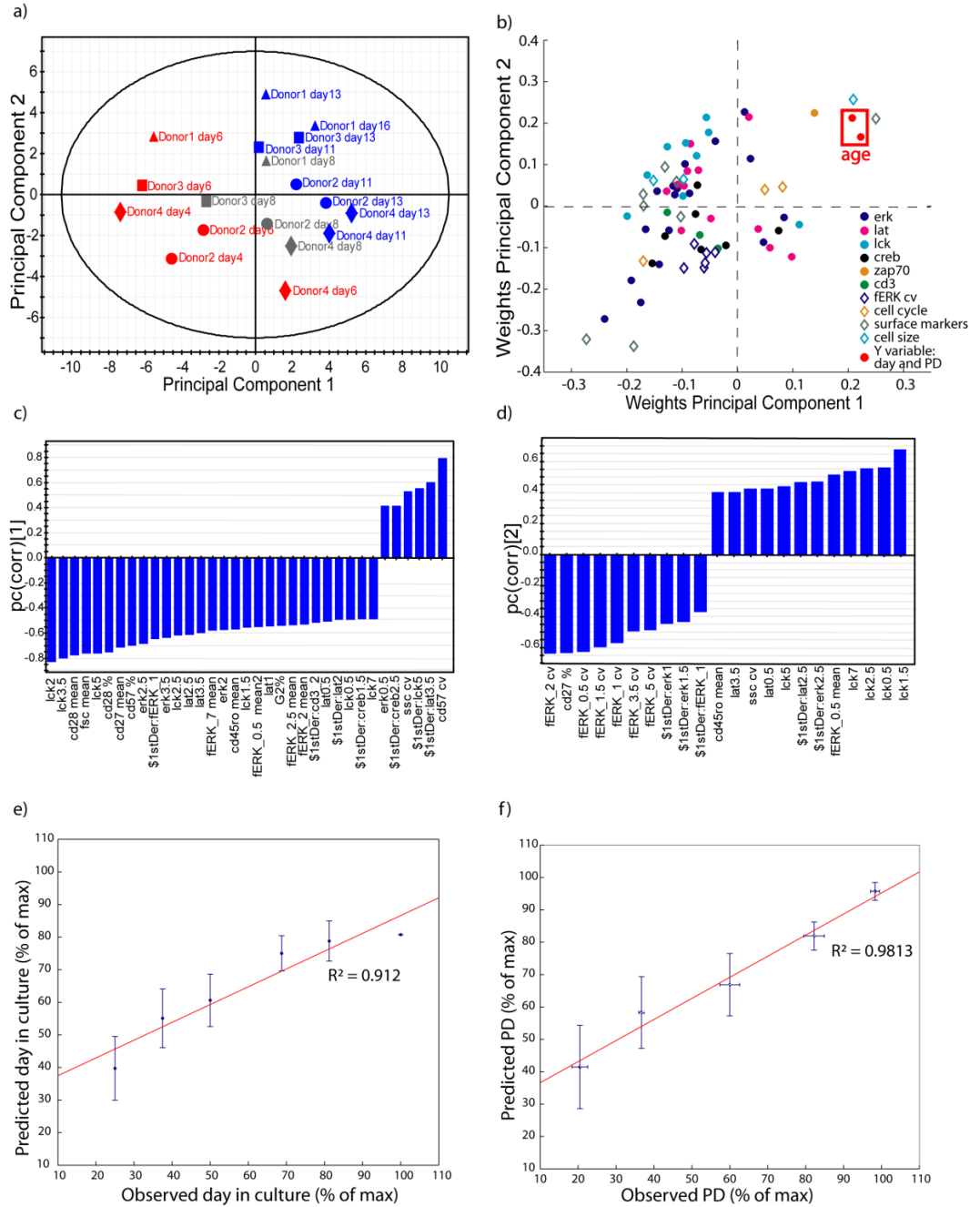


**Figure 3-7:** Cellular age prediction with signaling measurements and phenotypic markers using a multivariate regression model. a) Loading plot of the observations in the reduced principal component space. b) Score plot of the predictor variables on the principal components space. Y-variables are highlighted in red box. c-d) Weight of the most important variables (weight>0.4) in the first (c) and second component (d). e-f) Prediction of day (e) and number of divisions in culture (f).

*Signaling information alone is sufficient for aging prediction:* While surface markers are commonly used as metrics of aging, to date a multivariate characterization of replicative senescence as a function of signaling dynamics has not been attempted. We sought to determine if a model containing only signaling information from lysates and flow cytometry enabled cell age prediction. The X-variance captured by this reduced model is lower than in the model previously described, with a  $Q^2=0.54$ ; however this model is still able to accurately predict the number of days since isolation or the number of population doublings with a regression coefficient  $R^2Y$  of respectively 0.84 and 0.94 (Figure 3.8). As in the previous model containing all types of data, the first component is loosely partitioned as a measure of age (Figure 3.8a). The instant derivatives of signaling at very early time points enabled by the fast sampling of the microfluidic device are important in this model (Appendix A.S4-5); the instant derivative of ERK phosphorylation after one minute of stimulation emerged as the most significant anti-correlated variable while the model also extracted the instant derivative of Zap70 phosphorylation at 1.5 min as a significant predictor. A simple multiple regression based on just ERK and Zap70 metrics enables age prediction with  $R^2 = 0.65$ . The most heavily weighted signaling variables have been sampled between 1 and 3.5 min after stimulation, pointing to the importance of very early signaling dynamics (Figure 3.8b and Appendix A.T4). An analogous modeling exercise was performed with only surface marker data (Appendix A.S5). CD27 and CD28 expression, as well as CD57 coefficient of variation emerged as the most informative metrics. The PLSR prediction of days in culture was improved in the signaling model ( $R^2Y = 0.84$  vs. 0.78) but slightly less accurate in predicting population doubling ( $R^2Y = 0.95$  vs. 0.98).

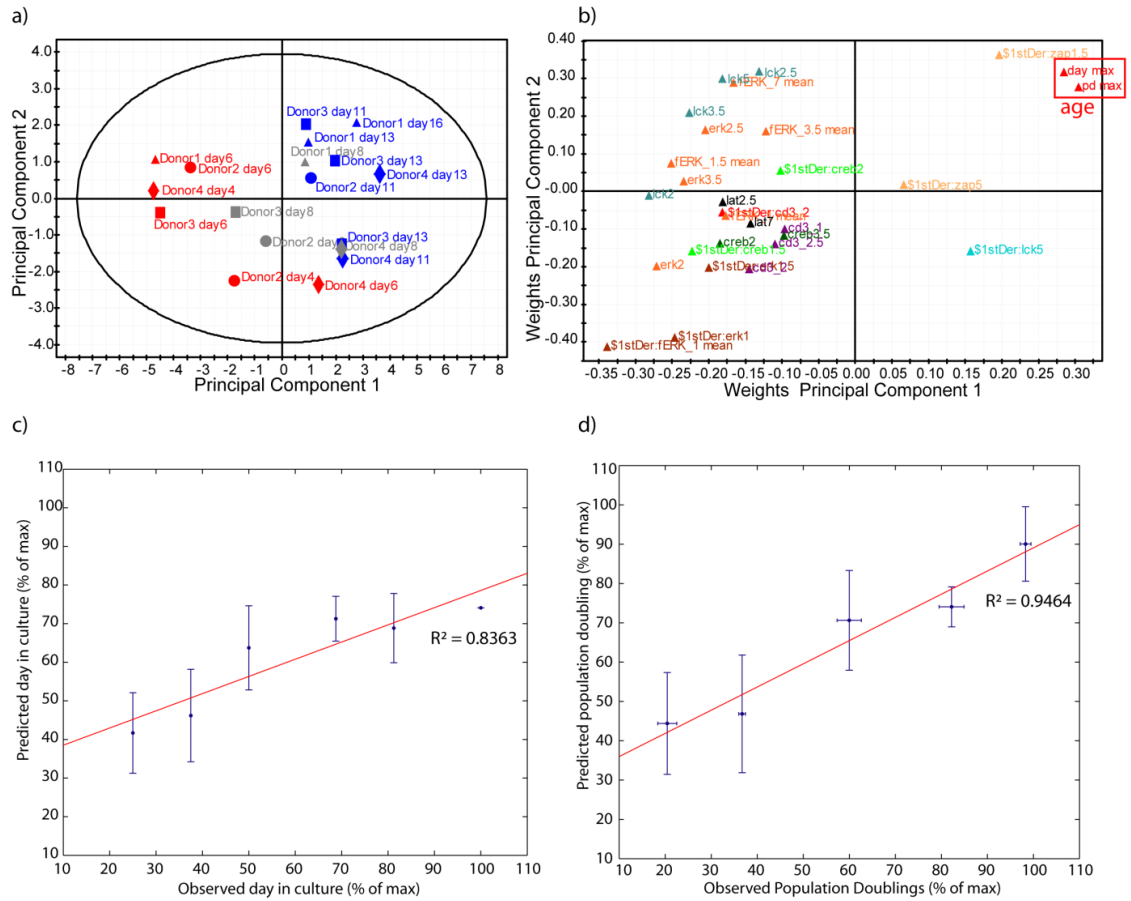


**Figure 3-8:** Cellular age prediction from signaling data only. a) Loading plot of the observations in the reduced principal component space. b) Score plot of the predictor variables on the principal components space. c-d) Prediction of day (c) and number of divisions in culture (d).

*Signaling information can predict co-stimulatory molecule expression:* CD27 co-stimulation with TCR enhances cell expansion and promotes cell survival (172). The co-stimulatory molecule CD28 is involved in T cell receptor signaling amplification by PI<sub>3</sub>K activation and downstream Ca<sup>2+</sup> mobilization (173) as well as indirect ERK activation via Lck (174, 175). Therefore, the loss of CD28 and CD27 with cellular age would be expected to be directly correlated to altered T cell receptor downstream signaling. To test these relationships, we built a model that predicts phosphorylation levels from surface protein expression markers. This model behaved poorly ( $R^2Y=0.27$ ;  $Q^2=0.1$ ). The

expression of CD27 and CD28 is not sufficient to accurately predict any of the signaling variables. In contrast, a model based on signaling time courses and regressed against costimulatory surface marker expression is able to successfully predict both CD28 and CD27 surface expression with a correlation coefficient ranging from 0.75 to 0.91 (Figure 3.9c-e). CD27 mean fluorescence intensity is highly correlated to the instant derivative of ERK phosphorylation after one minute of stimulation and anti-correlated to the slope of deactivation of CREB after 2.5 min of stimulation. Lck phosphorylation is strongly correlated to CD28 expression and the rate of decay in LAT phosphorylation after 3.5 min of stimulation is strongly anti-correlated to CD28 expression. Globally, CD28 expression clusters with early dynamics (0.5-3.5 minutes) of ERK, Lck and LAT (Figure 3.9b).

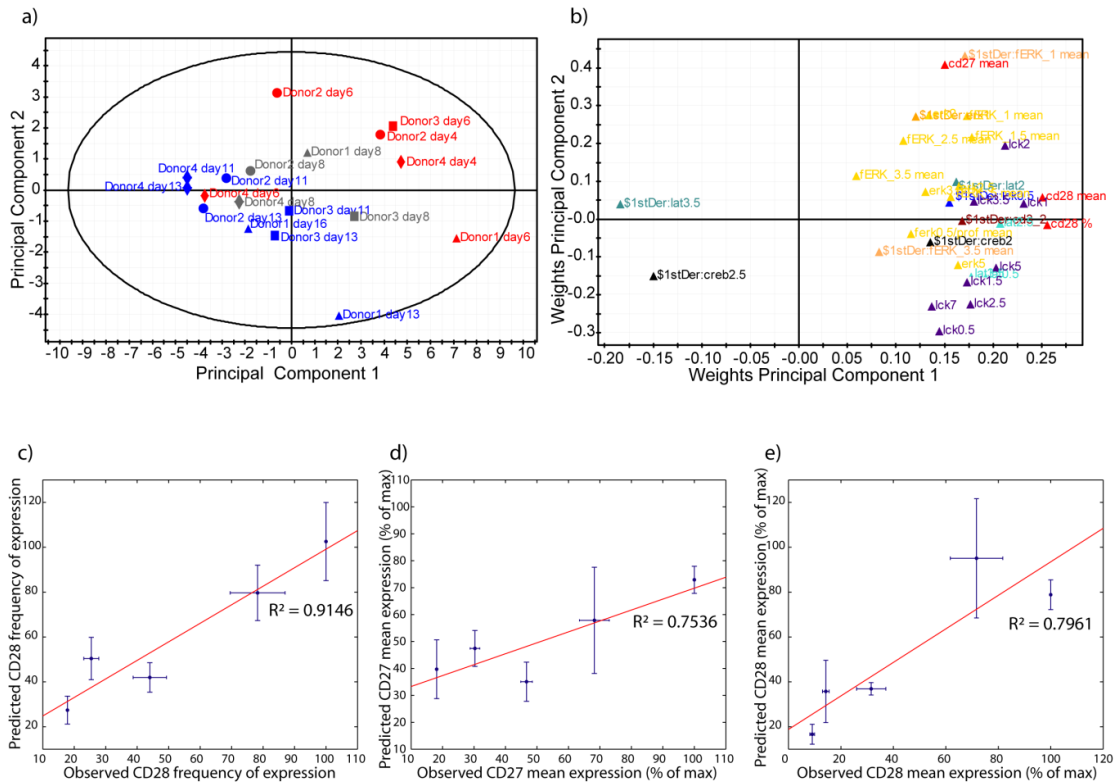


**Figure 3-9:** Surface marker prediction from signaling information during the aging process. a) Loading plot of the observations in the reduced principal component space. b) Score plot of the predictor variables on the principal components space. c-e) Prediction of the percentage of CD28+ cells (c), and CD27 (d) and CD28 (e) mean expression.

### **3.3. Discussion**

The outcome of immune based therapies, such as adoptive T cell transfer therapy or engineered vaccines, is dependent on the quality of T cell clones used (148). Progress has been achieved towards improved T cell expansion methods in the past few years (176): new culture mediums as well as improved stimulation techniques have been developed (177-179), and cord blood has been harnessed as a source of non-senescent lymphocytes for tumor immunotherapy (180).

To assess the quality of expanded cells, researchers/clinicians generally perform functional assays (e.g. cytokine production (181) or cytotoxic T-lymphocyte (CTL) assays) or examine surface marker expression, such as the extent of CD28 loss or the appearance of late differentiation markers such as CD57 (162). Univariate, static assays measuring expression of surface markers alone are not always accurate for prediction of cell functionality. While CD28 is considered as a biomarker of immunosenescence, its expression can be downregulated by tumor-necrosis factor (TNF) (17, 18) or upregulated by IL-12 in CD4<sup>+</sup> cells (19). It was also shown that CD8<sup>+</sup>CD28<sup>-</sup> cells are able to proliferate (20) and therefore the loss of CD28 is not necessarily associated with senescence. There is also contradictory evidence concerning loss of the co-stimulatory molecule CD28 and altered downstream signaling. Larbi *et al.* suggested that differential localization of CD28 in lipid rafts and not the actual number of receptor could explain disparities in response to stimulation for CD4<sup>+</sup> cells (182). Hence, CD28 alone cannot be considered as a direct marker of senescence, and combinations of biomarkers need to be considered to quantitatively predict the level of senescence in a population.

To measure T cell response, different assays exist to measure early (calcium influx, protein phosphorylation within a few minutes after stimulation), intermediate (degranulation or cytokine production) or late functions (proliferation and apoptosis) (183). Although cytolytic assays are very informative in assessing cell functionality, they rely on bulk population measurements which may mask deficiencies in subpopulations and usually require additional culture preparation of target cells (184). The analysis of signal transduction protein phosphorylation after T cell receptor stimulation can be used as a proxy for cell functionality, and offers insight on mechanistic details (166, 185). Flow cytometry can provide additional information regarding the heterogeneity of the early phosphorylation events in T cell signaling, while lysates provide multiplexed capabilities of many measurements at once. Although a combination of the two acquisition methods provided the optimal model, our results suggest that signaling information alone is comparable in prediction of cellular age and can also predict surface marker expression. In contrast, the reverse is not true: while surface markers alone provide information on cellular differentiation state and can predict cell age, they cannot predict protein phosphorylation changes as a measure of cell functionality (data not shown).

Determination of clusters of biomarkers and aging quantification is largely facilitated by the development of computational models, and several efforts to model and quantify cellular age in various cellular model systems have been published recently. Lawless *et al.* developed estimates of fraction of senescent cells in human and mouse fibroblasts using growth curves and candidate markers, such as p21 or DNA damage foci loci in



paraffin-embedded tissue sections (186). Tsygankov *et al.* created a stochastic model that links p16<sup>ink4</sup> expression with aging (187). Proteomic analysis of elderly patient-derived T cells expanded *in vitro* to senescence used statistical discriminant analysis to identify potential biomarkers (51). Each of these prior studies has relied on static information from the cells rather than functional dynamics of TCR activation. As there is no consensus for the best biomarkers of *in vitro* aging for CD8+ T cells, we chose to utilize a multivariate approach, combining surface phenotype of CD8+ lymphocytes and intracellular signaling.

In this work, we developed a microfluidic tool and a statistical model to evaluate cell responsiveness and accurately predict cell “age” and quality respectively. It has been observed that T cells are able to stimuli within seconds, such as TCR ligation initiating a burst of calcium (188). The design of the microfluidic device enabled sampling of the rapid protein phosphorylation dynamics in the first few minutes following stimulation with minimal standard error, and allowed us to obtain accurate measurements in a high-throughput manner. As shown previously, chaotic mixing and flow in narrow channels at low Reynolds number does not elicit adverse stress response (12). The ability to reproducibly sample with 30-90 second intervals enabled the use of instant derivatives as additional variables in the regression model; thus, the microfluidic device provided an additional benefit in enhancing the information content from the signaling data. Although others have reported derivatives of time courses to be less informative in PLSR analysis (130-132, 189, 190), these studies relied on signaling dynamics that extended for hours rather than minutes. Because the device can stimulate a small number of cells with high temporal resolution and subsequently lyse and fix them in parallel, we could seamlessly

“stitch” together complementary measurements for our statistical analysis from populations of cells treated identically, not only from day to day, but also within a particular stimulation experiment. Because donor-to-donor variability is a confounding factor in deriving robust biomarkers of senescence, the technological platform minimizes the experimental data variance so that meaningful dimension reduction could be performed, as shown by the conserved trends of signaling of phosphorylated ERK (Figure 3.3). Cheong *et al.* have developed a microfluidic device able to measure time courses of signaling responses to continuous or with wave form soluble stimuli with immunofluorescence on chip on adherent cells (124). In contrast to our design that performs off-chip biochemical and cellular analysis, their immunostaining was performed on chip. Their device provided single-cell data on fixed cells, similar to live cell imaging and could be used to discriminate single cell versus population signaling dynamics. As with flow cytometry or microscopy, however, one is limited by the number of proteins that can be measured simultaneously. With the microfluidic chip presented here, the simultaneous fixing and lysing of cell populations which have encountered the same environmental conditions allowed us to use multiplexed capabilities of lysates while being able to probe for the heterogeneity in ERK phosphorylation in aging populations with flow cytometry. This technique could also prove useful in future applications for distinguishing signaling in different subcellular compartments, e.g. nuclear transcription factors, not directly accessible with detergent-based lysing.

We developed multiple partial least square regression models to explore properties of the data and be able to predict physiological age of *ex vivo* expanded cells. PLSR models have been applied previously to understand complex signaling networks involving

multiple inputs and multiple outputs, without prior knowledge of the network structure (130-132, 189, 190). Prior application of this type of modeling approach has demonstrated that antigenic information content is encoded within downstream phosphorylation events in T cells (132). This data-driven modeling technique is particularly well suited to carry multivariate analysis and predictions in extensive datasets, and therefore could be applied to extract correlations between age, signaling, and surface phenotype expression. From the analysis, CD28 and CD27 expression emerged as key markers in determining cellular age and also correlated strongly to intracellular phospho-protein dynamics. Interestingly, the model did not find any positive correlation between the effector memory surface markers CD57 and CD45RO and age in culture, contrary to a previous observation (162). This might be due to the culture conditions specific to each study. It has been reported that  $\alpha$ -CD3/CD28 artificial antigen-presenting cells as used here preferentially expand CD45RO<sup>+</sup> cells (178). CD57 is a marker associated with the end-stage T cell differentiation. Elevated expression of CD57 has been observed on tumor-specific T cells. It may be the consequence of persistent chronic antigen stimulation, resulting in the accumulation of cells capable of rapidly secreting cytokines but that lack proliferative capacity (162). IL-2 supplementation may have induced an increased loss of CD28 expression (191), blocking cell proliferation before CD57 upregulation. Thus, this model is limited in scope to the culture conditions assayed yet provides a generalizable approach that could be used for other expansion methods.

Our model emphasizes the importance of early signaling dynamics (1-3.5 min after TCR engagement) to explain and predict cellular age. Others have reported alterations in

early signaling events in old mice (192) and in human T lymphocytes from elderly patients (193), furthering the common characteristics between *ex vivo* culture expansion and immunosenescence. Three major proteins, Lck, LAT and ERK, were extracted from the model as having primary roles in accurately predicting cellular age. Lck is the first protein to be phosphorylated after TCR engagement, leading to phosphorylation of the adaptor protein LAT via Zap70, and downstream phosphorylation of ERK. Impaired redox regulation (194), reduced calcium release (192, 195) and altered membrane rafts composition (194) are possible explanations for the impaired activation of those proteins. Previous studies have reported higher cell-to-cell variation with increasing age (196, 197); however the modeling results suggest that this trend is more nuanced and depends on the protein in question. We find that the heterogeneity in CD57 protein expression and cellular shape is correlated with cellular age. In contrast, no direct correlation between age and cell-to-cell variation of ERK phosphorylation was discovered (Appendix A.S4), and yet as part of a multivariate analysis this CV variable still possesses a high predictive power. This suggests robustness in ERK response to intracellular noise created with aging (198).

The multivariate PLSR model is able to assess the age and therefore the quality of a cell population for cells expanded using CD3-CD28 bead stimulation with IL-2 supplementation. Past multivariate models associated signaling information with cellular fate (189), cytokine production (132), or drug response (199). These models enabled the creation of new hypotheses to test the validity of the model. In this application, aging is not a cell fate that we can modify and the biomarkers extracted are not correlated in a causal fashion to the age of the cells. This lack of a testable mechanism poses a limitation

to the study; however, the model yields novel insight on the most informative markers of the array selected for sampling, and predicts cellular age from those specific markers. We also envision this model to be a possible diagnostic tool to quantify immune age of elderly individuals or individuals presenting accelerated immunosenescence, such as HIV patients.

### **3.4. Conclusion**

In summary, the design of a novel microfluidic chip enabled the statistical analysis of T cell aging by minimizing error in the sample handling between days and across multiple donors. We took advantage of chaotic mixing geometries and a modular chip design to capture the early phosphorylation events associated with TCR ligation, which in turn proved to be highly informative in the partial least square regression prediction of population doubling and days spent in culture. Our findings point to a cell signaling-based assessment method that could quickly evaluate patient-derived cells for degree of population doubling. The general approach described here, combining fixation and lysing on-chip, can facilitate the integration of single-cell information with population-averaged techniques such as multiplexed immunoassays or mass spectrometry.

### **3.5. Material & Methods**

#### **3.5.1. Cell isolation and expansion**

Following institutional review board (IRB) approval, CD8<sup>+</sup> T cells were obtained from blood donors using standard isolation procedures. Briefly, 40 mL of fresh blood was collected in EDTA coated tubes from four healthy donors (21-35 years old) under written

informed consent. Peripheral blood mononuclear cells were isolated by density centrifugation using Lymphoprep (VWR), and CD8<sup>+</sup> T cells further purified using the Dynabeads® Untouched™ Human CD8 T Cells isolation kit (Invitrogen) (>92 % purity as checked by flow cytometry). The cells were expanded in RPMI 1640 medium with L-glutamine (Sigma- Aldrich) with 10 mM HEPES, 1 mM sodium pyruvate, and 1X MEM nonessential amino acids, and 100 units.mL<sup>-1</sup> penicillin/streptomycin (Cellgro) and 10% certified heat-inactivated fetal bovine serum (Sigma-Aldrich). The culture medium was supplemented with 50 U/mL of recombinant IL-2 (Sigma-Aldrich) and Dynabeads® Human T-Activator CD3/CD28 (Invitrogen) at 1:1 bead to cell ratio (kept constant for the entire culture period) for rapid cell expansion (200, 201). Cell cultures were checked daily and resuspended in fresh medium when needed. The number of population doublings (PDs) was calculated from the average cell count using the following equation:

$$PD = \frac{\log_{10} n_{post} - \log_{10} n_{init}}{\log_{10} 2} \quad (3.4)$$

where  $n_{post}$  represents the number of cells counted after expansion and  $n_{init}$  represents the number of cells initially seeded.

The following table presents the different time points at which  $26 \cdot 10^6$  cells from each donor cell culture were assayed for signaling, intracellular and surface marker expression. Sample times were chosen when the total number of cells in culture for each donor exceeds  $32 \cdot 10^6$  cells.

**Table 3-1:** Day in culture when assayed and corresponding PD for each donor.

| Donor 1 |     | Donor 2 |      | Donor 3 |      | Donor 4 |      |
|---------|-----|---------|------|---------|------|---------|------|
| Day     | PD  | Day     | PD   | Day     | PD   | Day     | PD   |
| 4       | 2   | 6       | 3.8  | 4       | 2.5  | 6       | 4    |
| 6       | 4.1 | 8       | 6.5  | 6       | 4.1  | 9       | 6.5  |
| 8       | 5.9 | 11      | 9.5  | 8       | 7.3  | 13      | 8.1  |
| 11      | 8.6 | 13      | 10.5 | 11      | 9.7  | 16      | 10.8 |
| 13      | 9.1 |         |      | 13      | 10.9 |         |      |

### 3.5.2. Microfluidic device fabrication

The two-module device was fabricated using standard soft lithographic techniques (12, 202). Briefly, the modules were molded in poly-(dimethylsiloxane) (PDMS) (Dow Corning Sylgard 184, Essex-Brownwell Inc.) from a two-layer SU-8 (Microchem Corp.) master. One layer of 70  $\mu\text{m}$  thick SU-8 2050 was spun onto 100 mm silicon wafer, prebaked, and exposed under UV light to define a negative image of the channel system in the resist, following the manufacturer's instructions. After postbaking to crosslink the exposed resist, another layer of 40  $\mu\text{m}$  thick SU-8 2020 was spun on top. This layer formed the staggered herringbone arrays (12). After the same prebake and expose process, the wafers were developed using propylene glycol monomethyl ether acetate (Doe & Ingalls, Inc.). The wafer surface was treated with vapor-phase tridecafluoro-1,1,2,2-tetrahydrooctyl-1-trichlorosilane (United Chemical Technologies, Inc.) for passivation. PDMS was cast on the SU-8 master and baked for 3 h at 70°C to cross-link. The PDMS was then peeled off from the mold and individual devices were cut to size.

Access holes were punched using stainless steel needles (McMaster Carr). The devices were plasma bonded to glass slides or PDMS. Medical grade polyethylene (PE) tubing (Scientific Commodities) of various lengths and inner diameters were used for fluidic connections.

### **3.5.3. Device operation**

A syringe pump (Chemyx Fusion 200 series) controlled the flow to the four inlets at  $44 \mu\text{L}\cdot\text{min}^{-1}$ . Before running an experiment, a solution of 2% BSA in PBS was flown through the device with plugged outlets to pressurize the device and remove any air bubbles. Then the outlets were opened to atmospheric pressure and PBS with 2% BSA was flowed through the device for an additional 15 min. Seven hours before the device operation,  $20\cdot 10^6$  cells were resuspended in fresh medium without IL-2 and  $\alpha$ -CD3/CD28 beads. During device operation, cells were delivered in 1.5 mL of a PBS + 7% w/v dextran solution to match the cell density and avoid cell settling (12). To further avoid cell loss in the syringe, a small cubic magnet with 2-mm edges was inserted with the cell suspension, and intermittently agitated during the experiment. The stimulus consisted of PBS supplemented with  $2 \mu\text{g}/\text{mL}$  of  $\alpha$ -CD3, clone OKT3 (eBioscience), and  $2 \mu\text{g}/\text{mL}$  of  $\alpha$ -CD28 (BD Bioscience). Ice-cold freshly-prepared lysis buffer as previously described (12) and a 10% formalin solution (Sigma-Aldrich) were delivered at the inlets of the second module. Cells, stimulus, lysis buffer and fixing solution were flown for 9 min to allow steady state for the different time points to be reached before the 8 fixed samples and 8 lysates were collected in ice-cold 96-well plates covered with paraffin for 20 additional min.



#### **3.5.4. Signaling measurements**

Total protein concentration of the lysates was determined with a BCA assay kit (Pierce). The analysis of phosphorylation dynamics was performed with a Bio-Plex 200 instrument (Bio-Rad) using commercially available Luminex bead assays. The quantification of proteins downstream of TCR (Beadlyte 7-plex Human T cell Receptor Signaling Kit, Millipore) was completed according to manufacturers' protocols. Results for all data are presented as the average of triplicates, normalized to values from GAPDH beads (Millipore), and further normalized to the maximum value for separate sets of proteins per donor. Phosphoprotein staining was performed as described in Krutzik *et al.* (2003). Briefly, formalin-fixed stimulated cells eluted from the device were washed with PBS, permeabilized with ice-cold methanol and stored at -20°C. Cells were stained with pERK antibody pT202/pY204 (BD Bioscience) at a dilution of 1:100 (in 2% BSA in PBS). After 30 min of incubation at 4°C, cells were washed and resuspended in PBS with  $\alpha$ -mouse Alexa488 antibody (Invitrogen), incubated for 30 additional min at 4°C, washed and analyzed by flow cytometry.

#### **3.5.5. Flow Cytometry analysis**

Surface marker protein expression was determined by direct immunostaining. Stimulated CD8<sup>+</sup> T-cells ( $5 \cdot 10^5$  total) were removed from the beads and resuspended in 500  $\mu$ L solution of PBS, 2% BSA, with the following antibodies: 10  $\mu$ L of PE-labeled- $\alpha$ CD27, 10  $\mu$ L PeCy5-labeled- $\alpha$ CD28, 10  $\mu$ L FITC-labeled- $\alpha$ CD57 and 2.5  $\mu$ L PeCy7-labeled- $\alpha$ CD45RO (BDBioscience). After 30 min of incubation on ice, cells were washed with PBS and analyzed by flow cytometry. To determine p16<sup>ink4</sup> and profilin-1 expression as

well as cell cycle, stimulated CD8+ T-cells were removed from the beads, resuspended at  $10^7$  cells·mL<sup>-1</sup> in ice cold methanol and stored at -20°C. After being washed in PBS, cells were resuspended at  $10^7$  cells·mL<sup>-1</sup> in 50 µL of PBS, 2% BSA, and incubated for 30 min with  $\alpha$ profilin-1 antibody (Cell Signaling) , washed in PBS, incubated with FITC-labeled  $\alpha$ p16<sup>ink4</sup> antibody (BD Bioscience) and  $\alpha$ rabbit R-PE antibody (Invitrogen) for an additional 30 min at room temperature. After the final wash step, cells were resuspended in 500 µL of PBS and 2.5 µL of 7-AAD to measure DNA content. After 30 min of incubation at room temperature, samples were analyzed by flow cytometry. A minimum of 10,000 cells per condition were analyzed on a BD LSR II flow cytometer. Flow cytometry data were analyzed with appropriate gating and compensation controls using the software FlowJo (TreeStar, Inc.). Cell cycle analysis was performed on the FlowJo cell cycle analysis platform using the Dean Jett Fox model.

### 3.5.6. Partial Least Square Modeling

Statistical modeling was performed using the SIMCA-P software (Umetrics). All signals were mean centered and unit variance scaled prior to analysis to allow all variables to be considered equally scale in principal components (130). The data set was divided into two matrices:  $Y \in \mathbb{R}^{18 \times 2}$  consisting of measures of age in culture (dependent variable block), and  $X \in \mathbb{R}^{18 \times 140}$ , denoting the measured protein phosphorylation signals as well as surface markers, cell morphology and intracellular proteins (independent variable block). Instantaneous derivatives of the signaling dynamics, corresponding to the slopes of the phosphorylation dynamics signals, were also added to the X block. PLSR can accommodate data sets that are not fully complete (i.e., yielding matrices that are not

of full rank), providing the missing values are randomly distributed. The quality of a PLSR model can be summarized by two primary metrics: how well it is able to mathematically reproduce the data of the training set (given by the parameter  $R^2Y$ ) and how reliably we can predict the next experiment's outcome (given by  $Q^2$ ). A good  $Q^2$  is considered to be above 0.5.

$$R^2Y = 1 - \frac{RSS}{SSY_{tot.corr}} \quad (3.5)$$

$$Q^2Y = 1 - \frac{PRESS}{SSY_{tot.corr}} \quad (3.6)$$

where  $RSS$  represents the residual sum of squares of predicted  $Y$ ,  $SSY_{tot.corr}$  the total variation in the  $Y$  matrix after mean centering and scaling and  $PRESS$ , the predictive residual sum of squares defined as

$$PRESS = \sum (y_{im} - \widehat{y}_{im})^2 \quad (3.7)$$

calculated by cross validation. The appropriate number of components is defined as the optimum trade-off between goodness of fit and predictive ability. For more detailed description on PLSR modeling we refer to a previous explanation (204).

## CHAPTER 4

### REDOX-RELATED MARKERS OF SENESENCE ARE ALTERED BY *IN VITRO* LONG- TERM CULTURE OF CD8+ T CELLS

#### 4.1. Introduction

Immunosenescence is characterized by a decreased ability of the immune system to respond to foreign antigens and to maintain tolerance to self-antigens resulting in increased incidence of cancer, infection and autoimmune diseases in the elderly (23). The inability to respond to antigenic stimulation is also observed at the cellular level *in vitro* using long-term culturing conditions (205). In addition to being an *in vitro* framework of *in vivo* aging, T cells reaching senescence after many divisions are also a pitfall of large-scale T cell clonal expansion for immunotherapies, e.g. adoptive T cell transfer therapy (ACT) (38). Improvement of *ex vivo* cell expansion for these therapies requires a better understanding of the changes occurring at the molecular levels during *in vitro* aging.

Reactive oxygen species (ROS) are generated by the mitochondria during normal metabolism and NADPH oxidases during signaling, but can be effectively eliminated by cellular antioxidant defense mechanisms. Although T cells modulate their redox status for signaling purposes (206-209), excessive production of ROS can overwhelm the antioxidant defense system, leading to oxidative stress, improper signaling and tissue and DNA damage. Increased ROS levels could therefore be a potential molecular mechanism for the altered signaling dynamics in *in vitro* aging T cells described in Chapter 3.

Immunosenescence of T cells can be linked to the free-radical theory of aging. Increased mitochondrial leakage (68, 210, 211) and resulting mitochondrial DNA damage

(212) have been shown in aging lymphocytes. DNA damage increases and repair decreases (213, 214), advanced glycation end products (AGE) and oxidized non-functional proteins accumulate due to reduced proteasomal and methionine sulfoxide reductases activities (215-219).

Recent comprehensive microarray studies have been conducted to compare gene expression profiles in T cells between young and old mice or human subjects (220-222). These studies suggest the differential expression of several key redox regulatory genes, such as the upregulation of genes involved in oxidative phosphorylation (221) or the monotonic decline in antioxidant defense, more specifically in glutathione metabolism (222). At the proteomic level, Gautam *et al.* reported an age-dependent monotonic increase in the levels of lipid peroxidation and protein oxidation, as well as an age-dependent monotonic decline in glutathione levels and activities of the major antioxidant enzymes catalase, superoxide dismutase (Sod), glutathione reductase (GR), glutathione peroxidase (GPx) and glutathione S-transferase (GST) in mixed human T cell populations from various age groups (223). This study demonstrates a pro-oxidant shift in redox potential *in vivo*; yet such changes have not been characterized *in vitro* cell models, and in particular in culture conditions that mimic expansion methods for ACT.

Using quantitative RT-qPCR technologies, we report in this study that a similar redox remodeling towards a pro-oxidative environment occurs in CD8<sup>+</sup> T cells aging *in vitro*. Older T cells overexpress the NADPH oxidase Duox1 and downregulate key antioxidant enzymes, leading to an overall higher cellular redox potential as determined by the Trx and glutathione redox couples. Our results indicate that *in vitro* culture conditions consistent with ACT recapitulate features of the cellular redox status observed *in vivo*.

## **4.2. Results**

### **4.2.1. RT-qPCR gene expression profile of young CD8+ T cells**

We previously used an *in vitro* aging framework to identify biomarkers of aging associated with early T cell signaling and observed altered phosphorylation patterns in long-term cultured cells (224). Using the same *in vitro* aging conditions, the goal of this study was to determine the effects of *in vitro* aging on the redox status of CD8+ T cells. We extracted RNA from young (up to 3 population doublings) and old (more than 8 population doublings) CD8+ T cells of young healthy donors and measured gene expression profiles of 84 antioxidant and redox related genes (Appendix B.T1) using the Human Oxidative Stress and Antioxidant Defense PCR Array. Out of these 84 genes, only 58 were expressed in T cells. The normalized mRNA levels of individual genes expressed in the young CD8+ T cells are presented as  $\Delta C_T \pm \text{SEM}$  in Table 4.1. The inter-array coefficient of variation (CV) represents the donor to donor variability in gene expression and ranged from 0.9% to 19.06%, with a mean percentage of 4.4%.

Out of the 58 genes, p22-phox, a subunit of superoxide producing NADPH oxidases, is the most highly expressed in the young cells. At similar levels, several families of antioxidants are expressed including superoxide dismutases (Sod), glutathione peroxidases (Gpx) and peroxiredoxins (Prdx). Sod1, Gpx4 and Prdx6 are the most highly expressed antioxidant genes, followed by other isoforms Prdx3, Prdx2, Prdx5 and Prdx4, Gpx1 and Gpx7 and the mitochondrial Sod2.

**Table 4-1:** Normalized mRNA levels of individual genes expressed in young CD8+ T cells, ranked in descending order of expression (n=6).

| <b>Symbol</b> | <b>Protein Name</b>                                         | <b>Mean <math>\Delta\text{Ct} \pm \text{SEM}</math></b> | <b>% CV</b> |
|---------------|-------------------------------------------------------------|---------------------------------------------------------|-------------|
| <b>CYBA</b>   | P22-phox                                                    | $3.77 \pm 0.4$                                          | 10.64       |
| <b>CCL5</b>   | Chemokine (C-C motif) ligand 5                              | $3.58 \pm 0.68$                                         | 19.06       |
| <b>SOD1</b>   | Superoxide dismutase 1, soluble                             | $4.19 \pm 0.23$                                         | 5.56        |
| <b>GPX4</b>   | Glutathione peroxidase 4<br>(phospholipid hydroperoxidase)  | $4.38 \pm 0.40$                                         | 9.24        |
| <b>PRDX6</b>  | Peroxiredoxin 6                                             | $4.60 \pm 0.30$                                         | 6.48        |
| <b>GTF2I</b>  | General transcription factor Iii                            | $4.79 \pm 0.28$                                         | 5.93        |
| <b>PRDX3</b>  | Peroxiredoxin 3                                             | $4.61 \pm 0.46$                                         | 9.98        |
| <b>PRDX2</b>  | Peroxiredoxin 2                                             | $4.78 \pm 0.35$                                         | 7.24        |
| <b>GPX1</b>   | Glutathione peroxidase 1                                    | $5.17 \pm 0.23$                                         | 4.48        |
| <b>CSDE1</b>  | Cold shock domain containing E1, RNA-binding                | $5.19 \pm 0.23$                                         | 4.48        |
| <b>FOXM1</b>  | Forkhead box M1                                             | $5.39 \pm 0.18$                                         | 3.44        |
| <b>PRDX5</b>  | Peroxiredoxin 5                                             | $5.38 \pm 0.28$                                         | 5.25        |
| <b>ATOX1</b>  | ATX1 antioxidant protein 1 homolog (yeast)                  | $5.60 \pm 0.21$                                         | 3.70        |
| <b>TXNRD1</b> | Thioredoxin reductase 1                                     | $6.17 \pm 0.08$                                         | 1.33        |
| <b>DHCR24</b> | 24-dehydrocholesterol reductase                             | $6.38 \pm 0.18$                                         | 2.83        |
| <b>RNF7</b>   | Ring finger protein 7                                       | $6.58 \pm 0.21$                                         | 3.13        |
| <b>SOD2</b>   | Superoxide dismutase 2, mitochondrial                       | $6.59 \pm 0.21$                                         | 3.12        |
| <b>OXSRI</b>  | Oxidative-stress responsive 1                               | $6.98 \pm 0.10$                                         | 1.47        |
| <b>CAT</b>    | Catalase                                                    | $6.78 \pm 0.4$                                          | 5.92        |
| <b>PRDX4</b>  | Peroxiredoxin 4                                             | $6.99 \pm 0.36$                                         | 5.18        |
| <b>MGST3</b>  | Microsomal glutathione S-transferase 3                      | $7.18 \pm 0.23$                                         | 3.22        |
| <b>MPV17</b>  | MpV17 mitochondrial inner membrane protein                  | $7.18 \pm 0.23$                                         | 3.21        |
| <b>GLRX2</b>  | Glutaredoxin 2                                              | $7.39 \pm 0.18$                                         | 2.49        |
| <b>GSS</b>    | Glutathione synthetase                                      | $7.37 \pm 0.28$                                         | 3.81        |
| <b>BNIP3</b>  | BCL2/adenovirus E1B 19kDa interacting protein 3             | $7.38 \pm 0.34$                                         | 4.62        |
| <b>SELS</b>   | Selenoprotein S                                             | $7.78 \pm 0.28$                                         | 3.62        |
| <b>STK25</b>  | Serine/threonine kinase 25                                  | $7.98 \pm 0.10$                                         | 1.24        |
| <b>TXNRD2</b> | Thioredoxin reductase 2                                     | $7.79 \pm 0.34$                                         | 4.43        |
| <b>NUDT1</b>  | Nudix (nucleoside diphosphate linked moiety X)-type motif 1 | $8.18 \pm 0.09$                                         | 1.04        |
| <b>PNKP</b>   | Polynucleotide kinase 3'-phosphatase                        | $7.99 \pm 0.31$                                         | 3.89        |
| <b>GPX7</b>   | Glutathione peroxidase 7                                    | $8.00 \pm 0.31$                                         | 3.89        |
| <b>OXR1</b>   | Oxidation resistance 1                                      | $8.19 \pm 0.23$                                         | 2.85        |
| <b>PRDX1</b>  | Peroxiredoxin 1                                             | $8.19 \pm 0.30$                                         | 3.70        |
| <b>CCS</b>    | Copper chaperone for superoxide dismutase                   | $8.80 \pm 0.19$                                         | 2.13        |
| <b>IPCEF1</b> | Interaction protein for cytohesin exchange factors 1        | $8.57 \pm 0.58$                                         | 6.78        |
| <b>MTL5</b>   | Metallothionein-like 5, testis-specific (tesmin)            | $8.97 \pm 0.31$                                         | 3.46        |
| <b>SIRT2</b>  | Sirtuin 2                                                   | $9.01 \pm 0.38$                                         | 4.20        |

Table 4-1 continued

| Symbol         | Protein Name                                                             | Mean $\Delta\text{Ct} \pm \text{SEM}$ | % CV |
|----------------|--------------------------------------------------------------------------|---------------------------------------|------|
| <b>PREX1</b>   | Phosphatidylinositol-3,4,5-trisphosphate-dependent Rac exchange factor 1 | 9.18 $\pm$ 0.23                       | 2.49 |
| <b>GSTZ1</b>   | Glutathione transferase zeta 1                                           | 9.19 $\pm$ 0.37                       | 4.07 |
| <b>NCF2</b>    | Neutrophil cytosolic factor 2                                            | 9.38 $\pm$ 0.39                       | 4.20 |
| <b>NCF1</b>    | Neutrophil cytosolic factor 1                                            | 9.00 $\pm$ 0.89                       | 9.91 |
| <b>SRXN1</b>   | Sulfiredoxin 1                                                           | 10.18 $\pm$ 0.23                      | 2.26 |
| <b>MSRA</b>    | Methionine sulfoxide reductase A                                         | 10.18 $\pm$ 0.3                       | 2.93 |
| <b>DUSP1</b>   | Dual specificity phosphatase 1                                           | 10.19 $\pm$ 0.43                      | 4.19 |
| <b>GPX3</b>    | Glutathione peroxidase 3 (plasma)                                        | 10.37 $\pm$ 0.49                      | 4.76 |
| <b>SEPP1</b>   | Selenoprotein P, plasma, 1                                               | 10.57 $\pm$ 0.29                      | 2.80 |
| <b>PRNP</b>    | Prion protein                                                            | 11.01 $\pm$ 0.10                      | 0.90 |
| <b>GSR</b>     | Glutathione reductase                                                    | 10.78 $\pm$ 0.34                      | 3.17 |
| <b>PDLIM1</b>  | PDZ and LIM domain 1                                                     | 10.98 $\pm$ 0.3                       | 2.79 |
| <b>TTN</b>     | Titin                                                                    | 11.19 $\pm$ 0.42                      | 3.79 |
| <b>MT3</b>     | Metallothionein 3                                                        | 11.4 $\pm$ 0.73                       | 6.40 |
| <b>ANGPTL7</b> | Angiopoietin-like 7                                                      | 12.17 $\pm$ 0.23                      | 1.87 |
| <b>ALOX12</b>  | Arachidonate 12-lipoxygenase                                             | 12.17 $\pm$ 0.42                      | 3.48 |
| <b>EPX</b>     | Eosinophil peroxidase                                                    | 12.58 $\pm$ 0.41                      | 3.29 |
| <b>DUOX1</b>   | Dual oxidase 1                                                           | 12.78 $\pm$ 0.34                      | 2.68 |
| <b>SFTPD</b>   | Surfactant protein D                                                     | 12.57 $\pm$ 0.76                      | 6.07 |
| <b>PXDN</b>    | Peroxidasin homolog (Drosophila)                                         | 13.21 $\pm$ 0.62                      | 4.70 |
| <b>GPX2</b>    | Glutathione peroxidase 2 (gastrointestinal)                              | 13.99 $\pm$ 0.47                      | 3.36 |

#### 4.2.2. Age-related modifications in gene expression of redox-related proteins

The effects of *in vitro* aging on CD8+ T cell gene expression are shown in Figure 4.1 and Appendix B.S1. The list of all targets, their corresponding fold changes and p-value can be found in Appendix B.T2. Large age-related changes (fold change > 1.5) were observed in 8 genes, 4 of them downregulated and 4 upregulated ( $p < 0.1$ , Figure 4.1). Angiopoietin-like 7 (Angptl7), an ECM deposition protein (225), Titin (Ttn), a cytoskeletal protein, Dual oxidase 1 (Duox1), a H<sub>2</sub>O<sub>2</sub>-producing enzyme and Glutathione peroxidase 3 (Gpx3), the extracellular isoform of Gpx are upregulated during *in vitro* aging. It is interesting to note that all these targets are expressed at very low levels in



young cells, Gpx3 for example being the Gpx isoform with the least mRNA copy numbers in the young cells. Downregulated targets are Elfin, PDZ and LIM Domain Protein 1 (Pdlim1), involved in the reorganization of microtubules at the immune synapse (226), Metallothionein-like 5 (Mtl5), a zinc-binding protein acting as an antioxidant, Glutaredoxin 2 (Glr2), a mitochondrial oxidoreductase (227) and Thioredoxin reductase 1 (Txnrd1), a central component of the antioxidant thioredoxin system.

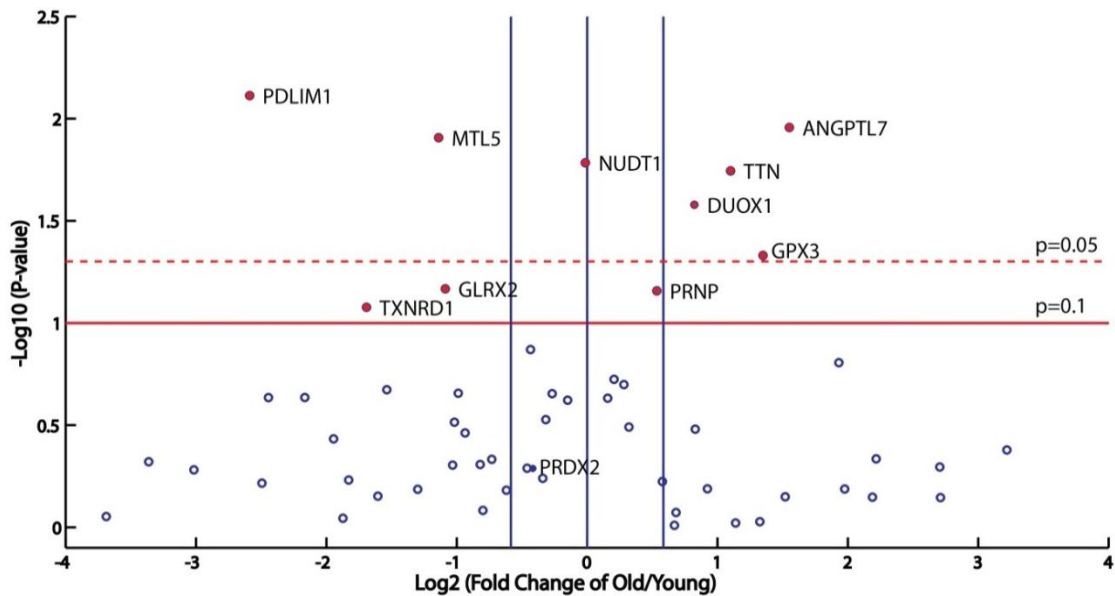


**Figure 4-1:** Fold changes in gene expression of redox related proteins during *in vitro* aging. Points above the dotted red line represent targets that show significant statistical difference (at  $p < 0.05$ ) between young and old samples. Points above the filled red line represent targets with significant statistical difference (at  $p < 0.1$ ). The blue lines represent fold changes above 1.5 fold up or down. (n=6)

#### 4.2.3. Age-related modifications in total protein amounts of the redox-related proteins Prx2, Grx1, Duox1

To compare our measurements in mRNA levels to protein expression, we conducted semi-quantitative Western blot analyses to determine the relative protein level of Duox1, Prx2 and Grx1.

The PCR array identified upregulated levels of Duox1 mRNA in older cells. Western blot analysis confirmed this increase at the protein level (Figure 4.2).

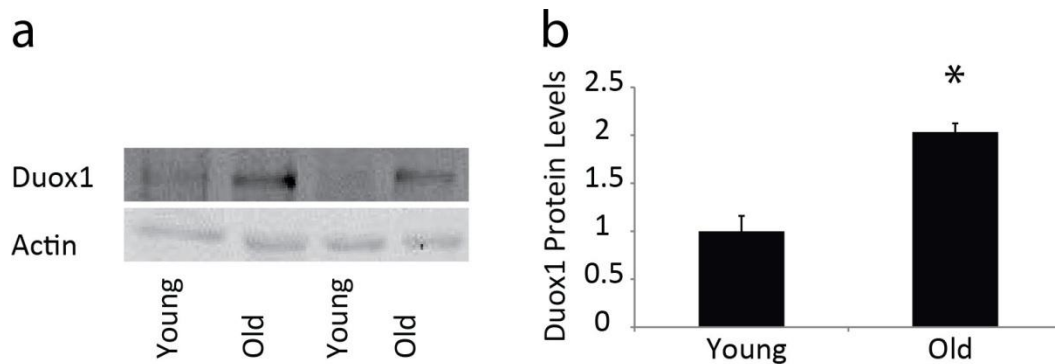


**Figure 4-2:** Duox1 protein levels. a) Representative Western Blot for 2 different donors. b) Quantification of the Western Blots. Protein levels are normalized to the young cells protein expression level. \*  $p < 0.05$  (paired 2-tail t-test).

Prx2, one of the most highly expressed Prx isoforms in T cells (Table 4.1) has been reported to be downregulated in aging bone marrow (228). Although it did not show significant downregulation of mRNA levels in our study, we probed its protein expression by Western blot, as protein levels do not always correlate directly to mRNA levels. Consistent with the mRNA results, we observed no significant changes in Prx2 levels with age ( $p=0.05$ ) despite a decreasing trend (Figure 4.3). In addition, we chose to probe for Grx1, a glutaredoxin isoform not found in the PCR array. Grx1 has been shown to be a survival factor that protects cells against apoptosis (229), a process altered in aging senescent T cells (230). As with Prx2, Grx1 protein levels show a decreasing trend, but no statistically significant changes (Figure 4.3). However to confirm these results, a higher sample number might be required as well as an additional timepoint (day 24)

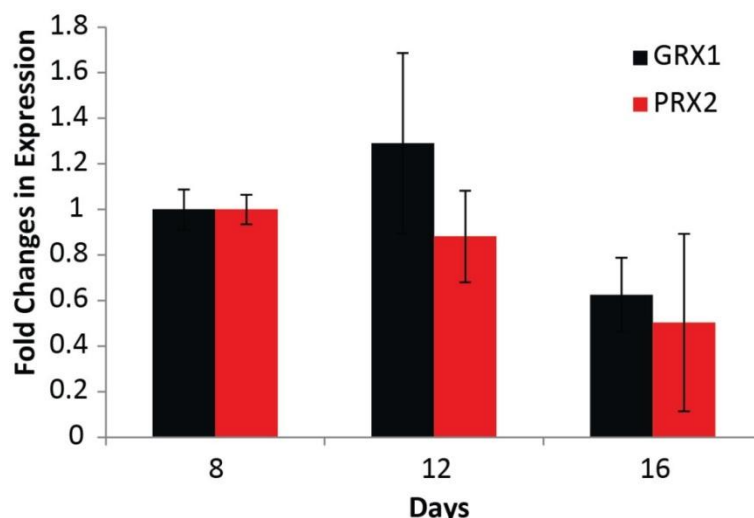


**Figure 4-3:** Relative fold changes in Grx1 and Prx2 protein expression (normalized to actin). Relative protein levels are normalized the levels at day 8.

#### 4.2.4. Age-related modifications in overall cellular redox status

Due to the technical difficulties of directly assessing oxidant levels in living cells (231), we measured the cellular redox couples as indirect measures of oxidative stress. Several indicators of *in vivo* redox status are available, including the ratios of GSH to GSSG, and the balance between reduced and oxidized thioredoxin (232).

*Glutathione redox couple:* Glutathione ( $\gamma$ -L-glutamyl-L-cysteinylglycine) is a tripeptide that functions as the major intracellular antioxidant and redox buffer against macromolecular oxidative damage. The glutathione thiol/disulfide redox couple (GSH/GSSG) is the predominant mechanism for maintaining the intracellular microenvironment in a highly reduced state that is essential for antioxidant/detoxification capacity, redox enzyme regulation, cell cycle progression, transcription of antioxidant response elements (ARE) and adequate immune response (233-236). Total levels of glutathione did not change significantly with time in culture ( $p=0.13$ ); however, the ratio

of oxidized to reduced glutathione increased with age, as indicated by an increase in the GSH/GSSG redox potential measured with HPLC (Figure 4.4).

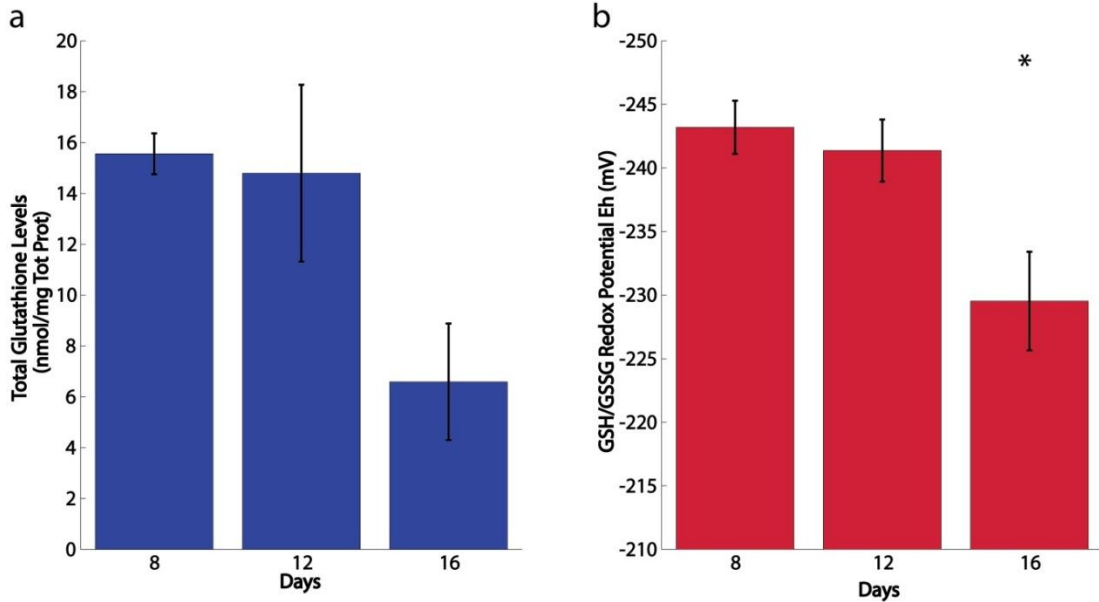


**Figure 4-4:** Total glutathione levels (a) and corresponding GSH/GSSG redox potential (b) in CD8<sup>+</sup> T cells with time in culture determined by HPLC (n=3). Statistical analysis: one-way Anova (p=0.038) followed by Scheffe's post-hoc test \* p<0.05 between day 8 and day 16

*Thioredoxin redox couple:* The thioredoxin reductive system is also an essential cellular mechanism facilitating the reduction of ROS by supporting the peroxidase action of peroxiredoxins (Prx) and directly repairing oxidatively damaged proteins (237). Pooled total levels of Trx-1 did not show significant changes among our four donors (data not shown); yet at the individual donor level, total Trx-1 expression was reduced at longer time in culture compared to day 4 and 8 (Figure 4.5a). Reduced and oxidized forms of Trx1 were determined by redox Western blots. The proportion of oxidized Trx1 increased with age (Figure 4.5a), leading to an overall increase in the cellular Trx1 redox potential between young and old cells (Figure 4.5b).

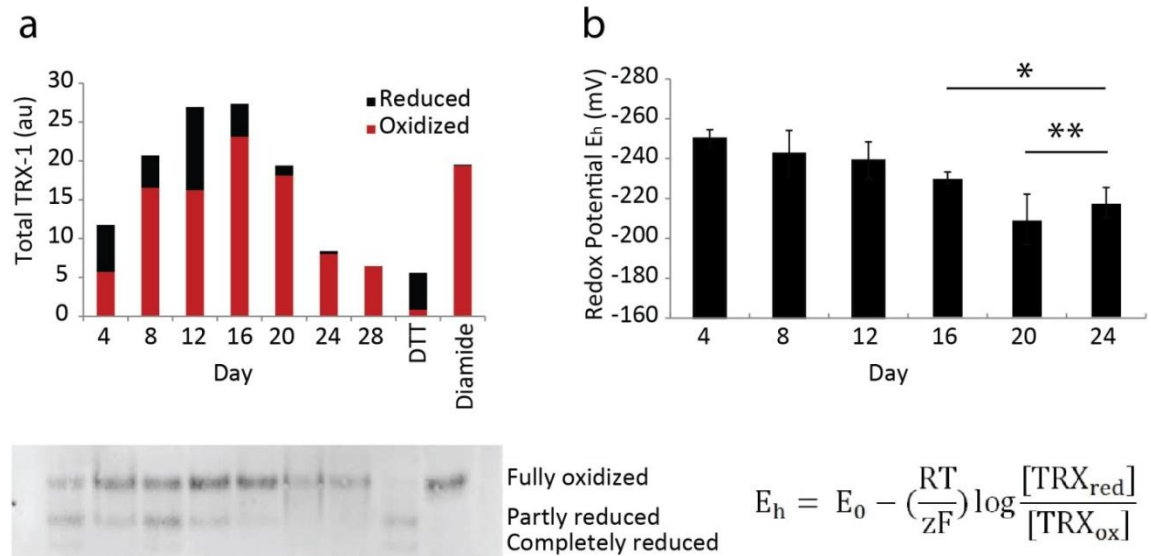


**Figure 4-5:** Trx levels in CD8+ T cells with time in culture. a) Total, reduced and oxidized Trx levels for a representative donor. DTT-treated lysates is included as a reduced control and diamide-treated lysates is included as an oxidized control. b) Cellular redox potential with respect to Trx1 (n=4). Statistical analysis: one-way Anova (p=0.007) followed by Scheffe's post-hoc test \* p<0.05 between day 4 and days 16-24. \*\* p<0.05 between days 8-12 and days 20-24.

### 4.3. Discussion

T cell responses in elderly humans show a dysregulation in intracellular transduction capacity, impaired proliferation in response to mitogenic stimuli and changes in cytokine production (238-240). We have observed a similar decrease in T cell activation in *in vitro* aging CD8+ T cells (224). A controlled T cell redox environment is essential for T cell activation and proliferation (236, 241); hence a dysregulation in cellular redox status would result in impaired signaling. For instance, a 10-30 % decrease in intracellular GSH abrogates TCR stimulated  $Ca^{2+}$  signaling (242).

In many tissues and cell types, aging is characterized by an imbalance between the formation and clearance of free radicals, resulting in a state of oxidative stress (243). Increased amounts of free radicals have been reported in cells of the immune system (218, 244) and also specifically in T cell populations from elderly subjects (223). In this

study, we have assessed changes in redox status in *in vitro* long term cultured CD8<sup>+</sup> T cells, as a potential biomolecular mechanism for the previously observed impaired T cell activation.

We used quantitative expression analysis of genes associated with the oxidative stress and antioxidant pathway in T cells to identify sources of ROS production and antioxidants in primary CD8<sup>+</sup> T cells. Large amounts of the superoxide producing NADPH oxidase 2 (Nox2) subunits including p22phox, p47phox and p67phox are expressed in T cells as well as low levels of the H<sub>2</sub>O<sub>2</sub> producing dual oxidase (Duox1). We did not detect the Nox5 and Duox2 isoforms that have been reported to be present in the Jurkat T cell line (245), while superoxide dismutases, glutathione peroxidases and peroxiredoxins were found to be expressed in high levels. Gpx4 and Gpx1 are selenoproteins, involved in the reduction of H<sub>2</sub>O<sub>2</sub> into water using reduced glutathione as a specific electron donor substrate (246). These two isoforms had previously been identified in Jurkat T cells as the predominant selenoproteins isoforms and have been reported to decrease during HIV infection, an accelerated immunosenescence state (247). Prdx 2, 3, 5 and 6 are expressed in similar high levels in CD8<sup>+</sup> T cells. Peroxiredoxins are low efficiency antioxidant enzymes that reduce H<sub>2</sub>O<sub>2</sub> using thiols as reductants (248) and have also been reported recently to be involved in cancer, inflammation and innate immunity (249).

Previous microarray results suggest that several key redox regulatory genes are differentially expressed in lymphocytes from young and old individuals (220-222). Cao *et al.* reported upregulation of genes involved in oxidative phosphorylation in CD8<sup>+</sup> T cells

from old healthy human subjects (221) while others observed a monotonic decline in antioxidant defense, more specifically in glutathione metabolism (222). In this study, we focused on changes in oxidative stress and antioxidant gene expression patterns during *in vitro* aging. Out of the genes expressed in T cells, 14% showed significant changes with age (Figure 41). Two structural proteins are upregulated with age, Angiopoietin-like 7 (Angptl7) and Titin (Ttn). Angptl7 is a secreted protein involved in blood vessel formation with an additional role in lipid metabolism by inhibition of phospholipid lipase. Plasma Angptl4, another Angptl isoform had been previously shown to be positively correlated with age (250). Titin is a giant protein controlling the structure and elasticity of vertebrate muscle sarcomeres (251). Its role in lymphocytes is not clearly defined but it has been identified as a gene signature for chronic lymphocytic leukemia (CLL) (252). An additional gene upregulated during *in vitro* aging is the H<sub>2</sub>O<sub>2</sub>-producing enzyme Duox1. We confirmed this increase by measuring protein levels of Duox1 in young and old T cells (Figure 4.2). Although it is the first time Duox1 is reported to be upregulated during aging, increased levels of other NADPH oxidases isoforms have been documented. Nox2 shows an age-dependent increase in the aging stomach (253), Nox2 and Nox4 an age-dependent increase in aging myocytes (254).

The decreased expression of major antioxidants is consistent with the microarray results mentioned above. Metallothioneins are low molecular weight proteins, scavenger of free radicals, associated with lifespan in mice and humans (255) and shown to be downregulated with age *in vivo* and *in vitro* systems of CD4<sup>+</sup> T cells (256). Glrx2 has been described as a critical component for the regulation of the mitochondrial redox status (227). A decrease in the Glrx2 levels would result in the dysregulation of the

mitochondrial detoxification system and mitochondrial oxidative stress, a central dogma of aging (257). Txnrd1 is a major redox regulator by reducing and activating thioredoxin and the thioredoxin system has previously been shown to be impaired during aging. Reduction in Trx1 and Trx reductase mRNA levels has been shown in skeletal muscles (258) and kidneys (259) from old rats.

Our RT-qPCR results (Figure 4.1) suggest a redox remodeling in various cellular compartments of *in vitro* aging T cells that would result in higher levels of cellular oxidation. Our group had previously demonstrated systemic remodeling of the redox regulatory network due to perturbation of specific antioxidant enzymes in Jurkat cells resulting in adaptation but differential response to exogenous oxidative stress (245). In both studies, insularity between the cytosol and mitochondrial compartments as well as strong covariance between peroxiredoxins and Prx2 and Grx1 were conserved. But in contrast to redox remodeling due to shRNA perturbation, remodeling of the redox regulatory pathway in aging T cells shows an upregulation of the ROS producing enzyme while major antioxidant enzymes transcripts levels are reduced. This suggests that redox remodeling during aging may be the result of a lost ability of the cell to adapt to an initial perturbation in its antioxidant pathway leading to a pro-oxidative environment.

Consistent with this adaptation, large changes in redox potential were observed for the Trx redox couple. Compared to redox potentials of the Jurkat cell line (260), young primary CD8<sup>+</sup> T cells show a more oxidized Trx redox couple simultaneously but a more reduced GSH redox couple. In particular, the GSH redox potential of old CD8<sup>+</sup> T cells has the same order of magnitude as Jurkat cells challenged with a 100  $\mu$ M H<sub>2</sub>O<sub>2</sub> bolus.



These dissimilarities suggest different contributions of the Trx and GSH redox machineries in the overall redox buffering system in related cell types

*In vivo* studies have shown decreases in total levels of glutathione (223, 261); yet despite a decreasing trend, the total protein levels of Trx1 and glutathione did not show significant changes in long-term cultured CD8 T cells. To validate this result, the experiment needs to be rerun with a higher sample number in order to mask donor-to-donor variability and increase statistical significance. In addition, direct techniques to probe ROS levels using ROS specific dyes, such as the H<sub>2</sub>O<sub>2</sub> specific dye H<sub>2</sub>-DCFDA or the superoxide specific indicator DH<sub>2</sub> have been used to compare cytoplasmic ROS levels in young and old lymphocytes (215) or in young and old human fibroblasts (262). The general consensus in the literature is that cytoplasmic ROS levels increase with age. We attempted to determine cytoplasmic H<sub>2</sub>O<sub>2</sub> and mitochondrial superoxide levels in living cells at various time in culture using H<sub>2</sub>-DCFDA and the mitochondrial superoxide indicator Mitosox but did not observe any significant trends with aging; however this might be due to limitations in the assay such as dye leakage or autoxidation (231).

#### **4.4. Conclusion**

The study in this Chapter suggests that there is a shift towards a pro-oxidizing cellular environment in *in vitro* aged CD8<sup>+</sup> T cells. Although hyperoxic conditions of *in vitro* T cell culture might contribute to this phenotype, the upregulation of an H<sub>2</sub>O<sub>2</sub>-producing enzyme and downregulation of key antioxidant proteins are also potential mechanisms resulting in this elevated oxidative state. Because T cell function relies on a controlled

intracellular redox status, elevated ROS levels in aged CD8<sup>+</sup> T cells are a possible cause of altered signaling observed in Chapter 3.

## **4.5. Materials & Methods**

Primary T cell isolation, cell culture and expansion have been described in Chapter 3.

### **4.5.1. RNA extraction and purification**

Total RNA from CD8<sup>+</sup> T cells was extracted using the RNeasy Mini isolation kit (SABiosciences, Frederick, MD) with RNase-free DNase set (Qiagen, Valencia, CA) according to the manufacturer's protocol. The integrity and concentration of intact total RNA was verified with a NanoDrop 1000 Spectrophotometer (Thermo Scientific).

### **4.5.2. Real-time quantitative reverse transcriptase PCR**

Real-time PCR was performed with a StepOnePlus RT-qPCR System instrument (Applied Biosystems, Carlsbad, CA) using the Human Oxidative Stress and Antioxidant Defense PCR Array (SABiosciences) containing 84 predesigned gene-specific primer and probe sets (PAHS-065C, SA Biosciences), according to manufacturer's protocol. A list of targets included in the array can be found in the Appendix B.T1. Briefly, 1 µg of total RNA was reverse transcribed and amplified using the RT<sub>2</sub> First Strand Kit (Quiagen) following the manufacturer's instructions. Amplified cDNA was mixed with RT<sub>2</sub> SYBR Green ROX qPCR Mastermix (Quiagen) and Nuclease-Free Water (Quiagen) and loaded on the PCR array plate. Initial denaturation of DNA was carried out at 95°C for 10 min.

Forty amplification cycles were performed, each cycle consisting of denaturation (95°C, 30 s) and annealing and extension (65°C, 1 min). Two individual arrays were performed for each donor, one for young cells and one for older cells. Relative expression levels were calculated using the  $\Delta\text{CT}$  method ( $2^{-\Delta\text{CT}}$ ) (263) and results were normalized using the geometric mean of the housekeeping genes GAPDH and HPRT1 (hypoxanthine phosphoribosyltransferase 1). Reference gene selection among the five housekeeping genes on the PCR array plate was performed by calculating the fold change and its corresponding p-value for the two age groups for any combination of one or more housekeeping genes. The gene combination with the highest p-value and the fold change closer to 1 was selected.

#### **4.5.3. Cell lysis for western blotting**

For western blotting,  $8 \times 10^6$  cells were lysed in 100  $\mu\text{l}$  lysis buffer containing 2% NP-40, 50 mM  $\beta$ -glycerophosphate, 10 mM NaP, 30 mM NaF, 50 mM Tris, pH 7.5, 150 mM NaCl, 1 mM benzamidine, 2 mM EGTA, 100  $\mu\text{M}$  sodium orthovanadate, 1 mM DTT, 10  $\mu\text{g/ml}$  aprotinin, 10  $\mu\text{g/ml}$  leupeptin, 1  $\mu\text{g/ml}$  pepstatin, 1  $\mu\text{g/ml}$  microcystin-LR, and 1 mM PMSF. Cells were lysed on ice for one hour and lysates stored at -80°C until analysis. Protein concentration was determined with the Micro BCA™ Assay Kit (ThermoFisher Scientific, Waltham, MA). For non-reducing western blot analysis, cells were lysed in a G lysis buffer (recipe: 2% NP-40, 50 mM Tris, pH 7.5, 150 mM NaCl, 1 mM benzamidine, 2 mM EGTA, 10  $\mu\text{g/ml}$  aprotinin, 10  $\mu\text{g/ml}$  leupeptin, 1  $\mu\text{g/ml}$  pepstatin, 20 mM ethylmaleimide, and 1 mM PMSF) with 9.3 mg/mL iodoacetate acid (IAA) for 30 minutes at 37°C. Lysates were spun through a G25 spin column to remove

excess IAA and frozen at -80°C until use. Total protein content was measured using a BCA modified by addition of iodoacetamide buffer.

#### **4.5.4. Western blotting**

For western blots, 20 to 40 µg of total protein/sample was subjected to SDS-PAGE and transferred to PVDF membranes. For redox western blots, native gel electrophoresis was performed under non-reducing conditions as previously described (264). The membrane was blocked with Near Infra-Red Blocking Buffer (Rockland Immunochemicals, Gilbertsville, PA) overnight at 4°C. Primary antibodies were used at a dilution of 1:1000 in 10 ml blocking buffer and incubated over night at 4°C, followed by three washes in TBS-T. Secondary antibodies (IR dye 680CW donkey anti-mouse, IR dye 800CW anti-goat or IR dye 800CW donkey anti-rabbit, all from LI-COR Biosciences (Lincoln, NE), were all used at a dilution of 1:10000 in 10 ml blocking buffer and incubated for 1h at room temperature. This was followed by two washes in TBS-T and one wash in TBS. Imaging and image analysis were done using the Li-Cor Odyssey Infrared Imaging System with the Odyssey 2.1 software.  $\beta$ -actin was used as loading control. Primary antibody for Grx1 was purchased from R&D Systems (Minneapolis, MN), for Trx1 from Sekisui Diagnostics (Framingham, MA), for Duox1 from Novus Biologicals (Littleton, CO), for Prx2 from Abcam (Cambridge, MA), and for  $\beta$ -actin from Sigma-Aldrich.

#### 4.5.5. Measurement of intracellular GSH and GSSG

GSH and GSSG were measured by high-performance liquid chromatography (HPLC) as S-carboxymethyl N-dansyl derivatives using  $\gamma$ -glutamylglutamate as an internal standard (265).

#### 4.5.6. Measurement of cellular redox potential

Cellular redox potential with respect to glutathione and thioredoxin was calculated using the Nernst equation:  $E_{GSH} = E_{GSH}^0 - \left(\frac{RT}{zF}\right) \log \frac{[GSH]^2}{[GSSG]}$  for glutathione and  $E_{TRX} = E_{TRX}^0 - \left(\frac{RT}{zF}\right) \log \frac{[TRX_{red}]}{[TRX_{ox}]}$  for thioredoxin, where R is the gas constant (9.315 J K<sup>-1</sup> mol<sup>-1</sup>), T the absolute temperature (298.15 K), z the number of transferred electrons (2), and F is the Faraday constant (96.485 C mol<sup>-1</sup>).

The standard redox potential of glutathione at pH 7  $E_{GSH}^0$  is -264mV (266, 267). The standard redox potential of thioredoxin 1 at pH 7  $E_{TRX}^0$  is -254mV (268).

## CHAPTER 5

### CALCIUM SIGNALING IS ALTERED IN *IN VITRO* LONG-TERM CULTURED CD8+ T CELLS

#### 5.1. Introduction

Calcium signaling is an essential step in T cell activation and regulates diverse cellular functions, such as proliferation, apoptosis, differentiation, effector function and gene transcription (269). Because of its importance, the  $\text{Ca}^{2+}$  signaling pathway has been extensively studied in T cells, with the discovery of new regulatory molecular mechanisms in the past few years (269-273). Briefly, after T cell receptor ligation, phosphorylation of  $\text{PLC}\gamma$  leads to  $\text{IP}_3$  formation and rapid  $\text{Ca}^{2+}$  release from the ER stores through the  $\text{IP}_3$  receptor channels. T cells sustain elevated cytoplasmic  $\text{Ca}^{2+}$  levels for gene transcription, by balancing store-operated  $\text{Ca}^{2+}$  entry (SOCE) through the plasma membrane and  $\text{Ca}^{2+}$  buffering by the mitochondria.

T cell function declines with age, rendering elderly more susceptible to cancer, infections and autoimmune diseases. The exact causes of T-cell functional decline are not known and several studies have demonstrated the development of defects in the early signal transduction events inducing  $\text{Ca}^{2+}$  release following mitogenic stimulation during the course of immunosenescence (224, 239). Altered  $\text{Ca}^{2+}$  dynamics in T cells have been associated with several age-related diseases, such as neurodegenerative, autoimmune and inflammatory disorders (274). More specifically, diminished activation-induced  $\text{Ca}^{2+}$

fluxes has been reported in CD8+ T cells from aged mice (275, 276) and T cells from elderly humans (277, 278) but predominantly in the CD4+ subset (279).

Computational models are useful tools to systematically analyze mechanisms in complex systems, interpret experimental data and provide new experimentally testable predictions. Because of the importance of  $\text{Ca}^{2+}$  signaling in various cellular systems, substantial efforts have been devoted at modeling  $\text{Ca}^{2+}$  dynamics. Most of these models describe  $\text{Ca}^{2+}$  dynamics in excitable cells, i.e. in neurons (280-282), cardiomyocytes and muscle cells (283-288) that display oscillations. Fewer computational models describe  $\text{Ca}^{2+}$  dynamics in non-excitable immune cells, and specifically T cells. Ahnadi *et al.* and Kim *et al.* published deterministic models of  $\text{Ca}^{2+}$  kinetics after T cell engagement in respectively Jurkat and murine T cells (289, 290). These models are able to reproduce cytoplasmic  $\text{Ca}^{2+}$  rise after T cell stimulation but do not include extracellular space, mitochondrial buffering and mechanistic details of SOCE. A more detailed computational model of  $\text{Ca}^{2+}$  dynamics in immune cells has been reported by Maurya *et al.* (291). This model predicts temporal responses of  $\text{Ca}^{2+}$  concentrations for various doses of stimulus and network perturbations in RAW 264.7 macrophages (291, 292).

Using an *in vitro* aging framework of CD8+ T cells (205, 293), we have shown an overall decrease in protein phosphorylation after T cell receptor ligation in Chapter 3 (224). Based on the *in vivo* data and the decreased protein phosphorylation after TCR stimulation, reduced  $\text{Ca}^{2+}$  dynamics are expected. Here, we report that amplitude of  $\text{Ca}^{2+}$  signaling does not change with age in culture; counterintuitively, we observed a faster  $\text{Ca}^{2+}$  rise and a faster decay in older T cells. Gene expression analysis of  $\text{Ca}^{2+}$  channels and pumps expressed in T cells by RT-qPCR identified overexpression of the plasma

membrane CRAC channel subunit ORAI1 and PMCA in older T cells. To test whether overexpression of plasma membrane  $\text{Ca}^{2+}$  channel is sufficient to explain the kinetic information we adapted the Maurya model (291, 292) with additional details on the SOCE process to recapitulate  $\text{Ca}^{2+}$  dynamics after T cell receptor stimulation and determine the defects in the  $\text{Ca}^{2+}$  signaling pathway responsible for alterations in  $\text{Ca}^{2+}$  dynamics during aging. Results of the model show that upregulation of these  $\text{Ca}^{2+}$  channels is not sufficient to explain the observed alterations in  $\text{Ca}^{2+}$  signaling and suggests changes in kinetic parameters associated with the  $\text{IP}_3\text{R}$  and SERCA channels as potential causes. This computational model is a useful tool to study T cell behavior and uncover dysregulated mechanisms in disease state and aging that alter  $\text{Ca}^{2+}$  fluxes.

## **5.2. Computational model of calcium dynamics in T lymphocytes**

We developed a mathematical model for calcium signaling after T cell receptor ligation. The model comprises a simplified module for  $\text{IP}_3$  formation, and calcium fluxes from the three major cellular compartments: cytosol, endoplasmic reticulum (ER), mitochondria as well as the extracellular space. It is based on previously published models of calcium dynamics (291, 294-296) with additional terms reflecting the recently discovered stromal interaction molecule STIM1 and CRAC subunit Orai.

### **5.2.1. Model Description**

Figure 5.1 shows an overall schematic of the computational model. The binding of a peptide/MHC complex to the TCR triggers the recruitment of tyrosine kinases Lck, LAT and Zap70 to the TCR/CD3 complex, ultimately resulting in the phosphorylation and



activation of phospholipase C- $\gamma$  (PLC- $\gamma$ ). The model represents these receptor-initiated events as a one-step input to phospho-PLC- $\gamma$  levels. Activated PLC- $\gamma$  cleaves PIP<sub>2</sub> in the plasma membrane to generate diacylglycerol (DAG) and 1, 4, 5-inositol triphosphate (IP<sub>3</sub>). Binding of IP<sub>3</sub> to the IP<sub>3</sub> receptor (IP<sub>3</sub>R) triggers the release of Ca<sup>2+</sup> stored in the ER (J<sub>IP3</sub>). The resulting drop in ER Ca<sup>2+</sup> levels activates the ER Ca<sup>2+</sup> sensor STIM1, which translocates to the ER-PM (plasma membrane) junctions to activate a more sustained influx in the cytosol through the calcium release activated Ca<sup>2+</sup> channels (CRAC) on the PM (J<sub>crac</sub>) (297, 298). The PM Ca<sup>2+</sup> ATP-ase (PMCA) pumps Ca<sup>2+</sup> out of the cytosol and maintains a steep gradient of Ca<sup>2+</sup> concentration from 50 nM inside the cell to 1.5 mM in the extracellular space (J<sub>pmca</sub>). Because of this steep gradient, we assume there is a very small Ca<sup>2+</sup> leak inside the cytosol from the extracellular space (J<sub>PMleak</sub>). The Sarco/ER Ca<sup>2+</sup> ATP-ase (SERCA) pumps cytosolic Ca<sup>2+</sup> back in the ER stores to maintain an ER luminal concentration of 350  $\mu$ M (J<sub>serca</sub>). Similarly, we consider a small leak of Ca<sup>2+</sup> ions from the ER to the cytosol (J<sub>ERleak</sub>). Mitochondria are essential for the activation and maintenance of the store-operated calcium entry (SOCE) by buffering Ca<sup>2+</sup> ions and preventing the negative feedback of Ca<sup>2+</sup> on the CRAC channels (299). Uptake of Ca<sup>2+</sup> ions in the mitochondria is mediated through the Ca<sup>2+</sup> uniporter (J<sub>mitin</sub>) and extrusion through the Na<sup>+</sup>/Ca<sup>2+</sup> exchanger (J<sub>mitout</sub>).

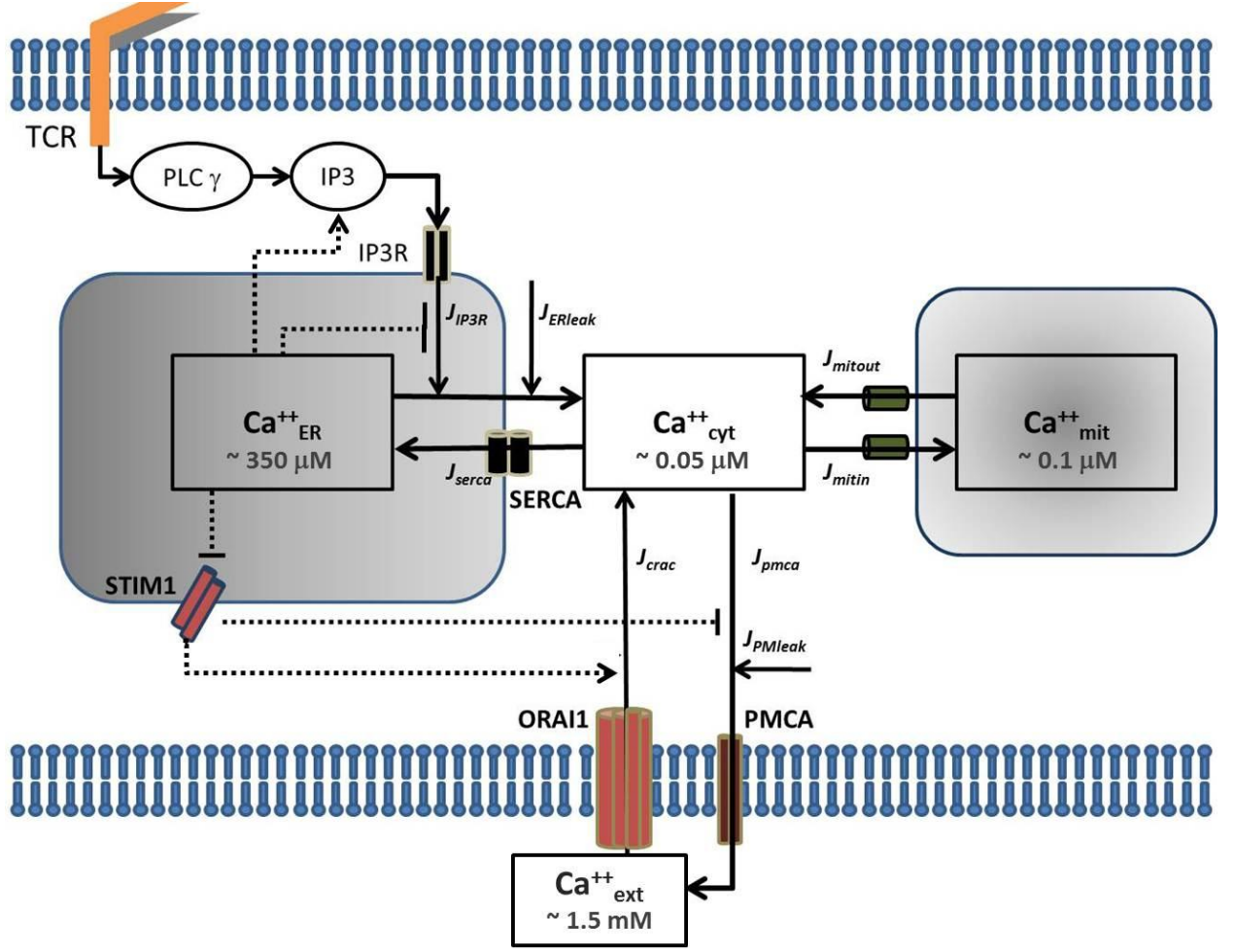


**Figure 5-1:** Schematic of the Ca<sup>2+</sup> signaling model

The fundamental equations of Ca<sup>2+</sup> kinetics in the various cellular compartments are described as follows:

$$\frac{dCa_{cyt}}{dt} = \beta_i((J_{IP3} - J_{serca} + J_{ERleak}) + (J_{mitin} - J_{mitout})) + (J_{crac} - J_{pmca} + J_{PMleak})) \quad (5-1)$$

$$\frac{dCa_{ER}}{dt} = \frac{\beta_{er}}{\rho_{er}}(J_{IP3} - J_{serca} + J_{ERleak}) \quad (5-2)$$

$$\frac{dCa_{mit}}{dt} = \frac{\beta_{mit}}{\rho_{mit}} (J_{mitin} - J_{mitout}) \quad (5-3)$$

$Ca_{cyt}$ ,  $Ca_{mit}$  and  $Ca_{ER}$  denote the concentration of free  $Ca^{2+}$  in the cytosol, mitochondria and ER respectively.  $\beta_i$ ,  $\beta_{er}$ ,  $\beta_{mit}$  are the ratio of free to total  $Ca^{2+}$ , assuming fast buffering with calcium-binding proteins in the cytosol, ER and mitochondria respectively (291, 296). In this model, we assume that the ratio of free to total  $Ca^{2+}$  is constant in the three cellular compartments and do not model explicitly the dynamics of free calcium-binding proteins.  $\rho_{er}$ ,  $\rho_{mit}$  are the ratios of the ER and mitochondria volume to that of the cytosol.

*IP<sub>3</sub> production:* Initiation of  $Ca^{2+}$  signaling after TCR binding requires formation of  $IP_3$  through PLC- $\gamma$  phosphorylation. We modeled PLC- $\gamma$  activation as a simplified one step mass action kinetics (5-5) following ligand ( $R$ ) unbinding from the TCR (5-4):

$$\frac{dR}{dt} = -k_{PLCact} \cdot R \quad (5-4)$$

$$\frac{dPLC\gamma}{dt} = k_{PLCact} \cdot R - k_{PLCdeact} \cdot PLC\gamma \quad (5-5)$$

where  $k_{PLCact}$  is the rate constant for PLC- $\gamma$  phosphorylation and  $k_{PLCdeact}$  the rate constant for PLC- $\gamma$  dephosphorylation.

The production of  $IP_3$  depends on the levels of phosphorylated PLC- $\gamma$  and cytoplasmic  $Ca^{2+}$  levels, creating a positive feedback enhancing  $IP_3$  formation:

$$\frac{dIP_3}{dt} = k_{IP_3prod} \cdot PLC\gamma \cdot Ca_{cyt} - k_{IP_3deg} \cdot IP_3 \quad (5-6)$$

where  $k_{IP3prod}$  is the rate constant for  $IP_3$  production and  $k_{IP3deg}$  the rate constant for  $IP_3$  degradation.

*Ca<sup>2+</sup> flux through the IP<sub>3</sub>R:*  $IP_3R$  is a tetramer of four identical subunits. Each unit has one  $IP_3$  binding site and two  $Ca^{2+}$  binding sites, one for activation and one for inhibition. The channel activity is cooperatively regulated by binding/unbinding of  $IP_3$  and  $Ca^{2+}$  at these binding sites. A number of mathematical models of  $IP_3R$  activation have been constructed, including Bezprozvanny *et al.* (300), De Young and Keizer (301), Atri *et al.* (302), Li and Rinzel (303), Sneyd *et al.* (304). In these models, the  $IP_3R$  is assumed to be modulated by cytosolic  $Ca^{2+}$  in a biphasic manner with  $Ca^{2+}$  release inhibited at low and high cytosolic  $Ca^{2+}$  levels, and facilitated by intermediate levels. We used the Li-Rinzel description of the  $IP_3R$  (303). The flux of  $Ca^{2+}$  through the  $IP_3R$  is given by:

$$J_{IP3} = V_{IP3} \cdot P_{IP3} \cdot Ca_{ER} \quad (5-7)$$

where  $V_{IP3}$  is the maximum flowrate and  $P_{IP3}$  the  $IP_3R$  open probability.  $P_{IP3}$  is assumed to be an instantaneous function of  $Ca^{2+}$ ,  $IP_3$  concentration and the fraction of  $IP_3R$  not inactivated by  $Ca^{2+}$  bound to the inhibitory site,  $h$ .  $P_{IP3}$  is described as:

$$P_{IP3} = \left( \frac{IP3}{IP3 + K_{IP3}} \right) \left( \frac{Ca_{cyt}}{Ca_{cyt} + K_{act}} \right) h^3 \quad (5-8)$$

where  $K_{IP3}$  is the  $IP_3$  dissociation constant from the  $IP_3$  binding site and  $K_{act}$  the affinity of  $Ca^{2+}$  to the activating site.

The fraction of inactivated  $IP_3R$  ( $1-h$ ), is a function of cytoplasmic  $Ca^{2+}$  and  $Q$ , the effective affinity of  $Ca^{2+}$  to the inhibitory site.

$$\frac{dh}{dt} = A((1-h)(Q + Ca_{cyt}) - Ca_{cyt}) \quad (5-9)$$

$$Q = K_{inh} \frac{IP3 + K_{IP3}}{IP3 + K_{IP3inh}} \quad (5-10)$$

where  $A$  is a variable controlling the relative time scales between the differential equations,  $K_{inh}$ , the  $Ca^{2+}$  affinity to the  $Ca^{2+}$  inhibitory site and  $K_{IP3inh}$  the affinity of  $IP_3$  to the  $IP_3$  binding site when the  $Ca^{2+}$  inhibitory site is occupied.

*Ca<sup>2+</sup> leak from the ER:* Because of the gradient of concentration between the ER and the cytosol, there is a constant leakage of  $Ca^{2+}$  ions from the ER to the cytoplasm.  $J_{ERleak}$  can be described as:

$$J_{ERleak} = K_{ERleak} \cdot Ca_{ER} \quad (5-11)$$

*Ca<sup>2+</sup> flux through the SERCA pumps:*

$$J_{serca} = V_{serca} \cdot \frac{Ca_{cyt}^2}{Ca_{cyt}^2 + K_{serca}^2} \quad (5-12)$$

where  $V_{serca}$  is the maximum flux across the SERCA pump and  $K_{serca}$  the SERCA activation constant by  $Ca^{2+}$ . Although T cells express both SERCA 2b and SERCA 3 isoforms, which have different affinities for  $Ca^{2+}$  and maximal pumping rate, we simplified the model by lumping these two isoforms into one average SERCA pump with a unique maximum velocity and  $Ca^{2+}$  affinity.

*Ca<sup>2+</sup> fluxes through the mitochondria:*  $Ca^{2+}$  intake in the mitochondria through the uniporter is modeled with a 4<sup>th</sup> order Hill function (278, 294):

$$J_{mitin} = V_{mitin} \cdot \frac{Ca_{cyt}^4}{Ca_{cyt}^4 + K_{mitin}^4} \quad (5-13)$$

where  $V_{mitin}$  is the maximum rate of  $Ca^{2+}$  uptake in the mitochondria and  $K_{mitin}$  the apparent  $Ca^{2+}$  affinity of the uniporter.

$Ca^{2+}$  efflux from the mitochondria through the  $Na^+/Ca^{2+}$  exchanger and permeability transition pores (PTP) is given by the lumped expression (291, 296):

$$J_{mitout} = V_{mitout} \cdot Ca_{mit} \cdot \frac{Ca_{cyt}^2}{Ca_{cyt}^2 + K_{mitout}^2} \quad (5-14)$$

where  $V_{mitout}$  is the maximum rate of  $Ca^{2+}$  efflux and  $K_{mitout}$  the half maximum  $Ca^{2+}$  concentration for efflux.

*Ca<sup>2+</sup> fluxes through the plasma membrane:* The details of store operated calcium entry (SOCE) have only been uncovered recently and previous mathematical descriptions of  $J_{crac}$  include order 2 Hill dynamics in respect to  $IP_3$  levels (291) or cytoplasmic  $Ca^{2+}$  levels (305) as well as a phenomenological model involving a diffusible messenger,  $Ca^{2+}$  diffusible factor (CIF) (306). More recently, after the discovery of the STIM1 and ORAI1 proteins and their interaction, Liu *et al.* (295) and Chen *et al.* (307) have attempted to provide a more accurate mathematical description of SOCE, by including activation of STIM1, dimerization, association with the ORAI1 CRAC channels and CRAC activation. More specifically, Liu *et al.* designed SOCE as a feedback controller to reject disturbances and track  $Ca^{2+}$  levels in the cytosol and in the ER (295). We simplified this system by neglecting the delay formed by STIM1 activation and assuming that the binding of STIM1 to ORAI is at a steady state only depending on the concentration of  $Ca^{2+}$  in the ER. Therefore,  $J_{crac}$  can be expressed as:

$$J_{crac} = V_{crac} * [SO] * \frac{Ca_{ext}}{Ca_{ext} + K_{soc}} \quad (5-15)$$

where  $V_{crac}$  is the maximum  $Ca^{2+}$  influx through the CRAC channels,  $K_{soc}$  is the Michaelis-Menten concentration for extracellular  $Ca^{2+}$ ,  $Ca_{ext}$  and  $[SO]$  the fraction of ORAI channels bound to STIM1.

Based on experimental data from Luik *et al.* (308) and steady state modeling of Liu *et al.* (295), we chose to model  $[SO]$  as a 3<sup>rd</sup> order Hill function depending on ER  $Ca^{2+}$ :

$$[SO] = \frac{Ca_{ER}^3}{Ca_{ER}^3 + K_{stim}^3} \quad (5-16)$$

where  $K_{stim}$  is the dissociation constant of ER  $Ca^{2+}$  to STIM1.

$Ca^{2+}$  influx through the plasma membrane is also permitted through a plasma membrane leak and is given by:

$$J_{PMleak} = K_{PMleak} * Ca_{ext} \quad (5-17)$$

where  $K_{PMleak}$  is the rate of leakage through the plasma membrane.

$Ca^{2+}$  efflux from the cytosol to the extracellular space is mainly due to the PMCA pumps and is described as:

$$J_{pmca} = V_{pmca} * \frac{Ca_{cyt}^2}{Ca_{cyt}^2 + K_{pmca}^2} * \frac{Ca_{ER}^2}{Ca_{ER}^2 + K_{STIMpmca}^2} \quad (5-18)$$

where  $V_{pmca}$  is the maximal PMCA efflux rate and  $K_{pmca}$  the  $Ca^{2+}$  affinity to the PMCA pump. STIM1 was recently shown to modulate PMCA mediated  $Ca^{2+}$  clearance in a nonlinear manner (294). We chose to represent this modulation by a 2<sup>nd</sup> order Hill kinetics with  $K_{STIMpmca}$  being the dissociation constant of ER  $Ca^{2+}$  on STIM1 allowing it to become activated and interact with PMCA probably through a conformational coupling mechanism.

### 5.2.2. Model Optimization and Simulation

The series of differential equations were solved using Matlab R2011a (Mathworks, Natick, MA). The ODE solver for stiff system ode23s was used. Initial conditions were chosen according to published experimental data before parameter optimization or computed at steady state (Table 5.1).

**Table 5-1:** Initial conditions

| State Variable    | Value                   | Reference                                                                           |
|-------------------|-------------------------|-------------------------------------------------------------------------------------|
| PLC $\gamma$      | 70 nM                   | This work                                                                           |
| IP <sub>3</sub>   | 0.54 $\mu$ M            | (309)                                                                               |
| Ca <sub>cyt</sub> | 50 nM                   | (310)                                                                               |
| Ca <sub>ER</sub>  | 350 $\mu$ M/400 $\mu$ M | (310)                                                                               |
| Ca <sub>mit</sub> | 0.1 $\mu$ M             | (311) followed by steady state computation: J <sub>mitin</sub> =J <sub>mitout</sub> |
| h                 | 0.02                    | (292)                                                                               |

Parameter estimation was performed by estimating the difference between the experimental data and the corresponding model prediction (sum of squared error) using a genetic algorithm followed by a combination of pattern search, simulated annealing and constrained nonlinear programming (Matlab Global Optimization Toolbox). Since the model parameters were estimated to fit different experimental conditions, the objective function consisted in the sum of errors across experimental conditions:

$$S = \sum_{t=1}^{t_{sim}} \sum_{n=1}^N \sum_{c=1}^C \left( \frac{x_{pred}(c, i, t) - x_{exp}(c, i, t)}{x_{data}(c, i, t)} \right)^2 \quad (5-19)$$

where  $t_{sim}$  is the maximal simulation time,  $N$  the number of state variables used for optimization and  $C$  the number of experimental conditions being optimized.

The parameter bounds were chosen based on previously published experimental or modeling parameter data (Table 5.2). The parameters  $k_{PLCact}$  and  $k_{PLCdeact}$  were fitted separately to fit our experimental data of PLC- $\gamma$  phosphorylation dynamics. The



remaining parameters were fit to three experimental datasets of  $\text{Ca}^{2+}$  dynamics following TCR ligation under no inhibitor, 50  $\mu\text{M}$  EGTA or 100  $\mu\text{M}$  TMB-8 inhibitor condition.

**Table 5-2:** Model parameters bounds for optimization

| Parameter      | Bounds                                    | Source/Explanation                                               |
|----------------|-------------------------------------------|------------------------------------------------------------------|
| $\beta_i$      | [0.001 1]                                 | SS value: 0.009 (298)                                            |
| $\beta_{er}$   | [0.001 1]                                 | SS value: 0.196 (298)                                            |
| $\beta_{mit}$  | [0.001 1]                                 | 0.0025 (297, 298)                                                |
| $\rho_{er}$    | 0.015                                     | (312)                                                            |
| $\rho_{mit}$   | 0.08                                      | (312)                                                            |
| $k_{PLCact}$   | [0.001 0.01] $\text{s}^{-1}$              | 0.047 (290)                                                      |
| $k_{PLCdeact}$ | [0.01 0.1] $\text{s}^{-1}$                |                                                                  |
| $k_{IP3prod}$  | [0.1 10] $\mu\text{M}^{-1} \text{s}^{-1}$ | 1 (290)                                                          |
| $k_{IP3deg}$   | [0.001 0.1] $\text{s}^{-1}$               |                                                                  |
| $V_{IP3}$      | [0.05 10] $\text{s}^{-1}$                 | 0.189 (291), 3 (294), 1.11 (305), 66.6 (307)                     |
| $K_{IP3}$      | [0.1 5] $\mu\text{M}$                     | 0.136 (291), 0.13 (305), 1 (307), 3 (294)                        |
| $K_{act}$      | [0.05 0.5] $\mu\text{M}$                  | 0.0814 (291), 0.08 (305), 0.4 (307), 0.13 (294)                  |
| $A$            | [0.01 0.5]                                | 0.104 (291), 0.032 (305), 0.5 (307)                              |
| $K_{inh}$      | 1 $\mu\text{M}$                           | 1 (291)                                                          |
| $K_{IP3inh}$   | [0.5 1.5] $\mu\text{M}$                   | 1.05 (291)                                                       |
| $K_{ERleak}$   | [0.0005 0.05] $\text{s}^{-1}$             | 0.002 (291), 0.02 (305), 0.0009 (307), 0.01 (294), 0.002 (295)   |
| $V_{serca}$    | [0.2 250] $\mu\text{M s}^{-1}$            | 114 (291), 0.9 (305), 1 (307), 0.27 (294), 1 (290)               |
| $K_{serca}$    | [0.15 0.8] $\mu\text{M}$                  | 0.754 (291), 0.1 (305), 0.15 (307), 0.175 (294), 0.2 (290)       |
| $V_{mitin}$    | [100 800] $\mu\text{M s}^{-1}$            | 300 (296), 506 (291)                                             |
| $K_{mitin}$    | [0.5 1.5] $\mu\text{M}$                   | 0.8 (296), 1 (291), 0.6 (294)                                    |
| $V_{mitout}$   | [5 500] $\mu\text{M s}^{-1}$              | 125 (296), 476 (291)                                             |
| $K_{mitout}$   | [1 10] $\mu\text{M}$                      | 5 (291, 296)                                                     |
| $V_{crac}$     | [0.01 10] $\mu\text{M s}^{-1}$            | 0.226 (291), 8.85 (295), 0.01 (289)                              |
| $K_{soc}$      | [100 1000] $\mu\text{M}$                  | 500 (295)                                                        |
| $K_{stim}$     | [100 300] $\mu\text{M}$                   | 152.3 (272)                                                      |
| $K_{PMleak}$   | [2.5e-7 3.5e-5] $\text{s}^{-1}$           | 5.6e-6 (289), 2.6e-7 (305), 4.6e-7 (294), 3.3e-5 (291)           |
| $V_{pmca}$     | [0.01 50] $\mu\text{M s}^{-1}$            | 0.05 (289), 0.01 (305), 0.013 (294), 0.0893/0.59 (291), 38 (295) |
| $K_{pmca}$     | [0.1 0.5] $\mu\text{M}$                   | 0.12 (305), 0.2 (294), 0.113/0.44 (291), 0.5 (295)               |
| $K_{STIMpmca}$ | [150 450] $\mu\text{M}$                   | Range in ER $\text{Ca}^{2+}$ concentration                       |

Sensitivity analysis was performed by perturbing each parameter value (one at a time) by 1 to 20% and comparing the new peak time, amplitude and decay constant to the feature values without perturbation:

$$Sensitivity = \frac{\Delta feature / feature}{\Delta p / p} \quad (5-20)$$

where  $p$  is the specific parameter used to perform the sensitivity analysis.

### 5.3. Results

#### 5.3.1. Parameter and species fitting

The  $Ca^{2+}$  signaling model presented here consists in 7 state variables and 29 parameters. It is divided into two major submodules. The first one represents TCR stimulation and PLC- $\gamma$  phosphorylation. The second module corresponds to  $IP_3$  formation and the downstream cytoplasmic  $Ca^{2+}$  increase. The first module has only two parameters, corresponding to PLC- $\gamma$  phosphorylation and degradation and was fitted individually to experimentally acquired dynamics of phosphorylated PLC- $\gamma$  after TCR stimulation in Jurkat cells (Figure 5.2).

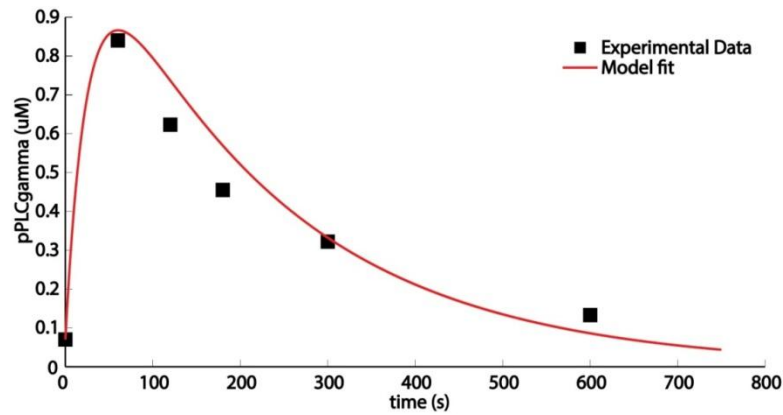


**Figure 5-2:** PLC- $\gamma$  phosphorylation dynamics following TCR stimulation in Jurkat cells

Using this specific PLC- $\gamma$  function, the second module was fitted to temporal changes in IP<sub>3</sub> concentration in the presence of EGTA (309) and Ca<sup>2+</sup> time courses model in the absence or presence of the chemical inhibitors EGTA and TMB-8. EGTA is a Ca<sup>2+</sup> chelator that buffers extracellular Ca<sup>2+</sup> and will reduce external Ca<sup>2+</sup> entry through the CRAC channels and PM leakage. TMB-8 is an IP<sub>3</sub>R blocker that will prevent the opening of the IP<sub>3</sub>R channel and therefore limits ER store Ca<sup>2+</sup> release. To fit the time courses with the inhibitors, two additional parameters were added,  $\lambda_1$  and  $\lambda_2$  that represent respectively the percent reduction in extracellular Ca<sup>2+</sup> and in J<sub>IP<sub>3</sub></sub>. After fitting,  $\lambda_1$  is equal to 0.45 and  $\lambda_2$  to 0.32. With a unique set of parameters, the model can recapitulate cytosolic Ca<sup>2+</sup> dynamics in the presence or absence of inhibitors (Figure 5.3). Figure 5.3 also presents the model prediction for the Ca<sup>2+</sup> levels in the T cell ER and mitochondria, which have not been measured experimentally in the current literature.

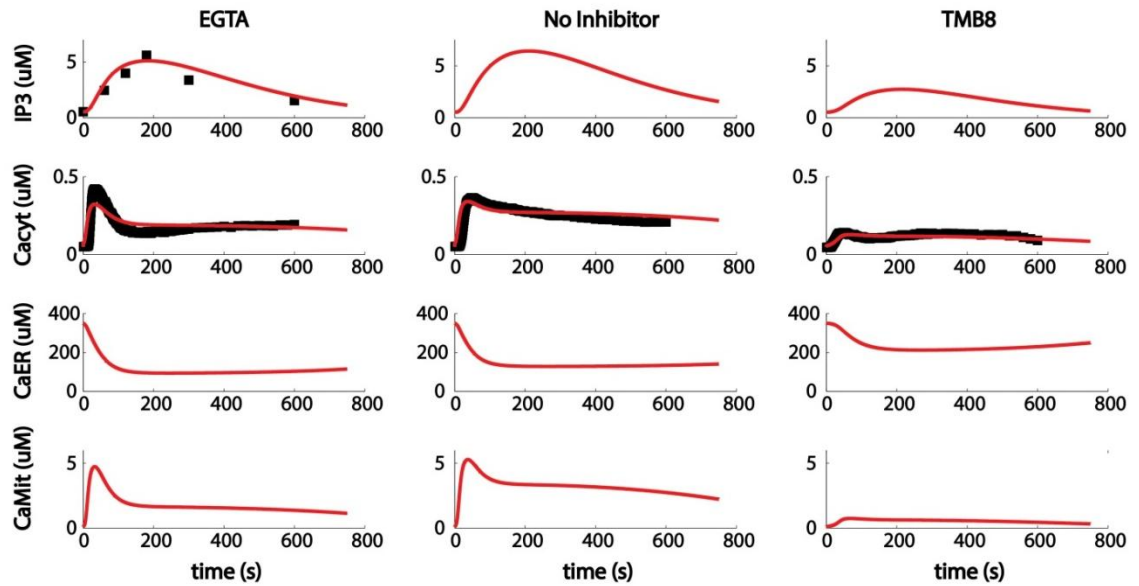


**Figure 5-3:** Time course of IP<sub>3</sub> and Ca<sup>2+</sup> in the various cellular compartments in response to TCR signaling in the presence of 50  $\mu\text{M}$  EGTA, 100  $\mu\text{M}$  TMB-8 and in the absence of inhibition in Jurkat cells. The filled black squares correspond to experimental data and the red curves to model predictions.

The same computational model was optimized to fit time courses from low passage primary CD8<sup>+</sup> T cells, while keeping the PLC- $\gamma$  activation module conserved between both cell types. For the “young” CD8<sup>+</sup> T cell model, parameter estimation was performed using constrained nonlinear programming and pattern search algorithms with the best fit Jurkat parameter for initial values. Figure 5.4 shows the experimental time courses and model predictions of IP<sub>3</sub> and Ca<sup>2+</sup> in the cytosol, mitochondria and ER. The model was fitted to no inhibitor conditions and can also predict Ca<sup>2+</sup> dynamics in the presence of chemical inhibitors.

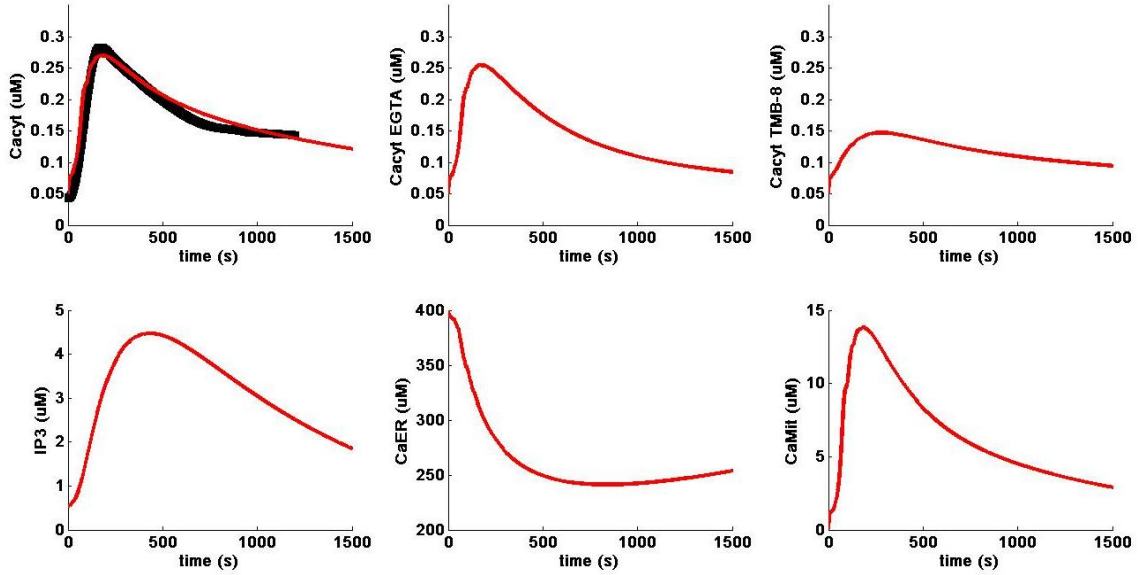


**Figure 5-4:** Model predictions of  $\text{IP}_3$  and  $\text{Ca}^{2+}$  in the various cellular compartments in response to TCR signaling in CD8+ T cells. The filled black squares correspond to experimental data and the red curves to model predictions. Top: Cytosolic  $\text{Ca}^{2+}$  dynamics in the absence (left) or presence of inhibitors (middle, right) at the same concentration as for Jurkat cells. Bottom: model predictions for other state variables in the no inhibitor simulation.

Because the time scales of  $\text{Ca}^{2+}$  dynamics are quite different in the Jurkat CD4+ T cell line and primary CD8+ T cells (rise time of 30 sec versus 150 sec), the optimized parameter values are quite different for those two cell types, especially the maximum velocities (Table 5.3), for instance the fluxes through the  $\text{IP}_3\text{R}$  and SERCA are respectively 5 and 2 times higher in primary cells.

**Table 5-3:** Optimized parameter values for the Jurkat cell model and the "young" CD8+ T cell model

| Parameter     | Jurkat T cells | Primary CD8+ T cells |
|---------------|----------------|----------------------|
| $\beta_i$     | 0.1678         | 0.0045               |
| $\beta_{er}$  | 0.0467         | 0.0153               |
| $\beta_{mit}$ | 0.716          | 1.13                 |
| $\rho_{er}$   | 0.015          | 0.015                |
| $\rho_{mit}$  | 0.08           | 0.08                 |

Table 5-3 continued:

| Parameter      | Jurkat T cells                         | Primary CD8+ T cells                    |
|----------------|----------------------------------------|-----------------------------------------|
| $k_{PLCact}$   | 0.0045 s <sup>-1</sup>                 | 0.0045 s <sup>-1</sup>                  |
| $k_{PLCdeact}$ | 0.0396 s <sup>-1</sup>                 | 0.0396 s <sup>-1</sup>                  |
| $k_{IP3prod}$  | 0.258 μM <sup>-1</sup> s <sup>-1</sup> | 0.1142 μM <sup>-1</sup> s <sup>-1</sup> |
| $k_{IP3deg}$   | 0.0208 s <sup>-1</sup>                 | 0.009 μs <sup>-1</sup>                  |
| $V_{IP3}$      | 1.626 s <sup>-1</sup>                  | 8.004 μs <sup>-1</sup>                  |
| $K_{IP3}$      | 0.106 μM                               | 0.1945 μM                               |
| $K_{act}$      | 0.16 μM                                | 0.48 μM                                 |
| $A$            | 0.0917                                 | 0.0885                                  |
| $K_{inh}$      | 1 μM                                   | 1 μM                                    |
| $K_{IP3inh}$   | 0.771 μM                               | 0.956 μM                                |
| $K_{ERleak}$   | 0.003 s <sup>-1</sup>                  | 0.0101 s <sup>-1</sup>                  |
| $V_{serca}$    | 85.8 μM s <sup>-1</sup>                | 187.88 μM s <sup>-1</sup>               |
| $K_{serca}$    | 0.4477 μM                              | 0.508 μM                                |
| $V_{mitin}$    | 794.07 μM s <sup>-1</sup>              | 378.1 μM s <sup>-1</sup>                |
| $K_{mitin}$    | 1.24 μM                                | 0.594 μM                                |
| $V_{mitout}$   | 484.44 μM s <sup>-1</sup>              | 261.67 μM s <sup>-1</sup>               |
| $K_{mitout}$   | 8.1285 μM                              | 4.114 μM                                |
| $V_{crac}$     | 3.1046 μM s <sup>-1</sup>              | 0.3962 μM s <sup>-1</sup>               |
| $K_{soc}$      | 996.83 μM                              | 4863 μM                                 |
| $K_{stim}$     | 195.73 μM                              | 321 μM                                  |
| $K_{PMleak}$   | 2.5e-7 s <sup>-1</sup>                 | 2.258e-5 s <sup>-1</sup>                |
| $V_{pmca}$     | 1.805 μM s <sup>-1</sup>               | 4.32 μM s <sup>-1</sup>                 |
| $K_{pmca}$     | 0.1269 μM                              | 0.5665 μM                               |
| $K_{STIMpmca}$ | 394 μM                                 | 279.88 μM                               |

### 5.3.2. $\text{Ca}^{2+}$ signaling of *in vitro* aging T cells

$\text{Ca}^{2+}$  signaling has been previously reported to be dampened in CD8+ T cells from old mice (276) or in T cell populations of elderly individuals (277-279); yet so far, the biochemical basis leading to this impairment are not known. With *in vitro* replicative senescence being used as a model for *in vivo* aging, we sought to determine what effects *in vitro* aging of cytotoxic CD8+ T cells have on  $\text{Ca}^{2+}$  dynamics and use our computational model to infer potential biochemical mechanisms responsible for the differences observed.

Using the long-term culturing protocol to accelerate human primary T cells to immunosenescence presented in Chapter 3, we measured baseline  $\text{Ca}^{2+}$  and dynamic responses to TCR activation by flow cytometry. We previously established that immunosenescence, as defined by an inability to divide, is achieved within 12 population doublings in about 24 days in culture (224). In resting CD8+ T cells, we observed elevated baseline levels of cytoplasmic  $\text{Ca}^{2+}$  very early and late in culture, when the cells had reached senescence (Figure 5.5a). To quantitatively define the differences observed among the dynamic traces, we defined the following parameters from a representative  $\text{Ca}^{2+}$  time course: peak amplitude, time to peak, area under the curve as well as four additional parameters to describe the decay due to the SERCA and CRAC channel opening,  $A_1$ ,  $A_2$ ,  $\tau_1$  and  $\tau_2$  (Figure 5.5b). From these 7 parameters, only the time to peak and the fast decay constant showed significant differences with time in culture ( $p < 0.05$ ). Older T cells reach their peak amplitude faster and have a faster decay time constant (Figure 5.5c-d). We did not observe monotonic trends in peak amplitude, integral or the second decay time constant (Appendix C.S1).

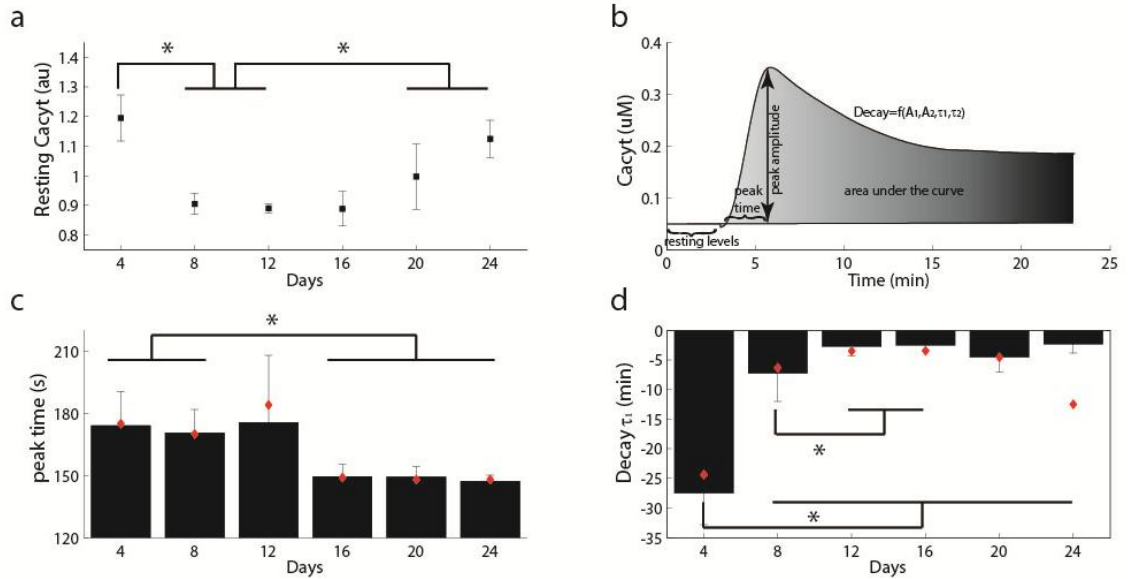


**Figure 5-5:** Age related  $\text{Ca}^{2+}$  changes in CD8<sup>+</sup> T cells. a) Cytoplasmic  $\text{Ca}^{2+}$  levels in resting T cells. Mean and SEM from 4 different donors. b) Representative trace of  $\text{Ca}^{2+}$  dynamics following TCR stimulation with the related parameters studied, peak time, peak amplitude, baseline and decay. The integral corresponds to the colored area under the curve. c) Time to peak in seconds. d) Fast decay time constant in minutes. For c-d), the data represents the mean of each calculated parameters for each donor and its standard deviation. The red diamonds correspond to the parameter calculated if the  $\text{Ca}^{2+}$  time courses are averaged for all donors for a specific day in culture.

### 5.3.3. Changes in mRNA levels of plasma membrane channels are not sufficient to explain age-related changes in cytoplasmic $\text{Ca}^{2+}$ dynamics

To determine if changes in  $\text{Ca}^{2+}$  signaling dynamics are due to changes in expression of the proteins involved in the  $\text{Ca}^{2+}$  signaling pathway, we measured mRNA levels of the major  $\text{Ca}^{2+}$  channels and pumps expressed in T cells (IP3R2, IP3R3, SERCA2B, SERCA3, ORAI1 and PMCA) for young (days 4-8 in culture) and old cells (days 20-24 in culture) (Appendix C.T1). Out of these six targets, PMCA and ORAI1 showed significant upregulation ( $p < 0.05$ ) with age (Figure 5.6).



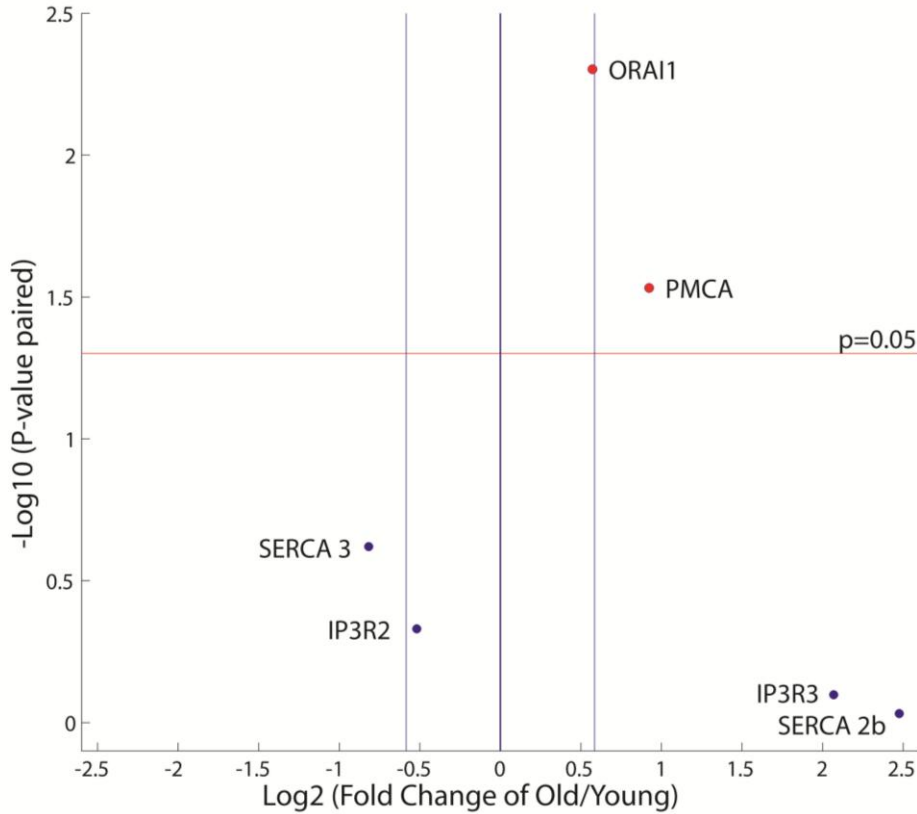


**Figure 5-6:** Changes in mRNA levels of  $\text{Ca}^{2+}$  channels and pumps with age (n=6). Points above the red line represent targets that show significant statistical difference (at  $p < 0.05$ ) between young and old samples. The blue lines represent fold changes that are above 1.5 fold up or down.

We then asked if the model could be used to determine if changes in PMCA and CRAC channels are sufficient to explain the faster peak time and decay observed during aging. The absolute number of channel/pumps proteins will affect directly the maximum flux through these proteins; hence we used the model described above and let the parameters  $V_{crac}$ ,  $V_{pmca}$  vary up to 100 times to fit data from old cells (day 20-24 in culture). These two parameters alone were not sufficient to fit simultaneously the time-to-peak, decay time constant and amplitude (Appendix C.S2 presents the best fit in respect to amplitude, time-to-peak and decay time constant).

#### 5.3.4. Model Predictions

To determine which parameters are most responsible for the features time-to-peak and decay time constant, a sensitivity analysis was performed on the “young cell” model (Figure 5.7). Each parameter was perturbed individually and the features (peak time, peak amplitude and decay time constant) measured for the new model output. For these three features, several parameters exhibit nonlinear behaviors; for instance certain parameter combinations led to oscillatory behaviors which might affect the calculated features. Higher parameter sensitivity to the feature decay time than peak time can be observed; however, the parameters involved in altering both the peak time and decay time constant are consistent. Amongst the initial 24 parameters tested, five parameters were identified as being the main drivers of the observed changes with age, all involved with  $\text{Ca}^{2+}$  exchange with the ER stores. Increases in  $K_{serca}$ ,  $V_{IP3}$  and decreases in  $K_{act}$ ,  $V_{serca}$  and  $K_{pmcastim}$  result in reduced peak time and faster decay, signatures representative of old T cell  $\text{Ca}^{2+}$  dynamics.

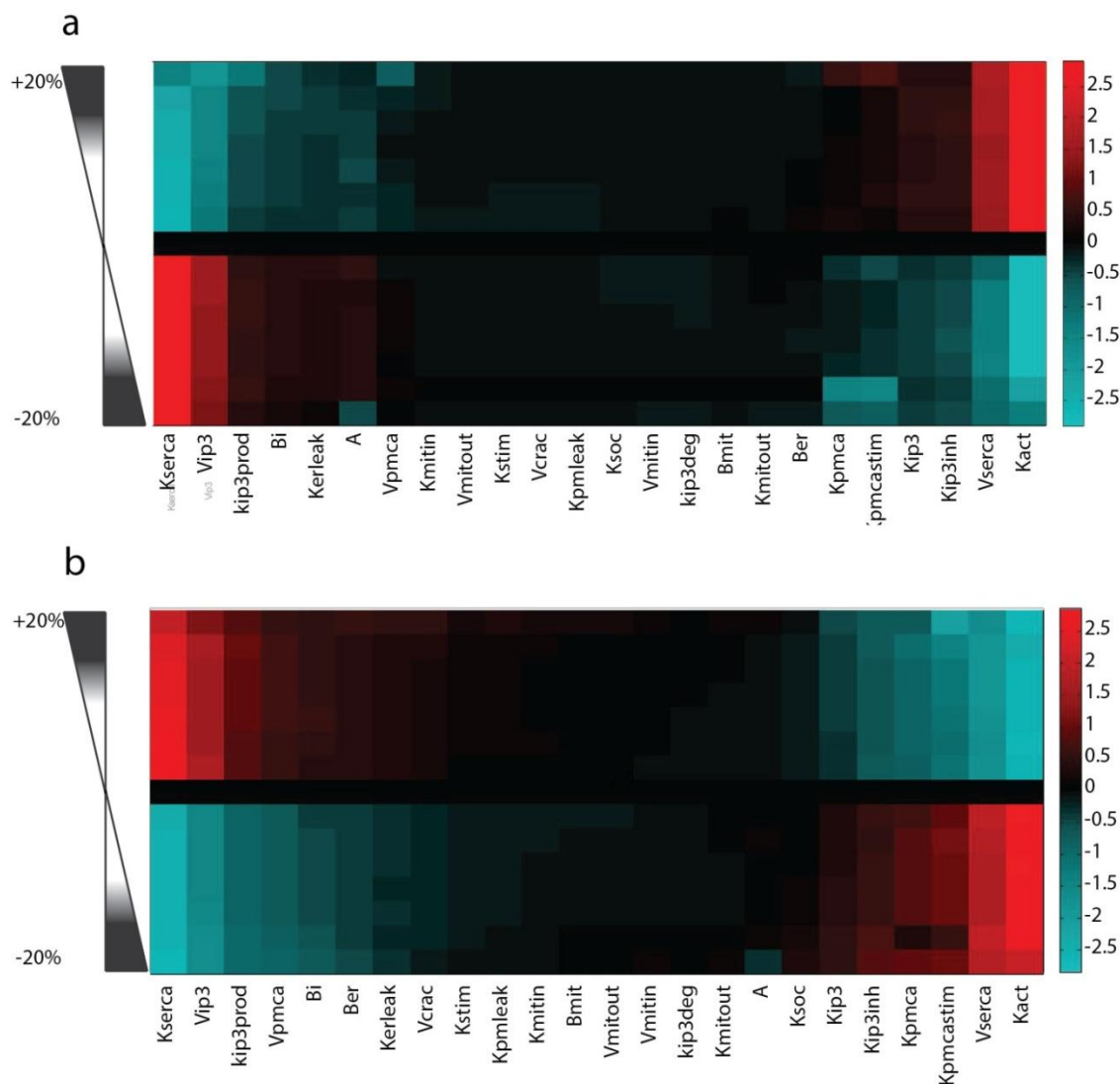


**Figure 5-7:** Model sensitivity analysis. a) Parameter sensitivity to the feature peak time. b) Parameter sensitivity to the feature decay time constant  $\tau_1$ . Parameters values were perturbed by a percentage up to 20% up and down and were clustered for easier visualization.

To ensure these parameters were the drivers of the observed old T cell phenotype, we used the parameter set from the “young cell” model and simultaneously varied these five parameters to fit the old T cell time course. The objective function consisted in the sum of squared difference between the model and the experimental time course, with additional constraints for peak amplitude, peak time and decay time constant. Figure 5.8 presents the best “old T cell” model fit. The new optimized parameter set shows up to 8

% difference compared to the “young T cell” model best parameter set, with no changes for  $K_{serca}$  and  $V_{serca}$ , 8 % upregulation for  $V_{IP3}$ , 1 % downregulation for  $K_{act}$ , and 8 % downregulation for  $K_{pmcastim}$ .

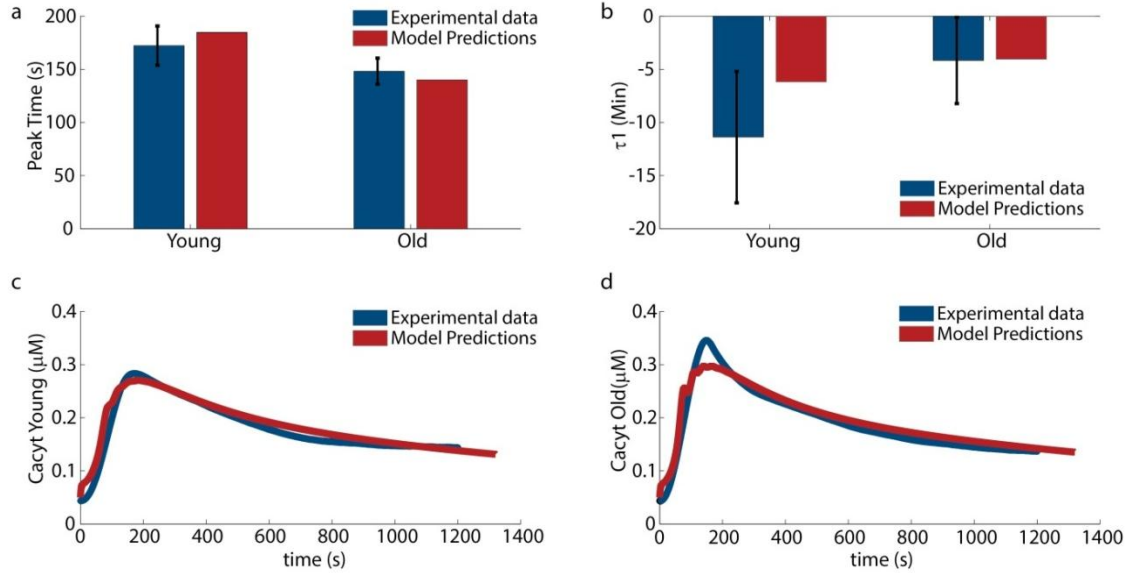


**Figure 5-8:** Model predictions of Ca<sup>2+</sup> dynamics in old T cells. a) Time to peak. b) Decay time constant  $\tau_1$ . c) Ca<sup>2+</sup> time course for young cells (day 4-8) d) Ca<sup>2+</sup> time course for old cells (day 20-24).

#### 5.4. Discussion

T cell responses from aged donors are typically slower and of lower amplitude than those from younger individuals, whether the response is measured in terms of cytokine production (240), gene activation for cell cycle entry and transcription (221, 313) or activation of protein kinase pathways (239). We have shown, along with other research groups, that the kinase activation upstream of Ca<sup>2+</sup> release from the ER stores are downregulated with time in culture (224, 239), which would suggest reduced Ca<sup>2+</sup> signaling. Induction of a sustained Ca<sup>2+</sup> signal is critical for CD8<sup>+</sup> T cell effector function (314, 315) and downstream gene regulation through the NFAT pathway; therefore a

strong  $\text{Ca}^{2+}$  signal is required for an efficient tumor-specific immune response in the context of adoptive T cell transfer. The literature is conflicted in the consequences of age on calcium mobilization. Although  $\text{Ca}^{2+}$  mobilization has been shown to be impaired in old mice for both CD4+ and CD8+ T cell subsets (275, 276, 316), in humans, CD8+ T cells from elderly donors had a slightly greater  $\text{Ca}^{2+}$  response to stimulation than CD4+ cells but a larger reduction in their proliferative potential (279). Similarly, reports of baseline  $\text{Ca}^{2+}$  levels in healthy elderly subjects have been controversial, with reports of unchanged (317) or reduced (277) basal  $\text{Ca}^{2+}$  levels. The differences between murine models and human aging suggest that the effects of *in vitro* aging on  $\text{Ca}^{2+}$  signaling, and in particular culture conditions consistent with ACT, may not be intuitive.

In our culture model, we did not observe a clear trend in baseline  $\text{Ca}^{2+}$  levels, or a reduction in peak amplitude or sustained levels after stimulation (Figure 5.5 and Appendix C.S1). We hypothesize that the high  $\text{Ca}^{2+}$  level that we observe at day 4 (Figure 5.5a) is a consequence of the high  $\text{Ca}^{2+}$  levels required for proliferation, and the elevated levels towards the end of our long-term culture to cellular damage. More importantly, we observed altered T cell dynamics after stimulation in older CD8+ T cells, these cells interestingly presenting faster dynamics, in particular a faster decay rate and a time to peak 20 second faster (Figure 5.5).

To find an underlying mechanism for these dynamic differences, we measured mRNA levels of the main channels and pumps involved in  $\text{Ca}^{2+}$  handling in T cells and found a small but significant overexpression of the plasma membrane ORAI1 channel and PMCA4b pump in older T cells while expression of the IP<sub>3</sub>R and SERCA isoforms remained unchanged (Figure 5.6). There are very few studies concerning transcript levels

of  $\text{Ca}^{2+}$  channels during aging, and to our knowledge none performed on lymphocytes. Zaidi *et al.* observed a general loss of PMCA and reduction of PMCA activity from the membrane of murine brain synaptic membranes (318). Another recent study reported reduced expression levels of STIM1 and ORAI in muscle fibers isolated from aged mice (319). Levels of SERCA2b have been shown to stay constant in old rat thoracic aortas (320), while levels of SERCA3 mRNA decreased in old rat central neurons but without a corresponding decrease in the SERCA3 protein levels (321). Aging was accompanied by a significant increase in the mRNA levels of  $\text{IP}_3\text{R1}$  in a rat's heart (322). These differences from our findings might be a result of using excitable cells and various animal models.

Intuitively, if the activities of  $\text{Ca}^{2+}$  channels and pumps in T cells are reduced with age, as it occurs in other cell types (318), simultaneous overexpression of the  $\text{Ca}^{2+}$  influx and efflux mechanisms from the plasma membrane may be a compensatory way for the older cells to sustain high levels of calcium for downstream signaling. Based upon the current knowledge of molecular mechanisms of  $\text{Ca}^{2+}$  signaling, this is an unlikely molecular basis for the faster time to peak and decay time constant. To gain a better understanding of the  $\text{Ca}^{2+}$  signaling pathway and the relative contribution of each flux towards an integrated dynamic cell response, we built a deterministic computational model of  $\text{Ca}^{2+}$  signaling in T cells after TCR stimulation. Single cell analysis of  $\text{Ca}^{2+}$  signaling in T cells show a variety of  $\text{Ca}^{2+}$  signals ranging from infrequent spikes to sustained oscillations and plateaus (310, 323). Because lymphocyte  $\text{Ca}^{2+}$  oscillations are not synchronized, we have chosen to model  $\text{Ca}^{2+}$  dynamics from a population rather than the dynamics of a single T cell.

Using sets of parameters found in previously published models of  $\text{Ca}^{2+}$  dynamics coupled with our PLC- $\gamma$  activation module did not recapitulate experimental time courses, which is not surprising as parameter values were collected across various cell types and *in vitro* conditions. To fit the parameters, we took an approach similar to Maurya *et al.* (292). For each flux, we perused the literature for a mathematical formulation, parameter values, and *in vitro* experimental data, which allowed us to specify upper and lower parameter bounds. It is interesting to notice that there is a large discrepancy in legacy values among similar parameters that can be estimated to be three orders of magnitude different (Table 5.2). The experimental dataset used to optimize the model summarizes the main molecular mechanisms of the  $\text{Ca}^{2+}$  signaling pathway after TCR stimulation, with the TMB-8 inhibitor condition emphasizing the early ER  $\text{Ca}^{2+}$  store release and the EGTA inhibitor condition the importance of extracellular  $\text{Ca}^{2+}$  to sustain elevated  $\text{Ca}^{2+}$  levels after ER stores have been emptied. If optimized using only the no inhibitor condition, the model will tend to fit the cytosolic  $\text{Ca}^{2+}$  time course by adjusting the rates of influx and efflux at the plasma membrane; however this set of parameters does not reproduce experimental data acquired under inhibitor conditions. By fitting the model simultaneously to our three experimental conditions we achieve sets of parameters that recapitulate  $\text{Ca}^{2+}$  under all experimental conditions. Confidence in our parameter would be improved with additional experimental data, for instance  $\text{Ca}^{2+}$  time courses from cell organelles.

Because experimental data on PLC- $\gamma$  and  $\text{IP}_3$  dynamics were acquired on Jurkat cells, a model CD4 T cell line easy to manipulate, we initially created a “Jurkat cell” model. This model and its parameter values were used as a starting point to create the “young”

primary CD8+ T cells model. Parameter values between both cell types show significant differences (Table 5.3), reflecting the differences in the  $\text{Ca}^{2+}$  time courses between those two cell types. These differences in time scale might be due to differential protein expression (Appendix C.S1, (324)) and are reflected by large variation in the maximal velocity parameters between these two cell types.

For both cell types, the model is able to capture the fast initial rise and sustained elevated levels of cytosolic  $\text{Ca}^{2+}$ . Interestingly, the model predicted a slow replenishment of the ER stores, and a fast  $\text{Ca}^{2+}$  buffering by the mitochondria, mirroring  $\text{Ca}^{2+}$  dynamics in the cytosol. Although the model does not include any spatial components and any additional control feedback, the network structure combined with optimized parameters under different inhibition conditions seems to recapitulate the role of the mitochondria at the ER/mitochondrial junctions (92) and SOCE-dependent  $\text{Ca}^{2+}$  release via IP3R/RyR while the stores are being replenished (325). The model demonstrates that a 2-fold overexpression of PMCA and 1.5 fold overexpression of ORAI1 maximal velocities result in a delayed  $\text{Ca}^{2+}$  rise of slightly lower amplitude and significantly lower sustained  $\text{Ca}^{2+}$  levels. Because changes in mRNA levels might not translate directly into the same fold changes in the maximal velocities, we varied those parameters in an attempt to recapitulate  $\text{Ca}^{2+}$  dynamics in aged cells but the best fit was not able to accurately reproduce these dynamics (Appendix C.S2). Sensitivity analysis of the model identified perturbations in SERCA pump and IP3R as best candidates of age-related alterations (Figure 5.7); yet when all 5 selected parameters were allowed to vary, IP3R and STIM1-mediated PMCA inhibition emerged as being the most important parameters to recapitulate dynamic information of aging cells. Interestingly, despite the importance of



$\text{Ca}^{2+}$  buffering by the mitochondria, the model did not recognize this organelle as being a major contributor to the old T cell phenotype.

Increase in  $\text{IP}_3\text{R}$  activity, simultaneously with decreased PMCA inhibition by STIM1, can be a consequence of post translational modifications in these proteins such as oxidation (326). PMCA, STIM1 and  $\text{IP}_3\text{R}$  contain several cysteine residues and are highly susceptible to oxidation (91, 103).  $\text{IP}_3\text{R}$  function has been reported to be affected by ROS by increasing  $\text{IP}_3\text{R}$  sensitivity to cytosolic  $\text{IP}_3$  levels (327) and inducing conformational change on the luminal side leading in modified channel activity (328). Additional experimental studies need to be performed to measure the overall redox status of *in vitro* aged T cells and the redox status of these proteins in young versus old cells. Single  $\text{Ca}^{2+}$  oscillations have not been the main focus of this study; however as intracellular  $\text{Ca}^{2+}$  signaling patterns reflect the differentiation status of human  $\text{CD4}^+$  T cells (329), a better discrimination between young and old T cells could be achieved by quantifying the heterogeneity of  $\text{Ca}^{2+}$  signaling patterns in young versus old cells and incorporating these features into our model of  $\text{Ca}^{2+}$  signaling.

## **5.5. Conclusion**

Altered  $\text{Ca}^{2+}$  signaling is a hallmark of aging and other various disease states, yet the biomolecular mechanisms leading to these alterations are unknown. To guide new experimental studies, we constructed a computational model of  $\text{Ca}^{2+}$  signaling in T cells that is capable of recapitulating key features of a typical  $\text{Ca}^{2+}$  time course in both a T cell line and primary T cells. The model suggests targets of regulation that may be altered during *in vitro* aging.

## **5.6. Materials & Methods**

Primary T cell isolation, cell culture and T cell expansion have been described in Chapter 3.

### **5.6.1. $\text{Ca}^{2+}$ kinetics acquisition**

Jurkat cells were incubated in phenol red free RPMI 1640 medium with 5  $\mu\text{M}$  Fura Red, 3  $\mu\text{M}$  Fluo-3 (Molecular Probes) and 0.05% Pluronic F127 for 40 minutes at 37°C, washed three times with cold PBS and resuspended in warm phenol red free medium in the presence or absence of specific chemical inhibitors (30 min pretreatment at the appropriate concentration). Cell fluorescence was read on a BD LSR II flowcytometer for 3 minutes to obtain the  $\text{Ca}^{2+}$  level baseline. 2  $\mu\text{g/mL}$   $\alpha\text{CD3}$  (clone OKT3),  $\alpha\text{CD28}$  antibody was added to the cells to activate the calcium signaling pathway then cell fluorescence was read for 30 additional minutes.  $\text{CD8}^+$  T cells were preincubated at 4°C with Fluo3, Fura Red and Pluronic F127 at the same concentrations with 2  $\mu\text{g/mL}$   $\alpha\text{CD3}$  (clone OKT3),  $\alpha\text{CD28}$  for 40 minutes. After a wash step in cold PBS, primary cells were resuspended in cold phenol red free media and fluorescence was read for 3 minutes to acquire the  $\text{Ca}^{2+}$  baseline. To activate the TCR pathway, cells were diluted 10 times in a 37°C solution of 20  $\mu\text{g/mL}$   $\alpha$ -mouse IgG to crosslink the  $\alpha\text{CD3}$  antibody and cell fluorescence was recorded for an additional 30 minutes. The ratio of Fluo3/Fura Red fluorescence was used to analyze the  $\text{Ca}^{2+}$  traces.

### 5.6.2. $\text{Ca}^{2+}$ time course preprocessing and kinetic parameter determination

All  $\text{Ca}^{2+}$  traces were first registered to ensure stimulation occurred at the same time. Time courses were smoothed using Savitzky-Golay filtering and normalized to the baseline fluorescence. Peak time, peak amplitude and integral under the curve were calculated using custom Matlab scripts (R2011a (Mathworks, Natick, MA)). Decay parameters were obtained by fitting the decay portion of the dynamics to a sum of exponentials:

$$\text{Decay} = A_1 e^{\frac{t}{\tau_1}} + A_2 e^{\frac{t}{\tau_2}} \quad (5-21)$$

### 5.6.3. Signaling measurements

To determine the levels of phosphorylated PLC- $\gamma$  following T cell receptor stimulation, Jurkat cells were stimulated with 2  $\mu\text{g/mL}$   $\alpha\text{CD3}$  (clone OKT3),  $\alpha\text{CD28}$  antibody for the desired time and lysed. Total protein concentration of the lysates was determined with a BCA assay kit (Pierce). Lysis and quantitative analysis of phosphorylation dynamics was performed with a Bio-Plex 200 instrument (Bio-Rad) using commercially available Luminex bead assays (EpiQuant Technology, Millipore EMD) according to manufacturers' protocols.

### 5.6.4. RNA extraction and purification

Total RNA from CD8 $^{+}$  T cells was extracted using the RNeasy Mini isolation kit (SABiosciences, Frederick, MD) with RNase-free DNase set (Qiagen, Valencia, CA) according to the manufacturer's protocol. The integrity and concentration of intact total RNA was verified with a NanoDrop 1000 Spectrophotometer (Thermo Scientific).

#### **5.6.5. Real-time quantitative reverse transcriptase PCR**

Real-time PCR was performed with a StepOnePlus RT-qPCR system instrument (Applied Biosystems, Carlsbad, CA) using predesigned gene-specific primer and probe sets for Actin, ORAI1, SERCA2b, SERCA3, PMCA, IP3R2 and IP3R3 (SA Biosciences). Briefly, 1 µg of total RNA was reverse transcribed and amplified using the RT-PCR kit (Quiagen) following the manufacturer's instructions. Each 20 µL reaction mixture aliquot contained 1 µL of primer mixture (SA Biosciences), 2 µL of universal PCR Master Mix (Quiagen) and 1–4 µL of cDNA or water as a negative control. Initial denaturation of DNA was carried out at 95°C for 10 min. Forty amplification cycles were performed, each cycle consisting of denaturation (95°C, 30 s) and annealing and extension (65°C, 1 min). Each sample was amplified in triplicate. Relative expression levels were calculated using the  $\Delta CT$  method ( $2^{-\Delta CT}$ ) and results were normalized using the housekeeping gene actin (330). Paired t-tests were performed for each normalized target for each donor to find significant changes in expression between young and aged cells.

## CHAPTER 6

# IMAGING SINGLE-CELL SIGNALING DYNAMICS WITH A DETERMINISTIC HIGH-DENSITY SINGLE-CELL TRAP ARRAY

### 6.1. Introduction

Clonal cell populations exhibit large heterogeneities in mRNA and protein transcripts at the single cell level, due to stochastic effects in gene expression (331, 332). A current view is that noise arising from stochastic fluctuations plays an essential role in key cellular activities (333-337). At a systems level, an effective immune response requires the cooperation of a mixed T cell population in terms of number of replication and differentiation status. We have previously observed impaired CD8<sup>+</sup> T cell activation (338), altered Ca<sup>2+</sup> dynamics (Chapter 5) and redox status (Chapter 4) in a population of aging T cells. A better understanding of these age-related changes requires simultaneous single-cell assessment of the differentiation status and single cell signaling dynamics tracking. At present, such experiments can be technically challenging if the cells of interests, such as T cells, are non-adherent, if stimuli need to be delivered, or if studies on long time scales are desired. Flow cytometry is often the technique of choice to measure heterogeneity of suspension cell populations, as it is high-throughput and can distinguish subpopulations of cells.

Adapted from Chung, K., C. A. Rivet, et al. (2011). "Imaging single-cell signaling dynamics with a deterministic high-density single-cell trap array." Anal Chem **83**(18): 7044-7052.

However, this technology is capable of neither monitoring temporal changes within the same cell, nor distinguishing population from noise due to temporal fluctuation within one cell. Quantitative time lapse microscopy is often required for these measurements, but it presents additional challenges, such as low throughput and movement of the target cells during imaging. It is particularly challenging to image suspension cells; one could use adhesion to a solid surface by use of an artificial membrane and receptor binding, but this may alter the biological behavior of the cells.

To overcome limitations of traditional real-time microscopy, microfluidics can be used to allow for increased throughput, control of cell location and extracellular conditions. Various microfluidic techniques have been developed to capture cells, retain them in a specific location, and control the environment surrounding them. Although very powerful, these methods have a limited throughput because the cell traps are spaced sparsely enough such that per view only a small number of cells are captured, and some are difficult to implement, or have side effects or other limitations. For example, active single-cell capture mechanisms use valves (339, 340) to control flow or dielectric forces with DEP (341, 342) or optical tweezers (343) to control the location of cells in various environments. The use of dielectric forces on living cells limits cell viability due to buffer cytotoxicity and heat damage. Passive capturing mechanisms have also been proposed using gravity (344-347) or fluid flow (348) to direct cells into traps. Most microwell arrays rely on gravity to capture cells. Careful design of the microwells enables up to 70% single cell capture in densely packed wells, but once trapped, exposure to varying chemical solutions and manipulation of the cells are limited because the cells are not actively held in the wells (344-347). Flow by diverting streamlines towards traps can also

be used to transport and dock cells at specific locations (129, 348-351). Once a trap contains cells, fluid towards the trap is significantly reduced, and therefore incoming cells will be diverted to the next empty trap. Optimization of trap dimensions, location and spacing has been performed to increase capture efficiency or single cell trapping (129, 351, 352). However, in most designs to date, there is a compromise between cell trap density per area and single cell capture efficiency.

To address the need of high-density and high-efficiency cell traps, we designed a microfluidic high-density single cell capture, stimulation, and imaging platform. The design principles of this chip were adapted from our previous work for high-density single embryo trapping (353) to accommodate single cells, using hydrodynamic flow in conjunction with a careful disposition of the cell traps in an array formed by a serpentine channel. Our device is capable of passively trapping thousands of cells in less than a minute with a single-cell loading efficiency of 95%. Cells are captured sequentially and deterministically on chip with minimal shear. At low magnification, the trap array enables tracking of hundreds of cells simultaneously over time. At high magnification, spatial information can be resolved on a few precisely located single cells. Imaging can be performed on either live or immunostained cells. We show that various soluble stimuli can be delivered to the captured cells, and the trap arrays can be easily integrated with upstream microfluidic components capable of multiplexing several experiments on a single chip. As an application of this microfluidic platform, we studied the heterogeneity in calcium dynamics in resting and stimulated single Jurkat T cells.

## **6.2. Author's contribution**

This work has been performed in collaboration with Dr. Kwanghun Chung. CAR participated in device design, cell loading testing, loading efficiency characterization, immunostaining and acquisition and analysis of calcium signaling dynamics and drafted the manuscript. KC participated in device design, fabrication, cell loading testing and manuscript drafting.

## **6.3. Results**

### **6.3.1. Design of an efficient microfluidic single-cell trap array**

To allow imaging of a large number of cells in a field of view, single cells need to be arranged with high efficiency and with uniform trapping conditions in an array of densely packed traps. To satisfy these requirements, we adapted the design principles that were previously developed in our group for high-density embryo trapping (353), and achieved capture of 4,000 single cells on  $4.5 \text{ mm}^2$  in 30 seconds, and with a loading efficiency over 95%.

The microfluidic devices made from one layer of polydimethylsiloxane (PDMS) contain arrays of highly packed single cell traps (Figure 6.1). Each array consists of a wide serpentine cell-delivery channel arranged in 26 column format and an array of cross-flow channels that connect each section of the serpentine channel (Figure 6.1a-b). The width ( $\sim 25 \text{ }\mu\text{m}$ ) and height ( $14 \text{ }\mu\text{m}$ ) of the cell-delivery channel are large enough to ensure cells easily moving without clogging. Each column includes 24 single cell traps (Figure 6.1b-c) in the middle and 8 dummy traps at each end (Figure 6.1d). The size of the cell trap is similar to that of cell of interest so that once a cell occupies a trap, it



physically excludes the next cell and reduces the possibility of trapping of more than one cell. The cell traps are connected to the 1.8  $\mu\text{m}$  deep shallow cross-flow channels (Figure 6.1b inset). By minimizing space between neighboring traps ( $\sim 8 \mu\text{m}$  in a column,  $\sim 33 \mu\text{m}$  between columns), we achieved a density of 860 traps /  $\text{mm}^2$ .

If flow through the traps has large variations throughout the array, the trap occupancy will be severely compromised. To make the trapping condition uniform, we engineered the geometry of the channels so that cells experience similar flow rates near each trap. Cells passing the focusing zones along the wide delivery channel are focused toward the traps by diverging (blue arrows in Figure 6.1e) and converging flow (red arrow in Figure 6.1e) through the dummy traps (Figure 6.1d-e). The number of the dummy traps is optimized to make cells move closer to the trap after passing the focusing zone. This increases the frequency with which cells contact the traps and are loaded into them (Figure 6.1g). After passing the focusing zone, cells close to a trap experience two streams; main stream (Q) flowing along the delivery channel and a stream (q) directing the cell into the trap (Figure 6.1f). If the Q/q is in a proper range, as described previously (349, 351, 353), cells can be guided into the trap and docked. Once all the traps in one row are occupied, extra cells pass another cell focusing zone without getting trapped and move to the next row. Despite the proximity of the dummy traps, cells are not captured because the size of the dummy traps is smaller than that of the cells. By optimizing various geometric parameters, such as the width and height of the channels and the number of traps, we were able to achieve over 95% single cell trapping efficiency throughout the device (Figure 6.1c).

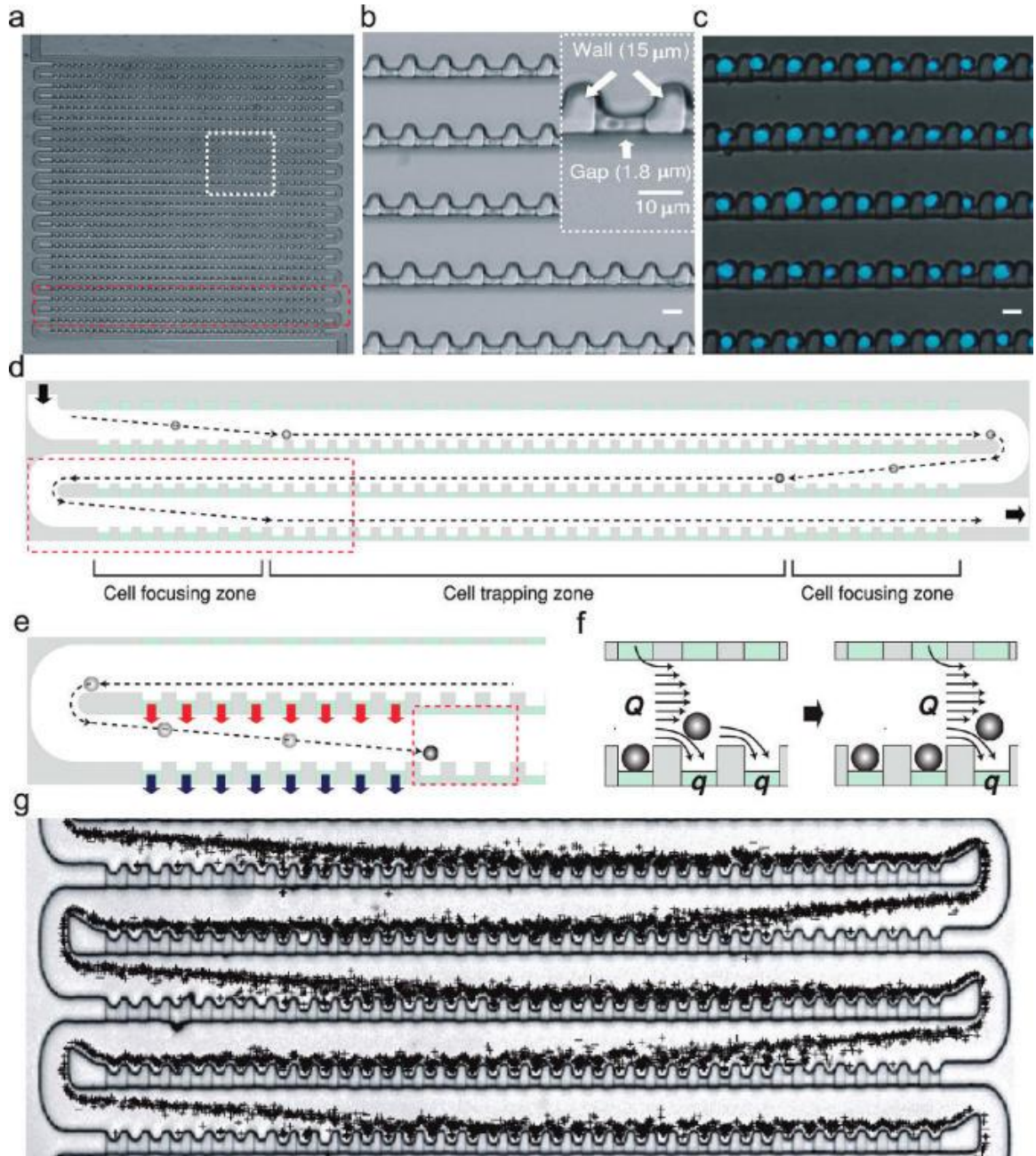


**Figure 6-1:** Design and principle of single-cell trapping array. a) Optical micrograph of the trap array fabricated via soft lithography. b) Details of cell trap design (boxed region in panel a). The inset shows dimensions of a single trap. Scale bar, 10  $\mu\text{m}$ . c) Overlay of phase contrast and fluorescent images showing single cells trapped in the array. d) Schematic drawing of three columns of the array showing trajectory of cells. Cell suspension enters the array from the top left and exits at the bottom right. Dotted lines represent trajectory of cells. e) Boxed region in panel d showing cell focusing mechanism. Converging flow (red arrow) and diverging flow (blue arrow) through the dummy traps focus cells toward the traps. f) Boxed region in panel e describing two major streams that cells experience: main stream ( $Q$ ) flowing along the delivery channel and a stream ( $q$ ) directing the cell into the trap. g) Overlay of a series of 1045 images showing cell trajectories during loading.

### 6.3.2. Optimization of single cell loading efficiency

Geometries of the docking sites were optimized in order to deterministically trap a single cell per trap. A cell close to a trap experiences forces in two directions due to the combined effect of the mainstream bulk flow ( $Q$ ) and the cross-flow ( $q$ ); large bulk flow moves the cell along the main channel and significant enough cross-flow guides the cell into the trap. However, with too large a cross-flow, additional cells can be forced to pile onto the already-occupied trap, reducing single-cell trapping efficiency. By optimizing the fluidic resistance of the cross-flow channel with respect to the resistance of the delivery channel, conditions for trapping a single cell in a single trap can be met. More specifically, if the cross-flow channel has significantly higher hydrodynamic resistance than that of the main delivery channel,  $Q/q$  stays relatively constant throughout the large array, ensuring  $Q/q$  at each traps being in a proper range for trapping single cells. By varying the length ( $L$ ), width ( $w$ ), and depth ( $h_{\text{gap}}$ ) of the trapping area and the overall depth of the main channel ( $h_{\text{mc}}$ ) (Figure 6.2a), we were able to empirically determine the optimal geometry for trapping Jurkat cells ( $9 \pm 1 \mu\text{m}$  of diameter). Figure 6.2b presents the experimentally determined probability for a trap to be filled (blue circles) as well as the probability for single-cell occupancy (red diamonds). A low resistance ratio results in all traps being occupied, at the cost of having multiple cells per trap (Figure 6.2c). For high resistance ratios, the flow going through the trap is not sufficient for optimal loading, resulting in very few traps being occupied but when occupied, only one cell is present (Figure 6.2e). At the optimal ratio,  $93 \pm 2\%$  of the traps are occupied with  $94 \pm 1\%$  of the occupied trap with a single cell trapped (Figure 6.2d).

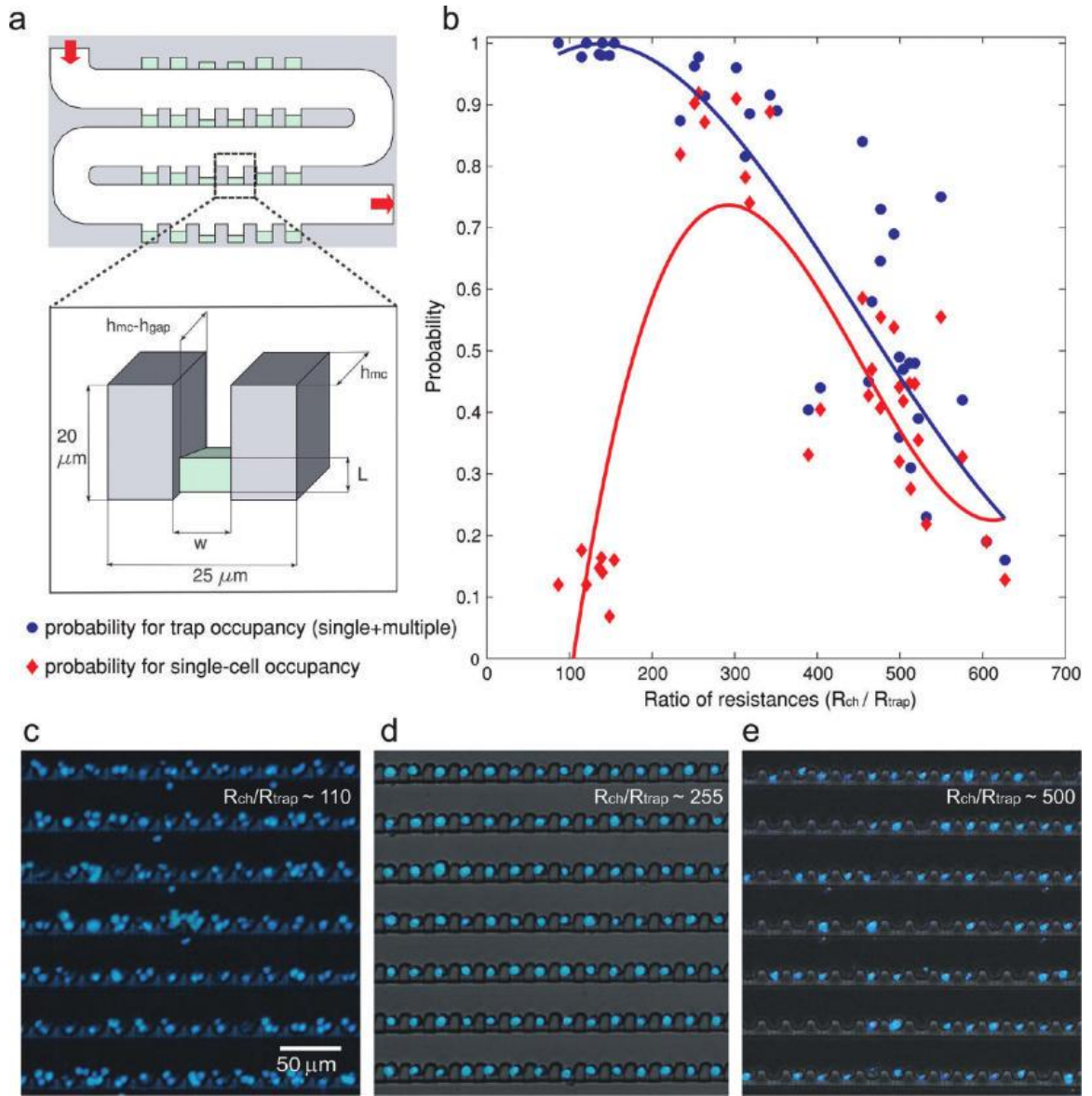


**Figure 6-2:** Characterizing trapping efficiency of the devices with various geometric dimensions. a) Schematic representing the variables involved in loading efficiency optimization. b) Plot showing probability of trap occupancy (blue circles) and probability of single-cell occupancy (red diamonds) for varying ratios of resistance ( $R_{ch}/R_{trap}$ ). The trapping efficiency in a single device will be represented by a red and a blue point. Blue and red lines are guides for the eye. c-e) Representative micrographs of cell trapping: (c)  $R_{ch}/R_{trap} \sim 110$ ; (d)  $R_{ch}/R_{trap} \sim 255$ ; (e)  $R_{ch}/R_{trap} \sim 500$ .

### 6.3.3. On-chip microscopy and cell study

We showed that this microfluidic platform can successfully capture and immobilize both fixed and live cells (Figure 6.3). To ensure trapping and perfusion rate

do not induce undesirable shear stress for long-term studies, we also performed a viability study on chip. Jurkat cells were loaded into the chip and perfused with medium for up to 24 hours in a microcontrolled chamber. After 24 hours, 94% of Jurkat cells were still viable by live-dead stain, comparable to conventional cell culture techniques in flasks. Viability was also observed to be uniform throughout the trap array chamber, suggesting the absence of high shear stress zones in the chamber and the compatibility of the chip with long-term dynamic studies.

Another advantage of the device is that the high trap density allows for imaging large number of cells. For very bright signals, such as a DNA stain or calcium staining with Fluo3, low NA (low magnification) objectives can be used, and up to 800 single cells can be monitored in a field of view (Figure 6.3a).

The microfluidic chip is also compatible with immunostaining. Fixation, permeabilization, immunostaining and necessary wash steps can be performed on chip following standard protocol after cells are loaded into the traps. It is also possible to capture already immunostained cells, although chances of having multiple cells per trap increase due to the increased probability of adhesion of fixed cells to each other or to the device. Figure 6.3b presents Jurkat cells immunostained off chip for calnexin (endoplasmic reticulum), profilin-1 (cytoplasmic cytoskeletal protein) and Hoechst (nucleus) and imaged by confocal microscopy (Figure 6.3b).

One advantage over flow cytometry is that our microfluidic chip coupled with real-time microscopy allows tracking of dynamic behavior of hundreds of cells and monitoring temporal changes within single cells, which cannot be measured by flow cytometry. As a proof of concept, we performed live cell imaging of intracellular calcium



concentration in Jurkat cells (Figure 6.3c). Two hundred trapped cells in a single chamber, loaded with a fluorescent intracellular dye specific for unbound calcium, were imaged every 3 seconds for duration of 15 minutes. The heat map presented in Figure 6.3c highlights heterogeneity in behaviors of individual clonal cells. About 25% of these cells exhibited calcium oscillations under resting conditions, and removal of extracellular calcium abolished the oscillations in all of these cells.

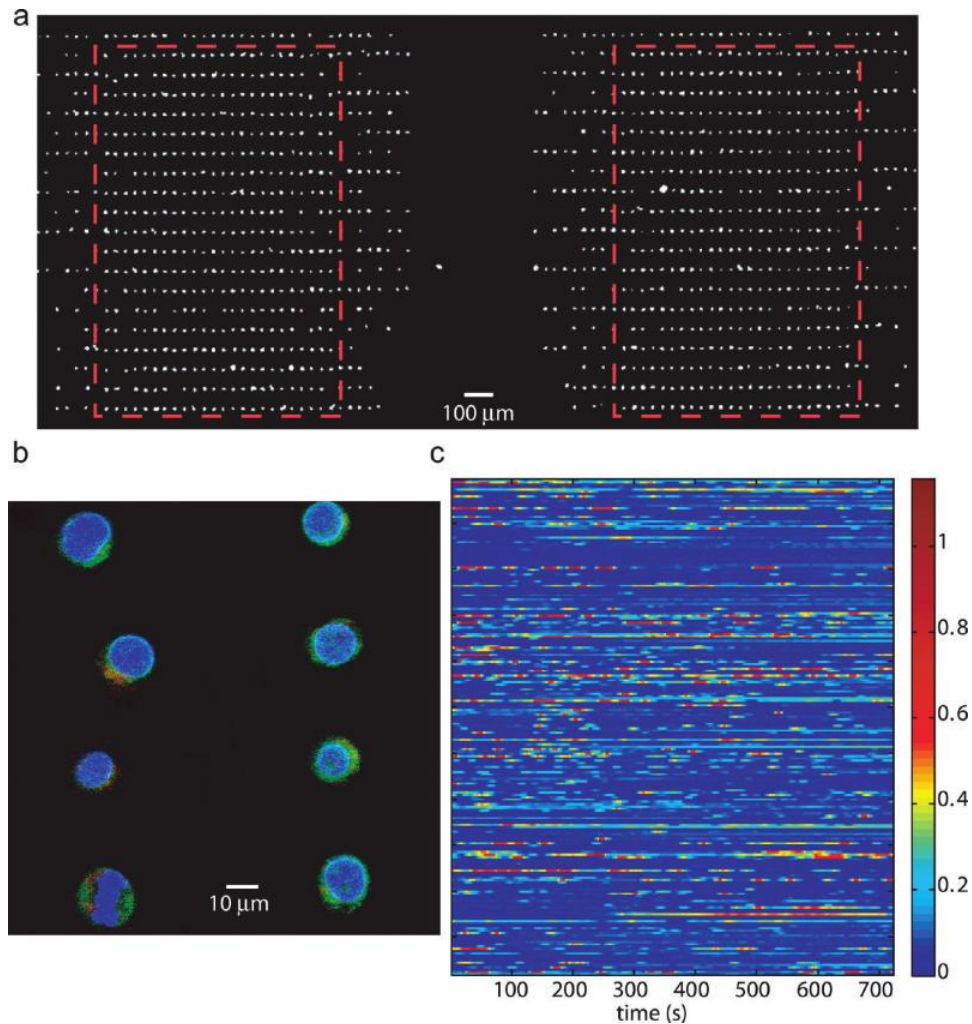


**Figure 6-3:** Use of the array chip for high-resolution imaging of cellular features and activities. a) Fluorescent microphotograph of two cell trap chambers (boxed areas). b) Fluorescent image of immunostained Jurkat cells with confocal microscopy (100X). In blue, Hoechst for the nucleus; in green, calnexin, an ER-bound protein; and in red, profilin-1, a cytoplasmic protein. c) Calcium dynamics in resting Jurkat cells: 216 cells are imaged every 3 s for 15 min. Each line corresponds to an individual cell in the array. The heat map indicates low (in blue) to high (in red) intracellular calcium concentration.

The trap arrays can also be easily integrated with upstream microfluidic components capable of multiplexing experiments, where one expose cells to different extracellular conditions on a single chip. To demonstrate this capability, we coupled the cell trap chambers with a linear serial dilution generator (354) to expose each chamber to a different concentration of the stimulus. By fluorescence measurement, the gradient of concentration was observed to be linear and not disturbed by the high resistance of the loaded cell traps (Figure 6.4b inset). After loading cells containing Fluo-3, more than 1,000 individual cells were monitored for an hour after the addition of different concentrations of the calcium ionophore ionomycin. Ionomycin increases intracellular calcium via mobilization of both extracellular and intracellular calcium stores (355) in T cells. As expected, increased concentration of stimulus lead to increased average intracellular calcium concentration (Figure 4b). Interestingly, when individual cells are monitored, it appears that only a fraction of the cell population are responding to the stimulus (Figure 6.4c-d), and the fraction of responding cells increases linearly with increasing concentration of stimulus ( $R^2 = 0.88$ ) as shown by unsupervised clustering for each chamber in Figure 6.4c and Table 6.1. Cellular response in terms of amplitude and duration of cytoplasmic calcium influx was not dependent on their respective position in the array nor to the presence of oscillations prior to stimulation.

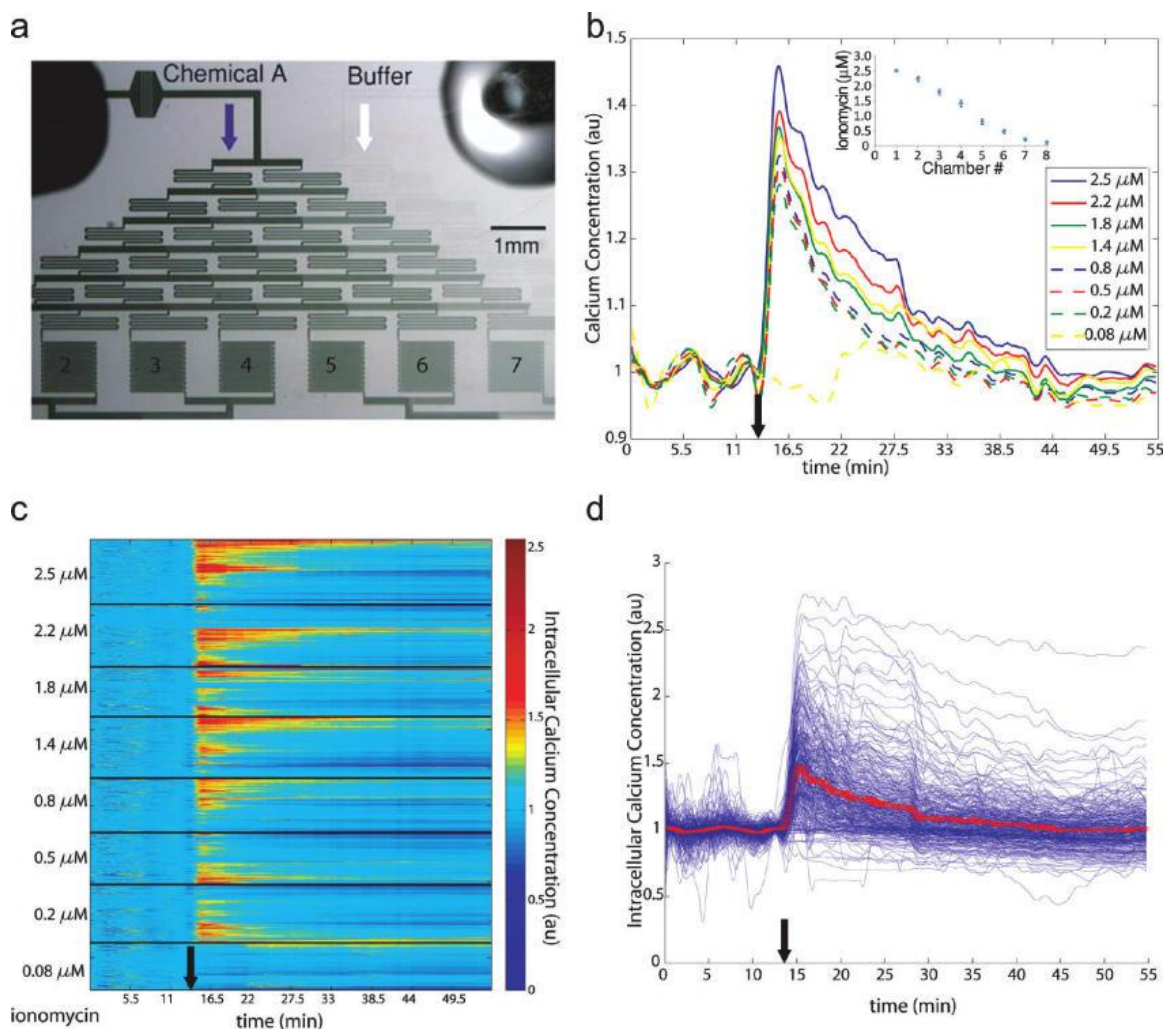


**Figure 6-4:** Calcium dynamics in response to ionomycin stimulation of multiple cells tracked on chip. a) Microphotograph of cell trap arrays interfaced with a concentration gradient generator. The numbers represent the chamber number. b) Average single-cell calcium response for different concentrations of ionomycin. The inset shows the linearity of the concentration gradient ( $n = 4$ ). c) Single-cell response to ionomycin. Each line of the heat map corresponds to the dynamics of a single cell. The heat map is subdivided into eight smaller heat maps, which correspond to decreasing ionomycin concentrations (cf Table 6.1 for details about number of cells imaged and ionomycin concentration). In each subset, unsupervised clustering has been performed to cluster cells with similar responses. d) Traces of single-cell responses to 2.5  $\mu\text{M}$  ionomycin. The red line corresponds to the average response  $\pm$  SEM. The black arrow represents time of ionomycin addition.



**Table 6-1:** Calcium response to various ionomycin concentrations

| Chamber N° | Number of<br>tracked cells | Ionomycin conc.<br>( $\mu$ M) | % Responding<br>cells |
|------------|----------------------------|-------------------------------|-----------------------|
| 1          | 342                        | 2.5                           | 44%                   |
| 2          | 328                        | 2.2                           | 33.2%                 |
| 3          | 263                        | 1.8                           | 31.9%                 |
| 4          | 322                        | 1.4                           | 31.1%                 |
| 5          | 287                        | 0.8                           | 25.4%                 |
| 6          | 273                        | 0.5                           | 19.1%                 |
| 7          | 306                        | 0.2                           | 17%                   |
| 8          | 250                        | 0.08                          | 4%                    |

#### **6.4. Discussion**

In aging, cancer and auto-immune disease states, cellular response is not homogeneous amongst genetically identical cell populations (197, 356). Improved therapies could be devised based on a better understanding of heterogeneity in cell populations and cellular response; however, technology is still a limiting factor to relate cell phenotype to cell signaling dynamics. The microfluidic platform presented here is a first step towards a fully automated and integrated platform for deterministic single-cell trapping, culture, stimulation and imaging. It is capable of passively trapping 4,000 single cells on a 4.5 mm<sup>2</sup> footprint in 30 seconds, with a single-cell loading efficiency of 95%.

Cell trapping chambers were designed so that single cells could be trapped in a deterministic fashion. When a cell enters the trapping area, hydrodynamic forces will focus the cell towards a trap. However, once all the traps in one row are occupied, incoming cells will not experience enough vertical flow to be focused towards filled traps and will pass another cell focusing zone and move to the next row. Similar to the fly embryo trap array previously designed in our group (353), the cross-flow channel

requires a significantly higher hydrodynamic resistance than that of the main delivery channel, resulting in a relatively constant  $Q/q$  ratio throughout the large array, ensuring  $Q/q$  at each traps being in a proper range for trapping single cells. This overall concept being robust to objects ranging from 500  $\mu\text{m}$  (fly embryo longer axis) to 10  $\mu\text{m}$  (Jurkat cells) diameters suggest that it could also be optimized for trapping smaller cellular systems such as yeast and bacteria (10  $\mu\text{m}$ ). In addition, although the device geometry was optimized for Jurkat cells (10  $\mu\text{m}$ ), using the same optimized device, we were able to trap efficiently other cell types (e.g. primary T cells and mouse embryonic stem cells size varying from 8 to 20  $\mu\text{m}$ ), suggesting that the optimal resistance ratio is conserved in this size range.

Deterministic trapping of spherical beads has been demonstrated in the past, using perpendicular hydrodynamical forces on the beads at the intersection of a bypass channel and a main channel (349). Our trapping mechanism also relies on diverging flow from a main channel, the bypass channel being composed of a series of parallel traps in an array format. This particular geometry ensures identical flowrates throughout the entire chamber and allows packing of traps at a higher density. Our design allows us to achieve a trap density of 860 traps /  $\text{mm}^2$ , which is 2-3 orders of magnitude higher than what has been previously reported for deterministic single cell traps (175 ~ 700 traps/ $\text{cm}^2$ ) (351).

This high trap density allows for imaging large number of cells in a field of view. For very bright signals, such as a DNA stain or calcium staining with Fluo3, low NA (low magnification) objectives can be used, and up to 800 single cells can be monitored in a field of view (Figure 6.3a), allowing us to achieve similar statistical significance as

flowcytometry with a largely reduced cell number (Appendix D.S1). More specifically, a typical flow cytometry experiment requires 1,000 to 10,000 data points, each data point corresponding to an individual cell. For kinetic reads, 100 to 500 data points are read every second, resulting in ~ 300,000 cells read for a 10 minute time course. Our system allows us to achieve a comparable resolution with only 250-800 cells. Moreover, flow cytometry does not enable to monitor the early kinetics after addition of the stimulus (20 seconds), and because fluctuations within one cell cannot be quantified, flow cytometry cannot easily discriminate between responding and non-responding cells. This technique is also not capable to measure single cell spiking or oscillatory behaviors.

Compared to most cell trap designs to date, including microwells (344-347) or hydrodynamic flow focusing (129, 348) that follows Poisson statistics, deterministic trapping allows us to increase single cell trapping efficiency from 70% to 95%. We also note that an additional benefit of this trap array design is the sequential capture of incoming cells, preventing undesirable cell loss. Of a small number of cells (e.g. 100 cells) entering the cell trap chamber, all cells will be effectively captured. This could be especially useful for precious sample capturing where the tolerance of cell loss is very low. In addition, loading efficiency is independent of the initial cell concentration; cell concentration only affects loading time with high concentration loading faster. Using 10,000 cells at  $5 \times 10^6$  cells mL<sup>-1</sup>, full loading of a chamber takes less than a minute at a flow rate of 1  $\mu$ L hr<sup>-1</sup>. At lower flow rates, loading time is longer and cells tend to settle in the inlet reservoir. For flow rates above 6  $\mu$ L hr<sup>-1</sup>, cells will experience high shear stress and sometimes squeeze through the 1.8  $\mu$ m deep shallow channel, but the time-saving is

not significant, so in normal use of the device, we chose a flow rate of 1-2  $\mu\text{l hr}^{-1}$ . Similar flowrates need to be used when delivering chemicals to trapped cells. These very low flowrates limit the use of a syringe pump to drive the flow; however, for most applications, it is possible to use gravity driven flow in a controlled manner. At such flowrates, diffusion plays a very important role, which ensure no large delay in chemical delivery between cells in the top and the bottom row of a chamber is introduced (Appendix D.S2).

Cell imaging at high and low resolution is facilitated by our chip. Cells are always located next to the coverslip, enabling high spatial resolution imaging of a few single cells at high magnification (Figure 6.3b). This is a benefit compared to cells trapped in microwells that are not always compatible with high magnification imaging due to the depth of the substrate forming the wells. In addition, because the cells are at known locations on the chip in an arrayed format, thousands of cells can be imaged in one single device repeatedly. Compared to the microwell technology, our system allows chemical stimulus delivery without disturbing cell position in the chip as well as easy integration with upstream chemical gradient generator.

Using this microfluidic platform, we observed heterogeneous calcium patterns among resting Jurkat cells, ranging from a steady-state baseline to periodic oscillations and random spiking. The molecular mechanism governing these asynchronous oscillations is not clearly defined and may arise from stochastic fluctuations in ER calcium channels clustering (87). This heterogeneity in the resting state is still present after stimulation.

When challenged with a calcium ionophore, only a fraction of cells are respondent, fraction that depends on the stimulus concentration. And amongst cellular responses, different response patterns can be defined such as fast, high amplitude oscillations or sharp calcium rise and sustained levels. Partial calcium response of a cell population to external stimulus is not unprecedented; as reported for clonal human embryonic kidney 293 cells when challenged with caffeine, only 40% respond with an elevation in intracellular calcium due to in endogenous protein expression levels (357).

## **6.5. Conclusion**

We present here a microfluidic platform for single-cell capture, stimulation, and imaging capable of passively trapping 4,000 single cells on a  $4.5 \text{ mm}^2$  footprint in 30 seconds, with a single-cell loading efficiency of 95%. The array format and optimized geometry allows for easy, robust and efficient single-cell loading, while maintaining captured cells in a low shear stress environment for long-term studies. Because cells are captured sequentially, this system is adequate for rare cell samples. Compared to previous designs, our higher cell trap density allows for imaging of increased cell numbers, therefore increasing throughput of single cell experiments, while being compatible with high resolution imaging at high magnification. Trapped cells can be exposed to various environmental conditions and chemical stimulus and their dynamic response can be monitored over time. The information gained from high-throughput, single-cell time lapsed imaging presents new opportunities in quantifying cellular responses, as averaged information by other measurement methods eliminates sub-population phenotypes. Because of the ease of use of this system, we envision this platform to be used for diverse

applications, such as fundamental studies of stochastic behavior, diagnosis of patient samples, drug screens in cancer biology, stem cell biology and aging.

## **6.6. Materials & Methods**

### **6.6.1. Fabrication of polydimethylsiloxane (PDMS) devices**

The microfluidic devices were fabricated using soft lithography (202). Negative molds were fabricated by UV photolithographic processes using a negative photoresist (SU8-2010, 14-16  $\mu\text{m}$ , and SU8-2002, 1.5-3  $\mu\text{m}$  in thickness) (Microchem, Newton, MA). Patterned wafers were then treated with tridecafluoro-1,1,2,2-tetrahydrooctyl-1-trichlorosilane vapor (United Chemical Technologies, Bristol, PA) in a vacuum desiccator to prevent adhesion of PDMS (Sylgard 184, Dow Corning, Midland, MI) before the molding process. PDMS mixture of A and B in 10:1 ratio was poured onto the mold to obtain a 5-mm thick layer and then fully cured at 70°C for 2 hours. The PDMS was peeled off the mold and individual devices were cut to size. Medical grade polyethylene (PE3) tubings (Scientific Commodities) were used for fluidic connections. Holes for fluidic connections were punched with 19 gauge needles. PDMS devices were plasma bonded onto either a cover glass or slide glass depending on applications.

### **6.6.2. Cell culture, stimulation and staining**

Jurkat E6-1 human acute T cell lymphoma cells (ATCC) were cultured in RPMI 1640 medium with L-glutamine (Sigma-Aldrich, St. Louis, MO) with 10mM HEPES, 1mM sodium pyruvate, 1X MEM nonessential amino acids, and 100 units  $\text{mL}^{-1}$  penicillin streptomycin (Cellgro), supplemented with 10% certified heat inactivated fetal bovine

serum (Sigma-Aldrich, St. Louis, MO), at 37°C in a humidified 5% CO<sub>2</sub> incubator. For nuclei visualisation, Jurkat cells were incubated with Hoechst 33258, at a final concentration of 1 µg mL<sup>-1</sup>, at 37 °C for 20 minutes. Cells were checked for viability using Live/Dead stain (Invitrogen) following manufacturer's protocol. For high resolution microscopy, 10<sup>6</sup> cells were fixed in a 5% formalin solution (Sigma-Aldrich, St. Louis, MO) for 15 minutes at 37°C, washed three times with cold PBS, and resuspended in 100 µL of ice cold 90% methanol. Immunostaining was performed on fixed cells using Hoechst 3342 for DNA staining, mouse α-calnexin (Abcam) for ER staining, and rabbit α-profilin-1 (Cell Signaling), as a cytoplasmic localized protein. Incubation with the primary antibody for one hour at room temperature was followed by three wash steps with a solution of 2% BSA in PBS and incubation for 40 minutes at room temperature with the following secondary antibodies, Alexa 488 α-mouse (Invitrogen) and goat α-rabbit TRITC (Southern Biotech). To monitor calcium signaling, Jurkat cells were incubated with 5 µM Fluo-3 (Invitrogen) for 20 minutes at 37°C, washed with cold PBS and loaded into the cell traps. Trapped cells were stimulated with ionomycin (Sigma, St. Louis, MO) at various concentrations to release intracellular calcium.

### **6.6.3. Microfluidic system operation**

Before each experiment, the microfluidic devices were primed using a solution of 2% BSA in PBS to remove any air bubbles and prevent undesirable cell adhesion to the wall. A pressure difference of 3.5 kPa (5.5 kPa for devices with upstream serial-dilution gradient generator) created by gravity was used to drive the flow, resulting to an average flow rate of ~ 2 µL h<sup>-1</sup>. Cell loading was obtained by pipetting 2 µL of 5.10<sup>6</sup> cell mL<sup>-1</sup> of

cell suspension on the chip positioned on the microscope stage. Further experiments (staining, stimulation) were performed by adding 5  $\mu\text{L}$  of  $4\times$  chemicals in the inlet hole and flowing over the trapped cells for the desired time. All experiments were performed in a microcontrolled environment (temperature set at  $37^\circ\text{C}$  in a humidified 5%  $\text{CO}_2$  environment). Details on device setup and operation for cell loading are presented in Appendix D.S3.

#### 6.6.4. Quantification of the trapping efficiency

To determine trapping efficiency, devices with varying geometries were built (Figure 6.2). The height of the main channel ( $h_{mc}$ ) was varied from 14 to 16  $\mu\text{m}$ . Width of the traps ( $w$ ) was varied from 8 to 15  $\mu\text{m}$ . The length of the narrow microchannel ( $L$ ) was varied from 3.3 to 8  $\mu\text{m}$ . The height of the narrow microchannel ( $h_{gap}$ ) ranged from 1.5 to 3  $\mu\text{m}$ . Conserved lengths are: width of the main channel (30  $\mu\text{m}$ ), total width of a trap (pocket and wall included: 25  $\mu\text{m}$ ) as well as total length of the trap (20  $\mu\text{m}$ ). Resistance of the main channel above a trap was estimated by

$$R_{ch} = \frac{30}{25 * h_{mc}^3} R_{ch} = \frac{25}{30 * h_{mc}^3} \quad (6-1)$$

and resistance of the trap

$$R_{trap} = \frac{20 - L}{w * h_{mc}^3} + \frac{L}{w * h_{gap}^3} \quad (6-2)$$



### **6.6.5. Data collection and analysis**

High resolution microscopy was performed on a 2-photon confocal microscope (Zeiss LSM 510 NLO). Time-lapse microscopy and device characterization experiments were performed on an epifluorescent (Nikon Eclipse Ti) microscope with an environment controlled chamber. Images from individual chambers were captured sequentially using an automated XYZ stage with a 0.7 second delay between each chamber. Custom Matlab® (MathWorks) scripts were written for semi-automated image processing. Briefly, images were cropped to contain the cell trapping area and a mask of the traps drawn from each picture by finding the areas of higher intensities. The ratio of the number of objects in the overlay of the mask on the original picture to the number of traps corresponds to the percentage of traps occupied. To discriminate traps occupied by a single versus multiple cells, several features were measured for each object, including area, convex area, eccentricity, solidity, perimeter, extent and orientation. A principal least square analysis (SIMCA-P, Umetrics) was run on a known dataset of objects to determine the two most informative predictors of the number of cells contained in an object. The perimeter and the extent (ratio of pixels in the object to pixels in the total bounding box) were found as being the most informative. To quantify single cell trapping efficiency, the distribution of objects in the perimeter-extent space was fitted to a 2-component Gaussian mixture model for each chamber trap array. The maximum likelihood parameters from each of the two subpopulations were retrieved and represented respectively the percentage of single cell objects and multiple cell objects. Single cell response intensities were obtained by tracking the mean intensity of each object considered as a single cell in the overlaid mask and image over time.

## CHAPTER 7

# FREQUENCY RESPONSE ANALYSIS OF CROSS-TALK BETWEEN ROS AND CALCIUM

### 7.1. Introduction

$\text{Ca}^{2+}$  and reactive oxygen species (ROS) share features of second messenger signaling molecules and are central to the regulation of various cellular functions.  $\text{Ca}^{2+}$  regulates proliferation, apoptosis, differentiation or gene transcription in T cells (269). ROS, on the other hand, can be deleterious to the cell at high concentration, but at low concentration is essential for regulating cell signaling (358). The  $\text{Ca}^{2+}$  and ROS signaling systems are integrated such that  $\text{Ca}^{2+}$ -dependent regulation of components of ROS homeostasis influences intracellular redox balance, and *vice versa* (91, 92, 94, 359). Disruption in the ROS balance resulting in oxidative stress and improper  $\text{Ca}^{2+}$  signaling has been associated with several diseases, including Alzheimer's and Parkinson's disease, diabetes, cardiac pathologies as well as aging (94, 360).

We have observed in long-term cultured T cells an increase in the intracellular redox status with age (Chapter 4) and altered  $\text{Ca}^{2+}$  signaling (Chapter 5). Our modeling analysis of  $\text{Ca}^{2+}$  signaling dysregulation as a function pointed to several kinetic parameters associated with purported oxidative modifications on calcium channels. To explore the network of complex interactions between  $\text{Ca}^{2+}$  and ROS further, we chose to take a different computational modeling approach in order to (1) draw a map of the interactions between these molecules in T cells and (2) understand these interactions and their role in signaling and pathophysiology.

The ROS/Ca<sup>2+</sup> cross-talk system is composed of many interactions forming various feedback mechanisms occurring on different timescales. The sum of these interactions determines the cell response to a perturbation; yet weighing the effects of each interaction at a specific timescale is required for a solid understanding of the system. Control systems engineers have developed tools to study dynamic behaviors of mechanical and electrical systems and have in particular derived the frequency response analysis to address time-varying processes. This analysis considers the system as a black-box and determines its overall behavior based on input-output relationships when the system is probed at different frequencies. This methodology has been recently applied to biological systems to study bacterial chemotaxis (361, 362) and cell signaling in yeast (135, 136, 363). In mammalian systems, due to technical limitations, it is difficult to probe cellular response to chemical stimuli of varying frequencies. Fourier analysis has been applied in *in silico* models to show the importance of inherent noise to drive sustained oscillations in the p53-Mdm2 naturally oscillating feedback system (364) and the low-pass filter effect of a three component AKT pathway resulting in the decoupling of the peak amplitudes of receptor phosphorylation and that of downstream effectors (365). However, in the latter example, validation of the model was performed in the time domain.

With the advance of the microfluidic field, generating controlled complex chemical patterns is now possible (366-369). Although very elegant, these techniques are often hard to implement and to integrate with cellular systems. When integrated with cellular systems for downstream biological applications, chemical pulse generation is either performed off-chip (135, 362), using on-chip valves (363) or laminar flow

properties (370, 371). However, all these techniques used yeast or adherent cells. Non-adherent cells, such as T cells, present an additional challenge as they require to be retained in specific location over time while exposed to changing stimuli. We have presented in Chapter 6 a new microfluidic platform for single T cell trapping, exposure to step stimuli and imaging. Integration of this platform with a chemical wave synthesizer would allow for validation of frequency response type models generated for non-adherent cells.

In this Chapter we present a model of ROS/ $\text{Ca}^{2+}$  cross-talk in T cells, based on the  $\text{Ca}^{2+}$  signaling model presented in Chapter 5, with the addition of a ROS homeostasis module. *In silico* frequency response analysis to periodic ROS stimuli suggests that the cell acts as a low pass filter with a larger bandwidth in the cytoplasm compared to the ER. *In vitro* single cell response to periodic  $\text{H}_2\text{O}_2$  stimulation shows a large heterogeneity in response amplitude and phase shift. We also observed a high  $\text{Ca}^{2+}$  response dependence on the stimulus amplitude. In average at lower  $\text{H}_2\text{O}_2$  concentration, cells follow the input stimulus with a larger delay compared to higher input concentrations. These non-linear effects can be recapitulated by the model when probed *in silico* for different stimulus amplitude.

## **7.2. Computational model of calcium-ROS cross-talk in T lymphocytes**

### **7.2.1. Model Description**

$\text{Ca}^{2+}$  influences ROS metabolism while ROS can modulate or even impair  $\text{Ca}^{2+}$  signaling. To better understand cross-talk effects between these two ubiquitous second messengers, we adapted the model of  $\text{Ca}^{2+}$  signaling in T cells presented in Chapter 5 and

incorporated ROS and  $\text{Ca}^{2+}$  interactions with proteins regulating ROS and  $\text{Ca}^{2+}$  metabolism in different cellular compartments. Figure 7.1 presents an overall schematic of the model. The model can be subdivided in two tightly interconnected modules that span across the various cellular compartments: cytosol, endoplasmic reticulum (ER), mitochondria as well as the extracellular space. The first module describes relatively simply ROS metabolism in the cytosol and ER (in maroon). The second module describes  $\text{Ca}^{2+}$  fluxes in the cell and is adapted from Chapter 5 (in black). The combination of these two modules provides a comprehensive description of ROS and  $\text{Ca}^{2+}$  cross-talk in T cells.

**Assumptions:** Species concentration is assumed to be spatially uniform in all compartments. Modulation of  $\text{Ca}^{2+}$  channels and pumps by ROS and effect of  $\text{Ca}^{2+}$  on the ROS metabolism pathway have not been mathematically described in the past. We have chosen to represent these biological processes as enzymatic reactions using Michaelis-Menten and Hill type functions.

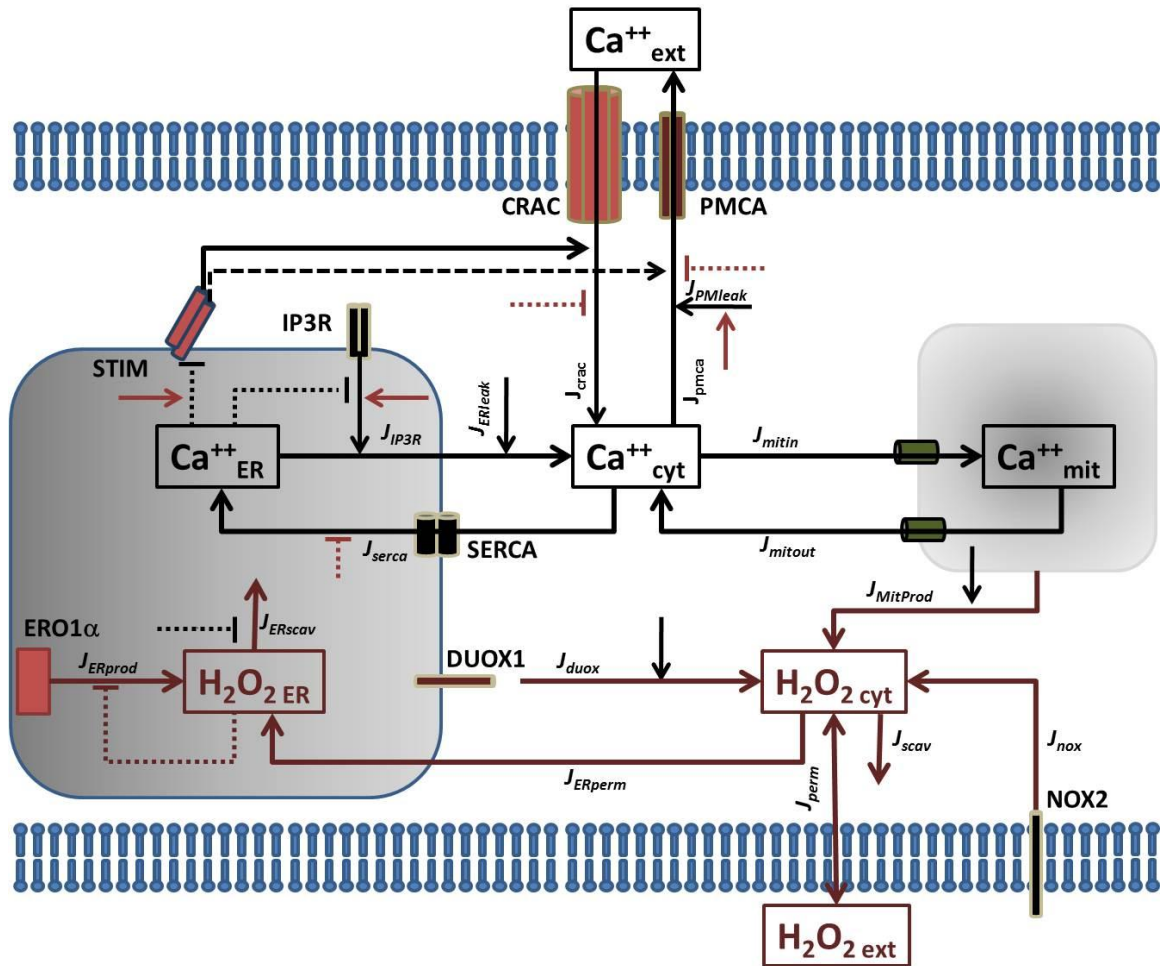


**Figure 7-1:** Schematic of the  $\text{Ca}^{2+}$ /ROS cross-talk model in T cells. The  $\text{Ca}^{2+}$  signaling module is depicted in black. The ROS metabolism module is depicted in maroon. Dashed lines correspond to inhibition, plain lines to activation. A black arrow on a maroon line represents positive modulation of a ROS flux by  $\text{Ca}^{2+}$ . A maroon dashed line on a black arrow corresponds to ROS inhibition of a  $\text{Ca}^{2+}$  flux.

### 7.2.2. Module 1

Module 1 describes ROS production and clearance mechanisms in basal conditions but also in response to extracellular ROS influx. This model does not discriminate between different sorts of ROS and lumps superoxide anions,  $\text{H}_2\text{O}_2$  and nitric oxide as a global species, i.e. ROS. Our group had previously published a comprehensive model of cytosolic  $\text{H}_2\text{O}_2$  clearance from Jurkat cells including pseudo-enzymatic oxidative turnover of protein thiols, the enzymatic actions of catalase,

glutathione peroxidase, peroxiredoxin, and glutaredoxin, and the redox reactions of thioredoxin and glutathione (260). Because a very detailed analysis of the antioxidant system is beyond the scope of this study, only the major production and clearance fluxes in each compartment are described.

The fundamental equations of ROS metabolism in the various cellular compartments are described as follows:

$$\frac{dROS_{cyt}}{dt} = J_{perm} + J_{nox} + J_{duox} + J_{MitProd} - J_{ERperm} - J_{scav} \quad (7-1)$$

$$\frac{dROS_{ER}}{dt} = \frac{1}{\rho_{er}} (J_{ERperm} + J_{ERprod} - J_{ERscav}) \quad (7-2)$$

$$\frac{dROS_{ext}}{dt} = -J_{perm} \quad (7-3)$$

$ROS_{cyt}$ ,  $ROS_{ER}$  and  $ROS_{ext}$  denote the concentration of reactive oxygen species in the cytosol, ER and extracellular space.  $\rho_{er}$  is the ratio of the ER volume to that of the cytosol.

*ROS influx from the extracellular space to the cytosol:* Rate of ROS transport across the cell membrane is described as in Adimora *et al.* (260):

$$J_{perm} = (ROS_{ext} - ROS_{cyt}) \cdot K_{perm} \quad (7-4)$$

where  $K_{perm}$  is the permeability coefficient of ROS through the cytoplasmic membrane.

As in (260), the value of  $K_{perm}$  is adjusted to take into account cell surface area and concentration.

*ROS production in the cytoplasm:* There are several sources of ROS production inside the cell. Electron leakage from the mitochondrial respiratory chain results in superoxide production ( $J_{MitProd}$ ). During signaling, NADPH oxidases are activated and produce either superoxide or  $H_2O_2$ . T cells express two NADPH oxidases isoforms, respectively Nox2 ( $J_{nox}$ ) and the  $Ca^{2+}$  sensitive Duox1 ( $J_{duox}$ ) (372, 373).

Mitochondrial respiration is a constant source of ROS,  $V_{MitProd}$ . It is suggested in the literature that during signaling and apoptosis, ROS production from the mitochondria increases. However, how mitochondrial  $Ca^{2+}$  buffering modulates ROS generation is still unknown; available results on this issue are conflicting.  $Ca^{2+}$  induces ROS production if mitochondria are treated with some inhibitor but reduces it under normal conditions (374, 375). For this reason, we chose to describe  $J_{MitProd}$  as a constant production rate.

$$J_{MitProd} = V_{MitProd} \quad (5-5)$$

Mature T cells express the phagocyte-type NADPH oxidase Nox2 that regulates elements of TCR signaling (372). Because of its importance in phagocytic oxidative burst, this Nox isoform has been extensively studied. Activation of Nox2 occurs through a complex series of protein/protein interactions, involving recruitment of the p22phox, p47phox and p67phox subunits and Rac2 to the membrane bound gp91phox subunit (376). Phosphorylation of specific subunits is required for proper Nox activation (377). A recent computational model of NADPH oxidase activation in endothelial cells developed by Yin *et al.* only considered activation and translocation of the Nox1 (isoform of gp91phox) and p47phox subunits to describe Nox activation (378). We further simplified



this representation by describing Nox activity as a sole function of  $IP_3$ , based on the fact that the same upstream reaction by PLC- $\gamma$  that generates  $IP_3$  and subsequent  $Ca^{2+}$  release also initiates diacylglycerol activation of protein kinase C (PKC), which phosphorylates p47phox (379) and Rac1/2 indirectly through Ras (380). Therefore, ROS production through Nox2 is given by:

$$J_{nox} = V_{nox} \frac{IP_3}{IP_3 + K_{nox}} \quad (7-6)$$

where  $V_{nox}$  is the maximal ROS production rate by Nox2 and  $K_{nox}$  the half maximal  $IP_3$  concentration resulting in Nox activation.

Duox1, a  $Ca^{2+}$  dependent nonphagocytic NADPH oxidase, has been reported to be responsible for rapid TCR stimulated generation of  $H_2O_2$  (373). Duox1 does not need to be associated with cytosolic factors to be active but is regulated by  $Ca^{2+}$  through two canonical EF-hand motifs and PKA/PKC-dependent phosphorylation (381). ROS production through Duox1 is therefore described as a linear function of  $IP_3$  and a 2<sup>nd</sup> order Hill function depending on cytosolic  $Ca^{2+}$  levels:

$$J_{duox} = V_{duox} \cdot IP_3 \cdot \frac{Ca_{cyt}^2}{Ca_{cyt}^2 + K_{duox}^2} \quad (7-7)$$

where  $V_{duox}$  is the maximal ROS production rate by Duox1 and  $K_{duox}$  the cytosolic  $Ca^{2+}$  dissociation constant.

*ROS scavenging in the cytoplasm:* Adimora *et al.* generated a network model of major redox reactions and cellular thiol modifications involved in  $H_2O_2$  metabolism in response to oxidative stress (260). We lumped all these reactions into a single 1<sup>st</sup> order mass action

kinetic function with a scavenging rate constant  $k_{scav}$  that fits the predicted cytosolic  $H_2O_2$  concentration showed in (260).

$$J_{scav} = k_{scav} \cdot ROS_{cyt} \quad (7-8)$$

*ROS influx from the cytosol to the ER:* Previous studies reported increased ER ROS levels upon the bolus addition of  $H_2O_2$  (382), suggesting an ability for cytoplasmic ROS to enter the ER, either by diffusion or active transport. We represented this flux as driven solely by changes in steady state cytoplasmic ROS levels:

$$J_{ERperm} = (ROS_{cyt} - ROS_{cytinit}) \cdot K_{ERperm} \quad (7-9)$$

where  $K_{ERperm}$  is the ER permeability membrane to ROS and  $ROS_{cytinit}$  the basal ROS concentration in the cell.

ROS leakage from the highly oxidized ER environment into the cytosol has not been demonstrated in the literature. In fact, an ER luminal  $H_2O_2$  sensor is oxidized while a similar reporter bound to the cytosolic ER membrane side is not (382). This flux has consequently not been included in our model.

*ROS production in the ER:* To maintain the high oxidative environment necessary for proper protein folding, the ER is rich in sources of ROS, including oxygenases and oxidases which often produce ROS as a byproduct (383). The membrane associated flavoprotein Ero1 $\alpha$  is a significant source of oxidized equivalents for the ER lumen and thus is responsible for setting the ER oxidation state (384, 385). Ero1 $\alpha$  activity can be modulated by changes in the redox state of its regulatory cysteine pairs as part of a

homeostatic feedback system in the ER that allows the cell to rapidly offset potentially detrimental fluctuations in the ER redox environment (386). A simplified description of ER ROS production by ERO1 $\alpha$  is therefore given by:

$$J_{ERprod} = V_{ero1} \left( \frac{K_{ero1}^{nprod}}{ROS_{ER}^{nprod} + K_{ero1}^{nprod}} \right) \quad (7-10)$$

where  $V_{ero1}$  is the maximal ROS production rate by Ero1,  $K_{ero1}$  is an equivalent oxidized species affinity constant to the regulatory cysteine pairs, and  $nprod$  the Hill coefficient.

*ROS scavenging in the ER:* The ER contains several reductants, such as the thiol/disulfide system including glutathione and newly synthesized proteins, glucose-6-phosphate (G6P) or pyridine nucleotides (379). Similar to the approach taken for the cytosolic scavenging system, we have lumped all these antioxidant systems into one single ROS degradation reaction. Using an ER-targeted H<sub>2</sub>O<sub>2</sub>-sensitive fluorescent probe Hyper, Enyedi *et al.* showed a decrease in ER H<sub>2</sub>O<sub>2</sub> levels after Ca<sup>2+</sup> mobilization from the ER stores independently of ERO1 $\alpha$  activity, suggesting an effect of intraluminal Ca<sup>2+</sup> on ER ROS degradation (381). This hypothesis is compatible with the well-studied ER stress process, where low intraluminal Ca<sup>2+</sup> leads to an increase in misfolded proteins, a consequence of altered redox status (387). We have thus selected the following mathematical representation:

$$J_{ERout} = k_{ERscav} \cdot ROS_{ER} \cdot \left( \frac{K_{ERscav}^{nscav}}{Ca_{ER}^{nscav} + K_{ERscav}^{nscav}} \right) \quad (7-11)$$

where  $k_{ERscav}$  is the maximal ROS scavenging rate in the ER and  $K_{ERscav}$  the equivalent half maximal ER Ca<sup>2+</sup> concentration leading to inhibition of the scavenging system and  $nscav$  the Hill coefficient.

### 7.2.3. Module 2

Module 2 describes  $\text{Ca}^{2+}$  fluxes between the cytosol, ER, mitochondria and extracellular space to a known function or a steady input of  $\text{IP}_3$ . Mathematical description of each flux is identical to ones used in Chapter 5, with the addition of ROS modularity effects. Briefly, binding of  $\text{IP}_3$  to the  $\text{IP}_3$  receptor ( $\text{IP}_3\text{R}$ ) triggers the release of  $\text{Ca}^{2+}$  stored in the ER ( $J_{\text{IP}_3}$ ). The resulting drop in ER  $\text{Ca}^{2+}$  levels activates the ER  $\text{Ca}^{2+}$  sensor STIM1, which translocates to the ER-PM (plasma membrane) junctions to activate a more sustained influx in the cytosol through the calcium-release-activated  $\text{Ca}^{2+}$  channels (CRAC) on the PM ( $J_{\text{crac}}$ ) (297, 298). The PM  $\text{Ca}^{2+}$  ATP-ase (PMCA) pumps  $\text{Ca}^{2+}$  out of the cytosol ( $J_{\text{pmca}}$ ). There is an additional very small  $\text{Ca}^{2+}$  leak from the extracellular space into the cytosol ( $J_{\text{PMleak}}$ ). The Sarco/ER  $\text{Ca}^{2+}$  ATP-ase (SERCA) pumps cytosolic  $\text{Ca}^{2+}$  back in the ER stores ( $J_{\text{SERCA}}$ ), while small quantities of  $\text{Ca}^{2+}$  ions leak from the ER to the cytosol ( $J_{\text{ERleak}}$ ). Cytosolic  $\text{Ca}^{2+}$  is buffered by the mitochondria ( $J_{\text{mitin}}$ ,  $J_{\text{mitout}}$ ).  $\text{IP}_3$  production and degradation are not included in this module.

As in Chapter 5, the fundamental equations of  $\text{Ca}^{2+}$  kinetics in the various cellular compartments are described as follows:

$$\frac{d\text{Ca}_{\text{cyt}}}{dt} = \beta_i((J_{\text{IP}_3} - J_{\text{serca}} + J_{\text{ERleak}}) + (J_{\text{mitin}} - J_{\text{mitout}}) + (J_{\text{crac}} - J_{\text{pmca}} + J_{\text{PMleak}})) \quad (7-12)$$

$$\frac{d\text{Ca}_{\text{ER}}}{dt} = \frac{\beta_{\text{er}}}{\rho_{\text{er}}}(J_{\text{IP}_3} - J_{\text{serca}} + J_{\text{ERleak}}) \quad (7-13)$$

$$\frac{d\text{Ca}_{\text{mit}}}{dt} = \frac{\beta_{\text{mit}}}{\rho_{\text{mit}}}(J_{\text{mitin}} - J_{\text{mitout}}) \quad (7-14)$$

$Ca_{\text{cyt}}$ ,  $Ca_{\text{mit}}$  and  $Ca_{\text{ER}}$  denote the concentration of free  $Ca^{2+}$  in the cytosol, mitochondria and ER respectively.  $\beta_i$ ,  $\beta_{er}$ ,  $\beta_{mit}$  are the ratio of free to total  $Ca^{2+}$ .  $\rho_{er}$ ,  $\rho_{mit}$  are the ratios of the ER and mitochondria volume to that of the cytosol. Several  $Ca^{2+}$  binding proteins involved in  $Ca^{2+}$  buffering in the cytosol and ER have been shown to be redox sensitive. The effect of oxidation on those proteins results in both increased and decreased affinity to  $Ca^{2+}$  depending on the protein (94). Because of these mixed effects, we omitted description of the redox effects on  $Ca^{2+}$  buffering.

*Ca<sup>2+</sup> flux through the IP<sub>3</sub>R:* IP<sub>3</sub>R channels are the primary  $Ca^{2+}$  release channel in the ER in T cells and contain several cysteine residues; for instance IP<sub>3</sub>R1 has 60 Cys residues, 70% of them being kept in reduced state with variable accessibility and variable regulatory significance (388). Oxidation of certain –SH groups via exposure to thimesoral or GSSG sensitizes IP<sub>3</sub>R activation by IP<sub>3</sub>, so that even resting levels of IP<sub>3</sub> would activate IP<sub>3</sub>R modified by oxidation (327, 389, 390). Duox1 has been shown to be co-expressed with IP<sub>3</sub>R T cells (108) which may imply a role of Duox1 H<sub>2</sub>O<sub>2</sub> production as a positive feedback to maintain IP<sub>3</sub>R open and amplify the  $Ca^{2+}$  signal. In addition, recent studies have suggested a possible link between the ER redox state and IP<sub>3</sub>R function (391-393); however, cysteine residues responsible for redox modifications of IP<sub>3</sub>R activity have not been identified, and it is still not very clear when, where and how these modifications take place.

Therefore we only described ROS effect on IP<sub>3</sub>R as a ROS-dependent modulation of IP<sub>3</sub> affinity constant. The modified flux of  $Ca^{2+}$  through the IP<sub>3</sub>R is given by:

$$J_{IP3} = V_{IP3} \cdot P_{IP3} \cdot Ca_{ER} \quad (7-15)$$

where  $V_{IP3}$  is the maximum flowrate and  $P_{IP3}$  the  $IP_3R$  open probability.  $P_{IP3}$  is assumed to be an instantaneous function of  $Ca^{2+}$ ,  $IP_3$  concentration and the fraction of  $IP_3R$  not inactivated by  $Ca^{2+}$  bound to the inhibitory site,  $h$ .  $P_{IP3}$  is described as:

$$P_{IP3} = \left( \left( \frac{IP3}{IP3 + K_{IP3ros}} \right) \left( \frac{Ca_{cyt}}{Ca_{cyt} + K_{act}} \right) h \right)^3 \quad (7-16)$$

where  $K_{IP3ros}$  is the ROS-modulated  $IP_3$  dissociation constant from the  $IP_3$  binding site and  $K_{act}$  the affinity of  $Ca^{2+}$  to the activating site.

$$K_{IP3ros} = K_{IP3} \left( \frac{k_{ip3ros}^{nrosIP3}}{ROS_{cyt}^{nrosIP3} + k_{ip3ros}^{nrosIP3}} \right) \quad (7-17)$$

where  $K_{IP3}$  is the unmodulated  $IP_3$  dissociation constant from the  $IP_3$  binding site.  $k_{ip3ros}$  is the half maximal ER ROS concentration that leads to a change in  $IP_3$ -binding affinity and  $nrosIP3$  the Hill coefficient.

The fraction of inactivated  $IP_3R$ ,  $1-h$ , is a function of cytoplasmic  $Ca^{2+}$  and  $Q$ , the effective affinity of  $Ca^{2+}$  to the inhibitory site.

$$\frac{dh}{dt} = A((1-h)(Q + Ca_{cyt}) - Ca_{cyt}) \quad (7-18)$$

$$Q = K_{inh} \left( \frac{IP3 + K_{IP3ros}}{IP3 + K_{IP3inh}} \right) \quad (7-19)$$

where  $A$  is a variable controlling the relative time scales between the differential equations,  $K_{inh}$ , the  $Ca^{2+}$  affinity to the  $Ca^{2+}$  inhibitory site and  $K_{IP3inh}$  the affinity of  $IP_3$  to the  $IP_3$  binding site when the  $Ca^{2+}$  inhibitory site is occupied.

*Ca<sup>2+</sup> leak from the ER:* Increased levels of intraluminal ROS result in a temporary increase in nonselective membrane permeability, which would allow the escape of a larger number of Ca<sup>2+</sup> ions from the ER to the cytoplasm. Modified  $J_{ERleak}$  can be described as:

$$J_{ERleak} = k_{ERleak} \cdot Ca_{ER} \cdot \left(1 + \frac{ROS_{ER} - ROS_{ERinit}}{ROS_{ERinit}}\right) \quad (7-20)$$

where  $k_{ERleak}$  is the unmodulated ER Ca<sup>2+</sup> leak rate and  $ROS_{ERinit}$  the resting ROS level in the ER.

*Ca<sup>2+</sup> flux through the SERCA pumps:* SERCA pumps plays a key role in maintaining low cytoplasmic Ca<sup>2+</sup> levels by actively sequestering Ca<sup>2+</sup> into the ER. The different SERCA isoforms channels contain from 22 to 28 cysteine residues, most of which display redox sensitivity resulting in inhibition of the Ca<sup>2+</sup> pump to cytoplasmic oxidative stress (108-110). The luminal regulation of SERCA2b isoform also involves a redox component. At high ER Ca<sup>2+</sup> levels and oxidizing conditions, the oxidoreductase ERp57 bound to SERCA C-terminal tail promotes disulfide bridge formation that reduces pump activity. For simplification purposes, we only modeled a general cytoplasmic ROS modulatory effect on SERCA activity, and the modified  $J_{serca}$  is given by:

$$J_{serca} = V_{serca} \cdot \left(\frac{Ca_{cyt}^2}{Ca_{cyt}^2 + K_{serca}^2}\right) \cdot \left(\frac{k_{sercaros}^{nsercaros}}{ROS_{cyt}^{nsercaros} + k_{sercaros}^{nsercaros}}\right) \quad (7-21)$$

where  $V_{serca}$  is the maximum flux across the SERCA pump and  $K_{serca}$  the SERCA activation constant by Ca<sup>2+</sup>,  $k_{sercaros}$  the half maximal cytosolic ROS concentration responsible for pump inhibition and  $nsercaros$  the Hill coefficient. Again, as in Chapter

5, we did not discriminate between different SERCA isoforms despite their differential  $\text{Ca}^{2+}$  affinities and susceptibility to redox inhibition (108).

*Ca<sup>2+</sup> fluxes through the mitochondria:* There are no reports of direct redox modulation of the uniporter or the mitochondrial  $\text{Na}^+/\text{Ca}^{2+}$  exchanger; hence we did not alter the expressions for mitochondrial  $\text{Ca}^{2+}$  uptake and efflux described in Chapter 5:

$$J_{mitin} = V_{mitin} \left( \frac{Ca_{cyt}^4}{Ca_{cyt}^4 + K_{mitin}^4} \right) \quad (7-22)$$

where  $V_{mitin}$  is the maximum rate of  $\text{Ca}^{2+}$  uptake in the mitochondria and  $K_{mitin}$  the apparent  $\text{Ca}^{2+}$  affinity of the uniporter.

$$J_{mitout} = V_{mitout} \cdot Ca_{mit} \cdot \left( * \frac{Ca_{cyt}^2}{Ca_{cyt}^2 + K_{mitout}^2} \right) \quad (7-23)$$

where  $V_{mitout}$  is the maximum rate of  $\text{Ca}^{2+}$  efflux and  $K_{mitout}$  the half maximum  $\text{Ca}^{2+}$  concentration for efflux.

*Ca<sup>2+</sup> fluxes through the plasma membrane:* Store operated calcium entry (SOCE) relies on ER  $\text{Ca}^{2+}$  store depletion, activation of STIM1, dimerization, association with the ORAI1 CRAC channels and CRAC activation (298, 308). Redox regulation of SOCE is not clear (102). Hawkins *et al.* studied redox mediated activation of STIM1 and found that oxidative stress leads to glutathionylation of STIM1's cysteine 56, triggering STIM1 oligomerization and punctae formation independently of ER  $\text{Ca}^{2+}$  levels (103); yet Prins *et al.* demonstrated that the ER oxidoreductase ERp57 is a binding partner with STIM1 and ERp57 deficiency results in increased SOCE, suggesting a negative role of oxidation on STIM1 (104). Orai1 is reported to be activated in a STIM1-dependent manner after



H<sub>2</sub>O<sub>2</sub> exposure (105); however, in another study, ORAI1 was observed to be inhibited by oxidation of Cys195 (106). Because of these discrepancies in the literature (102), we chose to ignore redox effects on CRAC channels.  $J_{crac}$  is therefore expressed as in Chapter 5:

$$J_{crac} = V_{crac} \cdot \left( \frac{K_{stim}^3}{Ca_{ER}^3 + K_{stim}^3} \right) \cdot \left( \frac{Ca_{ext}}{Ca_{ext} + K_{soc}} \right) \quad (7-24)$$

where  $V_{crac}$  is the maximum Ca<sup>2+</sup> influx through the CRAC channels,  $K_{stim}$  is the dissociation constant of ER Ca<sup>2+</sup> to STIM1 and  $K_{soc}$  the Michaelis-Menten concentration for extracellular Ca<sup>2+</sup>,  $Ca_{ext}$ .

Permeability of the plasma membrane has not been shown to be redox-dependent; hence we have used the PM Ca<sup>2+</sup> leakage expression from Chapter 5:

$$J_{PMleak} = K_{PMleak} \cdot Ca_{ext} \quad (7-25)$$

where  $K_{PMleak}$  is the rate of leakage through the plasma membrane.

As with the SERCA pump, the PMCA pump is also inhibited by oxidation, though at higher levels of ROS (394, 395). Ca<sup>2+</sup> efflux from the cytosol to the extracellular space is therefore described as:

$$J_{pmca} = V_{pmca} \cdot \left( \frac{Ca_{cyt}^2}{Ca_{cyt}^2 + K_{pmca}^2} \right) \cdot \left( \frac{Ca_{ER}^2}{Ca_{ER}^2 + K_{STIMpmca}^2} \right) \cdot \left( \frac{k_{pmcaros}^{npmcaros}}{ROS_{cyt}^{npmcaros} + k_{pmcaros}^{npmcaros}} \right) \quad (7-26)$$

where  $V_{pmca}$  is the maximal PMCA efflux rate,  $K_{pmca}$  the Ca<sup>2+</sup> affinity to the PMCA pump,  $K_{STIMpmca}$  the dissociation constant of ER Ca<sup>2+</sup> on STIM1 allowing it to become

activated and interact with PMCA.  $k_{pmcaros}$  is the half maximal cytosolic ROS concentration responsible for pump inhibition and  $npmcaros$  the Hill coefficient.

#### 7.2.4. Model Optimization and Simulation in the Time Domain

The series of differential equations were solved using Matlab R2011a (Mathworks, Natick, MA) using the ODE solver for stiff system ode23s. Initial conditions were chosen according to published experimental data before parameter optimization or computed at steady state (Table 7.1). There is very little information available in the literature concerning concentrations of ROS in living cells. Enyedi *et al.* reported an ER  $H_2O_2$  concentration similar to the cytosolic  $H_2O_2$  concentration after a bolus addition of 90  $\mu M$   $H_2O_2$ , suggesting ER ROS levels to be in the tens of  $\mu M$ . The ER environment being largely more oxidized than the cytosol ( $\sim -130mV$  difference in the redox potential) (396), we assumed the cytoplasmic concentration to be in the nM range, consistent with other estimates (260).

**Table 7-1:** Initial conditions

| State Variable                 | Value        | Reference                                               |
|--------------------------------|--------------|---------------------------------------------------------|
| $ROS_{cyt}$                    | 1 nM         | (260)                                                   |
| $ROS_{ER}$                     | 85 $\mu M$   | (382)                                                   |
| $Ca_{cyt}$                     | 50 nM        | (310)                                                   |
| $Ca_{ER}$                      | 350 $\mu M$  | (310)                                                   |
| $Ca_{mit}$                     | 0.1 $\mu M$  | (311) followed by SS computation $J_{mitin}=J_{mitout}$ |
| $IP_3$                         | 0.54 $\mu M$ | (309)                                                   |
| $h$ (fraction active $IP_3R$ ) | 0.02         | (292)                                                   |

We performed initial parameter estimation on each module individually, to constrain the number of free floating parameters to estimate. Parameter estimation for

Module 2 was described in Chapter 5. For Module 1,  $IP_3$ ,  $Ca_{cyt}$  and  $Ca_{ER}$  were maintained at steady state and unknowns were fitted to four different datasets: cytoplasmic ROS clearance after bolus addition of exogenous  $H_2O_2$  (260) (represented by an abrupt change in initial  $ROS_{media}$  concentration), as well as three datasets acquired by Enyedi *et al.* representing ER ROS dynamics in response to DTT (represented by 8-fold increase in the ROS scavenging rate in the cytosol and ER), thapsigargin (represented by a 85% reduction in the maximal SERCA pumping velocity) and histamine (382). Because the histamine  $Ca^{2+}$  time course resembled a  $Ca^{2+}$  trace after TCR stimulation, we used a 5 min pulse  $IP_3$  input function. Once parameters were found that fit all four datasets, we allowed the  $Ca^{2+}$  fluxes in the various cellular compartments to vary and empirically adjusted the velocities of the  $Ca^{2+}$  channels and pumps modulated by ROS. The other parameters in Module 2 were left unchanged and the parameters in Module 1 adjusted to fit the four datasets. This parameter set was used as a starting point for more robust parameter estimation based on constrained non-linear programming, with the objective function  $S$  consisting in the squared sum of errors across experimental conditions:

$$S = \sum_{t=1}^{t_{sim}} \sum_{n=1}^N \sum_{c=1}^C \left( \frac{x_{pred}(c, i, t) - x_{exp}(c, i, t)}{x_{data}(c, i, t)} \right)^2 \quad (7.27)$$

where  $t_{sim}$  is the maximal simulation time,  $N$  the number of state variables used for optimization and  $C$  the number of experimental conditions being optimized.

Table 7.2 presents the optimized parameters as well as the parameter bounds used.

**Table 7-2:**Model parameter values

| Parameter       | Optimized Value                      | Bounds                        | Source/Explanation                                                                                                                                                                                                                                                                |
|-----------------|--------------------------------------|-------------------------------|-----------------------------------------------------------------------------------------------------------------------------------------------------------------------------------------------------------------------------------------------------------------------------------|
| $K_{perm}$      | $4e-3 \text{ s}^{-1}$                | [1e-2 1e-1]                   | Adapted from (260),<br>$K_{perm} = P \left( \frac{cm}{s} \right) * 10^{-3} \left( \frac{L}{cm^3} \right) * A(cm^2) * 5 * 10^9 \frac{cells}{L}$ with<br>$P = 10^{-5}$ , $A = 7.85 * 10^{-5}$<br>corresponding to 10 $\mu\text{m}$ diameter cell and $5*10^6 \text{ cells.mL}^{-1}$ |
| $V_{MitProd}$   | $1.2e-6 \text{ } \mu\text{M s}^{-1}$ | 1.2e-6                        | SS analysis: $V_{MitProd} = k_{scav} * ROS_{cyt}$                                                                                                                                                                                                                                 |
| $V_{nox}$       | $1e-6 \text{ } \mu\text{M s}^{-1}$   | [1e-7 1e-4]                   | Physiological levels of $IP_3$ after T cell stimulation                                                                                                                                                                                                                           |
| $K_{nox}$       | $5 \text{ } \mu\text{M}$             | [1 8]                         |                                                                                                                                                                                                                                                                                   |
| $V_{duox}$      | $1e-6 \text{ } \mu\text{M s}^{-1}$   | [1e-7 1e-4]                   | Physiological levels of cytosolic $Ca^{2+}$ after T cell stimulation                                                                                                                                                                                                              |
| $K_{duox}$      | $0.15 \text{ } \mu\text{M}$          | [0.05 1]                      |                                                                                                                                                                                                                                                                                   |
| $k_{scav}$      | $1.2e-3 \text{ s}^{-1}$              | 1.2e-3                        | calculated from (260)                                                                                                                                                                                                                                                             |
| $K_{ERperm}$    | $4e-2 \text{ } \mu\text{M}$          | [0.1 1e-4]                    | Assuming $[ERO1\alpha] = 0.05 \text{ uM}$ ,<br>$V_{ero1} = 0.082(s^{-1}) *$<br>$ERO1\alpha(\mu M)$ (397)                                                                                                                                                                          |
| $ROS_{cytinit}$ | $0.0015 \text{ } \mu\text{M}$        | [0.001 0.05]                  |                                                                                                                                                                                                                                                                                   |
| $V_{ero1}$      | $3e-3 \text{ } \mu\text{M s}^{-1}$   | [1e-4 1e-2]                   | ER ROS levels > steady-state                                                                                                                                                                                                                                                      |
| $K_{ero1}$      | $95 \text{ } \mu\text{M}$            | [85 120]                      | Computed at SS with respect to<br>$J_{ERprod}$                                                                                                                                                                                                                                    |
| $nprod$         | 3                                    | [1 6]                         |                                                                                                                                                                                                                                                                                   |
| $k_{ERscav}$    | $5.45e-5 \text{ s}^{-1}$             | $5.45e-5 \text{ s}^{-1}$      | Physiological ER $Ca^{2+}$ levels                                                                                                                                                                                                                                                 |
| $K_{ERscav}$    | $280 \text{ } \mu\text{M}$           | [150 350]                     | Ch. 5                                                                                                                                                                                                                                                                             |
| $nscav$         | 2                                    | [1 6]                         |                                                                                                                                                                                                                                                                                   |
| $V_{IP3}$       | $1.626 \text{ s}^{-1}$               | [1 2]                         | Ch. 5                                                                                                                                                                                                                                                                             |
| $K_{act}$       | $0.16 \text{ } \mu\text{M}$          | $0.16 \text{ } \mu\text{M}$   |                                                                                                                                                                                                                                                                                   |
| $K_{IP3}$       | $0.2915 \text{ } \mu\text{M}$        | [0.1 5] $\mu\text{M}$         | Modulated from $0.106 \text{ } \mu\text{M}$ (Ch. 5)                                                                                                                                                                                                                               |
| $k_{IP3ros}$    | $0.0442 \text{ } \mu\text{M}$        | $0.0442 \text{ } \mu\text{M}$ | Fitted from (327) assuming $1 \text{ } \mu\text{M}$ thimesoral results in generation of $10 \text{ nM } ROS_{cyt}$ .                                                                                                                                                              |
| $nrosIP3$       | 0.462                                | 0.462                         |                                                                                                                                                                                                                                                                                   |
| $K_{inh}$       | $1 \text{ } \mu\text{M}$             | $1 \text{ } \mu\text{M}$      | 1 (291)                                                                                                                                                                                                                                                                           |
| $K_{IP3inh}$    | $0.771 \text{ } \mu\text{M}$         | [0.5 1.5] $\mu\text{M}$       | 1.05 (291)                                                                                                                                                                                                                                                                        |
| $A$             | 0.0917                               | [0.01 0.5]                    | Ch. 5                                                                                                                                                                                                                                                                             |

Table 7-2 continued:

| Parameter      | Optimized Value                      | Bounds                                                  | Source/Explanation                                                                      |
|----------------|--------------------------------------|---------------------------------------------------------|-----------------------------------------------------------------------------------------|
| $K_{ERleak}$   | $0.003 \text{ s}^{-1}$               | $[0.001 \text{ } 0.005] \text{ s}^{-1}$                 | Ch. 5                                                                                   |
| $V_{serca}$    | $233.75 \text{ } \mu\text{M s}^{-1}$ | $[85.8 \text{ } 300] \text{ } \mu\text{M s}^{-1}$       | Modulated from 85.8 (Ch.5)                                                              |
| $K_{serca}$    | $0.4477 \text{ } \mu\text{M}$        | $0.4477 \text{ } \mu\text{M}$                           | Ch. 5                                                                                   |
| $k_{sercaros}$ | $1.151 \text{ } \mu\text{M}$         | $1.151 \text{ } \mu\text{M}$                            | Fitted from (110), assuming the                                                         |
| $nsercaros$    | 0.38                                 | 0.38                                                    | SERCA pump is exposed to<br>$\text{ROS}_{\text{cyt}}=10^{-3}*(\text{ROS}_{\text{ext}})$ |
| $V_{mitin}$    | $794.07 \text{ } \mu\text{M s}^{-1}$ | $794.07 \text{ } \mu\text{M s}^{-1}$                    | Ch. 5                                                                                   |
| $K_{mitin}$    | $1.24 \text{ } \mu\text{M}$          | $1.24 \text{ } \mu\text{M}$                             | Ch. 5                                                                                   |
| $V_{mitout}$   | $484.44 \text{ } \mu\text{M s}^{-1}$ | $484.44 \text{ } \mu\text{M s}^{-1}$                    | Ch. 5                                                                                   |
| $K_{mitout}$   | $8.1285 \text{ } \mu\text{M}$        | $8.1285 \text{ } \mu\text{M}$                           | Ch. 5                                                                                   |
| $V_{crac}$     | $3.1046 \text{ } \mu\text{M s}^{-1}$ | $[1 \text{ } 10] \text{ } \mu\text{M s}^{-1}$           | Ch. 5                                                                                   |
| $K_{soc}$      | $996.83 \text{ } \mu\text{M}$        | $[200 \text{ } 1500] \text{ } \mu\text{M}$              | Ch. 5                                                                                   |
| $K_{stim}$     | $195.73 \text{ } \mu\text{M}$        | $195.73 \text{ } \mu\text{M}$                           | Ch. 5                                                                                   |
| $K_{PMleak}$   | $2.5\text{e-}7 \text{ s}^{-1}$       | $[1.5\text{e-}7 \text{ } 3.5\text{e-}7] \text{ s}^{-1}$ | Ch. 5                                                                                   |
| $V_{pmca}$     | $4.96 \text{ } \mu\text{M s}^{-1}$   | $[1.5 \text{ } 10] \text{ } \mu\text{M s}^{-1}$         | Modulated from 1.805 (Ch. 5)                                                            |
| $K_{pmca}$     | $0.1269 \text{ } \mu\text{M}$        | $0.1269 \text{ } \mu\text{M}$                           | Ch. 5                                                                                   |
| $K_{STIMpmca}$ | $394 \text{ } \mu\text{M}$           | $394 \text{ } \mu\text{M}$                              | Ch. 5                                                                                   |
| $k_{pmcaros}$  | $0.258 \text{ } \mu\text{M}$         | $0.258 \text{ } \mu\text{M}$                            | Fitted from (395), assuming the                                                         |
| $npmcaros$     | 1.147                                | 1.147                                                   | SERCA pump is exposed to<br>$\text{ROS}_{\text{cyt}}=10^{-3}*(\text{ROS}_{\text{ext}})$ |
| $\rho_{er}$    | 0.015                                | 0.015                                                   | (312)                                                                                   |
| $\rho_{mit}$   | 0.08                                 | 0.08                                                    | (312)                                                                                   |
| $\beta_i$      | 0.1678                               | 0.1678                                                  | Ch 5.                                                                                   |
| $\beta_{er}$   | 0.0467                               | 0.0467                                                  | Ch. 5                                                                                   |
| $\beta_{mit}$  | 0.716                                | 0.716                                                   | Ch. 5                                                                                   |

We included in this model Nox and Duox as sources of ROS production that are activated during T cell signaling. Because the datasets used to fit Module 1 are primarily related to ER redox balance and the effect of  $\text{Ca}^{2+}$  depletion on the ER redox status and not to ROS effects on a  $\text{Ca}^{2+}$  time course after T cell stimulation, the confidence on those parameters is very low. Additional optimization on experimental  $\text{Ca}^{2+}$  time course in the presence of NADPH oxidase inhibitors and combinations of  $\text{Ca}^{2+}$  channels and pumps

inhibitors are required to improve the confidence in the parameters and the quality of the fits.

We opted for an alternative approach for model validation. ROS-Ca<sup>2+</sup> cross-talk occur on different timescales based on various fluxes and affinities to the second messengers; therefore, the measured output to a step or impulse is the sum of simultaneous events occurring over a range of timescales. Usual time course analysis techniques do not easily discriminate these events and their respective contribution. The engineering community has long applied frequency response methodologies to address time-varying processes in mechanical and electrical systems. This methodology is only valid on linear systems, which is not the case with biological systems. For instance, saturation of an enzyme is an example of non-linear behavior. However, if a system operates close to its operating point or with small perturbations, it will behave as a linear system. As a first approximation, we will make the assumption that using small amplitude stimuli will not drive our biological system to saturation and hence be able to analyze it in the frequency domain. Coherence analysis can be performed to validate the frequency range in which the system is linear.

#### **7.2.5. Frequency Response Analysis**

Frequency response analysis is a method where the behavior of a system is characterized by its response to sinusoidal input signals. It relies on the decomposition of an input and output signal into its principal frequency components and the comparison of the output signal to the input in the frequency domain. Importantly, this technique does not require prior knowledge of the system.

Briefly, any signal can be decomposed as a sum of sine waves via Fourier transform. The Fourier coefficient,  $\hat{R}(w)$  of a signal  $\hat{R}(t)$ , at the angular input frequency  $w$  can be described as:

$$\hat{R}(w) = \frac{2}{nT} \int_0^{nT} e^{-i\omega t} R(t) dt \quad (7.28)$$

where  $\frac{2\pi}{\omega}$  is the period of the input signal and  $n$  the number of periods sampled.

The result of this integral is a complex number whose norm  $|\hat{R}(w)|$  corresponds to the amplitude of the output signal and whose argument  $\arg(\hat{R}(w))$  is 90 degrees below the output phase at frequency  $w$ .

Traditionally the frequency response of a system is assessed by measuring the output response to sinusoids of a given amplitude and different frequencies. The ratio of the amplitude of the output to the amplitude of the input represents the gain of the system. The time delay between the input and output signal corresponds to the phase of the system. Gain and phase of a system over a range of frequencies provides sufficient information to characterize the system's frequency-dependence and can be displayed in Bode plots.

The Bode plots provide direct insight into the dynamic behavior of the system. The gain plot presents the system's response to a perturbation at different timescales, in particular the frequency filtering properties of the system. The phase plot contains additional information about the way in which the system acts when connected to other systems, in cascade or in the presence of feedback, as well as delays.

Bode plots are generally constructed by experimentally probing a physical system. Although experimentally probing the response of a biological system to stimuli of different periods has been used in the past on bacteria (361, 362) and yeast (135, 136, 363, 398), technical hurdles make it difficult to apply it to mammalian cells. An alternative approach is to build the Bode plots *in silico* and use these modeling predictions as a tool to guide experimental validation using a selected few frequencies to probe.

Once in Bode plot form, it is possible to fit a mathematical description to the system's behavior. This mathematical representation takes the form of a transfer function. In the Laplace domain  $\mathcal{L}$ , it can be described as:

$$H(s) = \frac{Y(s)}{U(s)} = \frac{\mathcal{L}\{y(t)\}}{\mathcal{L}\{u(t)\}} = K \frac{\prod_m s + z_m}{\prod_n s + p_n} \quad (7.29)$$

where  $Y(s)$  is the Laplace transform of the output signal  $y(t)$ ,  $U(s)$ , the Laplace transform of the input signal  $u(t)$ ,  $m$ , the number of zeros in the nominator and  $n$ , the number of poles in the denominator with  $m \leq n$ .  $z_m$  and  $p_n$  correspond respectively to the zeros and poles of the system. When evaluated at  $s = i\omega$ , the Laplace transform yields the Fourier transform and  $H(i\omega)$  the frequency response of the system at this frequency.

It is also possible to evaluate the form of the transfer function based on the mechanistic ODE description of the system by linearizing around the operating point of the system. In this case, all poles and zeros of the transfer function are a function of the ODE model kinetic parameters and the Bode plots can be generated from the symbolic



version of the transfer function. Although extremely useful for simpler systems, this methodology is not adequate for complex systems with highly non-linear differential equations. Thus we chose the reverse approach of determining the Bode plots by probing our ODE system to periodic inputs and backcalculating the transfer function. This technique offers an additional advantage: the transfer function fitted to the Bode plots contains parameters that generally do not have a physical meaning; however it is often possible to find a description in the frequency domain with fewer parameters compared to the model in the time domain.

Systems identification is a common control-based approach to build mathematical models of dynamical systems. Most systems identification methods rely on statistical methods to fit parameters to a model structure. In our case, we attempt to fit a transfer function of the form presented in (7.29) to the *in silico* computed Bode plots. Before any fitting is attempted, the form of the transfer function must be specified. Corner frequencies correspond to the presence of a zero or pole (Appendix E.S1 for an example on a second order low-pass filter). The slope between these corner frequencies corresponds to the difference between the orders of the denominator and nominator of the transfer function ( $n - m$ ) for the zeros and poles with values below the specified corner frequency. For instance, a slope of -20 dB/decade would correspond to  $(n - m) = 1$ , while -40dB/decade would correspond to  $(n - m) = 2$ . Once the transfer function's mathematical form has been specified, we fitted the parameter values (zeros and poles) using non constrained optimization algorithms based on gradient search methods (fminsearch).

### 7.3. Results & Discussion

#### 7.3.1. Cellular redox status affects $\text{Ca}^{2+}$ response to T cell stimulation by $\alpha\text{-CD}_3$ and $\text{H}_2\text{O}_2$

$\text{Ca}^{2+}$  channels and pumps have been shown to be redox-sensitive *in vitro* and *in vivo* assays (103-105, 108-110, 327, 376, 377, 388-395). However, most of these assays have been performed in excitable cell types with large concentrations of exogenous  $\text{H}_2\text{O}_2$ . To verify if ROS plays a physiological role in Jurkat T cell signaling, we measured  $\text{Ca}^{2+}$  dynamics in response to TCR stimulation in the presence of various ROS inhibitors (Figure 7.2).

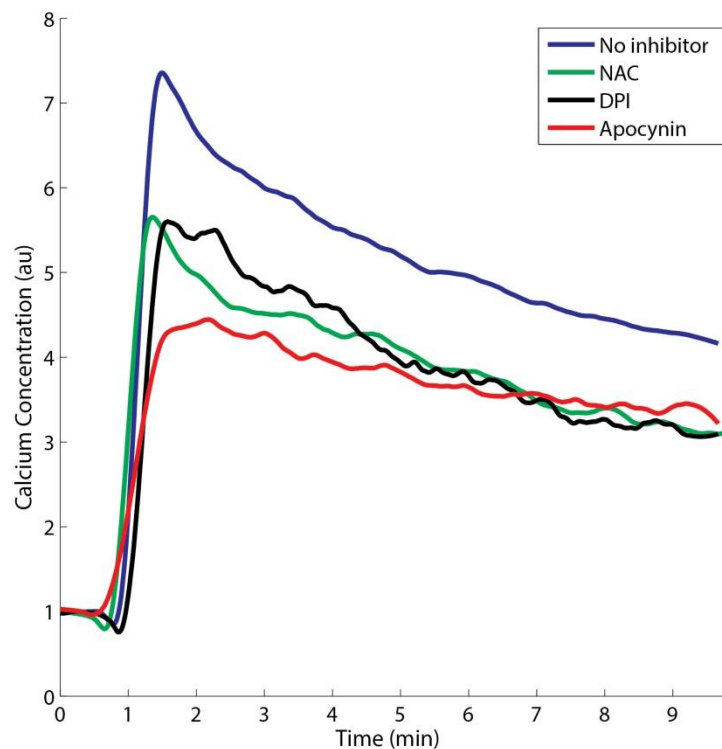


**Figure 7-2:** Average traces of  $\text{Ca}^{2+}$  dynamics following TCR stimulation with 2  $\mu\text{g/mL}$   $\alpha\text{-CD}_3$  in no inhibitor condition (blue), 5mM NAC (green), 2  $\mu\text{M}$  DPI (black) and 10  $\mu\text{M}$  Apocynin (red). (n=3)

Compared to the no inhibitor condition, the addition of N-acetylcysteine (NAC), a precursor of intracellular cysteine and GSH that acts like a non-specific cytosolic ROS buffer, and of DPI and apocynin, two specific NADPH oxidase inhibitors result in an overall decrease of  $\text{Ca}^{2+}$  signaling. Both the amplitude of the signal and the sustained  $\text{Ca}^{2+}$  levels are reduced, suggesting a ROS-dependent effect on  $\text{IP}_3$  release and SOCE. These results also suggest the importance of early ROS production by NADPH oxidases after TCR stimulation to promote signaling. Compared to NAC inhibition, the decay time constant (defined as in Chapter 5) is also altered, suggesting inhibition of the SERCA pump. These results are consistent with the recent findings of Kwon *et al.* who observed inhibition of SOCE in  $\text{Duox1}^{-/-}$  Jurkat cells (108). Contrary to antioxidant treatment, addition of low amounts of  $\text{H}_2\text{O}_2$  (25  $\mu\text{M}$ ) results in increased cytosolic  $\text{Ca}^{2+}$  levels (Appendix E.S2). Pretreatment with the external  $\text{Ca}^{2+}$  chelator EGTA or the non-specific cation channel blocker flufenamic acid (FFA) slightly reduces the signal while pretreatment with TMB-8, an  $\text{IP}_3\text{R}$  inhibitor completely abrogates the signal. These results suggest an initial effect of oxidation on the  $\text{IP}_3\text{R}$  that will in turn trigger SOCE. We observed smaller effects of oxidation on extracellular  $\text{Ca}^{2+}$  influx.

Because of the complexity of the  $\text{Ca}^{2+}$  signaling pathway and the number of simultaneous interconnected fluxes that occur, experimentally determining the effect of ROS on  $\text{Ca}^{2+}$  signaling requires a large number of additional experiments using chemical inhibitors and knock-down cell lines. We chose computational modeling as an alternative approach to investigate hypothetical features of cross-talk occurring between  $\text{Ca}^{2+}$  and ROS in T cells in the resting state and during stimulation.

### 7.3.2. Computational Model of Ca<sup>2+</sup>/ROS cross-talk

This model of Ca<sup>2+</sup>/ROS cross-talk is based upon the Ca<sup>2+</sup> signaling model described in Chapter 5 with an additional module of ROS homeostasis in the ER and cytoplasmic compartment. In addition, fluxes through redox-sensitive Ca<sup>2+</sup> channels and pumps are modulated by ROS levels to reflect the effect of an oxidative environment on Ca<sup>2+</sup> levels. The final model contains 7 ordinary differential equations and 48 parameters, divided into two tightly interconnected modules. Because we optimized most of the parameters of the Ca<sup>2+</sup> module in Chapter 5, we focused parameter optimization on the ROS homeostasis module and while constraining the Ca<sup>2+</sup> parameters (Table 7.2). The ROS module can be further subdivided into two semi-independent submodules consisting of the cytoplasmic and ER compartments. In the cell, these two compartments are largely insulated; the cell maintains a rather reduced redox level in the cytosol while a highly oxidizing environment is necessary in the ER for proper protein folding. The primary connection between those two modules is a unidirectional ROS flux from the cytosol to the ER when cytosolic ROS levels are above a threshold. Figure 7.3 depicts the ability of the cell to respond to the exogenous addition of DTT followed by a wash step and bolus of H<sub>2</sub>O<sub>2</sub>. The experimental values were digitized from the measurements of Enyedi *et al.*, acquired with a novel H<sub>2</sub>O<sub>2</sub> specific-fluorescent protein targeted to the ER (382). This model can also predict Ca<sup>2+</sup> dynamics in the ER and cytoplasm after a bolus addition of H<sub>2</sub>O<sub>2</sub> and shows rapid depletion of the ER Ca<sup>2+</sup> stores (Appendix E.S3).

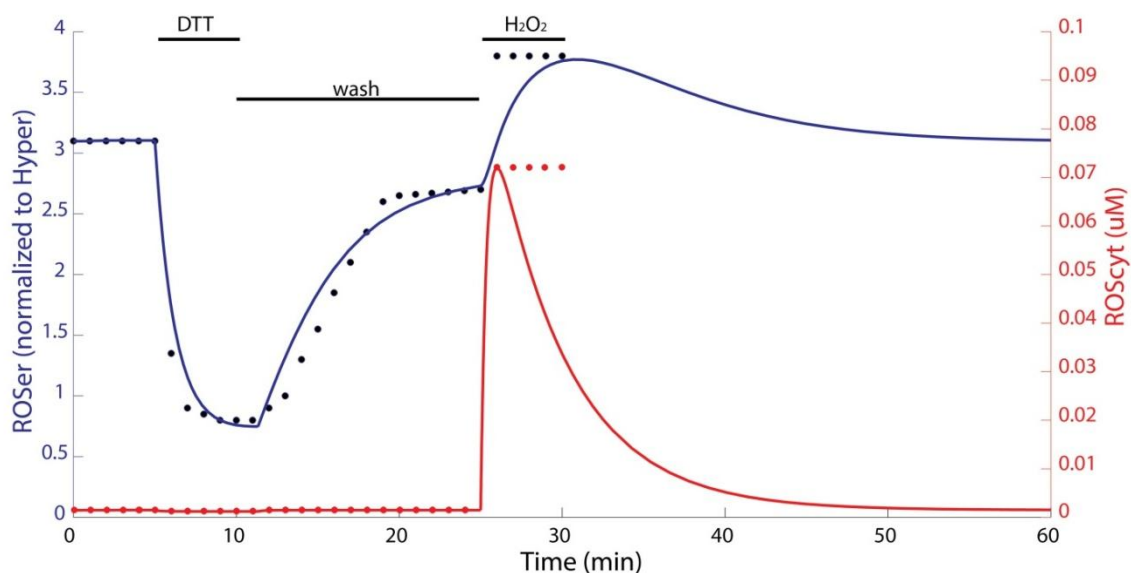


**Figure 7-3:** Cell response to 5 min perfusion with DTT (modeled as an 8-fold increase in the cytosolic and ER scavenging rate). DTT was then washed out of the medium for 15 min (modeled as a return to 1.2\*baseline cytosolic and ER scavenging rate) and 100  $\mu\text{M}$  H<sub>2</sub>O<sub>2</sub> was applied. In blue, ROS levels in the ER. In red, cytoplasmic ROS levels. Digitized experimental data are taken from (382). Model is fitted to the ER ROS levels. Cytoplasmic levels are predicted.

The model can recapitulate the drop in ER ROS due to ER Ca<sup>2+</sup> depletion observed by Enyedi *et al.* (382) assuming that the scavenging rate alone depends on luminal Ca<sup>2+</sup> levels (Figure 7.4). The reduction in ROS ER levels in the model are not as pronounced as in the experimental data probably because of a model constraint that does not allow ER Ca<sup>2+</sup> to drop below 200  $\mu\text{M}$ . Model predictions for the levels of cytoplasmic ROS, Ca<sup>2+</sup> and ER Ca<sup>2+</sup> are presented in the Appendix E.S4 and E.S5.

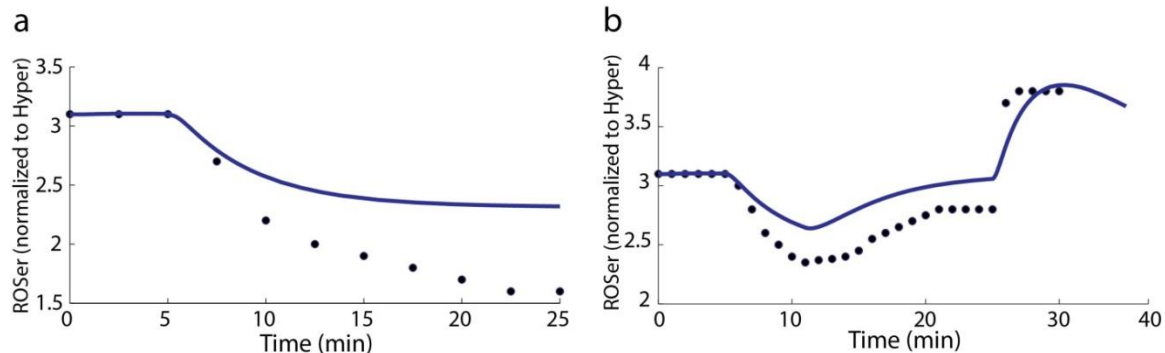


**Figure 7-4:** ER ROS levels after  $\text{Ca}^{2+}$  release from the ER intracellular stores. a) in response to thapsigargin treatment (modeled as a 85% reduction in SERCA maximal velocity). b) in response to histamine treatment followed by a bolus of 100  $\mu\text{M}$   $\text{H}_2\text{O}_2$  (histamine treatment modeled as a pulse of 5  $\mu\text{M}$   $\text{IP}_3$  between 5 and 10 min). Treatment time is at 5 min. Digitized experimental data are taken from (382).

To further optimize and validate the model, we applied the frequency response analysis methodology described above and generated *in silico* the system's output to sinusoidal stimuli of various frequencies. Because the output measured experimentally is cytoplasmic  $\text{Ca}^{2+}$ , details of the frequency response for this variable is described in the main text. Time courses and frequency response of the other species are described in the Appendix E.S6-10.

### 7.3.3. $\text{Ca}^{2+}$ /ROS cross-talk model frequency response

To generate the frequency response of the system, we applied *in silico* a sinusoidal wave of 25  $\mu\text{M}$  ROS of various periods. We chose a small ROS concentration to allow the system to stay in a relatively linear range. Each simulation was run for 18 periods, with a minimum of 250 sample timepoints by period (set in the ODE solver).

$\text{Ca}^{2+}$  time course response to a sinusoidal input of ROS with a 10 min period (corresponding to 1.7 mHz frequency) is represented in Figure 7.5. After a brief transient, cytoplasmic  $\text{Ca}^{2+}$  settles in a sinusoidal pattern of its own. The  $\text{Ca}^{2+}$  oscillation period is conserved.

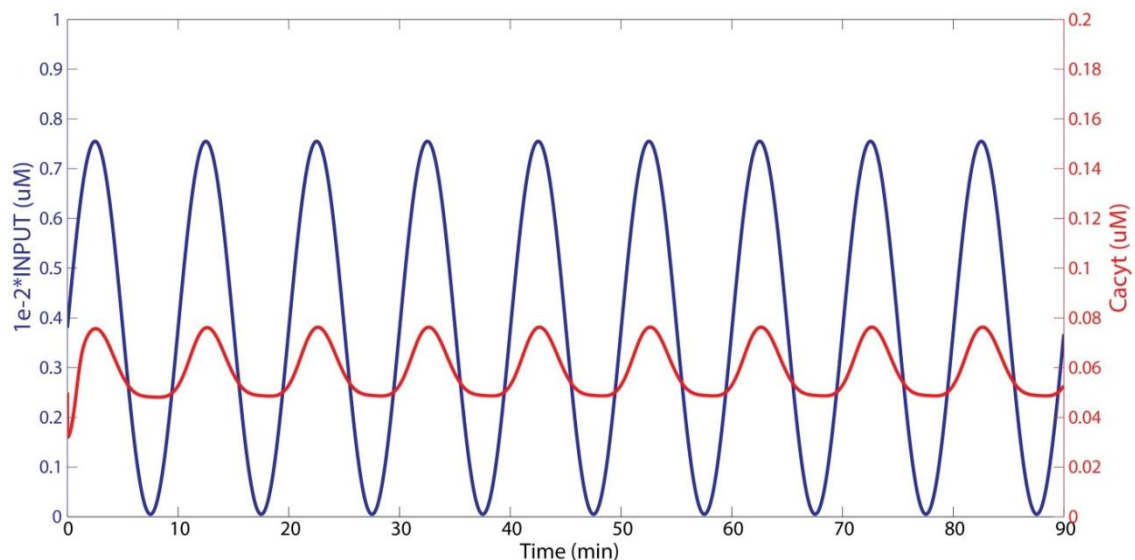


**Figure 7-5:** Transient response of cytosolic  $\text{Ca}^{2+}$  in response to a 10 min period ROS input. When compared across different periods of input stimuli,  $\text{Ca}^{2+}$  response in the time domain exhibits time delays and lower steady state amplitude for shorter periods (Figure 7.6). For instance, the 30 second period exhibits a 45deg phase shift between the input and output. At 10 minutes and 60 minutes both signals are in phase and share the same steady state concentration. These time courses suggest that the bandwidth of the system for cytoplasmic  $\text{Ca}^{2+}$  is between 30 seconds and 10 minutes. Time courses for the other species at different periods are depicted in Appendix E.S6-10.

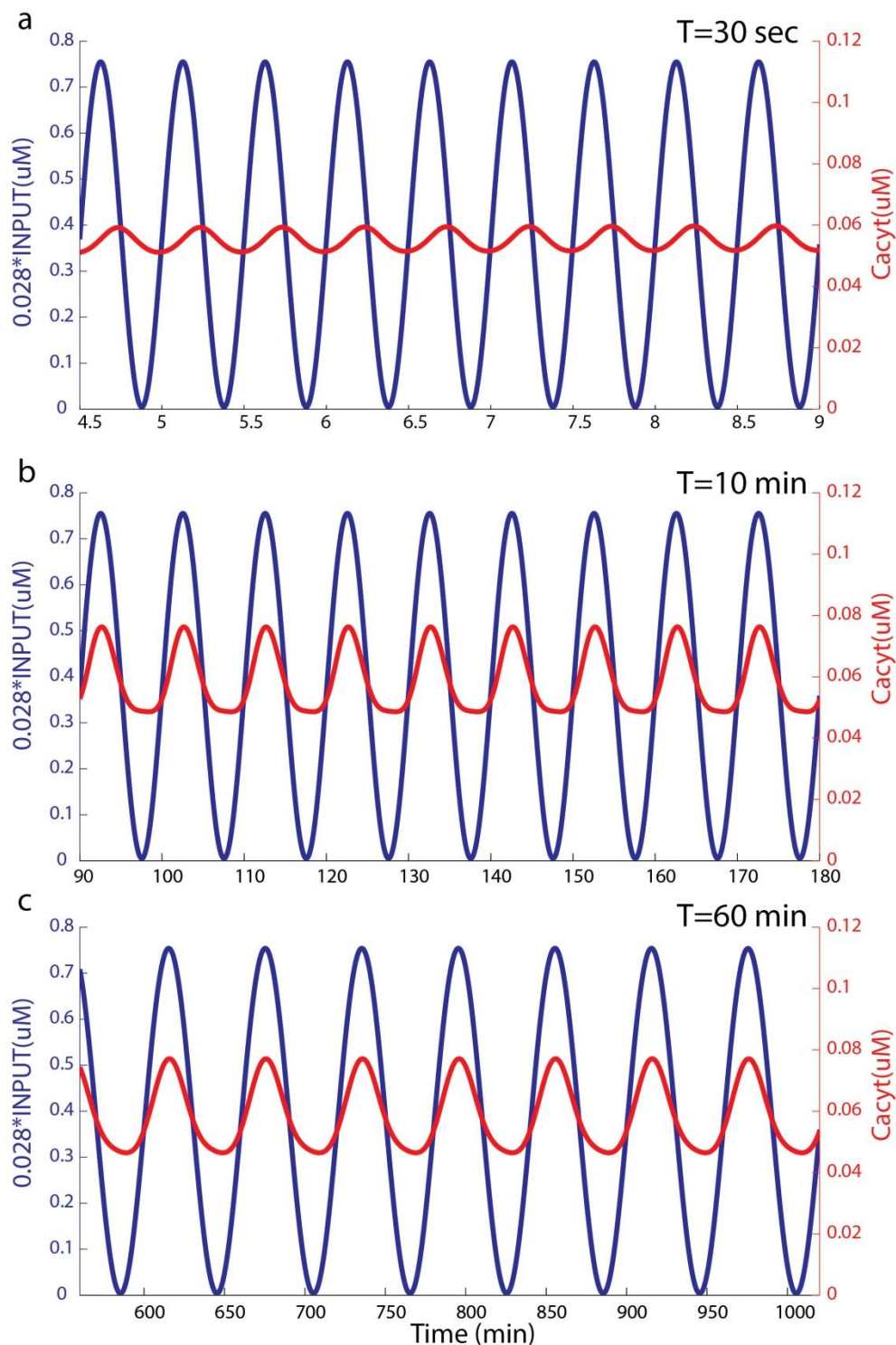


**Figure 7-6:** Cytosolic  $\text{Ca}^{2+}$  in response to ROS stimulus input of different periods. a) 30 second period. b) 10 minutes period. c) 1 hour period. Note the time scales on the x axis are different.

From these time courses, several interesting features emerge. In addition to a change in the amplitude and phase shift with frequency, we observe that the ER displays



highly non-linear behavior and functions as an integrator that accumulates the input signal over time (e.g. at 30 seconds). In addition, the output response of several species to the sinusoidal input is a periodic signal with the same frequency but not the same shape. This is particularly visible with ER  $\text{Ca}^{2+}$ ; however it is also the case with cytoplasmic  $\text{Ca}^{2+}$  at lower frequencies, which suggests non-linearity of the system with the addition of new frequency components.

As an initial approach, we used these time courses and their Fourier transform to generate the Bode plots (Figure 7.7).

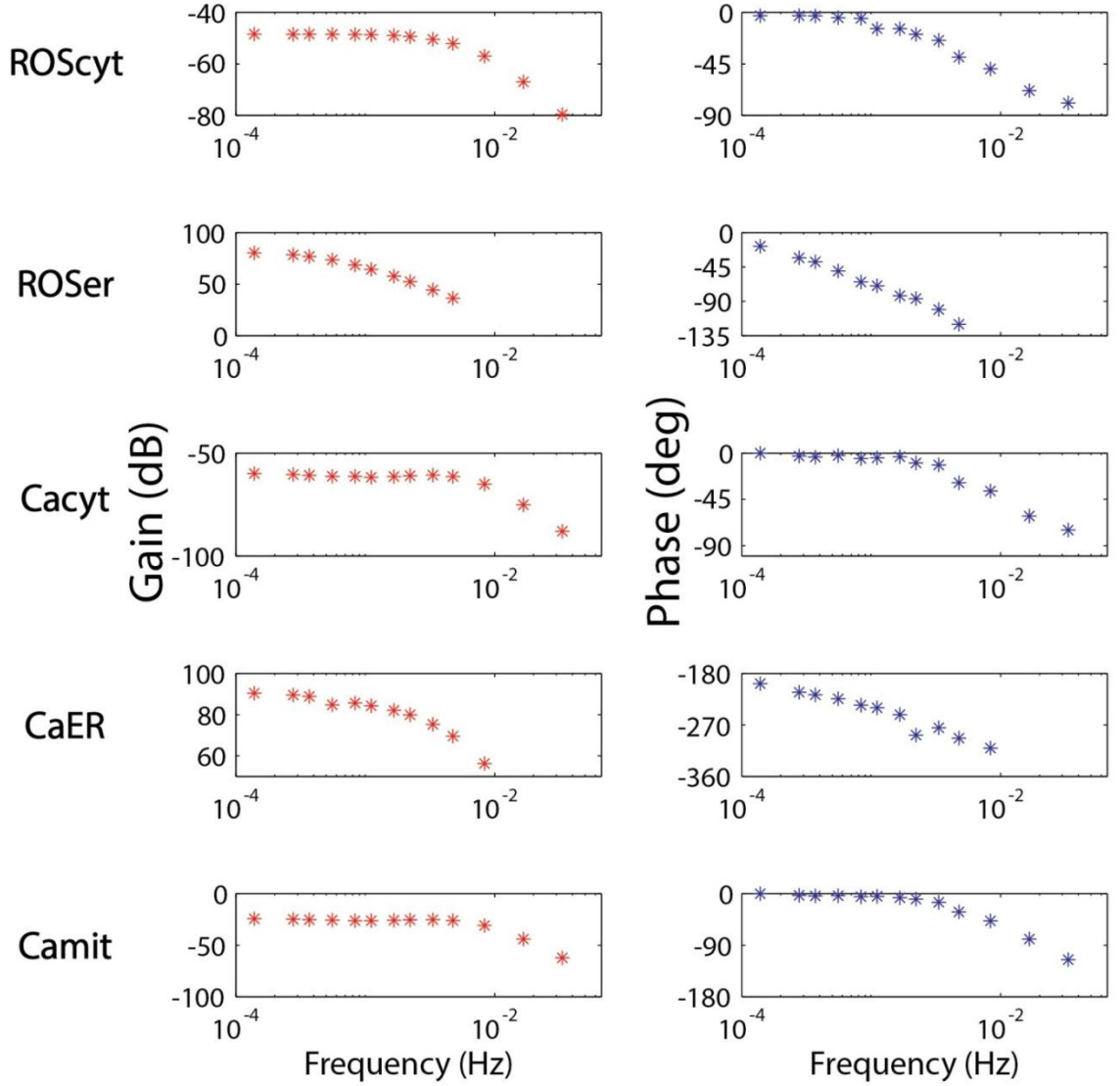


**Figure 7-7:** Bode plots of the multiple output system. In red, the gain of the system is displayed. In blue, the phase plot is displayed. Frequencies for which an output displayed a non-steady linear behavior is not displayed here.

From these Bode plots, we note that the ROS buffering capacity in the cytosol behaves like a first order low-pass filter with a bandwidth of about 2 minutes. This behavior is closely followed by cytosolic  $\text{Ca}^{2+}$  with a slightly larger bandwidth. The mitochondrial  $\text{Ca}^{2+}$  behaves like a second order low-pass filter of similar bandwidth. This difference may arise from the very fast mitochondria buffering kinetics compared to the

cytoplasmic  $\text{Ca}^{2+}$  homeostatic system. Both  $\text{Ca}^{2+}$  and ROS ER components display higher order transfer functions.

As described earlier, a mathematical description of these Bode plots can be given as the transfer function. Figure 7.8 shows the transfer function for the output cytoplasmic  $\text{Ca}^{2+}$ .

The best fit is given by the following transfer function:  $H(s) = K \frac{1}{1+\tau s}$  where  $\tau$  is the cut-off frequency, here 10.6 mHz, and K the gain of the system, here  $K=0.05$ .

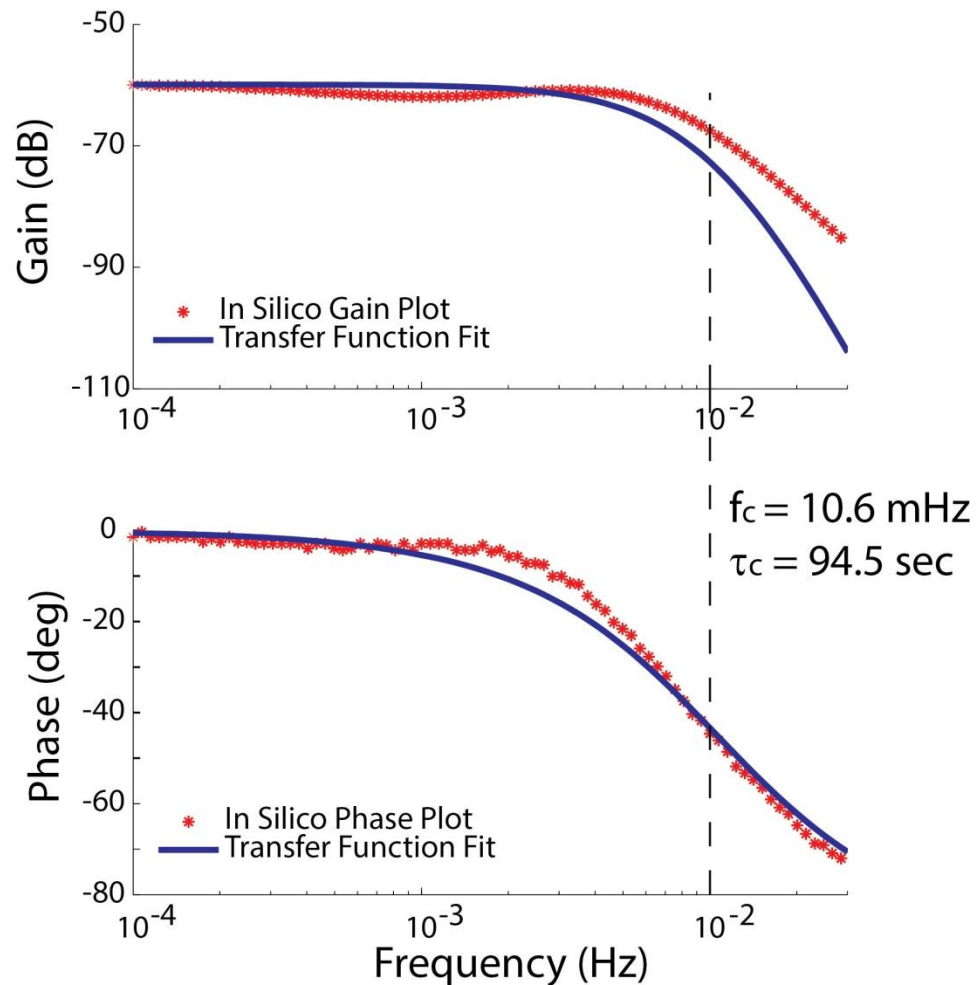


**Figure 7-8:** Fit of a first order transfer function for cytosolic  $\text{Ca}^{2+}$ . Gain  $K=0.05$ ; Corner frequency  $f_c = 10.6 \text{ mHz}$ .

This result suggests that a cell probed with exogenous ROS can follow the input stimulus if its period is greater than 1.5 minute. In terms of phase shift, at the 1.5 minute time

period, a 45deg phase shift will correspond in a 47 second delay. It is interesting to notice that such a complicated system can be reduced to a single parameter to describe the  $\text{Ca}^{2+}$  response to a specific input and be able to predict  $\text{Ca}^{2+}$  response to any kind of other ROS input shape. This feature of parameter reduction is a powerful motivation for utilizing the frequency response analysis for complex systems.

To test this model's predicted  $\text{Ca}^{2+}$  response to exogenous addition of ROS,  $\text{H}_2\text{O}_2$  must be measured. We chose to probe the system at different periods that would capture characteristics of the Bode plots, for instance, 30seconds, 1 minute, 2minutes, 5minutes, 10 minutes and 30 minutes. Delivering chemical pulses is not feasible with common techniques and requires the use of microfluidics to deliver controlled chemical waves.

#### **7.3.4. Generation and delivery of chemical pulses to Jurkat cells**

In the past three years, following the publication of the seminal papers using frequency response analysis to better understand signaling pathways in yeast, there has been a growing interest in creating tools able to deliver periodic signals (370, 371, 399, 400). When applied to biological systems, most designs to date have been focusing on delivering chemical waves to adherent cells. Our model cell line poses an additional challenge as these cells are non-adherent and will get washed away with fluids if not retained in a specific location over time. We presented in Chapter 6 a new microfluidic platform for single-cell imaging that traps very efficiently single cells in specific location in a dense array (323). We have also shown that a simple step input stimulus can be delivered to the cells. To deliver chemical pulses to the trapped cells, this microfluidic platform needs to be coupled with a microfluidic chemical pulse generator. Most designs

to date are not compatible with our microfluidic cell trap array because of the extremely low flowrates (2-5  $\mu\text{L}/\text{hour}$ ) required to avoid shear stress on the trapped cells. Off-chip components, such as pinch valves or switching valves, will create a well-defined pulse close to the valve but diffusion and Taylor dispersion in the tubing will smooth the plug, and the signals seen by the trapped cells will be an average of both solutions. Relying on laminar flow, it is possible to create chemical pulses by co-flowing two solutions and varying the flowrate of one versus the other automatically using a controllable syringe pump. Again, the low flowrates required lead to mixing by diffusion and large switching time. We used a simple alternative approach to create chemical waves in our microfluidic cell trap array by manually switching the inlet tubing connected to one of two solutions. Figure 7.9 shows the chemical signal, measured as FITC-BSA intensity delivered to the cells based on a theoretical input pulse (in blue) for different days and devices. The period of the signal is conserved with a maximal error of  $\pm 3\%$ . The presence of cells in the trapping area does not affect the quality of the pulses. For larger periods, the shape of the signal is maintained; however for higher frequencies, pulses become sinusoids because of diffusion. Device to device variability is significant (up to 20%); hence calibration of the device with a fluorescent solution is required after completion of a biological experiment (Appendix E.S11). Because of the slow flowrates and the combination of parallel and perpendicular flow in the trap array, there is an additional delay effect between the signal seen in the top and the bottom of the chamber (Appendix E.S12). Due to these limitations, this technique limits the frequency domain that can be experimentally probed to periods ranging from 6 minutes to 60 minutes.

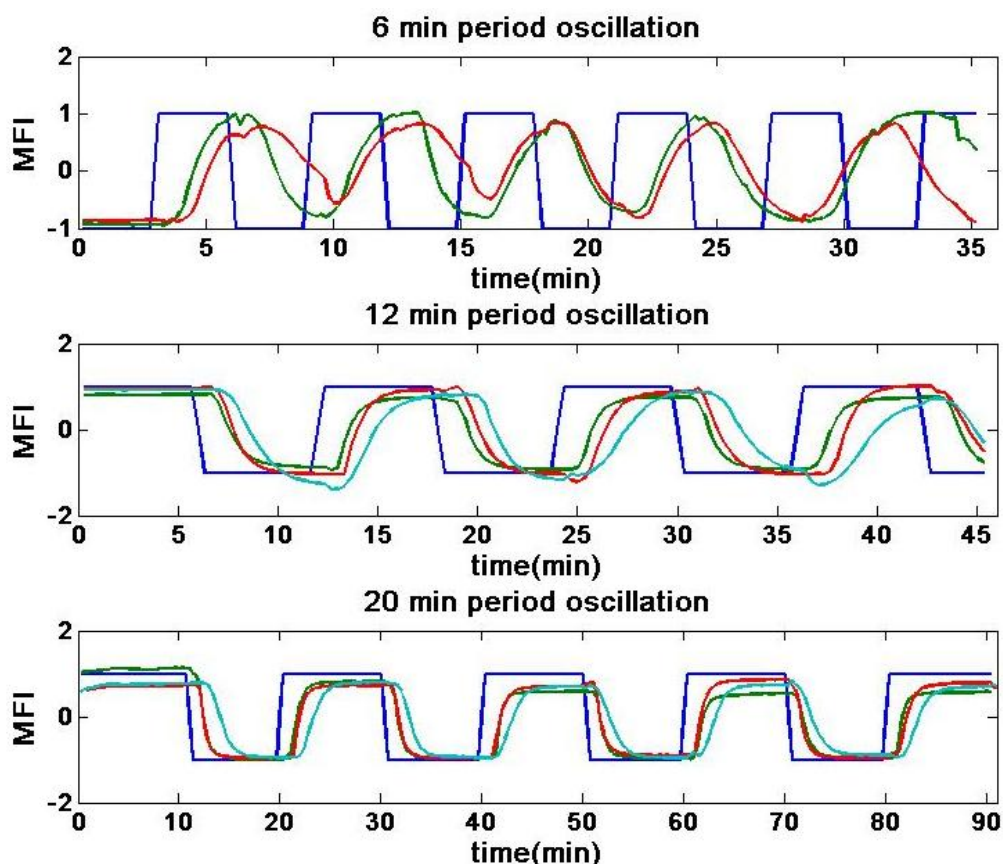


**Figure 7-9:** Characterization of on-chip chemical pulses. In blue is represented the theoretical or ideal input function. In other colors are represented the signals measured for 3 different devices for different input frequencies.

### 7.3.5. Cell response to a periodic input of $\text{H}_2\text{O}_2$

Figure 7.10 shows single-cell response to a 10 minute period application of 50  $\mu\text{M}$   $\text{H}_2\text{O}_2$ . Similar to our observations of Jurkat cell response to an ionomycin pulse (Chapter 6), there is a very large heterogeneity in cell response that includes a fraction of cells not responding to the stimulus. In average, cell response follows the input stimulus with a delay of 3 minutes for the first period; the magnitude of the delay keeps increasing with the number of periods. The average oscillation period of the averaged cell response is equal to 10.5 minutes, which is very close to the input signal period, given experimental errors in delivering the oscillations. In addition, the oscillations are

dampened (Figure 7.10a). At the single cell level, different patterns of behavior can be observed among responsive cells ranging from sustained oscillations to dampened oscillations or accumulation. The new steady state achieved as well as the phase shift between the single-cell response and the input greatly vary from cell to cell and does not correlate with cell position in the chip (Figure 7.10b). These large differences in amplitude and phase in single cell may arise from different mRNA copy numbers due to stochasticity in gene transcription (401) and consequently  $\text{Ca}^{2+}$  channel and pump levels. Fourier analysis of single cell traces shows that periodic stimulation shifts the basal cellular oscillation frequency of around 5 minutes to a slower oscillation frequency of about 16 minutes. This average has been computed by retaining the three major frequency components of the Fourier spectra for each single cell (Figure 7.10c).

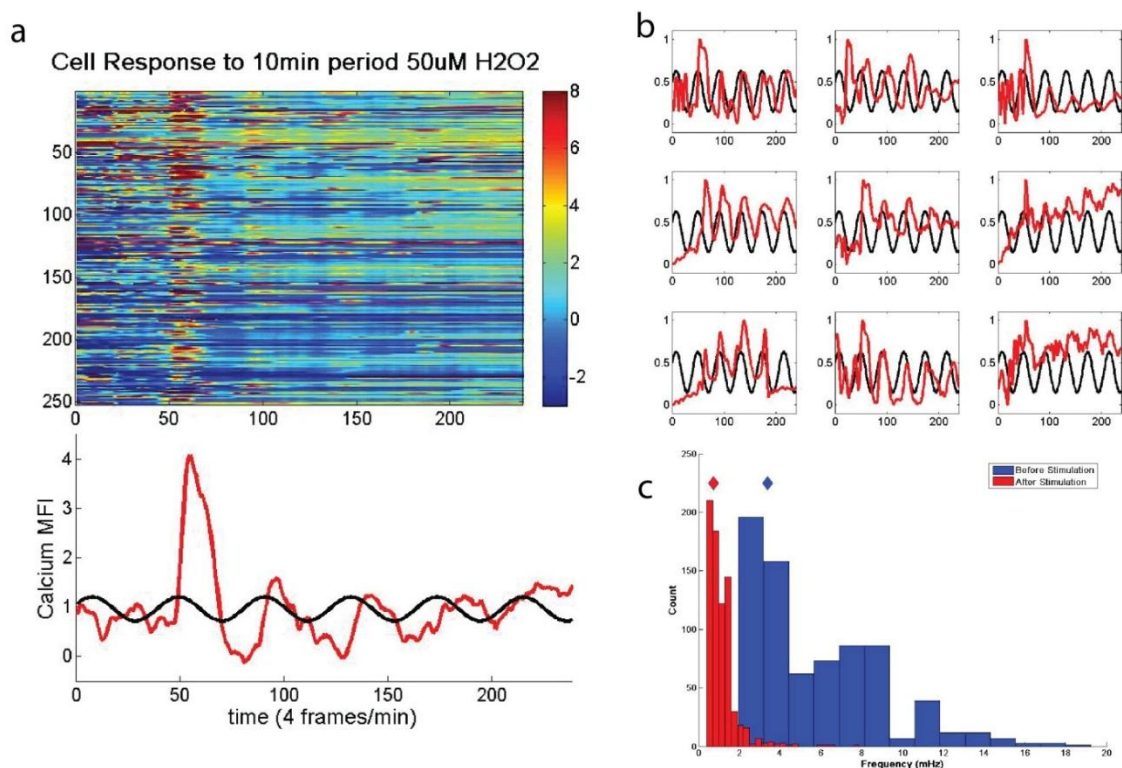


**Figure 7-10:** Single cell analysis of calcium responses to waves of  $\text{H}_2\text{O}_2$  (10 min period, 50  $\mu\text{M}$ ) and quantified for oscillations in fluorescence. a) Representation of experimental output from 250 cell traps. Each line is a time-dependent trace of fluorescence for a single cell.  $\text{H}_2\text{O}_2$  introduced at frame 50. The black line represents the input wave and the red line the average of cellular oscillations of the heatmap displayed above. b) Selected single cell traces (in red) and input signal (in black). c) Fourier transform of data showing distribution of basal (blue) and stimulated cell (red) frequencies for the 10 min period condition (1.7 mHz).

Based on this unique assayed frequency, there are large discrepancies between the model and the experimental data. For a 10 minute period oscillation, the model predicted a sinusoidal  $\text{Ca}^{2+}$  time course in phase with the input signal (Figure 7.8). Experimentally the  $\text{Ca}^{2+}$  time course is a periodic signal displaying ramping, dampened oscillations. Because the  $\text{Ca}^{2+}$  response is not sinusoidal, we further investigated if the concentration of 50  $\mu\text{M}$   $\text{H}_2\text{O}_2$  resulted in non-linear effects due to saturation. For this 10 minute period input signal, we varied the applied  $\text{H}_2\text{O}_2$  concentration from 25 to 1000  $\mu\text{M}$  (Figure 7.11). At the lowest concentration, the cells did not respond to the signal at all and



maintained their baseline spiking patterns. At the intermediate concentrations 50 and 200  $\mu\text{M}$ , the average cell response followed the input oscillation pattern with noticeable differences. Lower concentration results in higher phase shift and more pronounced transient behavior. The higher concentration leads to dampened oscillations around a steady-state while at the lower concentration, the oscillations - although dampened in amplitude - are integrating the input signal. At the highest concentration, 1mM  $\text{H}_2\text{O}_2$ , cells display a first peak of large amplitude and return to baseline.

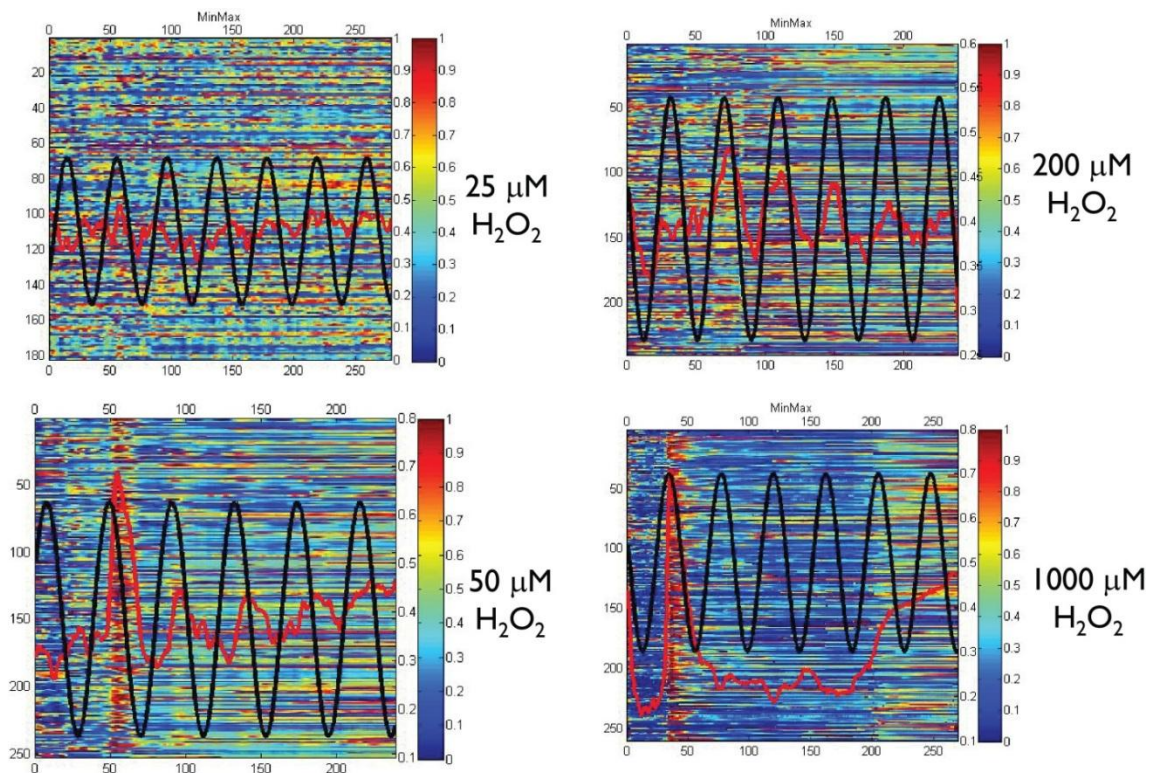


**Figure 7-11:** Impact of stimulus input amplitude on single cell response to a 10 minute period  $\text{H}_2\text{O}_2$  treatment. In black, the input signal. In red, the average cell response.

Non-linearities in the system were predicted by the model. We constructed the Bode plots of our system for input concentrations ranging from 8 to 200  $\mu\text{M}$  ROS (Figure 7.12 and Appendix E.S13). The model pointed to amplitude-related effects on the frequency response that are species dependent. For instance, frequency responses of ROS

in the cytosol and in the ER are not amplitude dependent (Appendix E.S13). On the other hand,  $\text{Ca}^{2+}$  frequency response is highly dependent on input amplitude in terms of gain but also bandwidth (Figure 7.12). Higher input concentration results in larger gain and bandwidth, suggesting the ability of the cell to filter high frequency, low amplitude ROS inputs, considered as noise by  $\text{Ca}^{2+}$  in the cell, and therefore preventing the elicitation of a cell response to noise. In contrast, at the input amplitude sampled, ROS does not have an amplitude-dependence, suggesting a higher sensitivity and large buffering system to clear out perturbances of various amplitudes. The shift in bandwidth with concentration was observed experimentally with the phase shift reduction between our 50 and 200  $\mu\text{M}$   $\text{H}_2\text{O}_2$  datasets.

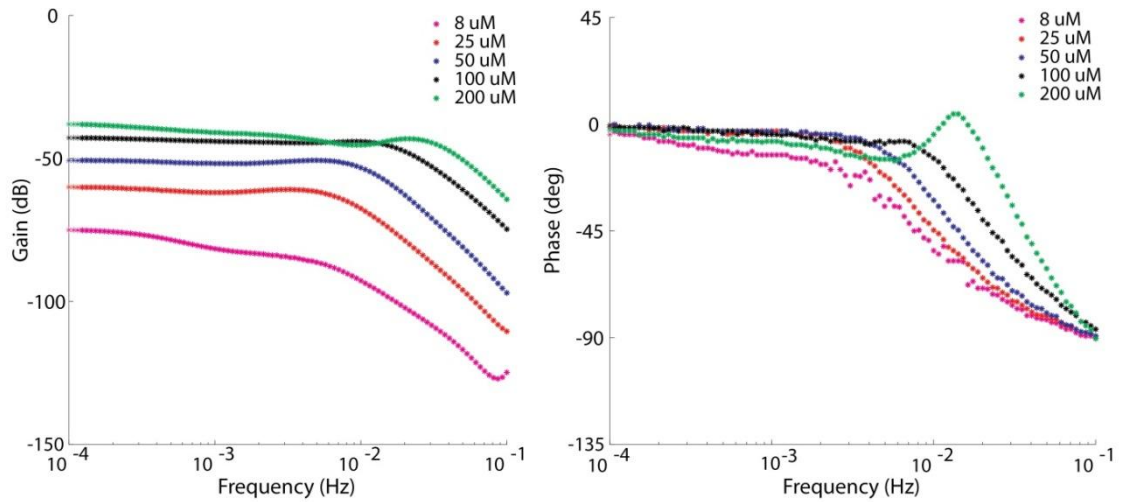


**Figure 7-12:** Effect of the input amplitude on cytosolic  $\text{Ca}^{2+}$  gain and phase.

#### **7.4. Conclusion**

Although the model can fit a subset of experimental data in the time domain, analysis of the network in the frequency domain show discrepancies between the experimental and modeling data. In particular, our experimental results indicate a higher

degree of non-linearity of the system than predicted by the model, suggesting errors in parameter values, inaccurate mathematical formulation of specific interactions or missing interactions in the network. For instance, this model does not take into account redox dependence of IP<sub>3</sub> formation, of Ca<sup>2+</sup>-binding protein to effectively buffer Ca<sup>2+</sup> in the cytosol and ER. We also did not explicitly model the impact of Ca<sup>2+</sup> buffering by the mitochondria on its ROS production. We also did not take into account the various isoforms of Ca<sup>2+</sup> channels and pumps expressed in T cell. Their relative levels as well as their differential redox sensitivities and Ca<sup>2+</sup> affinity may be a very important mechanism for the cell to regulate global Ca<sup>2+</sup> levels in the cell. Redox effects on SERCA are concentration and ROS dependent –between nitric oxide, superoxide and H<sub>2</sub>O<sub>2</sub>- with activation at low ROS levels (402) and deactivation at higher levels (108, 110); yet we only modeled all types of ROS as a single ROS species and did not take into account concentration-dependent activation and deactivation of the pump. The understanding of oxidation on proteins involved in the Ca<sup>2+</sup> signaling pathway is still in its infancy and large number of reports are contradictory (102, 371). When possible we used data acquired in T cells for lower levels of oxidation, however to be predictive in terms of signaling and response to oxidative stress, the ROS concentration dependence needs to be clearly formulated. Another important assumption in this model is that species are spatially uniformly distributed, which is physiologically not the case during signaling. ROS production for signaling purposes is believed to be heavily localized close to its targets, which results in very high concentrations in very specific microdomains. For example, co-localization of Duox1 with IP<sub>3</sub>R on the ER membrane (373) suggests that once Ca<sup>2+</sup> release from the ER stores have begun, some of these ions will bind to

Duox1's EF hands and lead to localized ROS production that will enhance IP<sub>3</sub>R activation. However, these ROS might not affect Ca<sup>2+</sup> channels on the plasma membrane. Similarly mitochondria-ER microjunctions, pivotal to Ca<sup>2+</sup> buffering during ER store depletion, might also play a role in increasing the local ROS concentration to modulate Ca<sup>2+</sup> channel dynamics (366).

Our approach consisted in creating the model, measure its frequency response *in silico*, compare it to experimentally acquired cell response to a few selected frequencies and refine the model in terms of parameter values and network connections. However, we encountered several technical difficulties. We were only able to measure a single output, cytosolic Ca<sup>2+</sup>. To validate the model accurately, measurement of ROS levels in the various cellular compartments during stimulation would be required. However, to date, there are very few reversible commercially available ROS sensors, making those measurements difficult, if not impossible in response to periodic stimuli. Additionally, the approach used to generate chemical pulses is limited in terms of repeatability and range of frequencies sampled. On-chip production of chemical waves in a robust and controllable manner, coupled with multiplexing to allow several frequencies to be simultaneously generated and delivered to cells, will allow easier Bode plot creation.

Model validation of the frequency response does not necessarily require experimentally probing the cells to periodic stimuli. One advantage of a transfer function is its ability to predict a system's output to any input. Therefore the system can be tested measuring cell response to a single pulse of varying lengths and duty ratios or cell

recovery after a few periods. Although easier experimentally, analysis might be more challenging. An additional assumption of the model was its linearity for low stimulus concentration. We showed experimentally that this assumption was not valid. To improve the fits, it is possible to add a non-linear rectifier (135). However in our case, it will probably not be sufficient, and a non-linear control theory approach might be necessary to properly examine the frequency response of the system.

Despite these shortcomings, an important proof of concept was demonstrated by our approach. Non-adherent mammalian cells have never been investigated by testing a range of periodic stimuli. This work demonstrates that by selecting an appropriate output measurement, we can observe response features that confirm global properties of the model simulations. Although model refinement is necessary to fully capture the observed cellular behavior and technical improvements to the device are needed to broaden the range of delivered frequencies, control systems analysis can yield insight in the regulation of complex biological signaling networks.

## **7.5. Materials and Methods**

### **7.5.1. Cell culture, stimulation and staining**

Jurkat E6-1 human acute T cell lymphoma cells (ATCC) were cultured in RPMI 1640 medium with L-glutamine (Sigma-Aldrich, St. Louis, MO) with 10mM HEPES, 1mM sodium pyruvate, 1X MEM nonessential amino acids, and 100 units mL<sup>-1</sup> penicillin streptomycin (Cellgro), supplemented with 10% certified heat inactivated fetal bovine serum (Sigma-Aldrich, St. Louis, MO), at 37°C in a humidified 5% CO<sub>2</sub> incubator. To

monitor calcium signaling, Jurkat cells were incubated with 5  $\mu$ M Fluo-3 (Invitrogen) for 40 minutes at 37°C, washed in PBS, resuspended in phenol-red free media and loaded into the cell traps. Trapped cells were stimulated with H<sub>2</sub>O<sub>2</sub> (Thermo-Fisher) at various concentrations to monitor cellular response to pulses of oxidative stress.

### **7.5.2. Fabrication of polydimethylsiloxane (PDMS) devices**

Single-cell trap microfluidic chips were fabricated as described in Chapter 6. Medical grade polyethylene (PE3) tubings (Scientific Commodities) were used for fluidic connections. Holes for fluidic connections were punched with 19 gauge needles. PDMS devices were plasma bonded onto slide glass.

### **7.5.3. Device operation**

Operation of the single-cell trap microfluidic platform has been described in Chapter 6. Briefly, devices were primed using a solution of 2% BSA in PBS and  $5 \times 10^5$  cells resuspended in phenol-red free media loaded using gravity-driven flow. Once efficient loading was achieved, the inlet hole was connected to a syringe filled with phenol-red free media via tubing. The syringe was placed above the microscope stage and the outlet tubing height adjusted to ensure on-chip flowrates in the proper range. This step allows excess cells remaining in the inlet hole to be washed away before the beginning of an experiment.

#### **7.5.4. Delivery of oscillatory input**

Chemical pulses were delivered to trapped cells by manually switching solutions in the inlet. More specifically, the two solutions (phenol-red free media and phenol-red free media supplemented with stimulus, here  $\text{H}_2\text{O}_2$ ) were stored in two 5 mL syringes above the microscope stage. The syringes were connected to 25 cm long PE-3 tubings and liquid allowed to fill the entire length of the tubing. Once filled, the tubing ending was raised and taped at syringe's height to prevent fluid leakage. To deliver the chemical pulses, the current tubing attached to the chip was removed 15 seconds before the time point and the other tubing connected to the inlet hole, making sure not to introduce any bubbles. All experiments were performed in a microcontrolled environment (temperature set at 37°C in a humidified 5%  $\text{CO}_2$  environment).

#### **7.5.5. Data collection and analysis**

Time-lapse microscopy experiments were performed on an epifluorescent (Nikon Eclipse Ti) microscope controlled with the NIS Element software in an environment controlled chamber. Images were acquired automatically at the desired sampling rate at a predefined location using the same exposure time and gain. Image analysis was performed using a custom Matlab® (MathWorks) script.

*Chemical pulses characterization:* Initial characterization of the chemical pulses was performed without any cells, with solutions of either PBS and PBS supplemented with BSA-FITC or water supplemented with red and green food coloring. Each frame was background subtracted and intensity in different locations in the array recorded for each

time point and averaged across these locations. When experiments were performed with color pictures, intensity was recorded for both the red and green channel of the RGB image and the ratio of intensities taken.

*Analysis of cell response to periodic stimuli:* After acquisition of a time course, all data points were projected onto a single image representing the average of the time course to define the location of each individual cell. Single cells were either cropped manually or using a mask of the traps created by finding the areas of higher intensities. Once the location of each cell was defined, its mean fluorescence intensity (MFI) was calculated for each frame. For each cell, calcium time courses were normalized to the first half-period of chemical stimulation to correct for uneven dye loading and normalized by the standard deviation of the time course. For Fourier analysis of individual time course, we adapted a previous protocol for performing spectral analysis of  $\text{Ca}^{2+}$  oscillations using Matlab (403).

*Device calibration for periodic stimuli:* Due to chip to chip variability, chemical oscillation amplitude and phase shift differed from experiment to experiment. Because fluids used in the chemical pulses were neither fluorescent nor colored, each device required pulse characterization after an actual experiment to ensure proper analysis of cellular response. This calibration was performed with FITC-BSA as described in the chemical pulses characterization section, by switching the phenol-red free media solution with a FITC-BSA solution. A sinusoidal wave was fitted to the calibration output using the following equation:



$$f = A * \cos(2\pi \frac{t}{T} + \varphi) \quad (7.30)$$

where A is the amplitude of the sinusoidal wave, T the period of the sinusoid and  $\varphi$  the phase shift. The parameters A, T and  $\varphi$  were fitted to the experimental time course between  $t_{calib1}$  and  $t_{calib2}$ , where  $t_{calib1}$  and  $t_{calib2}$  correspond respectively to the beginning and the end of the calibration period. Using the fitted function, the input oscillatory pattern delivered to the cells could be backcalculated.

## CHAPTER 8

### CONCLUSION AND FUTURE DIRECTIONS

I present in this dissertation an innovative combination of microfluidic tools and computational modeling to study age-related changes in *ex vivo* expanded T cells for adoptive T cell transfer therapy (ACT). Our biological findings point towards the acquisition of a senescent phenotype within 3 weeks of culture with an overall decrease in protein phosphorylation in signaling cascades activated downstream of the T cell receptor (TCR), loss of the co-stimulatory molecule CD28 and CD27 (Chapter 3), an increase in intracellular redox potential (Chapter 4) and altered  $\text{Ca}^{2+}$  dynamics (Chapter 5). The development of a new modular microfluidic platform for simultaneous multi time-point cell stimulation, fixation and lysis enabled the acquisition of early protein signaling dynamics with higher-throughput, controllability and robustness compared to traditional methods. Computational modeling was central to this study as it allowed us to identify biomarkers of *in vitro* aging, create a ‘senescence metric’ and determine potential targets of post-translational modifications responsible for altered  $\text{Ca}^{2+}$  signaling.

In the second part of this dissertation we focused on the cross-talk between reactive oxygen species (ROS) and  $\text{Ca}^{2+}$ , interactions that are fundamental for proper cell signaling and that are known to be altered in many age-related disorders, such as neurodegenerative or autoimmune diseases. We introduced a new microfluidic single-cell imaging platform and an original computational modeling approach to unravel features of cellular response to oxidative stress.

The contributions of this thesis to the scientific field are multiple. In terms of biological advances, this is the first large scale characterization of age-related changes in cell signaling and phenotype in ACT-consistent *ex vivo* cell expansion culture conditions with  $\alpha$ -CD3/CD28 coated beads (404-408). Compared to traditional models of *in vitro* aging used to study *in vivo* aging, such as the clonal model of replicative senescence developed by the Pawelec and Effros groups (205, 409), T cells expand and reach senescence faster. However, most changes that we observed, pointing towards a loss of function, are consistent with the literature. This suggests that *ex vivo* expanded T cells share common features with cells found in the elderly, thereby limiting the efficacy of ACT. It is also the first time that a ‘senescence metric’ for *in vitro* cultured T cells is described. The idea of a predictive senescence metric is not new. The OCTO and NONA longitudinal study defined an “immune risk profile”, based on the T cell repertoire of elderly populations (410, 411), but this metric relies on ratios of CD4/CD8 T cells and is not compatible with ACT that uses solely on CD8+ T cells. We found that a combination of metrics had the best descriptive potential compared to a single one, and interestingly very early signaling dynamics as well as heterogeneity in the cell population was heavily weighted in the final predictive metric. The importance of kinetic analysis was again demonstrated a few months after the publication of our article in a large microarray study wherein gene expression differences between young and old mice before and post TCR stimulation revealed novel age-related alterations (313). The ‘senescence metric’ we developed has however a few limitations. It predicts very well age in culture, characterized by the number of days in culture or the number of time the population has doubled. It can also predict surface marker expression from signaling information; yet

surface marker expression alone is not predictive of signaling, ie cell function. This highlights once again that a single metric is not sufficient to quantify senescence. An ideal ‘senescence metric’ would be able to determine quantitatively the fraction of senescent cells in a population and correlate it to the overall level of responsiveness of the population. Quantifying the percentage of senescent cells has been shown recently in fibroblasts, using a combination of markers including  $\beta$ -Gal staining and p21 (186), markers that have not been directly linked to senescence and loss of function in T cells. Single cell analysis of ERK phosphorylation after TCR stimulation, alone or in conjunction with markers of senescence profilin-1 and p16<sup>ink4</sup>, did not result in distinct subpopulations that would either be responsive or not responsive. This may suggest that the loss of T cell responsiveness and acquisition of a senescence phenotype is a continuous rather than a switch-like process. This is consistent with the recent findings of Nelson *et al.* who demonstrated senescence-induced-senescence via cell-cell contact ROS exchange (60). Despite being semi-quantitative, our ‘senescence metric’ can still be very useful in studies that aim at improving culture conditions for immunotherapies, the present culture conditions being the reference point.

Another notable biological finding is the increased intracellular oxidation in aging T cells, due to a reduction of the antioxidant capacity and overexpression of the NADPH oxidase Duox1. Nox2 and Nox4, other NADPH isoforms, have been shown to be upregulated with age (253, 254); yet this the first report of an age-related increase in Duox1 expression. Although we did not prove a direct causal effect between increased ROS levels and altered Ca<sup>2+</sup> and TCR signaling cascade dynamics, increased intracellular redox potential is generally linked with oxidative damage and a large number of

pathologies (412). Therefore preventing oxidative damage in long-term T cell culture by the use of antioxidants or hypoxic culture conditions may have beneficial effects.

This dissertation also significantly contributes to the microfluidics field. I present two distinct microfluidic platforms to study cellular processes in non-adherent cells. The first one performs controlled cell stimulation, followed by simultaneous lysis and fixation. The main advantages of this chip compared to traditional assays are: (1) its ability to reduce experimental variance in time and between samples due to sample handling, (2) the use of lower amounts of costly reagents and precious primary T cells, (3) the ability to robustly obtain stimulation time points with a high time resolution (down to 20 seconds). Its modular design allows versatility in the time-points sampled. A limiting factor however is its relatively large size and complexity, making the fabrication process in PDMS tedious (large number of holes). Although more expensive, if fabricated in glass, this chip would be reusable and could become a very useful part of a biologist's lab equipment or in a clinical setting.

Our second microfluidic platform, developed in collaboration with Dr K. Chung, allows passive hydrodynamic single-cell trapping and imaging. Compared to competing microfluidic technologies (129, 339-352), the advantages of our design include: (1) higher single-cell trapping efficiency due to deterministic cell trapping (up to 95% single cell trapping compared to 80%), (2) higher cell trap density (up to 100 fold), (3) ability to deliver a chemical stimulus or perform immunostaining on chip while retaining the cell in its location (compared to microwell technologies), (4) sequential cell trapping, avoiding loss of precious cells (5) easy to use (biologists with no microfluidics hands-on experience have been able to operate it alone). Data acquired with this chip is of similar

quality as flowcytometry data, while using 1000 fold less cells and being able to follow the signaling dynamics of the same individual cell over time. A potential limitation of this technology is the very low flowrates required to avoid shearing the cells, resulting in a very important diffusion effect. Although it is not an issue for cell loading, staining or stimulation with a simple step stimulus, we have found this the limiting factor to deliver complex temporal stimuli on chip. Use of this microfluidic platform has been essential to observe  $\text{Ca}^{2+}$  spiking in resting Jurkat cells, to study  $\text{Ca}^{2+}$  single cell response to gradients of ionomycin or  $\text{H}_2\text{O}_2$  and show the very large heterogeneity in cell response to a uniform stimulus.

Finally this work demonstrates the utility of computational modeling in biological systems. I used three different modeling approaches: a black-box modeling approach in Chapter 3, a deterministic modeling approach in Chapter 5 and a combination of both in Chapter 7. In Chapter 3 a partial least square regression (PLS) model was applied to identify the most significant biomarkers of aging and predict T cell age, without knowing any causal relationship between the input variables measured. This modeling technique had been used in the past to understand complex signaling networks and predict the behavior of a cellular system to new perturbations (189, 413, 414); however we added an additional dimension to this analysis by stitching together datasets from single cells and averaged populations as well as dynamic and static information. In Chapter 5, we developed a mechanistic model of  $\text{Ca}^{2+}$  signaling after TCR stimulation. Although there has been a considerable effort to model of  $\text{Ca}^{2+}$  dynamics in excitable cells, there are very few models of  $\text{Ca}^{2+}$  dynamics in immune cells, especially for T cells. The model presented here is the most complete to date, based on the current knowledge of the  $\text{Ca}^{2+}$

signaling pathway. It would be a very nice addition to the immunologist's toolbox. Lastly, we present a new modeling approach in Chapter 7 that relies on the union of time domain and frequency analysis, in order to understand the biochemical network of interactions between ROS and  $\text{Ca}^{2+}$ . Tools from control theory have been used extensively to study biological self-oscillatory and chaotic systems (415-418); however it's only recent that they have been used to study cell signaling (135, 361, 364). So far control-theory based mathematical models of mammalian signaling dynamics have not been validated in the frequency domain due to experimental limitations. Our approach, though in its infancy, shows the potential of ODE-based models analyzed and validated in the frequency domain to gain a better understanding of cellular regulatory systems.

## **FUTURE RESEARCH DIRECTIONS**

### *Senescence Metric*

Immunosenescence is thought to be a leading cause of aging due to its involvement in autoimmune disorders, inflammation or cancer. More specifically T cell immunosenescence has been linked with HIV (419, 420) and poor immunotherapy efficacy, including vaccination (421) and ACT (38). A reliable T cell 'senescence metric' would therefore be an invaluable tool for HIV patient prognosis, design of personalized vaccines and as described in this study improve ACT efficacy. We have presented here a first 'senescent metric'. This metric has been generated from a rather large but not exhaustive experimental dataset, chosen to mimic metrics that a clinician could easily acquire in the hospital. During the course of this dissertation, we have collected additional data relating age to  $\text{Ca}^{2+}$  signaling, mRNA levels of proteins

involved in ROS and  $\text{Ca}^{2+}$  homeostasis. Including these data into the original model would probably result in a more powerful senescent metric. The model has predictive power; however we were not able to verify its efficacy *in vivo* in the clinic, for example by correlating the predicted quality of T cell clones injected in the cancer patient to the clinical outcome of the treatment. We also have not verified whether the set of identified biomarkers is conserved in *in vivo* models of aging, such as elderly human subjects but also animal models extensively used in aging research. It is interesting to mention that during the course of this study, a similar approach was taken by a large European project, the MARK-AGE Project (2008-2013) to: “conduct a population study (3700 probands) in order to identify a set of biomarkers of ageing which, as a combination of parameters with appropriate weighting, would measure biological age better than any marker in isolation”.

Our model weighted heavily population variance in our ‘senescence metric’, suggesting that population heterogeneity is representative of the senescence process. Our lab has recently developed a method to easily perform single-cell PCR (unpublished data). Coupled with our single-cell microfluidic chip, heterogeneity in T cell population, in terms of differentiation status, dynamics, and transcriptomics could be assessed in young and old patient samples and incorporated in our ‘senescence model’, thereby providing new information regarding how the heterogeneity of the T cell repertoire affects the system’s overall response in aging.



### *Ca<sup>2+</sup> oscillations in T cells*

We have observed via our single-cell trap microfluidic platform a large heterogeneity in dynamic Ca<sup>2+</sup> patterns in resting T cells, with a large distribution of spiking frequencies in the frequency spectrum. Currently the mechanisms leading to these fluctuations are not understood, and there is controversy whether it is a deterministic or stochastic process (422). When stimulated with ionomycin, the frequency spectra tightens, but is not correlated to the initial oscillation frequency (data not shown). A seminal paper in Ca<sup>2+</sup> signaling in lymphocytes showed compelling evidence towards a direct relationship between Ca<sup>2+</sup> oscillation frequency and downstream gene activation (423); yet how the cell is able to transmit information through frequency encoded-Ca<sup>2+</sup> signal is still not fully understood. Computational modeling has provided some initial insights into protein phosphorylation driven by intracellular calcium oscillations (424, 425), but there is very limited amount of experimental data to support this theory. Coupled with various fluorescent protein reporters, our single-cell microfluidic platform would be an excellent tool to further study Ca<sup>2+</sup> oscillations in T cells and how they affect downstream signaling. Of particular interest would be the effect of Ca<sup>2+</sup> oscillations on ROS production through Duox1. We can hypothesize that its close proximity to the IP<sub>3</sub>R, and its activation by Ca<sup>2+</sup> binding to its EF-hand and phosphorylation make it a good candidate for frequency-encoded regulation.

### *Using control theory to understand complex biological systems*

Feedbacks, robustness and sensitivity are central to biological systems, therefore providing great value to tools developed by the control engineering community. The last

part of this thesis was a proof on concept that control systems theory could be applied to gain a better understanding of  $\text{Ca}^{2+}$ /ROS cross-talk in T cells. Model refinement is necessary to reduce discrepancies between our modeling and experimental results. The addition of non-linear rectifiers and additional points of feedback control can be included, in particular in the mitochondria and in the  $\text{Ca}^{2+}$ -binding protein buffering system. An interesting feature of this control theory based analysis is its ability to reduce the system into a few lumped parameters. For example, two parameters were sufficient to describe  $\text{Ca}^{2+}$  response to any input of oxidative stress. However, finding a biological meaning to these lumped parameters can be challenging and become a large hurdle for data interpretation.

Since it has been suggested that  $\text{Ca}^{2+}$  protein redox sensitivity might be ROS concentration dependent (94), this model could be subdivided into two ROS/ $\text{Ca}^{2+}$  cross-talk models with distinct parameter sets, one for signaling and one for pathologies involving high levels of ROS, such as inflammation, autoimmune disorders or aging. We also have been limited by the range of frequencies we could sample experimentally. To generate periodical stimuli of higher quality and increase the experimental throughput, our microfluidic chip must be integrated with on-chip chemical wave generators, potentially allowing several frequencies to be probed simultaneously in different chambers. Possible designs include on chip side valves, fully closed valves or simply alternating flowrates by gravity in a T junction. If modeling validation is not possible by directly sampling cell response to periodical stimuli, there are alternative methods such as measuring cell responses to a single pulse of different duration or to a ramp of concentration (362). Once validated, the impact of each flux or molecular interaction on

the overall system's dynamic behavior can be sampled in the frequency domain and a minimal model of ROS/Ca<sup>2+</sup> cross-talk generated. Because ROS and Ca<sup>2+</sup> are tightly regulated in many cell types and perturbations in these interactions result in pathologies, this model could provide new molecular targets for drug design.

## APPENDIX A

### APPENDIX CHAPTER 3

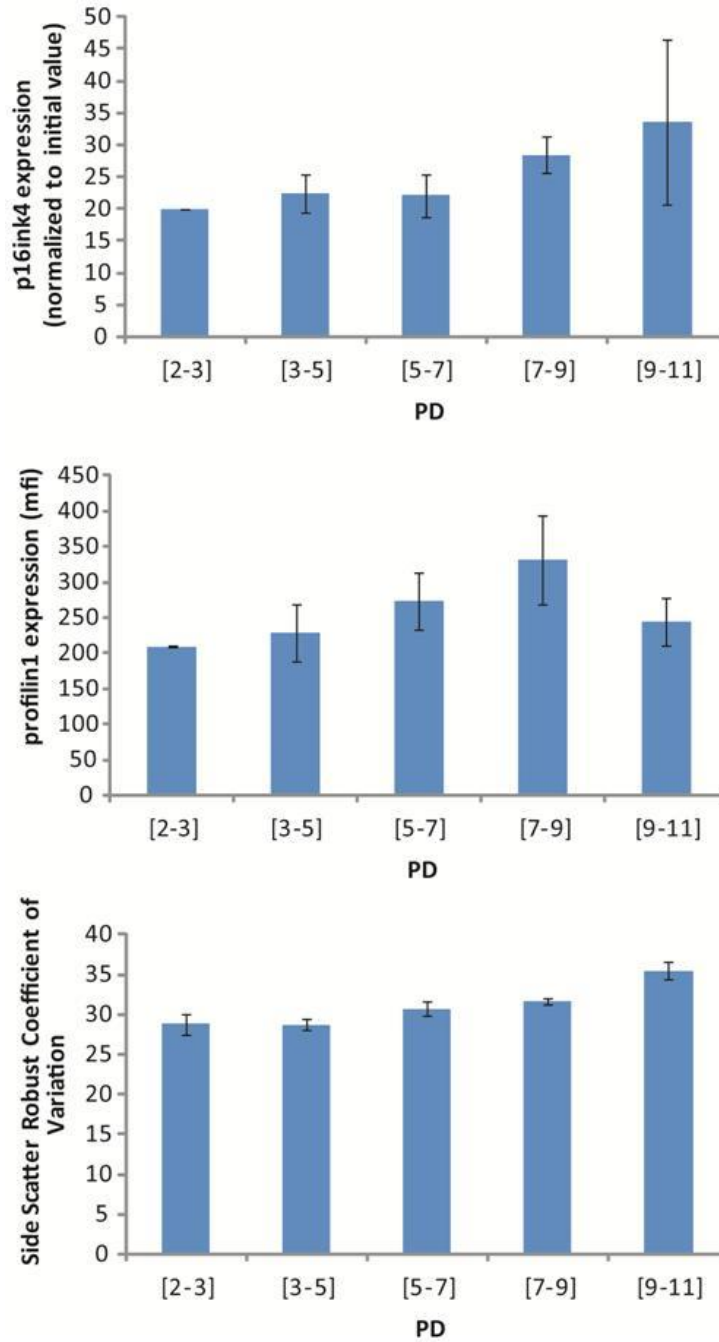


**Figure A.S1:** Flow cytometry data of intracellular protein expression p16<sup>ink4</sup>, profilin-1, and robust coefficient of variation of cell side scatter versus population doubling averaged for all donors  $\pm$  s.e.m.

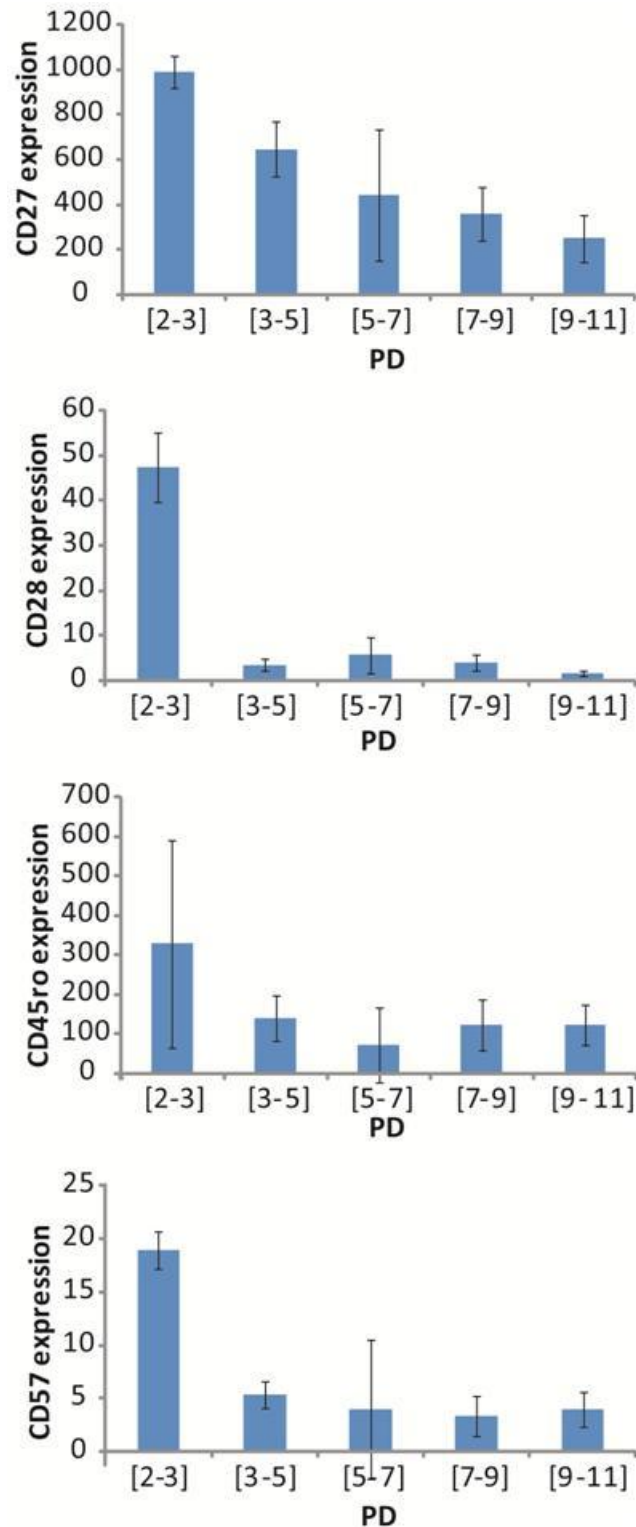


**Figure AS2:** Flow cytometry data of surface marker expression CD27, CD28, CD45RO and CD57 versus population doubling. The mean fluorescence intensity of positively gated cells for all donors is represented  $\pm$  standard error of the mean.

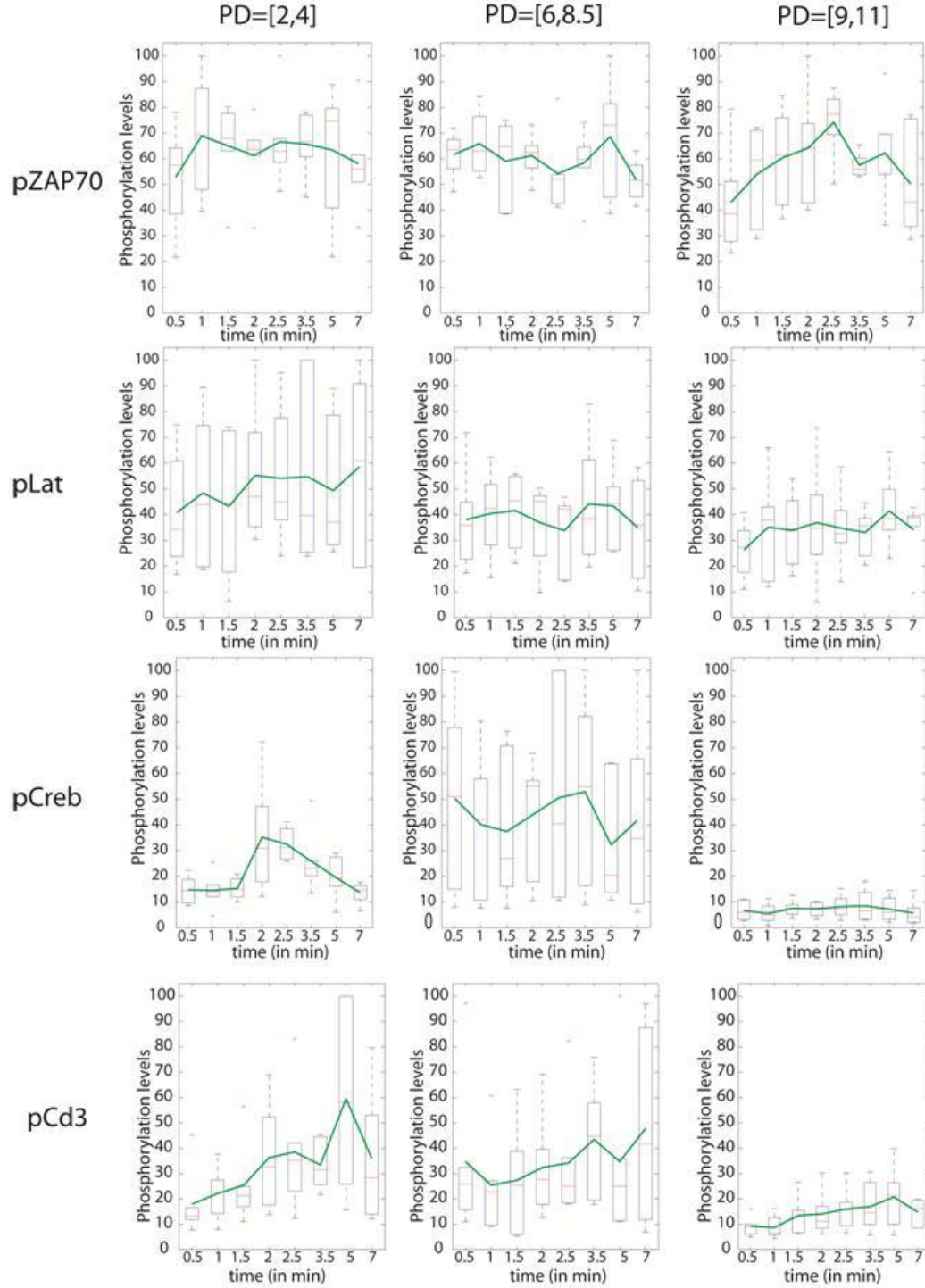


**Figure A.S3:** Signaling dynamics of pZap70, pLAT, pCreb and pCD3 at low, intermediate and late population doublings. The data is aggregated for the 4 donors. The green line corresponds to the mean signaling activation. The box plot presents the median, the 25<sup>th</sup> and 75<sup>th</sup> percentile as well as the outliers. A reduction in donor-donor variation as well as an overall decrease in protein activation occurs with time in culture for most proteins.

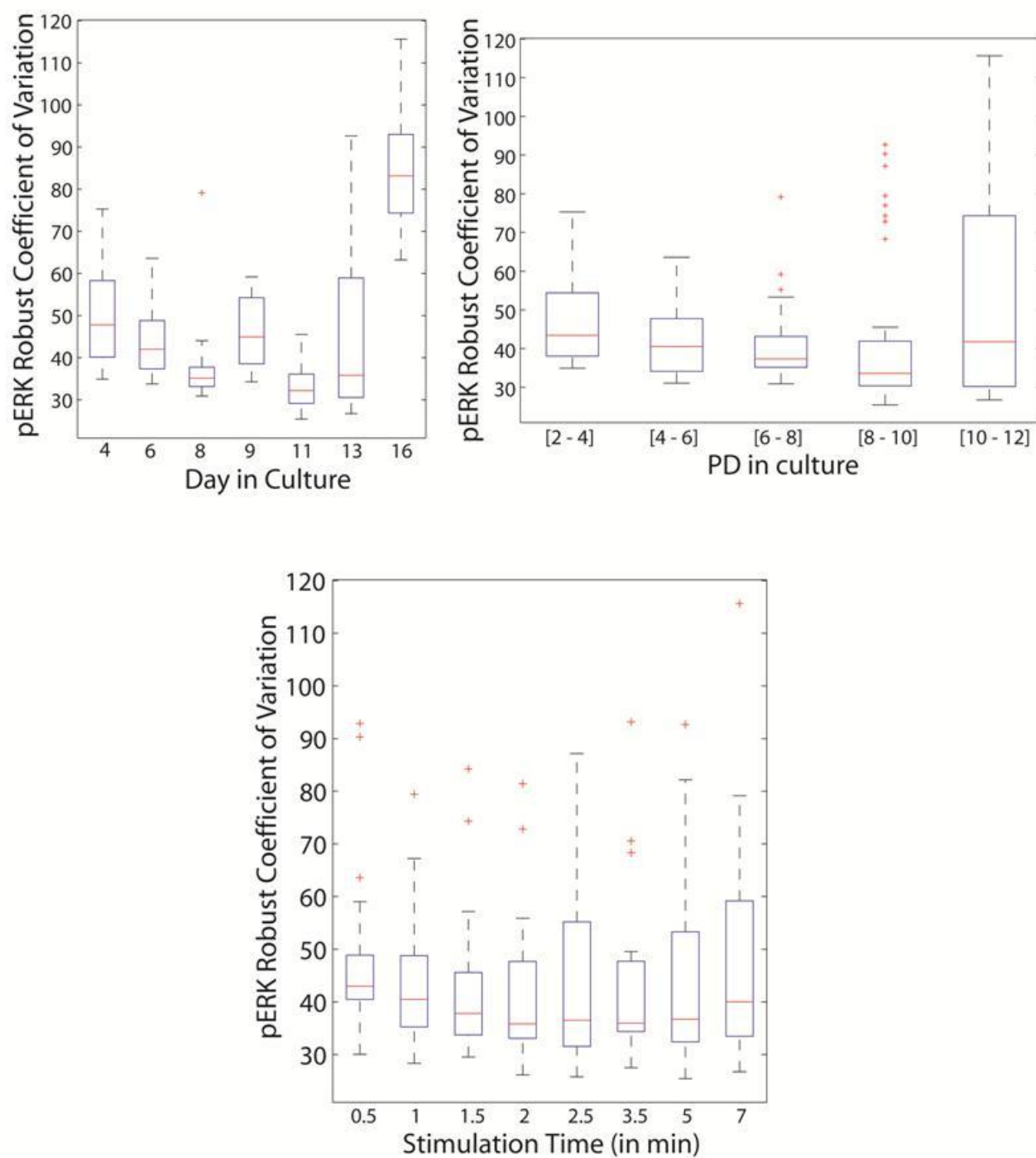


**Figure A.S4:** Changes in the robust coefficient of variation of pERK versus day or PD in culture or stimulation time for all four donors.

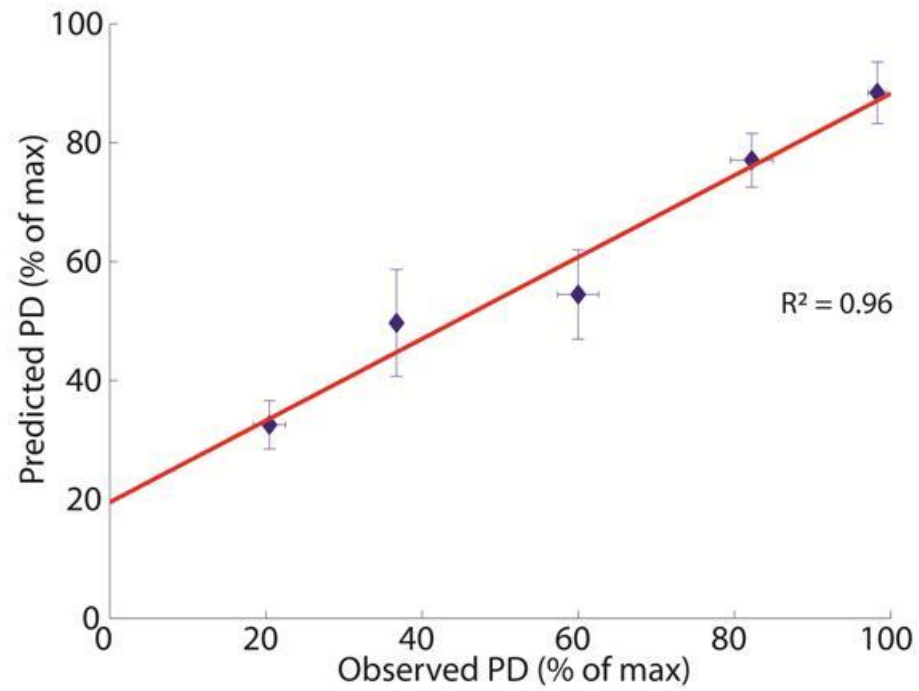
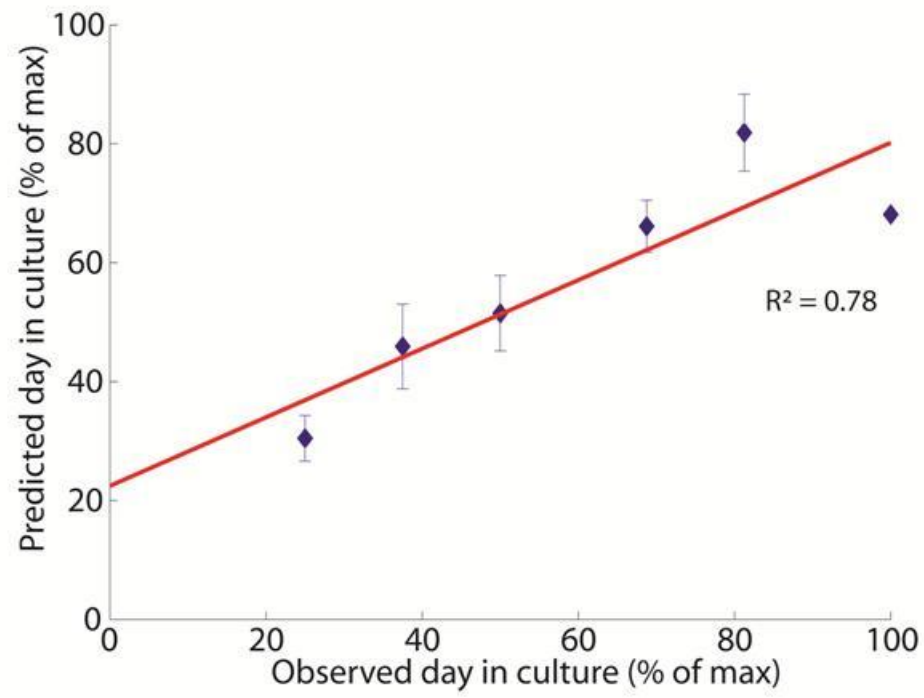


**Figure A.S5:** Model prediction with surface markers only.



**Table A.T1:** Prediction of number of day post-isolation and population doublings from signaling information and phenotypic markers: importance of the variables in the model projection.

|    | Variable             | Variable Importance<br>in the projection |    | Variable         | Variable Importance<br>in the projection |
|----|----------------------|------------------------------------------|----|------------------|------------------------------------------|
| 1  | cd27 mean            | 2.10807                                  | 36 | \$1stDer:lck5    | 0.85869                                  |
| 2  | \$1stDer:fERK_1 mean | 1.81841                                  | 37 | lck0.5           | 0.848903                                 |
| 3  | cd57 cv              | 1.807                                    | 38 | lat1             | 0.842587                                 |
| 4  | cd27 %               | 1.68825                                  | 39 | fERK_2 cv        | 0.839392                                 |
| 5  | ssc cv               | 1.61624                                  | 40 | fERK_2 mean      | 0.834191                                 |
| 6  | erk2                 | 1.39899                                  | 41 | fERK_0.5 cv      | 0.831355                                 |
| 7  | lck2                 | 1.39456                                  | 42 | fERK_2.5 mean    | 0.827579                                 |
| 8  | \$1stDer:erk1        | 1.3839                                   | 43 | erk0.5           | 0.826384                                 |
| 9  | lck3.5               | 1.23829                                  | 44 | G1%              | 0.823208                                 |
| 10 | cd28 mean            | 1.22894                                  | 45 | lat0.5           | 0.819776                                 |
| 11 | cd28 %               | 1.21613                                  | 46 | \$1stDer:erk2    | 0.815989                                 |
| 12 | G2%                  | 1.21511                                  | 47 | ssc mean         | 0.795274                                 |
| 13 | \$1stDer:zap1.5      | 1.20099                                  | 48 | fERK_3.5 cv      | 0.791876                                 |
| 14 | fsc mean             | 1.18049                                  | 49 | fERK_1.5 cv      | 0.789518                                 |
| 15 | lck5                 | 1.17463                                  | 50 | p16ink4 mean     | 0.769161                                 |
| 16 | \$1stDer:creb1.5     | 1.15728                                  | 51 | \$1stDer:lat2    | 0.765128                                 |
| 17 | erk3.5               | 1.15398                                  | 52 | cd57 mean        | 0.764364                                 |
| 18 | cd57 %               | 1.10823                                  | 53 | lat7             | 0.741126                                 |
| 19 | \$1stDer:erk1.5      | 1.10066                                  | 54 | fERK_1 cv        | 0.735429                                 |
| 20 | erk2.5               | 1.07066                                  | 55 | \$1stDer:lck0.5  | 0.728781                                 |
| 21 | lck1.5               | 1.04008                                  | 56 | \$1stDer:creb2.5 | 0.697429                                 |
| 22 | lck2.5               | 0.996836                                 | 57 | \$1stDer:lat0.5  | 0.682517                                 |
| 23 | lat3.5               | 0.965031                                 | 58 | fERK_3.5 mean    | 0.657546                                 |
| 24 | lat2.5               | 0.951935                                 | 59 | \$1stDer:lat1    | 0.643804                                 |
| 25 | \$1stDer:lat3.5      | 0.944874                                 | 60 | \$1stDer:creb2   | 0.613796                                 |
| 26 | fERK_1 mean          | 0.913745                                 | 61 | \$1stDer:lat5    | 0.595329                                 |
| 27 | creb2                | 0.911948                                 | 62 | creb3.5          | 0.579102                                 |
| 28 | fERK_0.5 mean        | 0.892883                                 | 63 | \$1stDer:erk2.5  | 0.573141                                 |
| 29 | cd45ro mean          | 0.892613                                 | 64 | \$1stDer:erk3.5  | 0.537731                                 |
| 30 | fERK_7 mean          | 0.892168                                 | 65 | cd3_1            | 0.534886                                 |
| 31 | \$1stDer:cd3_2       | 0.888851                                 | 66 | creb2.5          | 0.525642                                 |
| 32 | lck7                 | 0.881107                                 | 67 | cd3_7            | 0.478706                                 |
| 33 | \$1stDer:lat2.5      | 0.871192                                 | 68 | creb7            | 0.43545                                  |
| 34 | fERK_5 cv            | 0.87054                                  | 69 | lat5             | 0.404435                                 |
| 35 | ferk0.5/prof mean    | 0.866683                                 |    |                  |                                          |

**Table A.T2:** Prediction of number of day post-isolation and population doublings from signaling information and phenotypic markers: loadings of each variable on each of the 3 principal components of the model.

| Variable             | w*c1       | w*c2       | w*c3        |
|----------------------|------------|------------|-------------|
| \$1stDer:erk1        | -0.174735  | -0.232134  | -0.0908695  |
| \$1stDer:erk1.5      | -0.141475  | -0.140367  | 0.0938994   |
| \$1stDer:erk2        | -0.0400459 | 0.156462   | 0.22918     |
| \$1stDer:erk2.5      | 0.0235261  | 0.114418   | -0.0987679  |
| \$1stDer:erk3.5      | 0.0470348  | -0.0870041 | -0.026013   |
| \$1stDer:lat0.5      | -0.070525  | 0.0865824  | -0.0125435  |
| \$1stDer:lat1        | 0.0586355  | -0.100333  | -0.0723623  |
| \$1stDer:lat2        | -0.0966445 | 0.0486441  | 0.0881639   |
| \$1stDer:lat2.5      | 0.0185698  | 0.21766    | 0.161683    |
| \$1stDer:lat3.5      | 0.0979825  | -0.122032  | -0.120035   |
| \$1stDer:lat5        | 0.0374719  | -0.0550591 | -0.238662   |
| lat7                 | -0.101512  | -0.0587873 | -0.133811   |
| \$1stDer:lck0.5      | -0.0985907 | 0.0243995  | 0.0392244   |
| \$1stDer:lck5        | 0.111655   | -0.0445989 | -0.082137   |
| lck7                 | -0.0520531 | 0.177655   | 0.0661075   |
| \$1stDer:creb1.5     | -0.158113  | -0.135792  | 0.0328304   |
| \$1stDer:creb2       | -0.0723707 | 0.0504469  | 0.10062     |
| \$1stDer:creb2.5     | 0.0743857  | -0.0590914 | -0.173382   |
| creb7                | -0.0209155 | -0.0946879 | -0.146686   |
| \$1stDer:zap1.5      | 0.139095   | 0.224472   | 0.200751    |
| \$1stDer:cd3_2       | -0.12688   | -0.0150167 | -0.0308176  |
| cd3_7                | -0.035225  | -0.101849  | -0.146221   |
| \$1stDer:fERK_1 mean | -0.24009   | -0.271943  | -0.198951   |
| fERK_7 mean          | -0.116391  | 0.0485745  | 0.061525    |
| fERK_0.5 cv          | -0.0599215 | -0.141795  | 0.172195    |
| fERK_1 cv            | -0.044347  | -0.111548  | 0.193492    |
| fERK_1.5 cv          | -0.0521471 | -0.112453  | 0.214379    |
| fERK_2 cv            | -0.0589488 | -0.136059  | 0.191647    |
| fERK_3.5 cv          | -0.0749687 | -0.0937896 | 0.198218    |
| fERK_5 cv            | -0.0967359 | -0.149134  | 0.0697603   |
| G1%                  | 0.0814985  | 0.0461585  | 0.298878    |
| G2%                  | -0.166292  | -0.133064  | -0.195532   |
| ferk0.5/prof mean    | -0.0948355 | 0.101555   | 0.0956114   |
| p16ink4 mean         | 0.0494111  | 0.0397929  | 0.335506    |
| cd27 mean            | -0.273023  | -0.320813  | -0.318153   |
| cd57 mean            | -0.102538  | -0.0255534 | 0.115956    |
| cd45ro mean          | -0.110102  | 0.0594298  | -0.069633   |
| cd28 mean            | -0.170269  | 0.0216645  | -0.00581737 |
| cd27 %               | -0.187458  | -0.337764  | -0.191858   |

Table A.T2 continued

| Variable      | w*c1       | w*c2       | w*c3        |
|---------------|------------|------------|-------------|
| cd57 %        | -0.131084  | 0.0944223  | 0.165044    |
| cd28 %        | -0.169856  | 0.00777489 | -0.049675   |
| cd57 cv       | 0.250044   | 0.210905   | 0.220344    |
| fsc mean      | -0.154655  | 0.0643096  | 0.0367591   |
| ssc mean      | -0.0973969 | 0.0645275  | 0.0766865   |
| ssc cv        | 0.209221   | 0.25699    | 0.156991    |
| erk0.5        | 0.084169   | -0.0273094 | -0.26052    |
| erk2          | -0.191871  | -0.178974  | -0.0401264  |
| erk2.5        | -0.145261  | 0.0359882  | 0.0279075   |
| erk3.5        | -0.165977  | -0.0557326 | -0.0843158  |
| lat0.5        | -0.0905345 | 0.0844512  | -0.055538   |
| lat1          | -0.107915  | 0.051968   | -0.0199517  |
| lat2.5        | -0.12794   | 0.0358534  | -0.0166383  |
| lat3.5        | -0.0870264 | 0.150741   | 0.127775    |
| lat5          | -0.0480701 | -0.0298783 | -0.119469   |
| lck0.5        | -0.07377   | 0.121421   | -0.0759082  |
| lck1.5        | -0.0563096 | 0.213791   | 0.0513851   |
| lck2          | -0.19943   | -0.0241239 | -0.013126   |
| lck2.5        | -0.0913042 | 0.151789   | 0.0127265   |
| lck3.5        | -0.160331  | 0.0707907  | 0.0988252   |
| lck5          | -0.126817  | 0.143191   | 0.110661    |
| creb2         | -0.130935  | -0.0722269 | -0.00750945 |
| creb2.5       | -0.0757922 | -0.0189477 | -0.0162422  |
| creb3.5       | -0.0688577 | -0.100416  | -0.114246   |
| cd3_1         | -0.0681207 | -0.0696301 | -0.119838   |
| fERK_0.5 mean | 0.0146629  | 0.223794   | 0.134271    |
| fERK_1 mean   | -0.123783  | -0.058126  | -0.176445   |
| fERK_2 mean   | -0.113237  | 0.0275411  | 0.0266794   |
| fERK_2.5 mean | -0.109112  | 0.0421655  | 0.0298007   |
| fERK_3.5 mean | -0.0866206 | 0.0309205  | -0.0206491  |
| day max       | 0.207256   | 0.212431   | 0.0985998   |
| pd max        | 0.222709   | 0.166709   | 0.104857    |

**Table A.T3:** Prediction of number of day post-isolation and population doublings from signaling information: importance of the variables in the model projection.

|    | <b>Variable</b>             | <b>Variable Importance<br/>in the projection</b> |
|----|-----------------------------|--------------------------------------------------|
| 1  | <b>\$1stDer:fERK_1 mean</b> | 1.73925                                          |
| 2  | <b>\$1stDer:erk1</b>        | 1.37537                                          |
| 3  | <b>lck2</b>                 | 1.30379                                          |
| 4  | <b>erk2</b>                 | 1.28032                                          |
| 5  | <b>lck3.5</b>               | 1.23145                                          |
| 6  | <b>fERK_1.5 mean</b>        | 1.20802                                          |
| 7  | <b>\$1stDer:zap1.5</b>      | 1.17241                                          |
| 8  | <b>lck5</b>                 | 1.17047                                          |
| 9  | <b>fERK_7 mean</b>          | 1.10426                                          |
| 10 | <b>erk3.5</b>               | 1.09963                                          |
| 11 | <b>erk2.5</b>               | 1.08298                                          |
| 12 | <b>\$1stDer:creb1.5</b>     | 1.05263                                          |
| 13 | <b>lck2.5</b>               | 1.02912                                          |
| 14 | <b>\$1stDer:erk1.5</b>      | 0.984998                                         |
| 15 | <b>creb2</b>                | 0.8756                                           |
| 16 | <b>\$1stDer:lck5</b>        | 0.872824                                         |
| 17 | <b>lat2.5</b>               | 0.831813                                         |
| 18 | <b>\$1stDer:cd3_2</b>       | 0.823419                                         |
| 19 | <b>fERK_1 mean</b>          | 0.804746                                         |
| 20 | <b>cd3_2</b>                | 0.777253                                         |
| 21 | <b>fERK_3.5 mean</b>        | 0.733821                                         |
| 22 | <b>lat7</b>                 | 0.66729                                          |
| 23 | <b>cd3_2.5</b>              | 0.569716                                         |
| 24 | <b>\$1stDer:creb2</b>       | 0.51115                                          |
| 25 | <b>creb3.5</b>              | 0.496587                                         |
| 26 | <b>cd3_1</b>                | 0.475836                                         |
| 27 | <b>\$1stDer:zap5</b>        | 0.303936                                         |

**Table A.T4:** Prediction of number of day post-isolation and population doublings from signaling information: loadings of each variable on each of the 2 principal components of the model.

| <b>Variable</b>         | <b>w*c1</b> | <b>w*c2</b> |
|-------------------------|-------------|-------------|
| <b>\$1stDer:erk1</b>    | -0.24672    | -0.38857    |
| <b>\$1stDer:erk1.5</b>  | -0.19976    | -0.20195    |
| <b>lat7</b>             | -0.1433     | -0.08372    |
| <b>\$1stDer:lck5</b>    | 0.157624    | -0.15764    |
| <b>\$1stDer:creb1.5</b> | -0.22323    | -0.15839    |
| <b>\$1stDer:creb2</b>   | -0.10215    | 0.055449    |
| <b>\$1stDer:zap1.5</b>  | 0.196364    | 0.362386    |
| <b>\$1stDer:zap5</b>    | 0.065958    | 0.00881     |
| <b>\$1stDer:cd3_2</b>   | -0.17908    | -0.06051    |
| <b>\$1stDer:fERK_1</b>  | -0.33898    | -0.41176    |
| <b>mean</b>             |             |             |
| <b>fERK_7 mean</b>      | -0.16431    | 0.287251    |
| <b>erk2</b>             | -0.2709     | -0.19745    |
| <b>erk2.5</b>           | -0.20507    | 0.163903    |
| <b>erk3.5</b>           | -0.23431    | 0.02781     |
| <b>lat2.5</b>           | -0.18062    | -0.02704    |
| <b>lck2</b>             | -0.28153    | -0.01044    |
| <b>lck2.5</b>           | -0.12888    | 0.311747    |
| <b>lck3.5</b>           | -0.22634    | 0.209863    |
| <b>lck5</b>             | -0.17902    | 0.294292    |
| <b>creb2</b>            | -0.18484    | -0.13825    |
| <b>creb3.5</b>          | -0.0972     | -0.11608    |
| <b>cd3_1</b>            | -0.09614    | -0.0992     |
| <b>cd3_2</b>            | -0.14474    | -0.20543    |
| <b>cd3_2.5</b>          | -0.10951    | -0.14011    |
| <b>fERK_1 mean</b>      | -0.17474    | -0.06953    |
| <b>fERK_1.5 mean</b>    | -0.25161    | 0.075366    |
| <b>fERK_3.5 mean</b>    | -0.12228    | 0.161131    |
| <b>day max</b>          | 0.284475    | 0.317873    |
| <b>pd max</b>           | 0.304778    | 0.277479    |

**Table A.T5:** Prediction of CD27 and CD28 expression from signaling information: importance of the variables in the model projection.

|    | <b>Variable</b>        | <b>Variable Importance<br/>in the projection</b> |
|----|------------------------|--------------------------------------------------|
| 1  | \$1stDer:fERK_1 mean   | 1.64652                                          |
| 2  | fsc mean               | 1.31774                                          |
| 3  | lck0.5                 | 1.28017                                          |
| 4  | fERK_1 mean            | 1.19866                                          |
| 5  | lck2.5                 | 1.19778                                          |
| 6  | S%                     | 1.18034                                          |
| 7  | lck2                   | 1.17869                                          |
| 8  | lck1                   | 1.11446                                          |
| 9  | lck5                   | 1.10784                                          |
| 10 | erk2                   | 1.10597                                          |
| 11 | lat0.5                 | 1.09658                                          |
| 12 | fERK_1.5 mean          | 1.09389                                          |
| 13 | lck7                   | 1.07056                                          |
| 14 | \$1stDer:erk1          | 1.06315                                          |
| 15 | lck1.5                 | 1.05297                                          |
| 16 | lat3.5                 | 1.02674                                          |
| 17 | ssc mean               | 1.02009                                          |
| 18 | lat2.5                 | 1.0044                                           |
| 19 | G1%                    | 0.980289                                         |
| 20 | G2%                    | 0.952699                                         |
| 21 | erk5                   | 0.923509                                         |
| 22 | \$1stDer:lat3.5        | 0.908869                                         |
| 23 | lck3.5                 | 0.871187                                         |
| 24 | \$1stDer:creb2.5       | 0.855285                                         |
| 25 | fERK_2.5 mean          | 0.849749                                         |
| 26 | \$1stDer:cd3_2         | 0.81324                                          |
| 27 | erk2.5                 | 0.810829                                         |
| 28 | \$1stDer:lat2          | 0.810352                                         |
| 29 | fERK_5 mean            | 0.778315                                         |
| 30 | \$1stDer:lck0.5        | 0.769653                                         |
| 31 | \$1stDer:creb2         | 0.699023                                         |
| 32 | erk3.5                 | 0.657731                                         |
| 33 | ferk0.5/prof mean      | 0.58108                                          |
| 34 | \$1stDer:fERK_3.5 mean | 0.515929                                         |
| 35 | fERK_3.5 mean          | 0.469756                                         |

**Table A.T6:** Prediction of CD27 and CD28 expression from signaling information: loadings of each variable on each of the 2 principal components of the model.

| <b>variable</b>      | <b>w*c1</b> | <b>w*c2</b> | <b>variable</b> | <b>w*c1</b> | <b>w*c2</b> |
|----------------------|-------------|-------------|-----------------|-------------|-------------|
| \$1stDer:erk1        | 0.12008     | 0.272438    | lat0.5          | 0.192487    | -0.14947    |
| \$1stDer:lat2        | 0.16138     | 0.084998    | lat2.5          | 0.207234    | -0.01226    |
| \$1stDer:lat3.5      | -0.18408    | 0.038984    | lat3.5          | 0.17758     | -0.14594    |
| \$1stDer:lck0.5      | 0.157396    | 0.057062    | lck0.5          | 0.144682    | -0.29628    |
| lck7                 | 0.137086    | -0.22996    | lck1            | 0.23133     | 0.041295    |
| \$1stDer:creb2       | 0.135048    | -0.06005    | lck1.5          | 0.173469    | -0.16749    |
| \$1stDer:creb2.5     | -0.15006    | -0.14962    | lck2            | 0.212305    | 0.194088    |
| \$1stDer:cd3_2       | 0.168263    | -0.00377    | lck2.5          | 0.176806    | -0.22559    |
| \$1stDer:fERK_1 mean | 0.17111     | 0.433016    | lck3.5          | 0.180062    | 0.046183    |
| \$1stDer:fERK_3.5    | 0.082579    | -0.08656    | lck5            | 0.203264    | -0.12889    |
| mean                 |             |             |                 |             |             |
| G1%                  | -0.17027    | 0.137734    | fERK_1 mean     | 0.171662    | 0.271177    |
| G2%                  | 0.186448    | -0.07271    | fERK_1.5        | 0.178424    | 0.216498    |
|                      |             |             | mean            |             |             |
| S%                   | 0.169039    | 0.26703     | fERK_2.5        | 0.107858    | 0.207303    |
|                      |             |             | mean            |             |             |
| ferk0.5/prof mean    | 0.115097    | -0.03849    | fERK_3.5        | 0.059045    | 0.115159    |
|                      |             |             | mean            |             |             |
| fsc mean             | 0.269496    | -0.03853    | fERK_5 mean     | 0.158098    | 0.065121    |
| ssc mean             | 0.207179    | -0.04014    | cd27 mean       | 0.15003     | 0.409394    |
| erk2                 | 0.134016    | 0.275733    | cd28 mean       | 0.250892    | 0.057859    |
| erk2.5               | 0.162519    | 0.080063    | cd27 %          | 0.013671    | 0.439324    |
| erk3.5               | 0.130078    | 0.072976    | cd28 %          | 0.255681    | -0.01462    |
| erk5                 | 0.164127    | -0.1211     |                 |             |             |

## APPENDIX B

### APPENDIX CHAPTER 4

**Table B.T1:** List of all oxidative stress and antioxidant PCR primer targets on the PCR array. Red genes represent targets that are not expressed in CD8+ T cells.

|                |                                                 |               |                                                                |               |                                                                              |               |                                                                                       |
|----------------|-------------------------------------------------|---------------|----------------------------------------------------------------|---------------|------------------------------------------------------------------------------|---------------|---------------------------------------------------------------------------------------|
| <b>ALB</b>     | Albumin                                         | <b>GLRX2</b>  | Glutaredoxin 2                                                 | <b>MTL5</b>   | Metallothionein-like 5, testis-specific (tesmin)                             | <b>PTGS1</b>  | Prostaglandin-endoperoxide synthase 1 (prostaglandin G/H synthase and cyclooxygenase) |
| <b>ALOX12</b>  | Arachidonate 12-lipoxygenase                    | <b>GPR156</b> | G protein-coupled receptor 156                                 | <b>NCF1</b>   | Neutrophil cytosolic factor 1                                                | <b>PTGS2</b>  | Prostaglandin-endoperoxide synthase 2 (prostaglandin G/H synthase and cyclooxygenase) |
| <b>ANGPTL7</b> | Angiopoietin-like 7                             | <b>GPX1</b>   | Glutathione peroxidase 1                                       | <b>NCF2</b>   | Neutrophil cytosolic factor 2                                                | <b>PXDN</b>   | Peroxidasin homolog (Drosophila)                                                      |
| <b>AOX1</b>    | Aldehyde oxidase 1                              | <b>GPX2</b>   | Glutathione peroxidase 2 (gastrointestinal)                    | <b>NME5</b>   | Non-metastatic cells 5, protein expressed in (nucleoside-diphosphate kinase) | <b>PXDNL</b>  | Peroxidasin homolog (Drosophila)-like                                                 |
| <b>APOE</b>    | Apolipoprotein E                                | <b>GPX3</b>   | Glutathione peroxidase 3 (plasma)                              | <b>NOS2</b>   | Nitric oxide synthase 2, inducible                                           | <b>RNF7</b>   | Ring finger protein 7                                                                 |
| <b>ATOX1</b>   | ATX1 antioxidant protein 1 homolog (yeast)      | <b>GPX4</b>   | Glutathione peroxidase 4 (phospholipid hydroperoxidase)        | <b>NOX5</b>   | NADPH oxidase, EF-hand calcium binding domain 5                              | <b>SCARA3</b> | Scavenger receptor class A, member 3                                                  |
| <b>BNIP3</b>   | BCL2/adenovirus E1B 19kDa interacting protein 3 | <b>GPX5</b>   | Glutathione peroxidase 5 (epididymal androgen-related protein) | <b>NUDT1</b>  | Nudix (nucleoside diphosphate linked moiety X)-type motif 1                  | <b>SELS</b>   | Selenoprotein S                                                                       |
| <b>CAT</b>     | Catalase                                        | <b>GPX6</b>   | Glutathione peroxidase 6 (olfactory)                           | <b>OXR1</b>   | Oxidation resistance 1                                                       | <b>SEPP1</b>  | Selenoprotein P, plasma, 1                                                            |
| <b>CCL5</b>    | Chemokine (C-C motif) ligand 5                  | <b>GPX7</b>   | Glutathione peroxidase 7                                       | <b>OXSR1</b>  | Oxidative-stress responsive 1                                                | <b>SFTPD</b>  | Surfactant protein D                                                                  |
| <b>CCS</b>     | Copper chaperone for superoxide dismutase       | <b>GSR</b>    | Glutathione reductase                                          | <b>PDLIM1</b> | PDZ and LIM domain 1                                                         | <b>SGK2</b>   | Serum/glucocorticoid regulated kinase 2                                               |



**Table B.T1 continued**

|               |                                              |              |                                               |               |                                                                          |               |                                               |
|---------------|----------------------------------------------|--------------|-----------------------------------------------|---------------|--------------------------------------------------------------------------|---------------|-----------------------------------------------|
| <b>CSDE1</b>  | Cold shock domain containing E1, RNA-binding | <b>GSS</b>   | Glutathione synthetase                        | <b>IPCEF1</b> | Interaction protein for cytohesin exchange factors 1                     | <b>SIRT2</b>  | Sirtuin 2                                     |
| <b>CYBA</b>   | Cytochrome b-245, alpha polypeptide          | <b>GSTZ1</b> | Glutathione transferase zeta 1                | <b>PNKP</b>   | Polynucleotide kinase 3'-phosphatase                                     | <b>SOD1</b>   | Superoxide dismutase 1, soluble               |
| <b>CYGB</b>   | Cytoglobin                                   | <b>GTF2I</b> | General transcription factor Iii              | <b>PRDX1</b>  | Peroxiredoxin 1                                                          | <b>SOD2</b>   | Superoxide dismutase 2, mitochondrial         |
| <b>DGKK</b>   | Diacylglycerol kinase, kappa                 | <b>KRT1</b>  | Keratin 1                                     | <b>PRDX2</b>  | Peroxiredoxin 2                                                          | <b>SOD3</b>   | Superoxide dismutase 3, extracellular         |
| <b>DHCR24</b> | 24-dehydrocholesterol reductase              | <b>LPO</b>   | Lactoperoxidase                               | <b>PRDX3</b>  | Peroxiredoxin 3                                                          | <b>SRXN1</b>  | Sulfiredoxin 1                                |
| <b>DUOX1</b>  | Dual oxidase 1                               | <b>MBL2</b>  | Mannose-binding lectin (protein C) 2, soluble | <b>PRDX4</b>  | Peroxiredoxin 4                                                          | <b>STK25</b>  | Serine/threonine kinase 25                    |
| <b>DUOX2</b>  | Dual oxidase 2                               | <b>MGST3</b> | Microsomal glutathione S-transferase 3        | <b>PRDX5</b>  | Peroxiredoxin 5                                                          | <b>TPO</b>    | Thyroid peroxidase                            |
| <b>DUSP1</b>  | Dual specificity phosphatase 1               | <b>MPO</b>   | Myeloperoxidase                               | <b>PRDX6</b>  | Peroxiredoxin 6                                                          | <b>TTN</b>    | Titin                                         |
| <b>EPHX2</b>  | Epoxide hydrolase 2, cytoplasmic             | <b>MPV17</b> | MpV17 mitochondrial inner membrane protein    | <b>PREX1</b>  | Phosphatidylinositol-3,4,5-trisphosphate-dependent Rac exchange factor 1 | <b>TXNDC2</b> | Thioredoxin domain containing 2 (spermatozoa) |
| <b>EPX</b>    | Eosinophil peroxidase                        | <b>MSRA</b>  | Methionine sulfoxide reductase A              | <b>PRG3</b>   | Proteoglycan 3                                                           | <b>TXNRD1</b> | Thioredoxin reductase 1                       |
| <b>FOXM1</b>  | Forkhead box M1                              | <b>MT3</b>   | Metallothionein 3                             | <b>PRNP</b>   | Prion protein                                                            | <b>TXNRD2</b> | Thioredoxin reductase 2                       |

**Table B.T2:** Exhaustive list of fold changes and their corresponding p-values in targets expressed in CD8+ T cells. A fold change below 1 corresponds to a downregulation ( $2^{-\Delta CT}$ ).

| Symbol         | Protein Name                                                             | Fold Change<br>Old/Young | p-value |
|----------------|--------------------------------------------------------------------------|--------------------------|---------|
| <b>PDLIM1</b>  | PDZ and LIM domain 1                                                     | 0.17                     | 0.01    |
| <b>ANGPTL7</b> | Angiopoietin-like 7                                                      | 2.93                     | 0.01    |
| <b>MTL5</b>    | Metallothionein-like 5, testis-specific (tesmin)                         | 0.45                     | 0.01    |
| <b>NUDT1</b>   | Nudix (nucleoside diphosphate linked moiety X)-type motif 1              | 0.99                     | 0.01    |
| <b>TTN</b>     | Titin                                                                    | 2.14                     | 0.01    |
| <b>DUOX1</b>   | Dual oxidase 1                                                           | 1.68                     | 0.03    |
| <b>GPX3</b>    | Glutathione peroxidase 3 (plasma)                                        | 2.55                     | 0.04    |
| <b>GLRX2</b>   | Glutaredoxin 2                                                           | 0.47                     | 0.06    |
| <b>PRNP</b>    | Prion protein                                                            | 1.45                     | 0.07    |
| <b>TXNRD1</b>  | Thioredoxin reductase 1                                                  | 0.31                     | 0.08    |
| <b>PRDX1</b>   | Peroxiredoxin 1                                                          | 0.74                     | 0.13    |
| <b>CCL5</b>    | Chemokine (C-C motif) ligand 5                                           | 3.81                     | 0.15    |
| <b>TXNRD2</b>  | Thioredoxin reductase 2                                                  | 1.15                     | 0.18    |
| <b>GPX2</b>    | Glutathione peroxidase 2 (gastrointestinal)                              | 2.15                     | 0.20    |
| <b>SEPP1</b>   | Selenoprotein P, plasma, 1                                               | 0.34                     | 0.21    |
| <b>ATOX1</b>   | ATX1 antioxidant protein 1 homolog (yeast)                               | 0.50                     | 0.22    |
| <b>BNIP3</b>   | BCL2/adenovirus E1B 19kDa interacting protein 3                          | 1.12                     | 0.23    |
| <b>CCS</b>     | Copper chaperone for superoxide dismutase                                | 0.22                     | 0.23    |
| <b>PX1</b>     | Glutathione peroxidase 1                                                 | 0.18                     | 0.23    |
| <b>PREX1</b>   | Phosphatidylinositol-3,4,5-trisphosphate-dependent Rac exchange factor 1 | 0.90                     | 0.24    |
| <b>PRDX5</b>   | Peroxiredoxin 5                                                          | 0.80                     | 0.29    |
| <b>CSDE1</b>   | Cold shock domain containing E1, RNA-binding                             | 0.49                     | 0.30    |
| <b>SIRT2</b>   | Sirtuin 2                                                                | 1.25                     | 0.32    |
| <b>FOXM1</b>   | Forkhead box M1                                                          | 1.78                     | 0.33    |
| <b>GTF2I</b>   | General transcription factor Iii                                         | 0.52                     | 0.34    |
| <b>GSS</b>     | Glutathione synthetase                                                   | 0.26                     | 0.37    |
| <b>NCF1</b>    | Neutrophil cytosolic factor 1                                            | 9.32                     | 0.42    |
| <b>ALOX12</b>  | Arachidonate 12-lipoxygenase                                             | 0.60                     | 0.46    |
| <b>STK25</b>   | Serine/threonine kinase 25                                               | 4.65                     | 0.46    |
| <b>GPX4</b>    | Glutathione peroxidase 4 (phospholipid hydroperoxidase)                  | 0.02                     | 0.47    |
| <b>SELS</b>    | Selenoprotein S                                                          | 0.10                     | 0.48    |
| <b>MPV17</b>   | MpV17 mitochondrial inner membrane protein                               | 0.57                     | 0.49    |
| <b>MGST3</b>   | Microsomal glutathione S-transferase 3                                   | 0.49                     | 0.50    |
| <b>GSR</b>     | Glutathione reductase                                                    | 0.73                     | 0.51    |
| <b>PRDX2</b>   | Peroxiredoxin 2                                                          | 0.75                     | 0.51    |
| <b>SOD1</b>    | Superoxide dismutase 1, soluble                                          | 6.52                     | 0.51    |
| <b>SRXN1</b>   | Sulfiredoxin 1                                                           | 0.12                     | 0.52    |
| <b>CAT</b>     | Catalase                                                                 | 122.49                   | 0.56    |
| <b>MSRA</b>    | Methionine sulfoxide reductase A                                         | 0.79                     | 0.57    |
| <b>MT3</b>     | Metallothionein 3                                                        | 0.28                     | 0.59    |
| <b>NCF2</b>    | Neutrophil cytosolic factor 2                                            | 1.49                     | 0.59    |
| <b>OXR1</b>    | Oxidation resistance 1                                                   | 0.02                     | 0.59    |

**Table B.T2 continued:**

| <b>Symbol</b> | <b>Protein Name</b>                                  | <b>Fold Change<br/>Old/Young</b> | <b>p-value</b> |
|---------------|------------------------------------------------------|----------------------------------|----------------|
| <b>GPX7</b>   | Glutathione peroxidase 7                             | 0.17                             | 0.60           |
| <b>EPX</b>    | Eosinophil peroxidase                                | 0.83                             | 0.64           |
| <b>CYBA</b>   | Cytochrome b-245, alpha polypeptide                  | 0.41                             | 0.65           |
| <b>GSTZ1</b>  | Glutathione transferase zeta 1                       | 1.89                             | 0.65           |
| <b>PRDX6</b>  | Peroxiredoxin 6                                      | 3.93                             | 0.65           |
| <b>IPCEF1</b> | Interaction protein for cytohesin exchange factors 1 | 0.65                             | 0.66           |
| <b>PRDX4</b>  | Peroxiredoxin 4                                      | 2.87                             | 0.70           |
| <b>SOD2</b>   | Superoxide dismutase 2, mitochondrial                | 0.33                             | 0.70           |
| <b>DUSP1</b>  | Dual specificity phosphatase 1                       | 4.56                             | 0.71           |
| <b>RNF7</b>   | Ring finger protein 7                                | 6.55                             | 0.71           |
| <b>SFTPD</b>  | Surfactant protein D                                 | 3.35                             | 0.72           |
| <b>DHCR24</b> | 24-dehydrocholesterol reductase                      | 0.57                             | 0.82           |
| <b>PRDX3</b>  | Peroxiredoxin 3                                      | 1.60                             | 0.84           |
| <b>OXSRI</b>  | Oxidation resistance 1                               | 2.20                             | 0.95           |
| <b>PNKP</b>   | Polynucleotide kinase 3'-phosphatase                 | 1.59                             | 0.98           |

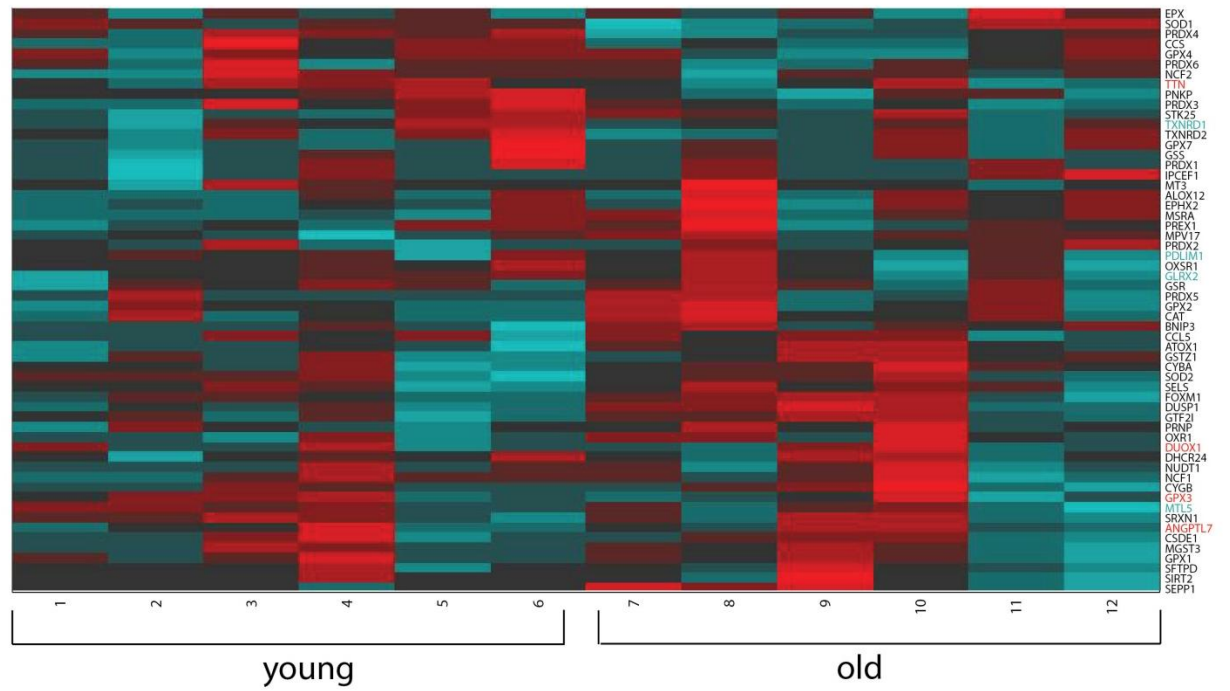


**Figure B.S1:** Heatmap representing gene expression for all expressed genes in young (Column 1-6) and old T cells (Column 7-12). Each gene has been normalized to its  $\Delta C_T$  mean value. Higher expression is displayed in red, lower in blue.

## APPENDIX C

### APPENDIX CHAPTER 5

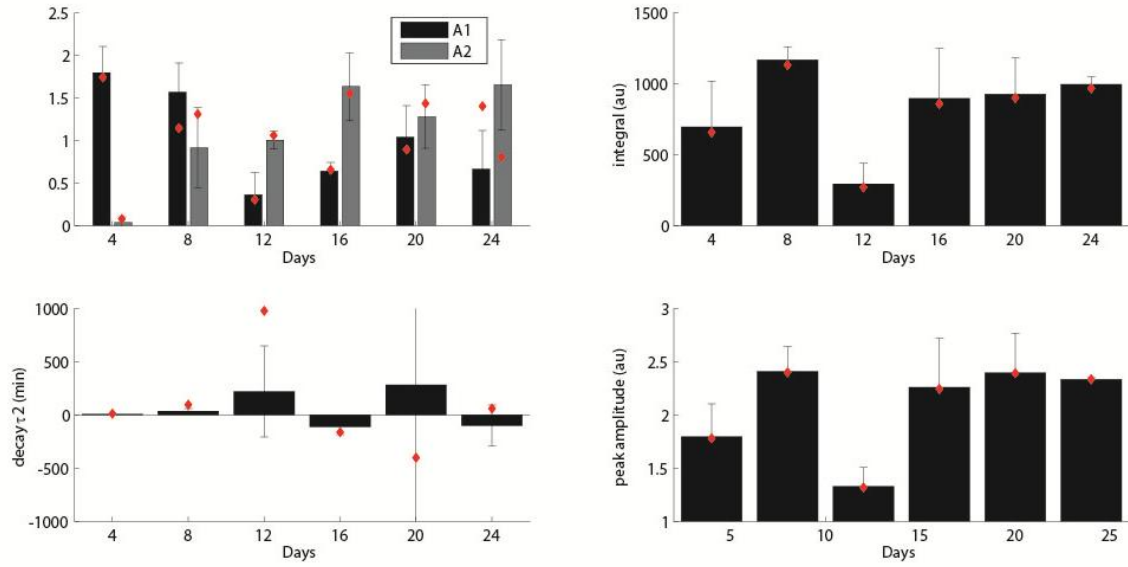


**Figure C.S1:** Age related  $\text{Ca}^{2+}$  changes in CD8<sup>+</sup> T cells. a) Amplitude of the exponential decays. b) Area under the curve. c) Second decay time constant. d) Peak amplitude For c-d), the data represents the mean of each calculated parameters for each donor and its standard deviation. The red diamonds correspond to the parameter calculated if the  $\text{Ca}^{2+}$  time courses are averaged for all donors for a specific day in culture.

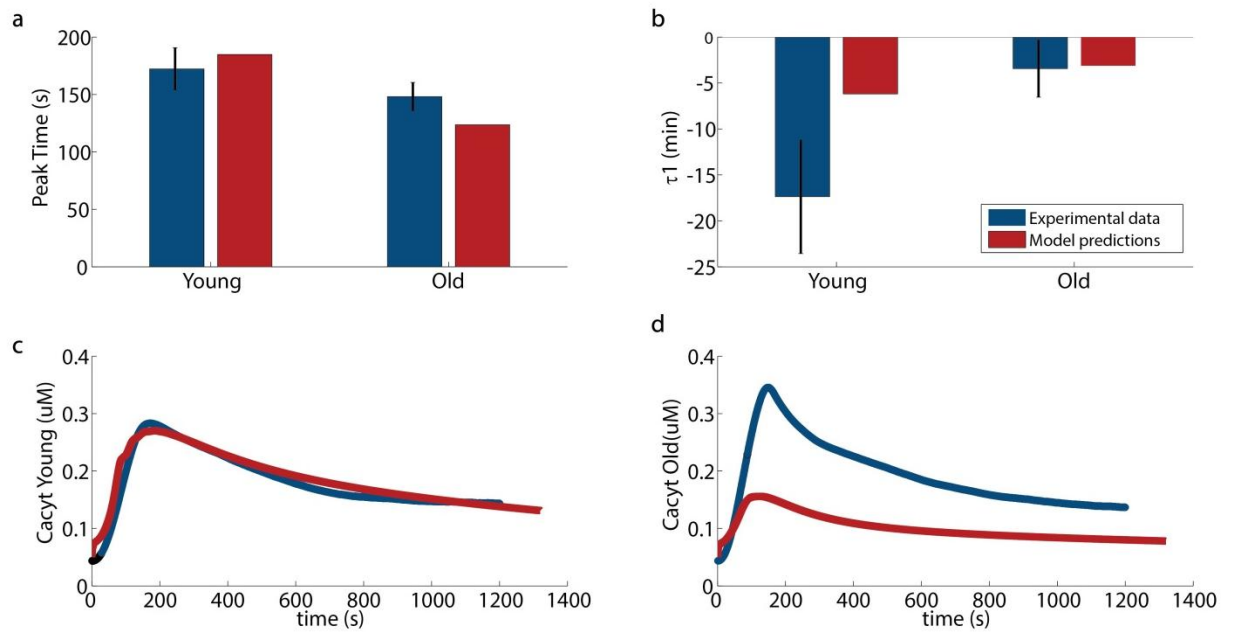


**Figure C.S2:** Effect of increased expression of PMCA and CRAC channels. a) Time to peak b) Decay time constant  $\tau_1$ . c)  $\text{Ca}^{2+}$  time course for young cells (day 4-8) d)  $\text{Ca}^{2+}$  time course for old cells (day 20-24).

**Table C.T1:** Relative mRNA levels of the major  $\text{Ca}^{2+}$  channels and pumps expressed in primary CD8+ T cells (n=6) and Jurkat cells (n=2). Relative gene expression is presented in terms of  $C_T$  normalized to actin levels.

|                 | Young T cells   | Old T cells     | Jurkat T cells  |
|-----------------|-----------------|-----------------|-----------------|
| <b>SERCA 2b</b> | $4.78 \pm 0.1$  | $4.94 \pm 0.2$  | $4.98 \pm 0.23$ |
| <b>SERCA 3</b>  | $4.89 \pm 0.27$ | $4.68 \pm 0.3$  | $5.52 \pm 0.61$ |
| <b>PMCA</b>     | $7.41 \pm 0.29$ | $6.60 \pm 0.25$ | $3.70 \pm 2.8$  |
| <b>IP3R2</b>    | $5.31 \pm 0.25$ | $4.96 \pm 0.34$ | $9.01 \pm 2.1$  |
| <b>IP3R3</b>    | $9.23 \pm 0.09$ | $9.46 \pm 0.21$ | $8.95 \pm 2.1$  |
| <b>ORAI1</b>    | $8.81 \pm 0.3$  | $8.04 \pm 0.29$ | $3.33 \pm 1.2$  |

## APPENDIX D

### APPENDIX CHAPTER 6

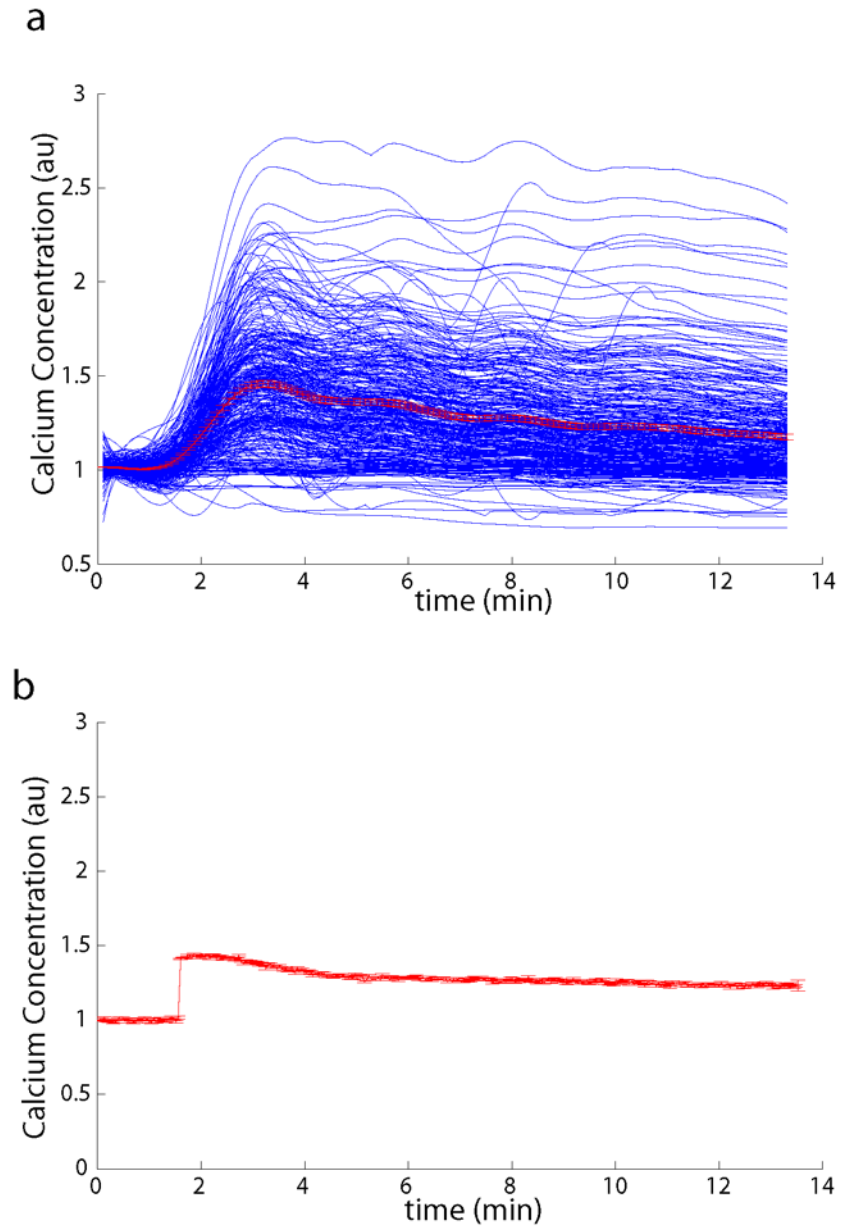


**Figure DS1.** Calcium kinetics of Jurkat cell in response to 2.5  $\mu\text{M}$  of ionomycin. a) Measurements using microfluidic single-cell trap array. b) Measurements by flow cytometry.

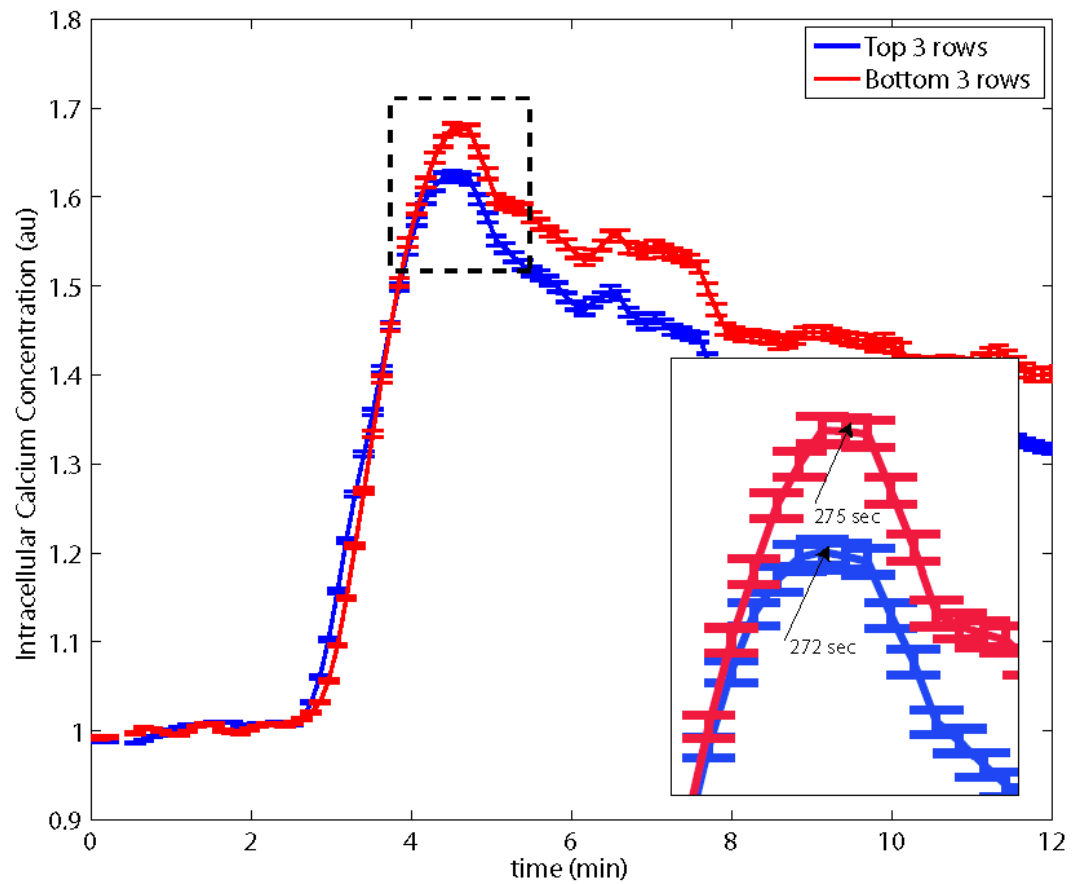


**Figure D.S2.** Calcium kinetics of Jurkat cell in response to 2.5  $\mu\text{M}$  of ionomycin. The average response of  $\sim 70$  cells in the top 3 rows and bottom 3 rows of the trap array shows little delay in the arrival of the stimulus for cells in the top versus the bottom of the array.



## Standard Operating Procedure for Cell Traps

Catherine Rivet, Kwanghun Chung, Melissa Kemp, Hang Lu

March 2012

### Required Items:

1. One microfluidic cell trap chip
2. A 5mL syringe filled with a solution of PBS, 2% w/v BSA (at room temperature) connected to a 0.2 $\mu$ m syringe filter (VWR #28144-050) and a 23 gauge needle (McMaster-Carr)
3. A pipette tip for 20-200 $\mu$ L pipettes
4. A 1.5mL tube containing 10<sup>6</sup> cells in 250  $\mu$ L of media
5. 25 cm of polyethylene tubing (0.023'' ID; 0.039'' OD, Scientific Commodities, BB31695-PE/3)

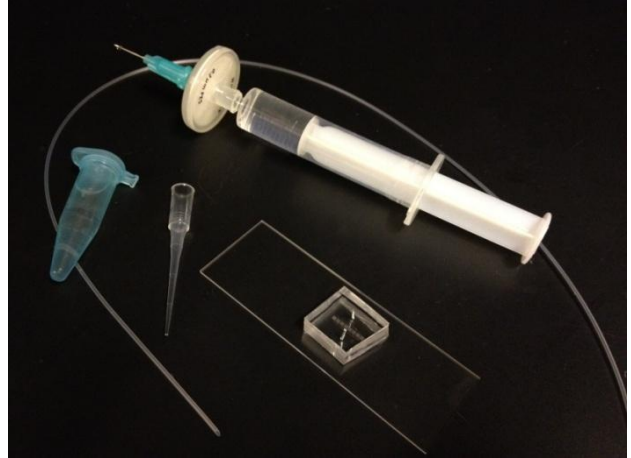


**Figure 1:** Required Apparatus

### Procedure:

1. Connect the syringe to the tubing and fill the tubing with the PBS, 2% BSA solution to remove any residual dust inside the tubing.

*NB:* Prepare 50mL of sterile filtered solution PBS, 2% BSA to test several chips. Leftover solution can be stored at 4C.

2. Connect the tubing to the outlet of the device (Figure 2).

*NB:* The inlet hole is the hole with the biggest outer diameter on the provided chips.

3. Place the chip connected with the syringe on the microscope stage (Figure 3a).

*NB:* To facilitate handling of the chip, it is easier to tape the syringe higher up than the microscope stage to allow liquid flow in the chip.

4. Press on the syringe to fill the device with solution. Make sure there are no leftover bubbles in the inlet filter area (Figure 3b). A small drop of solution should form on the inlet hole (Figure 3c).

*NB:* Priming the device with a solution of PBS, 2% BSA allows for the removal of any remaining bubbles and also prevents undesirable cell sticking to the channels by coating the surface with BSA.

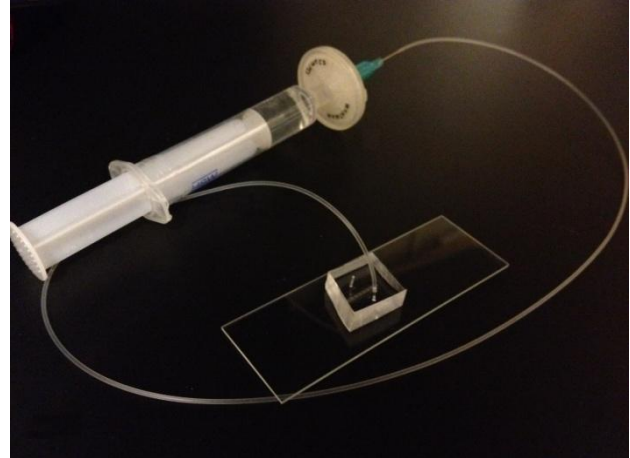


**Figure 2:** Connect a tubing filled with PBS, 2% BSA solution to the chip outlet.

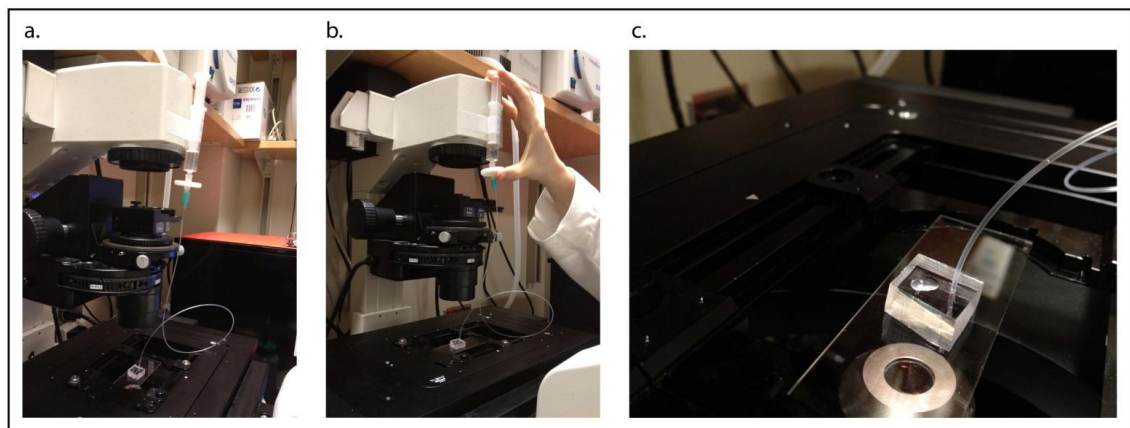


**Figure 3:** Chip priming. a) Place the chip on the microscope stage. b) Fill the chip with the PBS, 2% BSA solution. c) A small drop of liquid forms on the inlet hole.

5. Wet a pipette tip and insert it in the inlet hole (Figure 4a-b). Keep pressing on the syringe to ensure sufficient volume of solution in the pipette tip (~ 1cm high).

6. Clean the surface of the chip to get rid of excess solution. Disconnect the syringe from the tubing and tape the tubing below the chip (~15cm) to allow some solution to flow through the device (Figure 4c).

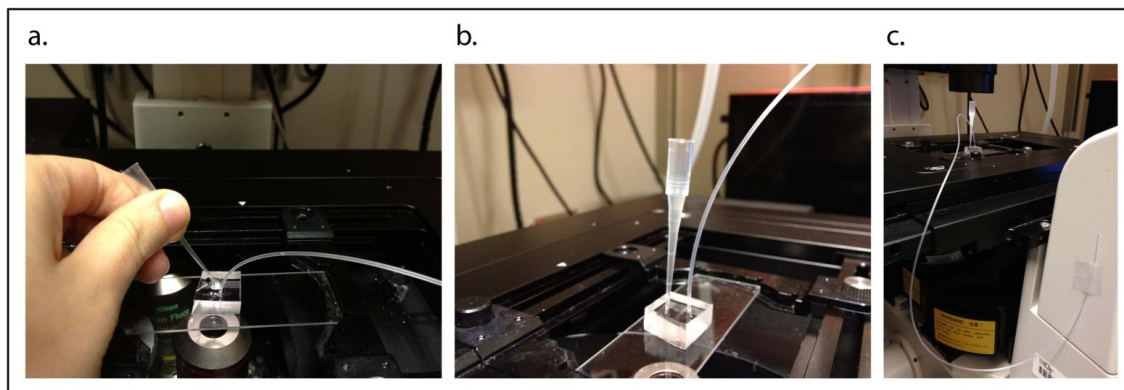


**Figure 4:** a-b) Insert a pipette tip in the inlet hole. c) Tape the outlet tubing below the microscope stage.

7. Pipette 10 $\mu$ L of cell solution in the inlet pipette tip. Wait for a few minutes for the cells to settle down in the pipette tip and start arriving in the chip. When the cells arrive in the chip, adjust the height of the outlet tubing to avoid large flowrate leading to cells squeezing through the trap gap (Figure 5).

*NB1:* If one desires to load cells faster, directly pipette the cells (10  $\mu$ L) inside this inlet hole, making sure that no air bubbles are getting introduced. Make sure to break cell clumps before loading. If the cells to be used tend to be very sticky, use a cell strainer before loading them.

*NB 2:* Because cells have different sizes and mechanical properties, the height of the outlet tubing should be adjusted empirically. A typical flowrate to be used to trap cells and to deliver chemicals to trapped cells ranges from 1-5 $\mu$ L/hour.

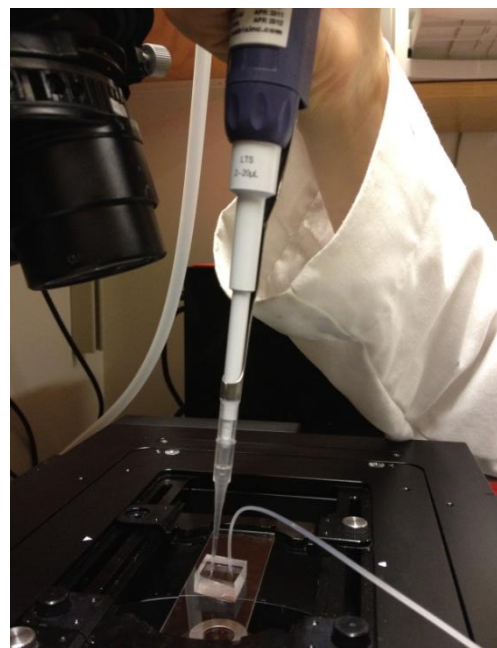
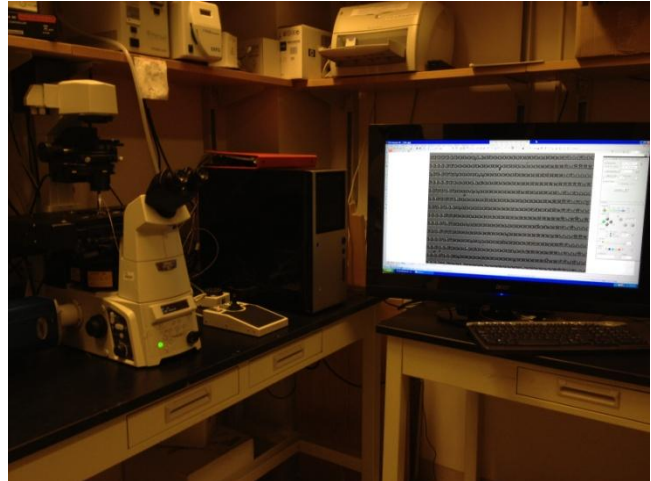


**Figure 5:** Cell loading.

*NB 3:* For long term experiments, one should equilibrate the microfluidic chip at the appropriate environmental conditions to allow cell survival ( $O_2$ ,  $CO_2$ , and temperature).

*NB 4:* If the flow stops, or cells come out of the traps, make sure there is no air bubble or debris clogging the device.



## APPENDIX E

### APPENDIX CHAPTER 7

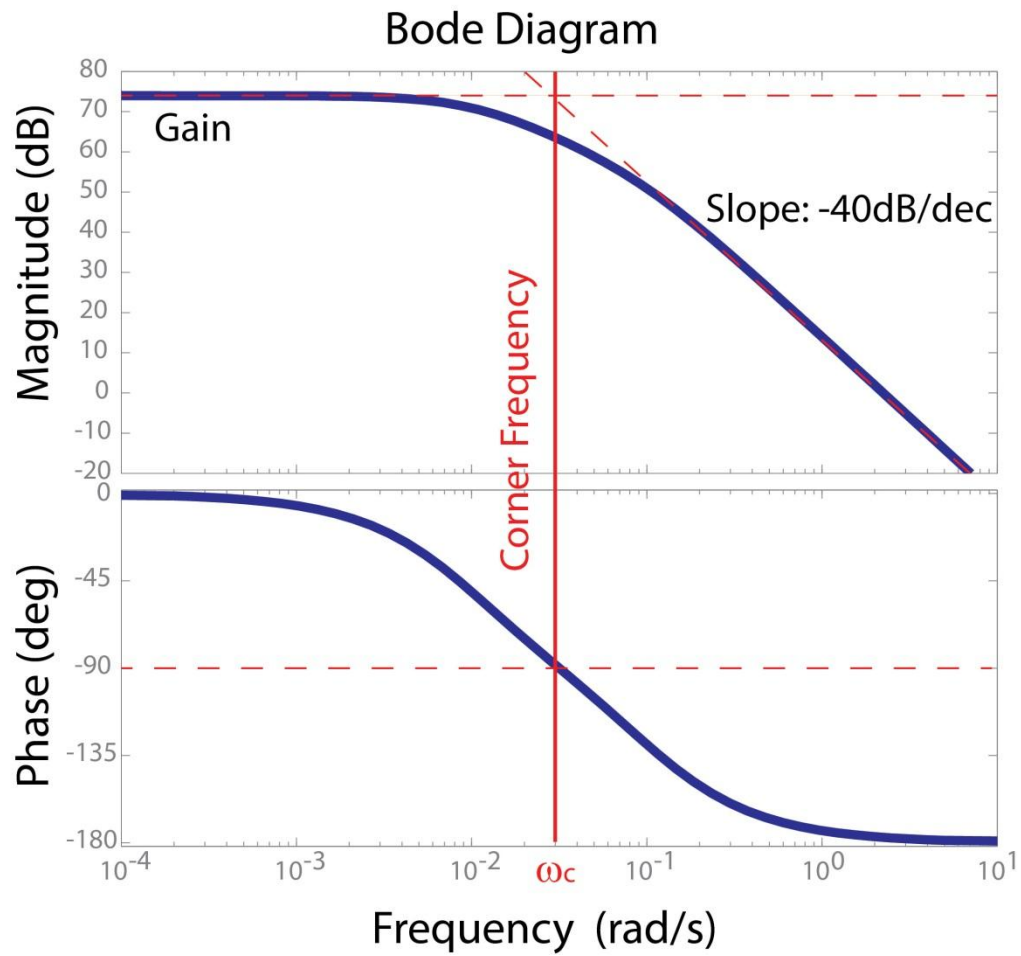


**Figure E.S1:** Bode plots (gain and phase) for a second order low pass filter transfer function

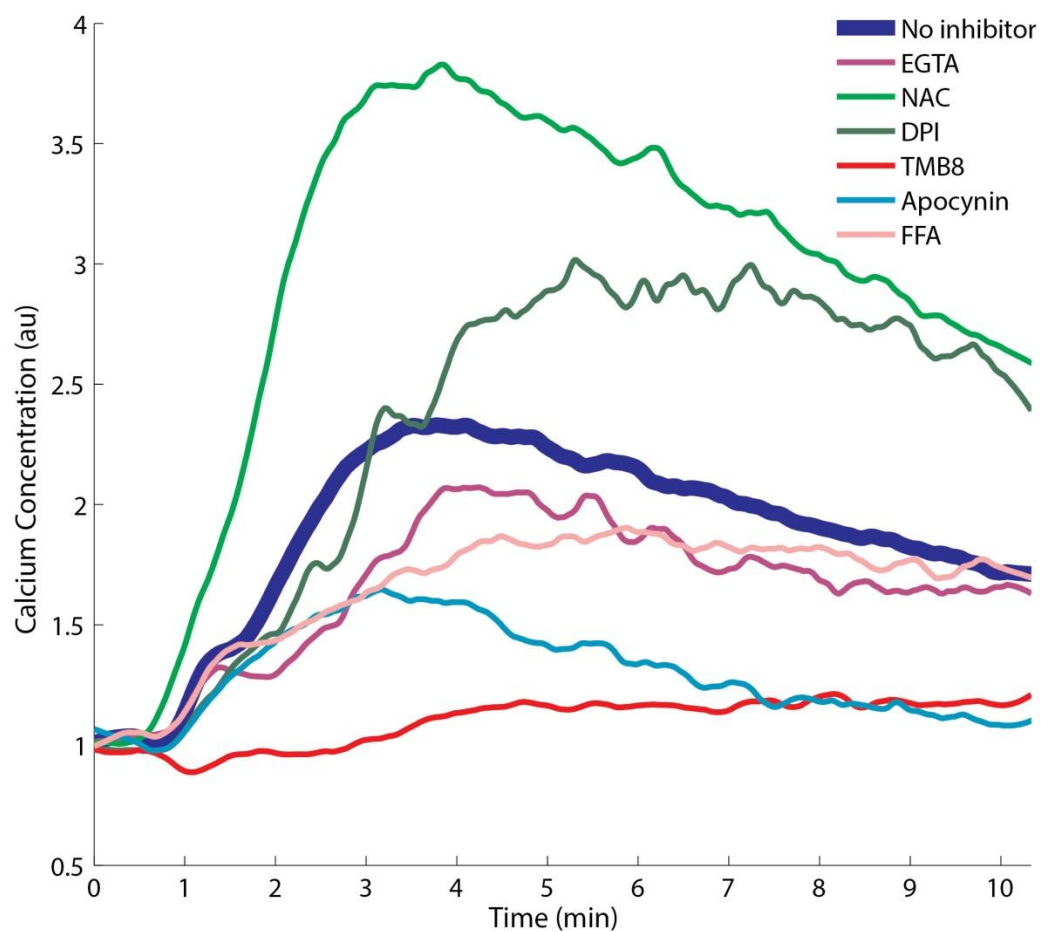


**Figure E.S2:** Representative traces of  $\text{Ca}^{2+}$  dynamics following exogenous addition of 25  $\mu\text{M}$   $\text{H}_2\text{O}_2$  in no inhibitor condition (blue), 5mM NAC (green), 2  $\mu\text{M}$  DPI (dark green), 10  $\mu\text{M}$  Apocynin (light blue), 0.05 mM EGTA (magenta), 100  $\mu\text{M}$  TMB-8 (red) and 100  $\mu\text{M}$  FFA (pink).

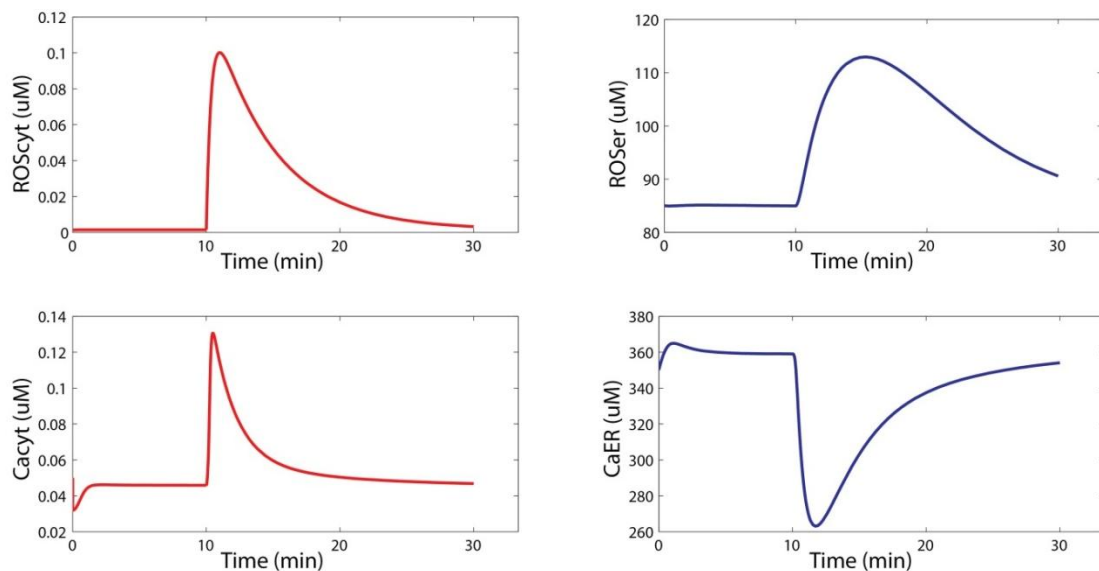


**Figure E.S3:** Model predictions to a bolus of 100  $\mu\text{M}$   $\text{H}_2\text{O}_2$  at  $t=10$  min. Note the faster  $\text{Ca}^{2+}$  dynamics than ROS to return to steady state levels.

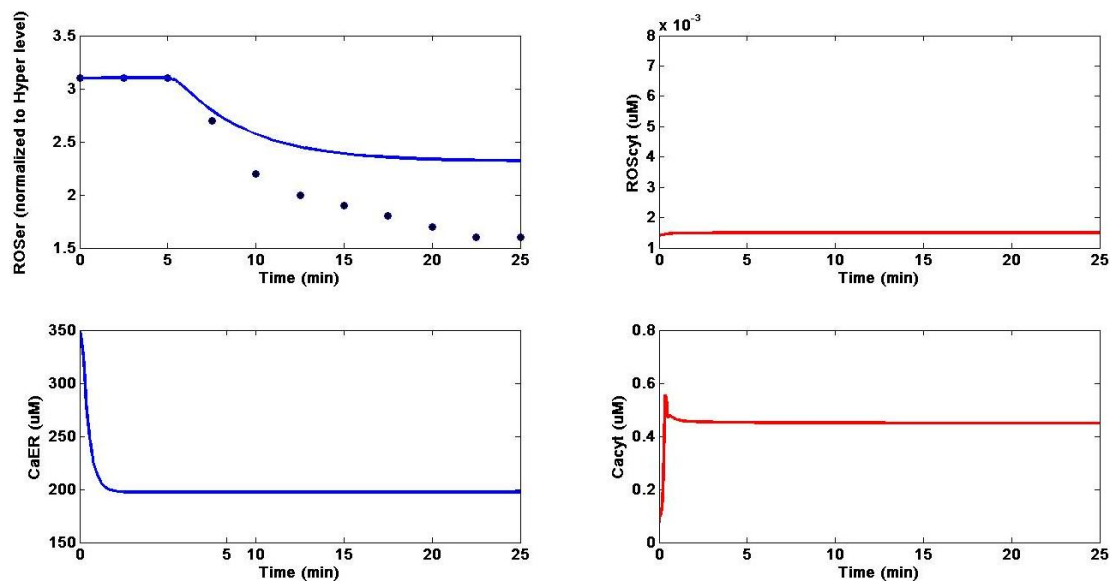


**Figure E.S4:** Model predictions to thapsigargin treatment at time=5min, modeled by reducing the maximal velocity of the SERCA pump to 85% its initial value. ER  $\text{Ca}^{2+}$  is depleted to 200  $\mu\text{M}$  and cytoplasmic  $\text{Ca}^{2+}$  levels stay elevated to 0.5  $\mu\text{M}$ .



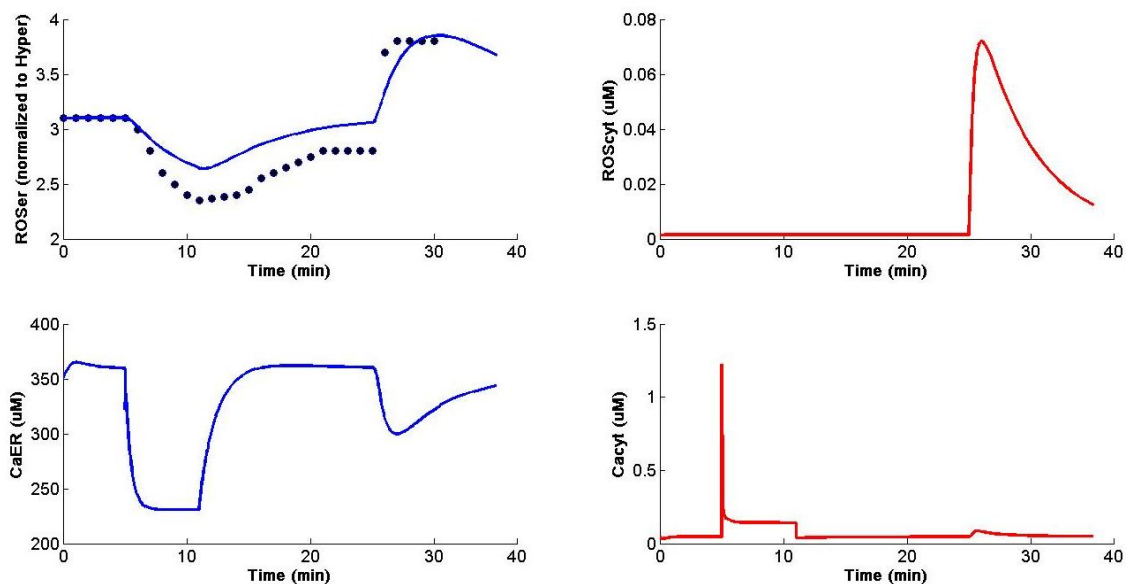
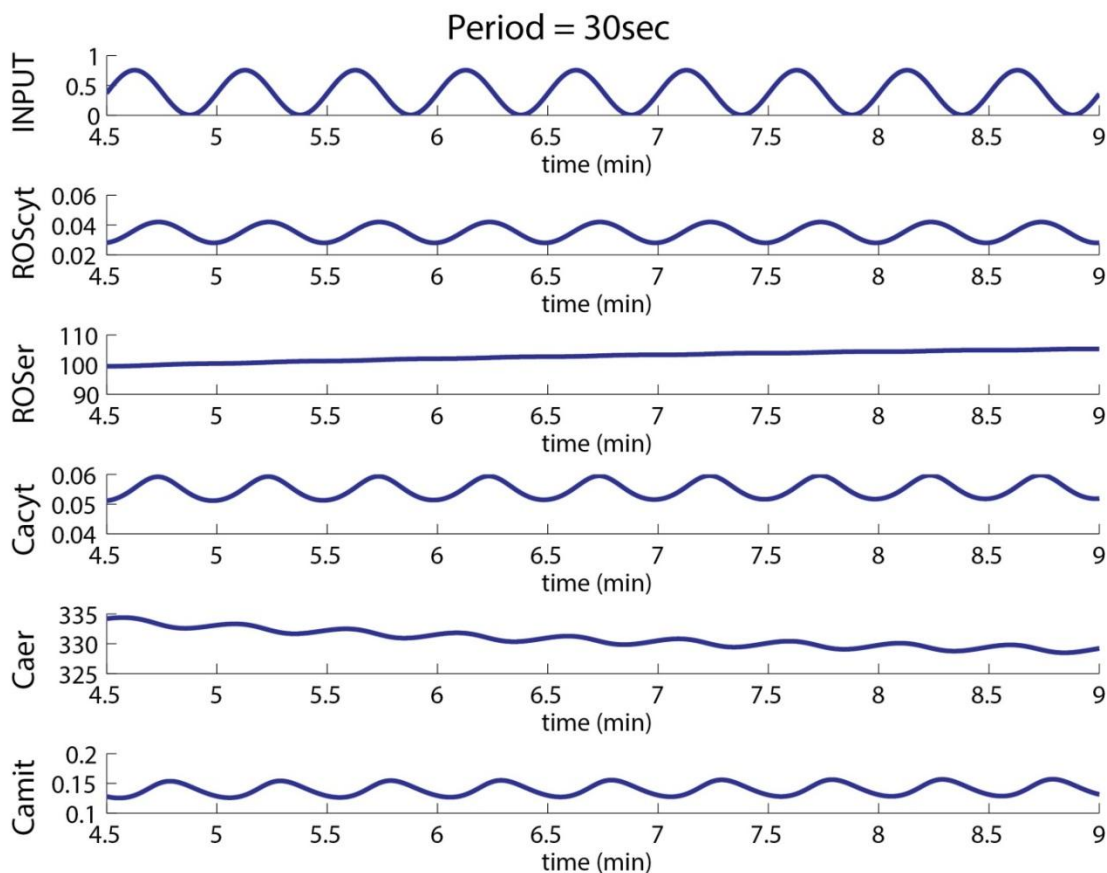


**Figure E.S5:** Model predictions to histamine treatment at time=5 min followed by a bolus of 100  $\mu\text{M}$   $\text{H}_2\text{O}_2$  at time  $t=25$  min, modeled by forcing the  $\text{IP}_3$  levels to be at 5  $\mu\text{M}$  between  $t=5$  min and  $t=10$  min. We observe an increase in cytoplasmic  $\text{Ca}^{2+}$  in response to histamine and  $\text{H}_2\text{O}_2$  treatment.



**A7S6:** Time course of the various species in the system to a 30 seconds period input stimulus. Note the non-linear behavior of both species in the ER.



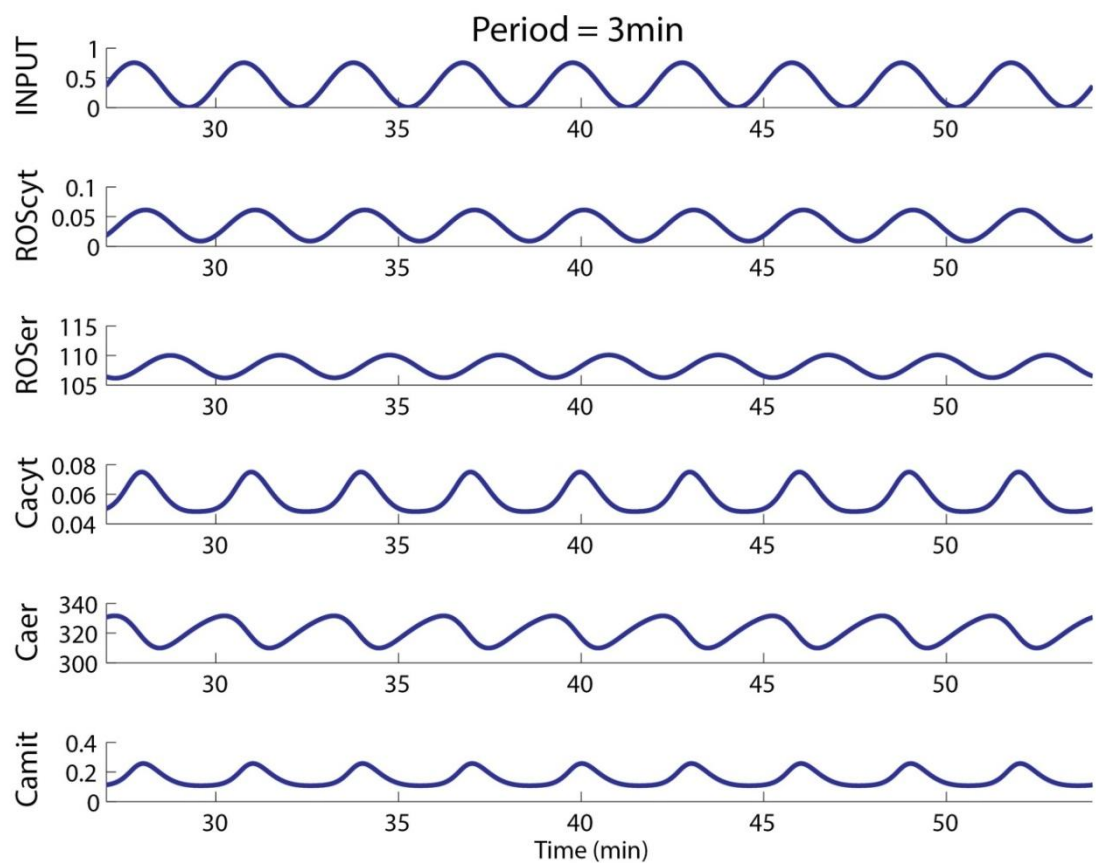


**Figure E.S7:** Time course of the various species in the system to a 3 min period input stimulus. The ROS levels in the ER now follow the input stimulus. The  $\text{Ca}^{2+}$  levels in the ER and in the mitochondria show a periodic behavior; however they do not display a perfectly sinusoidal behavior.

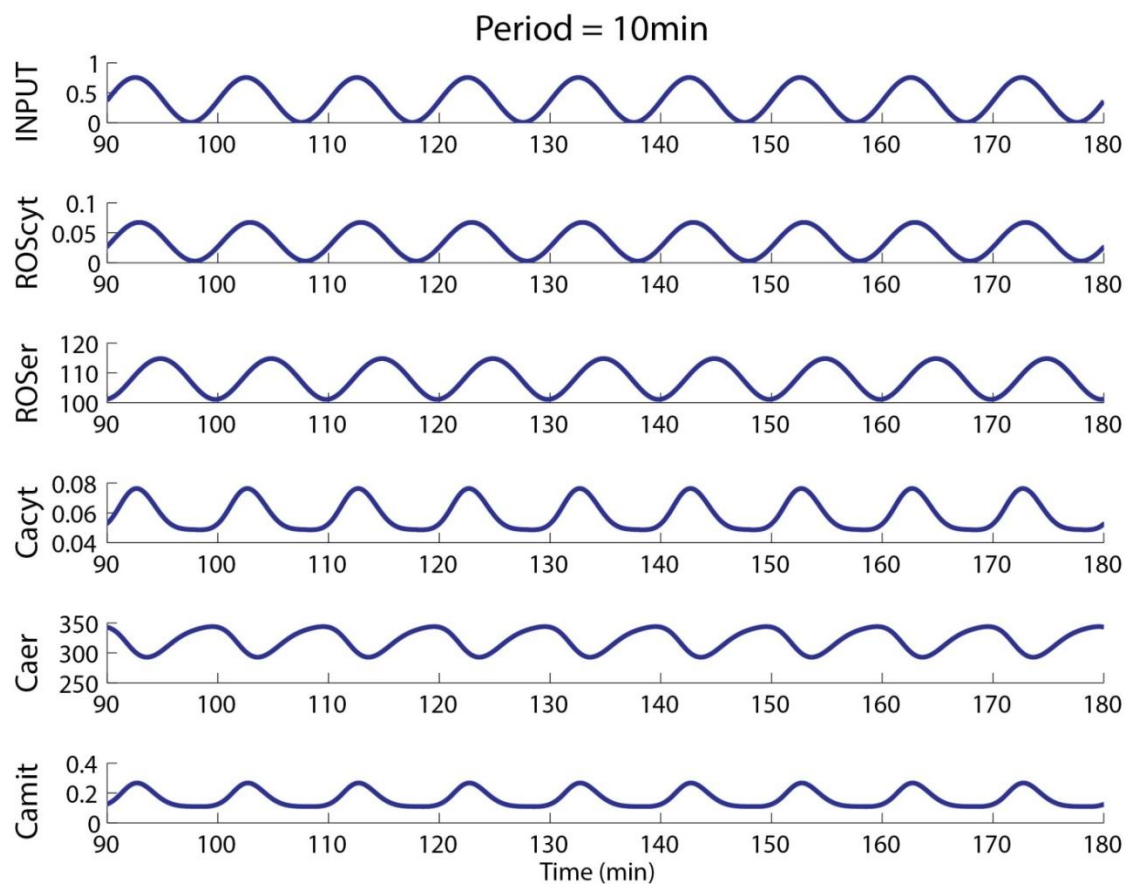


**Figure E.S8:** Time course of the various species in the system to a 10 minute period input stimulus.

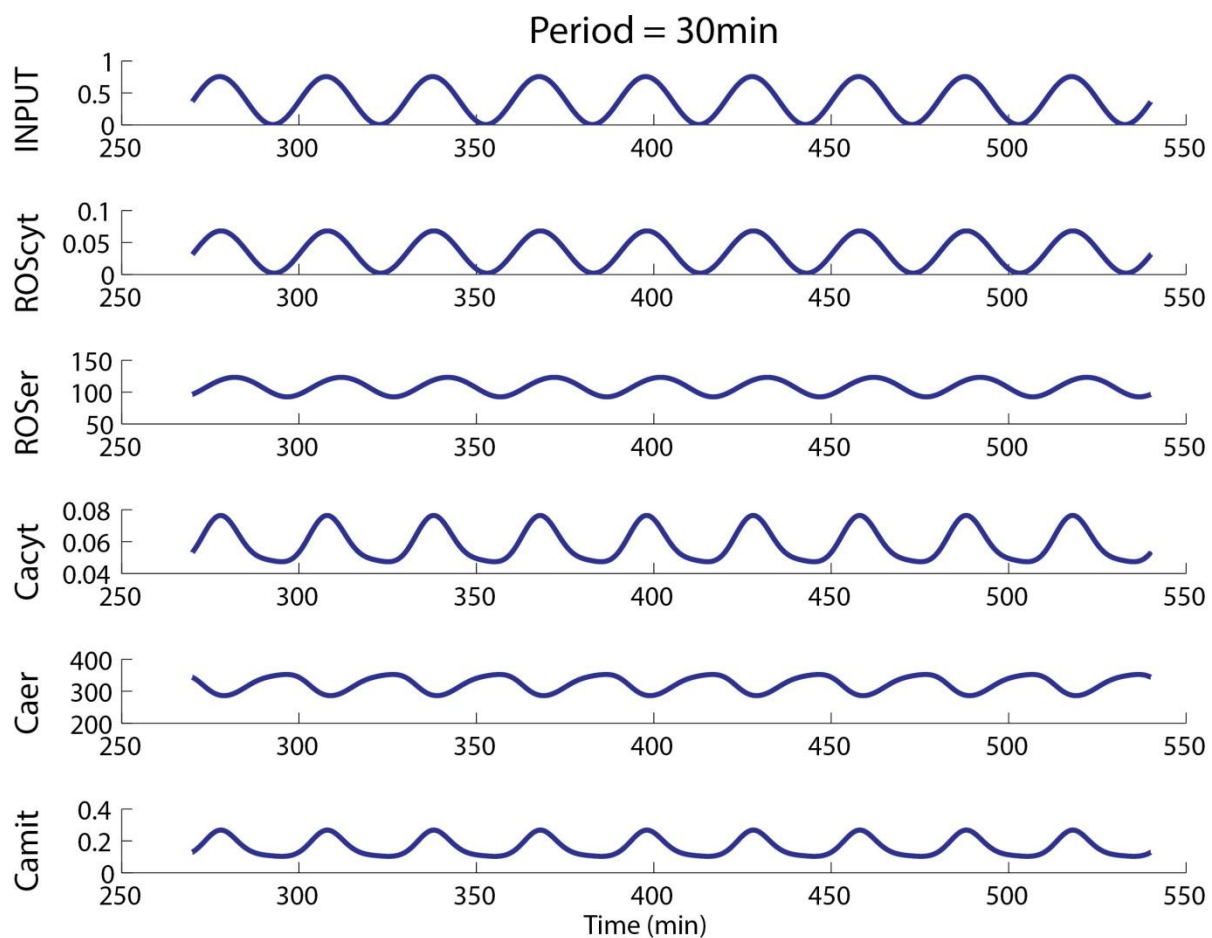


**Figure E.S9:** Time course of the various species in the system to a 30 minute period input stimulus.

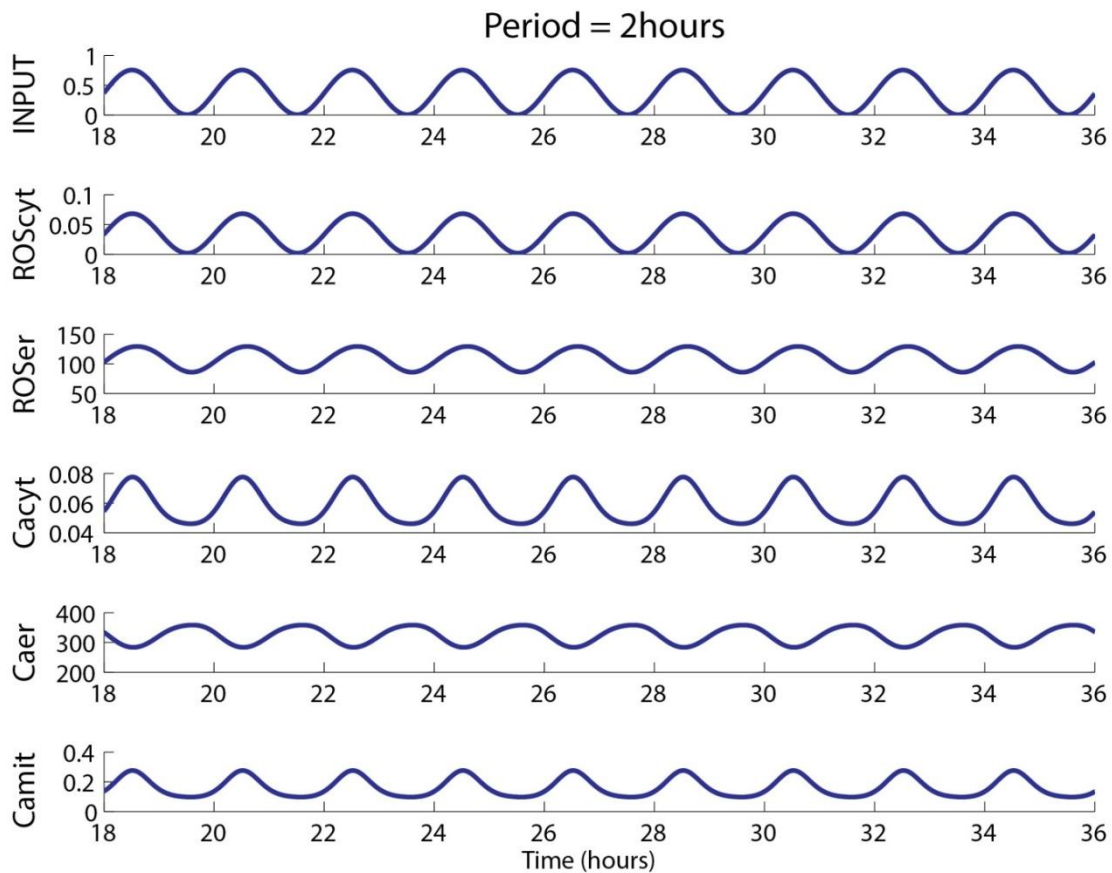


**Figure E.S10:** Time course of the various species in the system to a 30 minute period input stimulus.

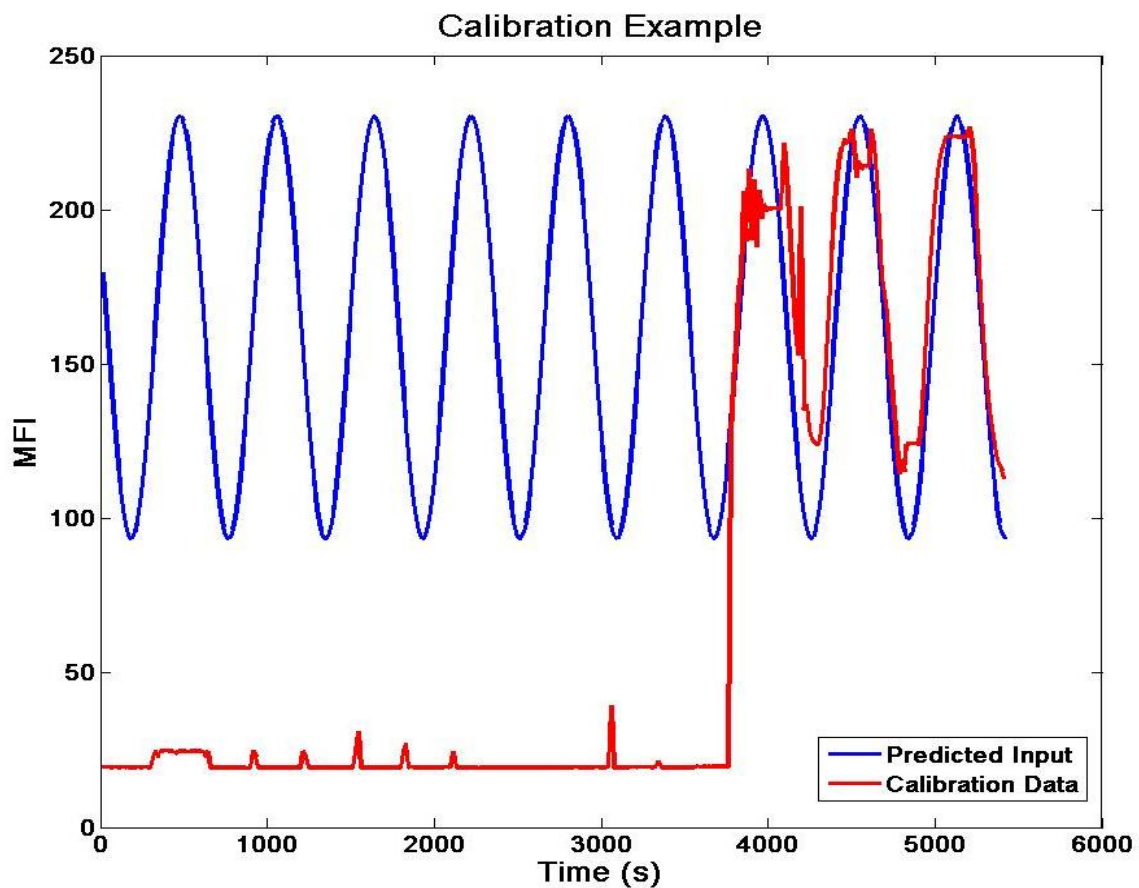
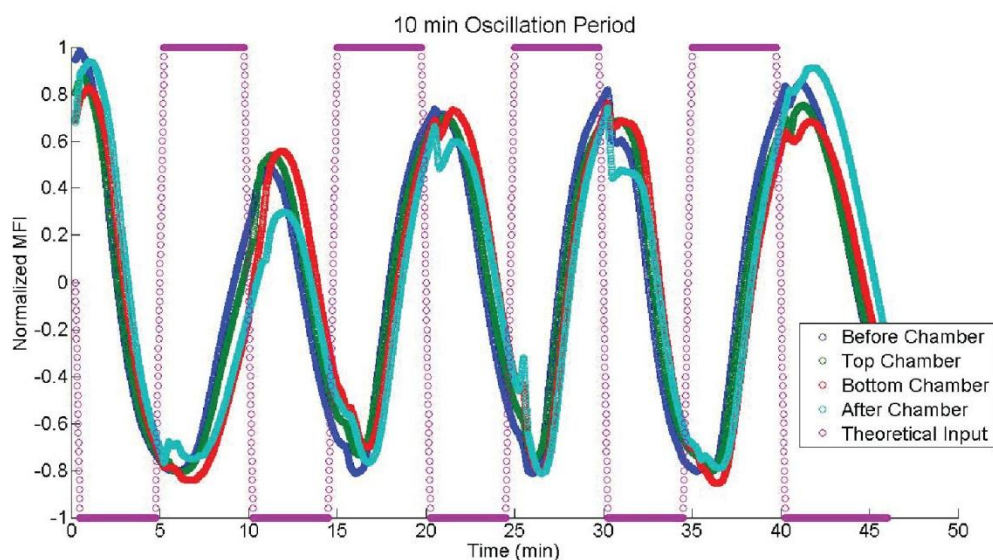


**Figure E.S11:** Calibration example. After the completion of a biological experiment, periods of buffer and a fluorescent fluid should be generated in the same device to measure the oscillation pattern and quantify the time delay of the real signal from the ideal input. A sinusoidal curve can be fitted to the experimental data and be used as the real input signal when cell responses are quantified.

a



b

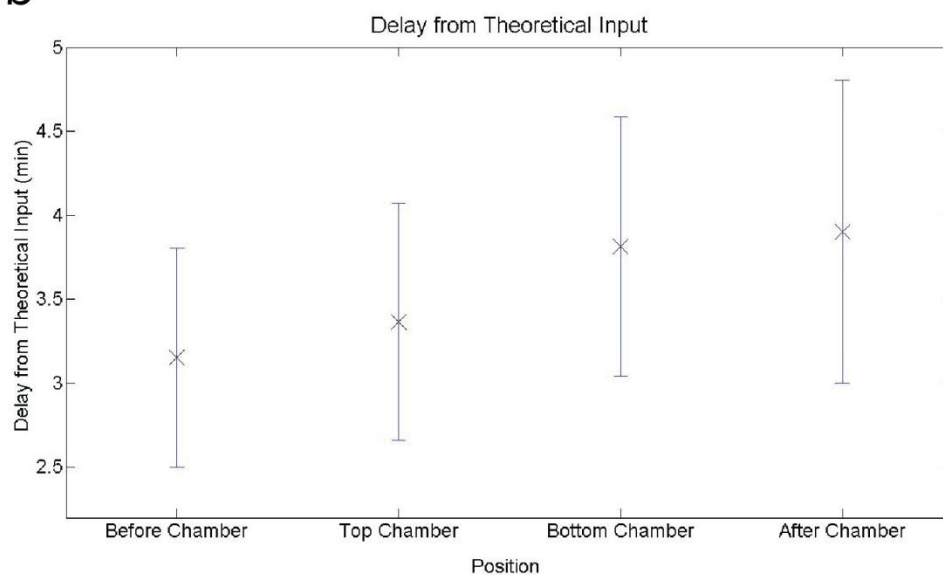


**Figure E.S12:** Characterization of a 10 min chemical pulse in terms of position in the chip. a) Comparison of a theoretical pulse input and the signal observed by the cells in different locations in a specific chip. b) Quantification of the delay, defined as the time difference between the maximum of the output and the maximum of the input, if considered as a sinusoid. Data are displayed as mean  $\pm$  sd, averaged across 4 periods and 3 different devices.

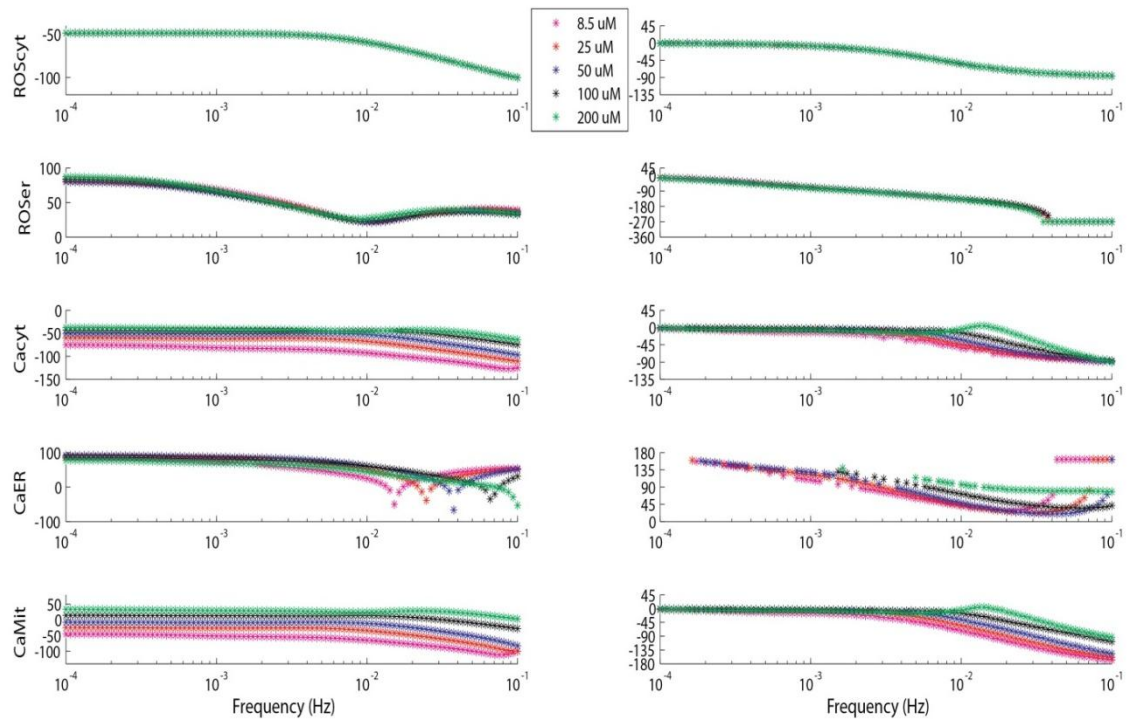


**Figure E.S13:** Amplitude effect on the phase and gain of the system demonstrating the non-linearity of the system.



## APPENDIX F

### CA<sup>2+</sup> SIGNALING MODEL

```
%% Model for parameter optimization
%%-----%%
function S = OFModel11(b)
global tdata xdata x0 CaEx
%% EGTA Model
function dx = f1(t,x)
    CaEx=500;
    dx = zeros(7,1);
    Jplcact= 0.0045*x(3); %activation of PLCp by ligand binding
    Jplcdeact= 0.0396*x(2); %dephosphorylation of PLCp
    dx(3)=-Jplcact; %Ligand
    dx(2)= Jplcact-Jplcdeact; %PLCgammap

    Jplc= b(14)*x(2)*x(4); %production of IP3 from PLCp
    Jip3deg= b(15)*b(14)*x(1); %degradation of IP3 by phosphatase
    dx(1)=Jplc-Jip3deg;

    Jserca=b(1)*x(4)^2/(x(4)^2+b(2)^2); %%serca
    Jerleak = x(6)*b(5);

    Jip3=x(6)*b(10)*(x(1)/(x(1)+b(12)))^3*(x(4)/(x(4)+b(13)))^3*x(5)^3;
    b20=1*(x(1)+b(12))/(x(1)+b(20));
    dx(5)=b(19)*(b20-x(5)*(x(4)+b(20))); %h

    Jpmleak=b(8)*CaEx;
    Jcrac=b(7)*(b(9)^3/(b(9)^3+x(6)^3))*CaEx/(b(24)+CaEx);
    Jpmca=b(3)*(x(4).^2/(x(4).^2+b(4)^2))*((x(6).^4)/(x(6).^4+b(22).^4));
    Jmitin=b(16)*(x(4).^4/(x(4).^4+b(17)^4));
    Jmitout= b(18)*x(7)*(x(4)^2/(x(4)^2+b(23)^2));
    Jmitleak=b(6)*x(7);

    dx(4)=b(27)*(Jcrac-Jpmca-Jserca+Jerleak+Jip3+Jpmleak+Jmitout-Jmitin); %Cacyt
    dx(6)=b(11)*Jserca-b(11)*Jip3-b(11)*Jerleak; %CaER
    dx(7)=b(21)*Jmitin-b(21)*Jmitout; %Camit
end

%% No inhibitor condition model
function dx = f2(t,x)
    CaEx=1500;
    dx = zeros(7,1);
    Jplcact= 0.0045*x(3); %activation of PLCp by ligand binding
    Jplcdeact= 0.0396*x(2); %dephosphorylation of PLCp
    dx(3)=-Jplcact; %Ligand
    dx(2)= Jplcact-Jplcdeact; %PLCgammap

    Jplc= b(14)*x(2)*x(4); %production of IP3 from PLCp
    Jip3deg= b(15)*b(14)*x(1); %degradation of IP3 by phosphatase
```



```

dx(1)=Jplc-Jip3deg;
Jserca=b(1)*x(4)^2/(x(4)^2+b(2)^2); %%serca
Jerleak = x(6)*b(5);

Jip3=x(6)*b(10)*(x(1)/(x(1)+b(12)))^3*(x(4)/(x(4)+b(13)))^3*x(5)^
3; %Maurya , Chen...
b20=1*(x(1)+b(12))/(x(1)+b(20));
dx(5)=b(19)*(b20-x(5)*(x(4)+b20)); %h

Jpmleak=b(8)*CaEx;
Jcrac=b(7)*(b(9)^3./(b(9)^3+x(6)^3))*CaEx/(b(24)+CaEx);
Jpmca=b(3)*(x(4).^2./(x(4).^2+b(4)^2))*((x(6).^4)./(x(6).^4+b(22)
.^4)); %pmca
Jmitin=b(16)*(x(4).^4./(x(4).^4+b(17)^4));
Jmitout= b(18)*x(7)*(x(4)^2/(x(4)^2+b(23)^2);
Jmitleak=b(6)*x(7);

dx(4)=b(27)*(Jcrac-Jpmca-Jserca+Jerleak+Jip3+Jpmleak+Jmitout-
Jmitin); %Cacyt
dx(6)=b(11)*Jserca-b(11)*Jip3-b(11)*Jerleak; %CaER
dx(7)=b(21)*Jmitin-b(21)*Jmitout; %Camit
end

%% TMB8 Model
function dx = f3(t,x)
CaEx=1500;
dx = zeros(7,1);
Jplcact= 0.0045*x(3); %activation of PLCp by ligand binding
Jplcdeact= 0.0396*x(2); %dephosphorylation of PLCp
dx(3)=-Jplcact; %Ligand
dx(2)= Jplcact-Jplcdeact; %PLCgammmap

Jplc= b(14)*x(2)*x(4); %production of IP3 from PLCp
Jip3deg= b(15)*b(14)*x(1); %degradation of IP3 by phosphatase
dx(1)=Jplc-Jip3deg;

Jserca=b(1)*x(4)^2/(x(4)^2+b(2)^2); %%serca
Jerleak = x(6)*b(5);

Jip3=x(6)*b(10)*(x(1)/(x(1)+b(12)))^3*(x(4)/(x(4)+b(13)))^3*x(5)^
3; %Maurya , Chen...
b20=1*(x(1)+b(12))/(x(1)+b(20));
dx(5)=b(19)*(b20-x(5)*(x(4)+b20)); %h
Jip3=b(28)*Jip3;

Jpmleak=b(8)*CaEx;
Jcrac=b(7)*(b(9)^3./(b(9)^3+x(6)^3))*CaEx/(b(24)+CaEx);

Jpmca=b(3)*(x(4).^2./(x(4).^2+b(4)^2))*((x(6).^4)./(x(6).^4+b(22)
.^4)); %pmca
Jmitin=b(16)*(x(4).^4./(x(4).^4+b(17)^4
Jmitout= b(18)*x(7)*(x(4)^2/(x(4)^2+b(23)^2));
Jmitleak=b(6)*x(7);

dx(4)=b(27)*(Jcrac-Jpmca-Jserca+Jerleak+Jip3+Jpmleak+Jmitout-
Jmitin); %Cacyt

```

```

        dx(6)=b(11)*Jserca-b(11)*Jip3-b(11)*Jerleak; %CaER
        dx(7)=b(21)*Jmitin-b(21)*Jmitout; %Camit
    end

%% numerical integration set up
tspan = [0:0.1:max(tdata)];
[tsol1,xsol1] = ode23s(@f1,tspan,x0);
[tsol2,xsol2] = ode23s(@f2,tspan,x0);
[tsol3,xsol3] = ode23s(@f3,tspan,x0);

%% find predicted values x(tdata)
xpred1 = interp1(tsol1,xsol1,tdata);
xpred2 = interp1(tsol2,xsol2,tdata);
xpred3 = interp1(tsol3,xsol3,tdata);

%% compute total error
S=0;
for i=1:length(tdata)
    S = S + ((xpred1(i,1)-xdata(i,1))./xdata(i,1)).^2 ...
          + ((xpred1(i,4)-xdata(i,5))./xdata(i,5)).^2 ...
          + ((xpred2(i,4)-xdata(i,4))./xdata(i,4)).^2 ...
          + ((xpred3(i,4)-xdata(i,8))./xdata(i,8)).^2;
end

end

%% Parameter optimization
%%-----%%
function paramFitOFModel11

% main program for fitting parameters of an ODE model to data
% the model and the error function are defined in the file OFModel11.m

clearvars -global
global tdata xdata x0 CaEx;

%% initial conditions
x0(1) = 0.54; x0(2) = 0.07;
x0(3) = 10; x0(4)=0.05;
x0(5)=0.1; x0(6)=350;
x0(7)=0.1; CaEx=500; %uM

%% data for the model
load ExpData
xdata(:,2)=x0(2)*xdata(:,2); %plcgamma
xdata(:,4)=x0(4)*xdata(:,4); %Cacyt
xdata(:,5)=x0(4)*xdata(:,5); %Cacyt EGTA
xdata(:,8)=x0(4)*xdata(:,8); %Cacyt TMB8

%% initial guess of parameter values
lb=zeros(1,28);
ub=ones(1,28);

lb(14)=0.1; ub(14)=1;
lb(15)=0.01; ub(15)=0.1;

```

```

lb(1)=0.2; ub(1)=250; %Vserca
lb(2)=.15; ub(2)=0.8; %kserca

lb(3)=0.01; ub(3)=50; %Vpmca
lb(4)=0.1; ub(4)=0.5; %kPMCA
lb(22)=5; ub(22)=450; %% kSTIMPMCA full ER stores of Calcium 300uM

lb(5)=5e-4; ub(5)=0.05; %ERleak
lb(6)=1e-4; ub(6)=1e-2; %DirTransf
lb(10)=0.05; ub(10)=80; %IP3R
lb(12)=.1; ub(12)=1; %kIP3R
lb(13)=0.05; ub(13)=0.5; %kIP3Rca

lb(7)=0.01; ub(7)=10; %STIM
lb(8)=2.5e-7; ub(8)=3.5e-5; %PMleak
lb(9)=150; ub(9)=250; %kStim

lb(19)=0.01; ub(19)=0.5; %IP3Rinh
lb(20)=0.5; ub(20)=1.5; %IP3Rrecov
lb(21)=0.1; ub(21)=10; %kg

lb(16)=100; ub(16)=800; %Vmitin
lb(17)=0.5; ub(17)=1.5; %kMITIN

lb(18)=50; ub(18)=1000; %Vmitout
lb(23)=1; ub(23)=10; %kMITOUT

lb(11)=1; ub(11)=500; %ratio volume cytoplasm to ER
lb(24)=50; ub(24)=1000; %ratio volume cytoplasm to mitochondria
lb(25)=0.1; ub(25)=1;
lb(26)=1; ub(26)=8;
lb(27)=1e-3; ub(27)=10;
lb(28)=0.1; ub(28)=0.5;

popsize=100;
M=zeros(popsize,length(lb));
for i=1:popsize
    for j=1:length(lb)
        M(i,j)=10^(log10(lb(j))+rand*(log10(ub(j))-log10(lb(j))));
    end
end

%% minimization step
load('bfinal');
b= bmin;

% options=gaoptimset('PopulationSize',popsize,'InitialPopulation',M,...
%'PlotFcns',{@gaplotbestf,@gaplotscores,@gaplotselection,@gaplotdistanc
e});
%[bmin,Smin,exitflag]=ga(@OFModel11,length(lb),[],[],[],[],lb,ub,[],opt
ions);

% options=optimset('PlotFcns',{@optimplotfval,@optimplotstepsize});

```

```

% [bmin, Smin,exitflag] =
fmincon(@OFModel11,b,[],[],[],[],lb,ub,[],options);

% options=psoptimset('PlotFcns',{@psplotbestf,@psplotmeshsize});
% [bmin, Smin,exitflag] =
patternsearch(@OFModel11,b,[],[],[],[],lb,ub,[],options);

% options=saoptimset('PlotFcns',{@saplotbestf,@saplotbestx, @saplotf,
@saplottemperature});
% [bmin, Smin,exitflag] = simulannealbnd(@OFModel11,b,lb,ub,options);

disp('Estimated parameters b(i):');
disp(bmin)
disp('Smallest value of the error S:');
disp(Smin)
save('bnice2','bmin')
end

%% Solve model once parameters are known and plot
%%-----%%
function solveModel11
global b CaEx x0 tdata xdata

%% data for the model
x0(5)=0.5;
load ExpData
xdata(:,2)=x0(2)*xdata(:,2); %plcgamma
xdata(:,4)=x0(4)*xdata(:,4); %Cacyt
xdata(:,5)=x0(4)*xdata(:,5); %Cacyt EGTA
xdata(:,8)=x0(4)*xdata(:,8); %Cacyt TMB8

tdata1=60*[0 1 2 3 5 10];
xdata1=[0.54 2.46 4 5.62 3.38 1.54];
xdata2=[1 12 8.9 6.5 4.6 1.9];

load('bfinal');
b= bmin;
binit=b;

tspan = [0:0.1:3*max(tdata)];
[tsol1,xsol1] = ode23s(@f1,tspan,x0);
[tsol2,xsol2] = ode23s(@f2,tspan,x0);
[tsol3,xsol3] = ode23s(@f3,tspan,x0);

% figure (1),
%     plot(tdata1,x0(2)*xdata2,'x','MarkerSize',6);
%     hold on
%     plot(tsol2(1:end),xsol2(1:end,2),'r','LineWidth',3);
%     ylabel('pPLCgamma (uM)')
%     xlabel('time (s)')

figure (2),
    subplot(4,3,1)
    plot(tdata1,xdata1,'o','MarkerSize',1);

```

```

hold on
plot(tsol1(1:end),xsol1(1:end,1),'k','LineWidth',3);
ylabel('IP3 (uM)'); ylim=[0 6]; xlabel('time (s)');
title('EGTA');

subplot(4,3,2)
plot(tdata1,xdata1,'o','MarkerSize',6);
hold on
plot(tsol2(1:end),xsol2(1:end,1),'k','LineWidth',3);
ylabel('IP3 (uM)'); ylim=[0 6]; xlabel('time (s)'); title('No
Inhibitor');

subplot(4,3,3)
plot(tdata1,xdata1,'o','MarkerSize',6);
hold on
plot(tsol3(1:end),xsol3(1:end,1),'k','LineWidth',3);
ylabel('IP3 (uM)'); ylim=[0 6]; xlabel('time (s)');
title('TMB8')

% subplot(2,3,1)
% plot(tsol1(1:end),xsol1(1:end,3),'r','LineWidth',3);
% ylabel('Ligand (au)');
% xlabel('time (s)')
%
% subplot(2,3,2)
% plot(tdata1,xdata2,'x','MarkerSize',6);
% hold on
% plot(tsol1(1:end),xsol1(1:end,2),'r','LineWidth',3);
% ylabel('pPLCgamma (uM)')
% xlabel('time (s)')

subplot(4,3,4)
plot(tdata(1:end),xdata(1:end,5),'o','MarkerSize',6);
hold on
plot(tsol1(1:end),xsol1(1:end,4),'k','LineWidth',3);
ylabel('Cacyt (uM)');ylim=[0 0.5]; xlabel('time (s)')

subplot(4,3,5)
plot(tdata(1:end),xdata(1:end,4),'o','MarkerSize',6);
hold on
plot(tsol2(1:end),xsol2(1:end,4),'k','LineWidth',3);
ylabel('Cacyt (uM)'); ylim=[0 0.5]; xlabel('time (s)')

subplot(4,3,6)
plot(tdata(1:end),xdata(1:end,8),'o','MarkerSize',6);
hold on
plot(tsol3(1:end),xsol3(1:end,4),'k','LineWidth',3);
ylabel('Cacyt (uM)'); ylim=[0 0.5]; xlabel('time (s)')

subplot(4,3,7)
plot(tdata(1:end),xdata(1:end,6),'o','MarkerSize',6);
hold on
plot(tsol1(1:end),xsol1(1:end,6),'k','LineWidth',3);
ylabel('CaER (uM)'); ylim=[0 400]; xlabel('time (s)')

```

```

subplot(4,3,8)
plot(tdata(1:end),xdata(1:end,6),'o','MarkerSize',6);
hold on
plot(tsol2(1:end),xsol2(1:end,6),'k','LineWidth',3);
ylabel('CaER (uM)');ylim=[0 400]; xlabel('time (s)')

subplot(4,3,9)
plot(tdata(1:end),xdata(1:end,6),'o','MarkerSize',6);
hold on
plot(tsol3(1:end),xsol3(1:end,6),'k','LineWidth',3);
ylabel('CaER (uM)');ylim=[0 400]; xlabel('time (s)')

subplot(4,3,10)
plot(tdata(1:end),xdata(1:end,7),'x','MarkerSize',6);
hold on
plot(tsol1(1:end),xsol1(1:end,7),'k','LineWidth',3);
ylabel('CaMit (uM)'); ylim=[0 10]; xlabel('time (s)')
subplot(4,3,11)
plot(tdata(1:end),xdata(1:end,7),'x','MarkerSize',6);
hold on
plot(tsol2(1:end),xsol2(1:end,7),'k','LineWidth',3);
ylabel('CaMit (uM)'); ylim=[0 10]; xlabel('time (s)')
subplot(4,3,12)
plot(tdata(1:end),xdata(1:end,7),'x','MarkerSize',6);
hold on
plot(tsol3(1:end),xsol3(1:end,7),'k','LineWidth',3);
ylabel('CaMit (uM)'); ylim=[0 10]; xlabel('time (s)')

figure(2),
subplot(4,3,1)
plot(tdata1,xdata1,'o','MarkerSize',1);
hold on
plot(tsol1(1:end),xsol1(1:end,1),'k','LineWidth',3);
ylabel('IP3 (uM)'); ylim=[0 6]; xlabel('time (s)');
title('EGTA');

subplot(4,3,2)
plot(tdata1,xdata1,'o','MarkerSize',6);
hold on
plot(tsol2(1:end),xsol2(1:end,1),'k','LineWidth',3);
ylabel('IP3 (uM)'); ylim=[0 6]; xlabel('time (s)'); title('No
Inhibitor');

subplot(4,3,3)
plot(tdata1,xdata1,'o','MarkerSize',6);
hold on
plot(tsol3(1:end),xsol3(1:end,1),'k','LineWidth',3);
ylabel('IP3 (uM)'); ylim=[0 6]; xlabel('time (s)');
title('TMB8')

% subplot(2,3,1)
% plot(tsol1(1:end),xsol1(1:end,3),'r','LineWidth',3);
% ylabel('Ligand (au)');
% xlabel('time (s)')
%
% subplot(2,3,2)

```

```

%     plot(tdata1,xdata2,'x','MarkerSize',6);
%     hold on
%     plot(tsol1(1:end),xsol1(1:end,2),'r','LineWidth',3);
%     ylabel('pPLCgamma (uM)')
%     xlabel('time (s)')
figure (3)
subplot(4,3,4)
plot(tdata(1:end),xdata(1:end,5),'o','MarkerSize',6);
hold on
plot(tsol1(1:end),xsol1(1:end,4),'k','LineWidth',3);
ylabel('Cacyt (uM)');ylim=[0 0.5]; xlabel('time (s)')

subplot(4,3,5)
plot(tdata(1:end),xdata(1:end,4),'o','MarkerSize',6);
hold on
plot(tsol2(1:end),xsol2(1:end,4),'k','LineWidth',3);
ylabel('Cacyt (uM)'); ylim=[0 0.5]; xlabel('time (s)')

subplot(4,3,6)
plot(tdata(1:end),xdata(1:end,8),'o','MarkerSize',6);
hold on
plot(tsol3(1:end),xsol3(1:end,4),'k','LineWidth',3);
ylabel('Cacyt (uM)'); ylim=[0 0.5]; xlabel('time (s)')

subplot(4,3,7)
plot(tdata(1:end),xdata(1:end,6),'o','MarkerSize',6);
hold on
plot(tsol1(1:end),xsol1(1:end,6),'k','LineWidth',3);
ylabel('CaER (uM)'); ylim=[0 400]; xlabel('time (s)')

subplot(4,3,8)
plot(tdata(1:end),xdata(1:end,6),'o','MarkerSize',6);
hold on
plot(tsol2(1:end),xsol2(1:end,6),'k','LineWidth',3);
ylabel('CaER (uM)');ylim=[0 400]; xlabel('time (s)')

subplot(4,3,9)
plot(tdata(1:end),xdata(1:end,6),'o','MarkerSize',6);
hold on
plot(tsol3(1:end),xsol3(1:end,6),'k','LineWidth',3);
ylabel('CaER (uM)');ylim=[0 400]; xlabel('time (s)')

subplot(4,3,10)
plot(tdata(1:end),xdata(1:end,7),'x','MarkerSize',6);
hold on
plot(tsol1(1:end),xsol1(1:end,7),'k','LineWidth',3);
ylabel('CaMit (uM)'); ylim=[0 10]; xlabel('time (s)')
    subplot(4,3,11)
plot(tdata(1:end),xdata(1:end,7),'x','MarkerSize',6);
hold on
plot(tsol2(1:end),xsol2(1:end,7),'k','LineWidth',3);
ylabel('CaMit (uM)'); ylim=[0 10]; xlabel('time (s)')
    subplot(4,3,12)
plot(tdata(1:end),xdata(1:end,7),'x','MarkerSize',6);
hold on
plot(tsol3(1:end),xsol3(1:end,7),'k','LineWidth',3);

```

```

ylabel('CaMit (uM)'); ylim=[0 10]; xlabel('time (s)')

function dx = f1(t,x)
    global b
    CaEx=750;
    dx = zeros(7,1);
    Jplcact= 0.0045*x(3); %activation of PLCp by ligand binding
    Jplcdeact= 0.0396*x(2); %dephosphorylation of PLCp
    dx(3)=-Jplcact; %Ligand
    dx(2)= Jplcact-Jplcdeact; %PLCgammap

    Jplc= b(14)*x(2)*x(4); %production of IP3 from PLCp
    Jip3deg= b(15)*b(14)*x(1); %degradation of IP3 by phosphatase
    dx(1)=Jplc-Jip3deg;

    Jserca=b(1)*x(4)^2/(x(4)^2+b(2)^2); %%serca
    Jerleak = x(6)*b(5);

    Jip3=x(6)*b(10)*(x(1)/(x(1)+b(12)))^3*(x(4)/(x(4)+b(13)))^3*x(5)^
    3; %Maurya , Chen...
    b20=1*(x(1)+b(12))/(x(1)+b(20));
    dx(5)=b(19)*(b20-x(5)*(x(4)+b(20))); %h

    Jpmleak=b(8)*CaEx;
    Jcrac=b(7)*(b(9)^3/(b(9)^3+x(6)^3))*CaEx/(b(24)+CaEx);
    Jpmca=b(3)*(x(4).^2/(x(4).^2+b(4)^2))*((x(6).^4)/(x(6).^4+b(22)
    .^4)); %pmca
    Jmitin=b(16)*(x(4).^4/(x(4).^4+b(17)^4));
    Jmitout= b(18)*x(7)*(x(4)^2/(x(4)^2+b(23)^2));
    Jmitleak=b(6)*x(7);

    dx(4)=b(27)*(Jcrac-Jpmca-Jserca+Jerleak+Jip3+Jpmleak+Jmitout-
    Jmitin); %Cacyt
    dx(6)=b(11)*Jserca-b(11)*Jip3-b(11)*Jerleak; %CaER
    dx(7)=b(21)*Jmitin-b(21)*Jmitout; %Camit

function dx = f2(t,x)
    global b
    CaEx=1500;
    dx = zeros(7,1);
    Jplcact= 0.0045*x(3); %activation of PLCp by ligand binding
    Jplcdeact= 0.0396*x(2); %dephosphorylation of PLCp
    dx(3)=-Jplcact; %Ligand
    dx(2)= Jplcact-Jplcdeact; %PLCgammap

    Jplc= b(14)*x(2)*x(4); %production of IP3 from PLCp
    Jip3deg= b(15)*b(14)*x(1); %degradation of IP3 by phosphatase
    dx(1)=Jplc-Jip3deg;

    Jserca=b(1)*x(4)^2/(x(4)^2+b(2)^2); %%serca
    Jerleak = x(6)*b(5);

    Jip3=x(6)*b(10)*(x(1)/(x(1)+b(12)))^3*(x(4)/(x(4)+b(13)))^3*x(5)^
    3; %Maurya , Chen...
    b20=1*(x(1)+b(12))/(x(1)+b(20));
    dx(5)=b(19)*(b20-x(5)*(x(4)+b(20))); %h

```



```

Jpmleak=b(8)*CaEx;
Jcrac=b(7)*(b(9)^3./(b(9)^3+x(6)^3))*CaEx/(b(24)+CaEx);
Jpmca=b(3)*(x(4).^2./(x(4).^2+b(4)^2))*((x(6).^4)./(x(6).^4+b(22).^4)); %pmca
Jmitin=b(16)*(x(4).^4./(x(4).^4+b(17)^4));
Jmitout= b(18)*x(7)*(x(4)^2/(x(4)^2+b(23)^2));
Jmitleak=b(6)*x(7);

dx(4)=b(27)*(Jcrac-Jpmca-Jserca+Jerleak+Jip3+Jpmleak+Jmitout-
Jmitin); %Cacyt
dx(6)=b(11)*Jserca-b(11)*Jip3-b(11)*Jerleak; %CaER
dx(7)=b(21)*Jmitin-b(21)*Jmitout; %Camit

function dx = f3(t,x)
    global b
    CaEx=1500;
    dx = zeros(7,1);
    Jplcact= 0.0045*x(3); %activation of PLCp by ligand binding
    Jplcdeact= 0.0396*x(2); %dephosphorylation of PLCp
    dx(3)=-Jplcact; %Ligand
    dx(2)= Jplcact-Jplcdeact; %PLCgammmap

    Jplc= b(14)*x(2)*x(4); %production of IP3 from PLCp
    Jip3deg= b(15)*b(14)*x(1); %degradation of IP3 by phosphatase
    dx(1)=Jplc-Jip3deg;

    Jserca=b(1)*x(4)^2/(x(4)^2+b(2)^2); %%serca
    Jerleak = x(6)*b(5);

    Jip3=x(6)*b(10)*(x(1)/(x(1)+b(12)))^3*(x(4)/(x(4)+b(13)))^3*x(5)^3;
    b20=1*(x(1)+b(12))/(x(1)+b(20));
    dx(5)=b(19)*(b20-x(5)*(x(4)+b(20))); %g or inactivation of IP3R by
Cacyt
    Jip3=b(28)*Jip3;

    Jpmleak=b(8)*CaEx;
    Jcrac=b(7)*(b(9)^3./(b(9)^3+x(6)^3))*CaEx/(b(24)+CaEx);
    Jpmca=b(3)*(x(4).^2./(x(4).^2+b(4)^2))*((x(6).^4)./(x(6).^4+b(22).^4)); %pmca
    Jmitin=b(16)*(x(4).^4./(x(4).^4+b(17)^4));
    Jmitout= b(18)*x(7)*(x(4)^2/(x(4)^2+b(23)^2));
    Jmitleak=b(6)*x(7);

    dx(4)=b(27)*(Jcrac-Jpmca-Jserca+Jerleak+Jip3+Jpmleak+Jmitout-
Jmitin); %Cacyt
    dx(6)=b(11)*Jserca-b(11)*Jip3-b(11)*Jerleak; %CaER
    dx(7)=b(21)*Jmitin-b(21)*Jmitout; %Camit

```

## APPENDIX G

### ROS/CA<sup>2+</sup> SIGNALING MODEL

```
function solveROSCaModel1
clearvars -global
global b CaEx x0 tdata IP3 ROSerinit

%% data for the model
x0(1)=1.4e-3; x0(2)=0.0014; x0(3)=85;
x0(4)=0.05; x0(5)=0.02; x0(6)=350; x0(7)=0.1;
IP3=0.54; CaEx=1500; ROSerinit=x0(3);

b=zeros(1,44);
b(1,1:9)=[6.4e-3 1.2e-6 1e-6 5 1e-6 0.15 1.2e-3 40e-3 0.0015];
b(1,10:12)=[3e-3 95 3];
b(1,13:15)=[b(10)/55 280 2]; % [0.5e-3 95 3 b(10)/54.5 300 3];
b(1,16:22)=[1.626 0.16 0.106*2.75 0.15 2 0.771 0.0917];
b(1,23:31)=[3e-3 85.8*2.75 0.4477 0.1 2 794.07 1.24 484.44 8.1285];
b(1,32:41)=[0 3.1046 195.73 996.83 2.5e-7 1.805*2.75 0.1269 394 10 2];
b(1,42:44)=[0.1678 0.0467 0.716];

binit=b;
tdata=1:1:1800;
kscaverinit=binit(13);
kscavinit=binit(7);
Vsercainit=binit(24);

% t1=0;
% t2=600;
% [T,y] = ode15s(@f1,[t1 t2],x0);
% subplot(2,2,2), plot(T,y(:,3)); title('ROSer')
% subplot(2,2,1), plot(T,y(:,2)); title('ROScyt')
% subplot(2,2,4), plot(T,y(:,6)); title('Caer')
% subplot(2,2,3), plot(T,y(:,4)); title('Cacyt')
% y0=[1.4;y(end,2);y(end,3);y(end,4);y(end,5);y(end,6);y(end,7)];
% t3=1800;
% [T,y] = ode15s(@f1,[t2 t3],y0);
% subplot(2,2,2), hold on, plot(T,y(:,3)); %title('ROSer')
% subplot(2,2,1), hold on, plot(T,y(:,2)); %title('ROScyt')
% subplot(2,2,4), hold on, plot(T,y(:,6)); %title('Caer')
% subplot(2,2,3), hold on, plot(T,y(:,4)); %title('Cacyt')
%
% figure(1),
% T1=0:60:30*60;
% ROSer=[3.1 3.1 3.1 3.1 3.1 3.1 1.35 0.9 0.85 0.8 0.8 0.8 0.9 1 1.3...
% 1.55 1.85 2.1 2.35 2.6 2.65 2.66 2.67 2.68 2.69 2.7 3.8 3.8 3.8
% 3.8 3.8];
% scatter(T1, ROSer,'b')
%
%
%
%
% t1=0;
% t2=300;
```

```

% [T,y] = ode15s(@f1,[t1 t2],x0);
% hold on, plot(T,y(:,3)*(3.1/ROSerinit))
% ax1 = gca;
% set(ax1,'YColor','b')
% ylim([0 4])
% ax2 = axes('Position',get(ax1,'Position'),...
%           'YAxisLocation','right',...
%           'Color','none',...
%           'YColor','r')
%           ylim([0 1])
%
% hold on, plot(T,y(:,2),'r','Parent',ax2)
% y0=[y(end,1);y(end,2);y(end,3);y(end,4);y(end,5);y(end,6);y(end,7)];
% t3=680;
% b(13)=kscaverinit*7;
% b(7)=kscavinit*7;
% [T,y] = ode15s(@f1,[t2 t3],y0);
% hold on, plot(T,y(:,3)*(3.1/ROSerinit),'Parent',ax1)
% hold on, plot(T,y(:,2),'r','Parent',ax2)
%
% y0=[y(end,1);y(end,2);y(end,3);y(end,4);y(end,5);y(end,6);y(end,7)];
% t4=1500;
% b(13)=kscaverinit*1.25;
% b(7)=kscavinit*1.25;
% [T,y] = ode15s(@f1,[t3 t4],y0);
% hold on, plot(T,y(:,3)*(3.1/ROSerinit),'Parent',ax1)
% hold on, plot(T,y(:,2),'r','Parent',ax2)
% y0=[1;y(end,2);y(end,3);y(end,4);y(end,4);y(end,6);y(end,7)];
% t5=65*60;
% b(13)=kscaverinit;
% b(7)=kscavinit;
% [T,y] = ode15s(@f1,[t4 t5],y0);
% hold on, plot(T,y(:,3)*(3.1/ROSerinit),'Parent',ax1)
% hold on, plot(T,y(:,2),'r','Parent',ax2)

%% response to calcium release
% figure(2),
T2=0:60:30*60;
T3=0*60:2.5*60:25*60;
ROSerthapsigargin=[3.1 3.1 3.1 2.7 2.2 2 1.9 1.8 1.7 1.6 1.6];
Ca=[0.45 0.45 0.45 0.75 0.65 0.5 0.45 0.45 0.45 0.45 0.45];
ROSerhistamine=[3.1 3.1 3.1 3.1 3.1 3.1 3 2.8 2.6 2.5 2.4 2.35 2.37
2.38 2.4...
2.45 2.55 2.6 2.65 2.7 2.75 2.8 2.8 2.8 2.8 2.8 3.7 3.8 3.8 3.8 3.8];
% hold on
subplot(2,2,1)
% , scatter(T3, ROSerthapsigargin,'g')
hold on
scatter(T2, ROSerhistamine,'b')
%
% y0=[y(end,1);y(end,2);y(end,3);y(end,4);y(end,5);y(end,6);y(end,7)];
y0=x0;

t1=0;
t2=5*60;
[T,y] = ode15s(@f1,[t1 t2],y0);

```

```

    subplot(2,2,1),
hold on, plot(T,y(:,3)*(3.1/ROSerinit),'b')
y0=[y(end,1);y(end,2);y(end,3);y(end,4);y(end,5);y(end,6);y(end,7)];
IP3=5; b(24)=0.9999*Vsercainit;
t3=11*60;
[T,y] = ode15s(@f1,[t2 t3],y0);
subplot(2,2,1),hold on, plot(T,y(:,3)*(3.1/ROSerinit),'b')
y0=[y(end,1);y(end,2);y(end,3);y(end,4);y(end,5);y(end,6);y(end,7)];
IP3=0.54; b(24)=Vsercainit;
t4=25*60;
[T,y] = ode15s(@f1,[t3 t4],y0);
subplot(2,2,1), hold on, plot(T,y(:,3)*(3.1/ROSerinit),'b')
y0=[1.5;y(end,2);y(end,3);y(end,4);y(end,5);y(end,6);y(end,7)];
t5=35*60;
[T,y] = ode15s(@f1,[t4 t5],y0);
subplot(2,2,1), hold on, plot(T,y(:,3)*(3.1/ROSerinit),'b')
y0=x0;
t1=0;
t2=5*60;
[T,y] = ode15s(@f1,[t1 t2],y0);
    subplot(2,2,2),hold on, plot(T,y(:,2),'r')
y0=[y(end,1);y(end,2);y(end,3);y(end,4);y(end,5);y(end,6);y(end,7)];
IP3=5; b(24)=0.9999*Vsercainit;
t3=11*60;
[T,y] = ode15s(@f1,[t2 t3],y0);
    subplot(2,2,2),hold on, plot(T,y(:,2),'r')
y0=[y(end,1);y(end,2);y(end,3);y(end,4);y(end,5);y(end,6);y(end,7)];
IP3=0.54; b(24)=Vsercainit;
t4=25*60;
[T,y] = ode15s(@f1,[t3 t4],y0);
    subplot(2,2,2),hold on, plot(T,y(:,2),'r')
y0=[1.5;y(end,2);y(end,3);y(end,4);y(end,5);y(end,6);y(end,7)];
t5=35*60;
[T,y] = ode15s(@f1,[t4 t5],y0);
    subplot(2,2,2),hold on, plot(T,y(:,2),'r')
y0=x0;
t1=0;
t2=5*60;
[T,y] = ode15s(@f1,[t1 t2],y0);
    subplot(2,2,3),hold on, plot(T,y(:,6),'b')
y0=[y(end,1);y(end,2);y(end,3);y(end,4);y(end,5);y(end,6);y(end,7)];
IP3=5; b(24)=0.9999*Vsercainit;
t3=11*60;
[T,y] = ode15s(@f1,[t2 t3],y0);
    subplot(2,2,3),hold on, plot(T,y(:,6),'b')
y0=[y(end,1);y(end,2);y(end,3);y(end,4);y(end,5);y(end,6);y(end,7)];
IP3=0.54; b(24)=Vsercainit;
t4=25*60;
[T,y] = ode15s(@f1,[t3 t4],y0);
    subplot(2,2,3),hold on, plot(T,y(:,6),'b')
y0=[1.5;y(end,2);y(end,3);y(end,4);y(end,5);y(end,6);y(end,7)];
t5=35*60;
[T,y] = ode15s(@f1,[t4 t5],y0);
    subplot(2,2,3),hold on, plot(T,y(:,6),'b')
y0=x0;
t1=0;
t2=5*60;

```

```

[T,y] = ode15s(@f1,[t1 t2],y0);
    subplot(2,2,4),hold on, plot(T,y(:,4),'r')
y0=[y(end,1);y(end,2);y(end,3);y(end,4);y(end,5);y(end,6);y(end,7)];
IP3=5; b(24)=0.9999*Vsercainit;
t3=11*60;
[T,y] = ode15s(@f1,[t2 t3],y0);
    subplot(2,2,4),hold on, plot(T,y(:,4),'r')
y0=[y(end,1);y(end,2);y(end,3);y(end,4);y(end,5);y(end,6);y(end,7)];
IP3=0.54; b(24)=Vsercainit;
t4=25*60;
[T,y] = ode15s(@f1,[t3 t4],y0);
    subplot(2,2,4),hold on, plot(T,y(:,4),'r')
y0=[1.5;y(end,2);y(end,3);y(end,4);y(end,5);y(end,6);y(end,7)];
t5=35*60;
[T,y] = ode15s(@f1,[t4 t5],y0);
    subplot(2,2,4),hold on, plot(T,y(:,4),'r')

function dx = f1(t,x)
global b CaEx ROSerinit IP3 x0 tdata
dx = zeros(7,1);

%ROS in media
Vcytin=-(x(2)-x(1)).*b(1);
dx(1)=-Vcytin;
% dx(1)=amp*(1./2*pi*freq)*cos(2*pi*freq*t);
Vmitprod=b(2);
Vnox=b(3).*IP3./(IP3+b(4));
Vduox=b(5).*IP3.*x(4).^2./(b(6).^2+x(4).^2);
Vscav=b(7).*x(2);
Verin=b(8).*(x(2)-b(9)); %influx of ROS from cytoplasm
dx(2)= Vcytin+Vnox+Vduox-Vscav+Vmitprod-Verin;

%production of ROS in ER
Verprod=b(10)*b(11)^b(12)./(b(11)^b(12)+x(3).^b(12)); %production
from erolalpha, redox dependent
Verout=b(13)*x(3)*((b(14).^b(15))./(b(14).^b(15)+x(6).^b(15)));
dx(3)=1/0.015*(Verin+Verprod-Verout);

%IP3 flux
Kip3ros=b(18)*(b(19)^b(20))/(x(2)^b(20)+b(19)^b(20));
Jip3=x(6)*b(16)*(IP3/(IP3+Kip3ros))^3*(x(4)/(x(4)+b(17)))^3*x(5)^3;
Q=1*(IP3+Kip3ros)/(IP3+1.05);
dx(5)=b(22)*(Q-x(5)*(x(4)+Q)); %h
Jerleak = x(6)*b(23)*(1+((x(3)-ROSerinit)/ROSerinit));

Jserca=b(24)*(x(4)^2/(x(4)^2+b(25)^2))*(b(26)^b(27)/(b(26)^b(27)+
x(2)^b(27))); %serca
Jmitin= b(28)*(x(4).^4/(x(4).^4+b(29)^4));
Jmitout= b(30)*x(7)*(x(4)^2/(x(4)^2+b(31)^2));
Jcrac=b(33)*(b(34)^3/(b(34)^3+x(6)^3))*CaEx/(b(35)+CaEx);
Jpmleak=b(36).*CaEx;
Jpmca=b(37)*(x(4).^2/(x(4).^2+b(38)^2))*((x(6).^2)/(x(6).^2+b(3
9).^2))*(b(40)^b(41)/b(40)^b(41)+x(2)^b(41)); %pmca

dx(4)=b(42)*(Jcrac-Jpmca-Jserca+Jerleak+Jip3+Jpmleak+Jmitout-
Jmitin); %Cacyt

```

```

dx(6)=(b(43)/0.015)*(Jserca-Jip3-Jerleak); %CaER
dx(7)=(b(44)/0.08)*(Jmitin-Jmitout); %Camit

%% Solve model once parameters are known in the frequency domain
%%-----%%
function solveROSCaModelFreq2
clearvars -global
global b CaEx x0 IP3 ROSerinit amp freq
%% data for the model
x0(2)=0.0014; x0(3)=85;
x0(4)=0.05; x0(5)=0.02; x0(6)=350; x0(7)=0.1;
IP3=0.54; CaEx=1500; ROSerinit=x0(3);

b=zeros(1,44);
b(1,1:9)=[0.4e-2 1.2e-6 1e-6 5 1e-6 0.15 1.2e-3 40e-3 0.0015];
b(1,10:12)=[3e-3 95 3];
b(1,13:15)=[b(10)/55 280 2]; %[0.5e-3 95 3 b(10)/54.5 300 3];
b(1,16:22)=[1.626 0.16 0.106*2.75 0.15 2 0.771 0.0917];
b(1,23:31)=[3e-3 85.8*2.75 0.4477 0.1 2 794.07 1.24 484.44 8.1285];
b(1,32:41)=[0 3.1046 195.73 996.83 2.5e-7 1.805*2.75 0.1269...
394 10 2];
b(1,42:44)=[0.1678 0.0467 0.716];

binit=b;

%% creation of the Frequency Response
t1=0;
freqstep=logspace(-4,-1,100);
Amp=30; %%there is a ratio factor : 100uM corresponds to 1.5
X0=0.25*Amp+1.1e-3;
ls=length(Amp); %length of the parameter to sweep
periodstep=1./freqstep;
FqcySweepLength=length(freqstep);
c={'r','g','b','k','y','m','c'};
j=1;
n1=1;
mag_x=cell(1,ls);
idx_x=cell(1,ls);
px=cell(1,ls);
id=ones(length(freqstep),7);
Max0=ones(length(freqstep),7);
for i=freqstep %in seconds
    freq=i; tstep=1/freq;
    t2=18*tstep; stepxi=tstep/1000;
    xi=0:stepxi:t2;
    options=odeset('MaxStep',tstep/250);

    for n1=1:ls
        amp=Amp(n1); x0(1)=X0(n1);
        n1
        y0=x0;
        [T{n1},y{n1}] = ode15s(@f1,[t1 t2],y0,options);
        for k=1:7 %for each species
            z{n1}(:,k)=interp1(T{n1},y{n1}(:,k),xi');
            z{n1}(:,k)=z{n1}(:,k)-
            mean(z{n1}((end+1)/2:end,k)); %remove bias

```

```

        zou=z{n1}(14*length(xi)/15:end,k);
        MaxO(j,k)=max(zou);
        id(j,k)=max(find(zou==max(zou)));
        % Z{n1}(:,k)=fft(z{n1}(:,k)); %take the fft
        % [mag_x{n1}(j,k) idx_x{n1}(j,k)] =
        %max(abs(Z{n1}(ceil((t2-
        %6*tstep+1)/stepxi):end,k))); % Determine the
        %max value and max point.
        % px{n1}(j,k) = angle(Z{n1}(idx_x{n1}(j,k),k));
        % determine the phase difference at the max
        point
        % clear z
        % clear Z
    end

end

end
n1=n1+1;
j=j+1
end

A={freqstep,MaxO,id};
save ('Amplitude500','A')

function dx = f1(t,x)
global b CaEx ROSerinit IP3 x0 tdata amp freq
dx = zeros(7,1);

%ROS in media
Vcytin=-(x(2)-x(1)).*b(1);
% dx(1)=-Vcytin;
dx(1)=amp.*(1./2*pi.*freq).*cos(2*pi.*freq.*t);
Vmitprod=b(2);
Vnox=b(3).*IP3./(IP3+b(4));
Vduox=b(5).*IP3.*x(4).^2./(b(6).^2+x(4).^2);
Vscav=b(7).*x(2);
Verin=b(8).*(x(2)-b(9)); %influx of ROS from cytoplasm, if more
than homeostatic levels
dx(2)= Vcytin+Vnox+Vduox-Vscav+Vmitprod-Verin;

%production of ROS in ER
Verprod=b(10)*b(11)^b(12)./(b(11)^b(12)+x(3).^b(12)); %Ero1alpha
Verout=b(13)*x(3)*((b(14).^b(15))./(b(14).^b(15)+x(6).^b(15)));
dx(3)=1/0.015*(Verin+Verprod-Verout);

%IP3 flux
Kip3ros=b(18)*(b(19)^b(20))/(x(2)^b(20)+b(19)^b(20));
Jip3=x(6)*b(16)*(IP3/(IP3+Kip3ros))^3*(x(4)/(x(4)+b(17)))^3*x(5)^3;
Q=1*(IP3+Kip3ros)/(IP3+1.05);
dx(5)=b(22)*(Q-x(5)*(x(4)+Q)); %h

Jerleak = x(6)*b(23)*(1+((x(3)-ROSerinit)/ROSerinit));

Jserca=b(24)*(x(4)^2/(x(4)^2+b(25)^2))*(b(26)^b(27)/(b(26)^b(27)+
x(2)^b(27))); %%serca

```

```

Jmitin= b(28)*(x(4).^4./(x(4).^4+b(29)^4));
Jmitout= b(30)*x(7)*(x(4)^2/(x(4)^2+b(31)^2));
Jcrac=b(33)*(b(34)^3./(b(34)^3+x(6)^3))*CaEx/(b(35)+CaEx);
Jpmleak=b(36).*CaEx;

Jpmca=b(37)*(x(4).^2./(x(4).^2+b(38)^2))*((x(6).^2)./(x(6).^2+b(39).^2))*b(40)^b(41)/b(40)^b(41)+x(2)^b(41)); %pmca
dx(4)=b(42)*(Jcrac-Jpmca-Jserca+Jerleak+Jip3+Jpmleak+Jmitout-Jmitin); %Cacyt
dx(6)=(b(43)/0.015)*(Jserca-Jip3-Jerleak); %CaER
dx(7)=(b(44)/0.08)*(Jmitin-Jmitout); %Camit

%% Solve model once parameters are known in the frequency domain
%%-----%%
load Amplitude25
Freq=A{1,1}'; TimeDelay=A{1,3}'; Amp=A{1,2}';
Gain=Amp; Phase=TimeDelay; Period=1./Freq;

for i=1:7
    Gain(i,:)=Amp(i,:)./Amp(1,:);
    Gain(i,:)=20*log(Gain(i,:));
end

for i=1:7
    Phase(i,)=(TimeDelay(i,:)-TimeDelay(1,:));
end

Gain=[Gain(2,:);Gain(3,:); Gain(4,:);Gain(6,:);Gain(7,:)];
Phase=[Phase(2,:);Phase(3,:); Phase(4,:);Phase(6,:);Phase(7,:)];

for i=1:5
    subplot(5,2,2*i-1)
    hold on, semilogx(Freq, Gain(i,:), 'g*')
    subplot(5,2,2*i)
    hold on, semilogx(Freq, -0.36*Phase(i,:), 'g*')
    ylim([-180 180])
end

% Freq2=logspace(-4,-1,100); Freq2=Freq2(1,1:85);
% Gain2=zeros(6,length(Freq2));
% Gain2(3,:)=interp1(Freq,Gain(3,:),Freq2);
% Phase2=zeros(6,length(Freq2));
% Phase2(3,:)=interp1(Freq,Phase(3,:),Freq2);
% A2=zeros(1,length(Freq2));
% A2=interp1(Freq,(Amp(3,:)./Amp(6,:)),Freq2);
%
% % num=0.001; den=[200 1];
% % sys=tf(num,den); grid;
% % hold on, bodeplot(sys)
% error=[];
% for tau=90:0.05:100
% K=0.05; tau=94.5
% figure,
% subplot(2,1,1)
% hold on, semilogx(Freq2, Gain2(3,:), 'r*')

```



```

% hold on, semilogx(Freq2,+20*log(K)-20*log((1+(Freq2.^2*tau^2))))
% % hold on, semilogx(Freq, Gain(3,:), 'b*')
% subplot(2,1,2)
% hold on, semilogx(Freq2, -0.36*Phase2(3,:), 'b*')
% hold on, semilogx(Freq2, -360/(2*pi)*atan(Freq2*tau))
% S=0;
% for i=1:length(Freq2)
%     S=S+(+20*log(K)-20*log((1+(Freq2.^2*tau^2)))-
Gain2(3,:)/Gain2(3,:))^2+...
%     ((-360/(2*pi)*atan(Freq2*tau)+0.36*Phase2(3,:))/(-
0.36*Phase2(3,:)))^2;
% end
% error=[error S]
% end
% plot(Freq, Phase(3,:))
% figure,
% for i=1:5
% subplot(5,1,i)
% semilogx(Freq, Phase(i,:), '*')
% end

```

## APPENDIX H

### MATLAB SCRIPT SINGLE CELL ANALYSIS

```
clear all
%-----
----
% Load Images

N = 423;
Im = cell(1,N);
FNAMEFMT = 'switch5min_50umh2o2001t00%d.tif';
FNAMEFMT2 = 'switch5min_50umh2o2001t0%d.tif';
FNAMEFMT3 = 'switch5min_50umh2o2001t%d.tif';
for i=1:9
    Im{i} = imread(sprintf(FNAMEFMT,i));
end
for i=10:99
    Im{i} = imread(sprintf(FNAMEFMT2,i));
    i
end
for i=100:N
    Im{i} = imread(sprintf(FNAMEFMT3,i));
    i
end

for j=1:N
    Im{j}=Im{j}(:, :, 2);
end

clear FNAMEFMT FNAMEFMT2 FNAMEFMT3
save Im
% clear all
%-----
----

% clear all
%-----

%% Create the composite image to get the background and the individual
cells from.

load Im
N = 423;

% Create Packs of pics for each semi period
Npack=20; %nb of pics per semi period
Nstack=21; %nb of semi periods (4+10+8)
for i=1:Nstack
    Stack{i}=Im(Npack*(i-1)+1:Npack*i);
```

```

end

% For each stack of pics, create a composite of all the pics
Y=cell(1,Nstack);
for j=1:Nstack
    Y{j}=uint8(zeros(1040,1392));
    for i=1:Npack
        Y{j}=imadd((1./Npack)*Stack{1,j}{1,i},Y{j});
    %       figure, imshow(Y{j})
    end
end
for i=1:Nstack
    figure, imshow(Y{i})
end

%composite of all
N2=239; %number of pics before calibration
Ytotal=uint8(zeros(1040,1392));
for j=1:N2
    Ytotal=imadd((4/N2)*Im{j},Ytotal);
end
imshow(Ytotal)
clear Y
save Step2

% load Step2

%% Crop the picture from the best composite

% Crop a few backgrounds and get the means
N2=239;
IM=Ytotal;
Nbackgrounds=4;
for i=1:Nbackgrounds
    [X,Y,Icrop,rect] = imcrop(IM);
    XX{i}=X; YY{i}=Y;
    IIcrop{i}=Icrop;
    Rect{i}=rect;
end

% apply the backgrounds to the various pics

for j=1:N
    for i=1:Nbackgrounds
        Imcropbackground{j,i}=imcrop(Im{j},Rect{i});
    end
end

Cbckgd=zeros(Nbackgrounds,N);
C=zeros(Nbackgrounds,N2);
for j=1:N
    for i=1:Nbackgrounds
        Abckgd=mean(Imcropbackground{j,i},1);
        Bbckgd=mean(Abckgd,2);
    end
end

```

```

        Cbckgd(i,j)=Bbckgd;
    end
end
BCKGD=mean(Cbckgd);
plot(BCKGD)
BCKGDoriginal=BCKGD;

%% Get the calibration data and the Input curve
Calib=BCKGD(N2-1:N2+130);
plot(Calib)
hold on, plot(1:length(Calib),mean(Calib),'r')
hold on, plot(1:length(Calib),mean(Calib)+1*std(Calib),'r-')
hold on, plot(1:length(Calib),mean(Calib)-1*std(Calib),'r-')
OutlierIndex=[];
for i=1:length(Calib)
    if Calib(i)>mean(Calib)+1*std(Calib)|Calib(i)<mean(Calib)-
1*std(Calib)
        OutlierIndex=[OutlierIndex i];
    end
end
for i=3:length(OutlierIndex)
    Calib(OutlierIndex(i))=0.5*(Calib(OutlierIndex(i)-
2)+Calib(OutlierIndex(i)-1));
end

BCKGD=[BCKGD(1:N2-2) Calib BCKGD(N2+131:end)];

figure, plot(1:N,BCKGD)

T = 15; % Sample time
Fs = 1/T; % Sampling frequency
L = length(Calib); % Length of signal
t = (0:L-1)*T; % Time vector
y=Calib;
figure,
plot(t,y)
title('Signal'); xlabel('time (seconds)')

Calib1=Calib; Calibmean=mean(Calib1);
ff = fittype('sin1'); %a*sin(b*x+c)
t1=15*(N2-1:N2+130)
[c2,gof2] = fit(t1,(Calib1-Calibmean)',ff);

%% input the function
Tf=2*pi/c2.b1;
INPUT=c2.a1*sin((2*pi/Tf)*(15*(1:N)))+c2.c1)+Calibmean;

figure, plot(15*(1:N), INPUT)
hold on, plot(15*(1:N),BCKGD,'r')

xlswrite('25uMH202',[Cbckgd' BCKGD'],'background')
xlswrite('25uMH202',INPUT','predicted input')

clear Abckgd Bbckgd C Calib Calib1 Calibmean Cbckgd Fs IIcrop...
Icrop Imcropbackground L Nbackgrounds Npack Nstack OutlierIndex...

```

```

    Rect Stack X XX Y YY c2 ff gof2 i j rect y t t1
save Step3

% load Step3
% imshow(imadjust(IM))
%-----
%% Crop a few cells and get the traces
Ncell=252;
for i=1:Ncell
[X,Y,Icrop,rect] = imcrop(imadjust(IM));
XX{i}=X; YY{i}=Y;
IIcrop{i}=Icrop; Rect{i}=rect;
end

% apply the ROI to the various pics
for j=1:N
    for i=1:Ncell
        Imcrop{j,i}=imcrop(Im{j},Rect{i});
    end
end

% Get MFI for each ROI
C=zeros(Ncell,N);
for j=1:N
    for i=1:Ncell
        A=mean(Imcrop{j,i},1);
        B=mean(A,2); C(i,j)=B;
    end
end
C=C(:,1:N2);
figure, imagesc(C)

% Subtract Background
temp=xlsread('25uMH2O2','background');
BCKGD=temp(1:N2,4);
clear temp

C2=zeros(Ncell,N2);
for i=1:Ncell
C2(i,:)=C(i,:)-BCKGD';
end
figure, imagesc(C2(:,1:N2))
xlswrite('50uMH2O2',C,'celldata')
xlswrite('50uMH2O2',C2,'celldatanormalized')
clear A B IIcrop Icrop Imcrop Nbackgrounds Rect X XX Y YY i j rect
save Step4
clear all

N2=239;
Ncell=252;
C=xlsread('50uMH2O2','celldata'); C=C';
C2=xlsread('50uMH2O2','celldatanormalized'); C2=C2';
A=xlsread('50uMH2O2','background');
INPUT=xlsread('50uMH2O2','predicted input'); INPUT=INPUT';
BCKGD=A(1:N2,4);
plot(BCKGD)

```

```

hold on, plot(1:length(BCKGD),mean(BCKGD),'r')
hold on, plot(1:length(BCKGD),mean(BCKGD)+0.5*std(BCKGD),'r-')
hold on, plot(1:length(BCKGD),mean(BCKGD)-0.5*std(BCKGD),'r-')
OutlierIndex=[];
for i=3:length(BCKGD)
    if (BCKGD(i)>mean(BCKGD)+0.5*std(BCKGD)) | (BCKGD(i)<mean(BCKGD)-
0.5*std(BCKGD))
        OutlierIndex=[OutlierIndex i];
    end
end
for i=1:length(OutlierIndex)
    BCKGD(OutlierIndex(i))=0.5*(BCKGD(OutlierIndex(i)-
2)+BCKGD(OutlierIndex(i)+1));
end
hold on, plot(BCKGD,'r')
subplot(3,1,1)
imagesc(C2,[-4 12])
C3=C2;
for i=1:length(OutlierIndex)
    C3(:,OutlierIndex(i))=0.5*(C3(:,OutlierIndex(i)-
2)+C3(:,OutlierIndex(i)+1));
end
subplot(3,1,2)
imagesc(C3,[-5 15])

%% additional outliers at positions:
OutlierIndex2=[21 47 78 145 212 223];
for i=1:length(OutlierIndex2)
    C3(:,OutlierIndex2(i))=0.5*(C3(:,OutlierIndex2(i)-
1)+C3(:,OutlierIndex2(i)+1));
end
subplot(3,1,3)
imagesc(C3,[-5 15])
C3orig=C3;

C3origmean=mean(C3orig);
ff = fitype('exp1'); %a*exp(b*x)
t1=1*(1:N2);
[c2,gof2] = fit(t1',C3origmean',ff);

% input the function
TREND=c2.a*exp(c2.b*t1);

figure, plot(1:N2, TREND)
hold on, plot(1:N2,C3origmean,'r')
hold on, plot(1:N2,C3origmean-TREND,'g')
%-----
C4=C3;
for i=1:Ncell
    C4(i,:)=C3(i,:)-TREND+ones(1,length(TREND));
end

CC4=[]; %% to have an idea of how to limit the colorbar
for i=1:Ncell
    CC4=[CC4 C4(i,:)];
end

```

```

figure, hist(CC4,1000)
figure, imagesc(C4,[-6 10])

%-----
AverageBeforeStim=mean(C4(:,5:40),2);
C5=C4;
for i=1:Ncell
    C5(i,:)=sgolayfilt(C4(i,:),3,9); %filter/smoothen
    % figure, plot(C3(i,1:N2))
    % hold on, plot(C2(i,1:N2),'r')
    % C5(i,:)=C5(i,:)./AverageBeforeStim(i);
end

figure, imagesc(C5,[-3 8])
colorbar('EastOutside')
xlim([0 N2]);
ax1=gca;
ax2 = axes('Position',get(ax1,'Position'),...
    'YAxisLocation','right',...
    'XAxisLocation','top',...
    'Color','none','YColor','k');
hold on, line(1:N2,mean(C5),'Color','r','LineWidth',3.5,'Parent',ax2)
xlim([0 N2]); ylim([-0.5 4.5]);
hold on, line(1:N2,0.05*(INPUT(1:N2)-
    mean(INPUT))+mean(C5(80:end)),'Color','k','LineWidth',3.5,'Parent',ax2)
xlim([0 N2]);
title('Cell Response to 10min period 50uM H2O2 ')
cmapuv=colormap;

%% -----

CC5=[]; %% to have an idea of how to limit the colorbar
for i=1:Ncell
    CC5=[CC5 C5(i,:)];
end
figure, hist(CC5,1000)
figure, imagesc(C5,[-8 12])

% normalize each cell trace between 0 and 1
C4=C3;
l=20;
subplot(2,4,1)
for i=1:l
    hold on, plot(C4(i,:))
end
subplot(2,4,2), imagesc(C4(1:l,:))
title('Only Normalized to buffer levels')

C4mc=C4; C4uv=C4; C4minmaxnorm=C4;
for i=1:Ncell
    C4mc(i,:)=C4(i,:)-mean(C4(i,:))*ones(1,N2);
    % C4uv(i,:)=C4mc(i,:)./std(C4mc(i,:));
    C4uv(i,:)=C4mc(i,:);

```

```

        C4minmaxnorm(i,:)=(C4(i,:)-min(C4(i,:)))/max(C4(i,:)-
min(C4(i,:)));
end
subplot(2,4,3)
for i=1:l
    hold on, plot(C4mc(i,:))
end
subplot(2,4,4), imagesc(C4mc(1:l,:))
title('MeanCentered')

subplot(2,4,5)
for i=1:l
    hold on, plot(C4uv(i,:))
end
subplot(2,4,6), imagesc(C4uv(1:l,:))
title('MeanCentered and UV')

subplot(2,4,7)
for i=1:l
    hold on, plot(C4minmaxnorm(i,:))
end
subplot(2,4,8), imagesc(C4minmaxnorm(1:l,:))
title('MinMax')

CC4uv=[]; %% to have an idea of how to limit the colorbar
for i=1:Ncell
    CC4uv=[CC4uv C4uv(i,:)];
end
figure, hist(CC4uv,1000)

figure, imagesc(C4uv,[-5 5])
colorbar('EastOutside')
xlim([0 N2]);
ax1=gca;
ax2 = axes('Position',get(ax1,'Position'),...
'YAxisLocation','right',...
'XAxisLocation','top',...
'Color','none','YColor','k');
hold on, line(1:N2,mean(C4uv),'Color','r','LineWidth',3.5,'Parent',ax2)
xlim([0 N2]); ylim([-0.5 2]);
hold on, line(1:N2,0.05*(INPUT(1:N2)-
mean(INPUT))+mean(C4uv(80:end)),'Color','k','LineWidth',3.5,'Parent',ax
2)
xlim([0 N2]);
title('UV and MeanCentered')
cmapuv=colormap;

figure, imagesc(C4minmaxnorm)
colorbar('EastOutside')
xlim([0 N2]);
ax1=gca;
ax2 = axes('Position',get(ax1,'Position'),...
'YAxisLocation','right',...
'XAxisLocation','top',...
'Color','none','YColor','k');

```



```

hold on,
line(1*(1:N2),mean(C4minmaxnorm(:,1:N2)), 'Color','r','LineWidth',3.5,'Parent',ax2)
xlim([0 N2]);
hold on, line(1:N2,0.05*(INPUT(1:N2)-
mean(INPUT))+mean(mean(C4minmaxnorm(80:end))), 'Color','k','LineWidth',3
.5,'Parent',ax2)
xlim([0 N2]);
title('MinMax')
cmapminmax=colormap;

Cluster1=clustergram(C4minmaxnorm,'Cluster',1,...
    'Standardize',3,...
    'DisplayRange',1,'Symmetric',false,'Colormap',cmapminmax)
addTitle(Cluster1,'MinMax Clustergram')

Cluster2=clustergram(C4uv,'Cluster',1,...
    'Standardize',3,...
    'DisplayRange',3,'Symmetric',false,'Colormap',cmapuv)
addTitle(Cluster2,'UV MC Clustergram')

%% manually oscillating cells
ID=[2 18 23 31 34 44 47 122 148];

for i=1:length(ID)
subplot (3,3,i)
plot(0.2*(INPUT(1:N2)-
mean(INPUT))+mean(C4minmaxnorm(80:end)), 'Color','k','LineWidth',3.5)
hold on, plot(C4minmaxnorm(ID(i),:), 'r','Linewidth',3)
xlim([0 N2])
end

xlswrite('50uMH2O2',C4uv,'celldatanorm_smoothed_uvmc')
xlswrite('50uMH2O2',C4minmaxnorm,'celldatanorm_smoothed_minmax')

```

## REFERENCES

1. Dudley ME, Wunderlich JR, Robbins PF, Yang JC, Hwu P, et al. 2002. *Science* 298: 850-4
2. Rosenberg SA, Yang JC, Sherry RM, Kammula US, Hughes MS, et al. 2011. *Clin Cancer Res* 17: 4550-7
3. Jotereau F, Gervois N, Labarriere N. 2012. *Target Oncol* 7: 3-14
4. Gattinoni L, Klebanoff CA, Palmer DC, Wrzesinski C, Kerstann K, et al. 2005. *J Clin Invest* 115: 1616-26
5. Pawelec G, Koch S, Griesemann H, Rehbein A, Hähnel K, Gouttefangeas C. 2006. *Cancer Immunology, Immunotherapy* 55: 981-6
6. Goronzy JJ, Fujii H, Weyand CM. 2006. *Experimental Gerontology* 41: 246-51
7. Humphries KM, Szweda PA, Szweda LI. 2006. *Free Radical Research* 40: 1239-43
8. Muller M. 2009. *Antioxidants & Redox Signaling* 11: 59-98
9. Lu T, Finkel T. 2008. *Experimental Cell Research* 314: 1918-22
10. Colavitti R, Finkel T. 2005. *Iubmb Life* 57: 277-81
11. Das R, Ponnappan S, Ponnappan U. 2007. *Free Radical Biology and Medicine* 42: 541-51
12. Hirsch AM, Rivet CA, Zhang B, Kemp ML, Lu H. 2009. *Lab on a Chip* 9: 536-44
13. Rivet C, Lee H, Hirsch A, Hamilton S, Lu H. *Chemical Engineering Science* In Press, Corrected Proof
14. Beebe DJ, Mensing GA, Walker GM. 2002. *Annual Review of Biomedical Engineering* 4: 261-86
15. El-Ali J, Sorger PK, Jensen KF. 2006. *Nature* 442: 403-11
16. Effros RB, Boucher N, Porter V, Zhu X, Spaulding C, et al. 1994. *Exp Gerontol* 29: 601-9
17. Parish ST, Wu JE, Effros RB. 2009. *Journal of Immunology* 182: 4237-43
18. Bryl E, Vallejo AN, Weyand CM, Goronzy JJ. 2001. *Journal of Immunology* 167: 3231-8
19. Warrington KJ, Vallejo AN, Weyand CM, Goronzy JJ. 2003. *Blood* 101: 3543-9
20. Brzezinska A, Magalska A, Szybinska A, Sikora E. 2004. *Experimental Gerontology* 39: 539-44
21. Passos JF, Nelson G, Wang C, Richter T, Simillion C, et al. 2010. *Mol Syst Biol* 6: 347
22. Effros RB. 2007. *Vaccine* 25: 599-604
23. Larbi A, Franceschi C, Mazzatti D, Solana R, Wikby A, Pawelec G. 2008. *Physiology* 23: 64-74
24. McElhaney JE, Dutz JP. 2008. *Journal of Infectious Diseases* 198: 632-4
25. Gomez CR, Boehmer ED, Kovacs EJ. 2005. *Current Opinion in Immunology* 17: 457-62
26. Shaw AC, Joshi S, Greenwood H, Panda A, Lord JM. 2010. *Current Opinion in Immunology* 22: 507-13
27. Kovacs EJ, Palmer JL, Fortin CF, Fulop T, Goldstein DR, Linton PJ. 2009. *Trends in Immunology* 30: 319-24
28. Solana R, Pawelec G, Tarazona R. 2006. *Immunity* 24: 491-4
29. Gruver AL, Hudson LL, Sennpowski GD. 2007. *Journal of Pathology* 211: 144-56
30. Vallejo AN, Nestel AR, Schirmer M, Weyand CM, Goronzy JJ. 1998. *Journal of Biological Chemistry* 273: 8119-29
31. Effros RB, Boucher N, Porter V, Zhu XM, Spaulding C, et al. 1994. *Experimental Gerontology* 29: 601-9
32. Effros RB, Dagarag M, Spaulding C, Man J. 2005. *Immunological Reviews* 205: 147-57
33. Plunkett FJ, Franzese O, Finney HM, Fletcher JM, Belaramani LL, et al. 2007. *Journal of Immunology* 178: 7710-9

34. Pawelec G, Ouyang Q, Colonna-Romano G, Candore G, Lio D, Caruso C. 2002. *Trends in Immunology* 23: 330-2
35. Khan N, Shariff N, Cobbold M, Bruton R, Ainsworth JA, et al. 2002. *Journal of Immunology* 169: 1984-92
36. Koch S, Larbi A, Ozcelik D, Solana R, Gouttenfangeas C, et al. 2007. *Healthy Aging and Longevity* 1114: 23-35
37. Galluzzi L, Vacchelli E, Eggermont A, Fridman WH, Galon J, et al. 2012. *OncoImmunology* 1: 306-15
38. June CH. 2007. *J Clin Invest* 117: 1204-12
39. Pawelec G, Kempf J, Larbi A. 2009. In *Handbook on Immunosenescence*, ed. T Fulop, C Franceschi, K Hirokawa, G Pawelec, pp. 107-15: Springer Netherlands
40. Pawelec G, Hirokawa K, Fülöp T. 2001. *Mechanisms of Ageing and Development* 122: 1613-37
41. Larbi A, Douziech N, Dupuis G, Khalil A, Pelletier H, et al. 2004. *Journal of Leukocyte Biology* 75: 373-81
42. Larbi A, Dupuis G, Khalil A, Douziech N, Fortin C, Fülöp JT. 2006. *Cellular Signalling* 18: 1017-30
43. Ohno-Iwashita Y, Shimada Y, Hayashi M, Inomata M. 2010. *Geriatrics & Gerontology International* 10: S41-S52
44. Garcia GG, Miller RA. 1998. *Cellular Immunology* 190: 91-100
45. Fülöp Jr T, Gagné D, Goulet A-C, Desgeorges S, Lacombe G, et al. 1999. *Experimental Gerontology* 34: 197-216
46. Strindhall J, Nilsson BO, Lofgren S, Ernerudh J, Pawelec G, et al. 2007. *Experimental Gerontology* 42: 753-61
47. Hirokawa K, Utsuyama M, Ishikawa T, Kikuchi Y, Kitagawa M, et al. *Mechanisms of Ageing and Development* 130: 86-91
48. Brenchley JM, Karandikar NJ, Betts MR, Ambrozak DR, Hill BJ, et al. 2003. *Blood* 101: 2711-20
49. Wilson S, Mazzatti DJ. 2008. *Expert Review of Proteomics* 5: 561-9
50. Mazzatti DJ, Pawelec G, Longdin R, Powell JR, Forsey RJ. 2007. *Proteome Science* 5: -
51. Mazzatti DJ, White A, Forsey RJ, Powell JR, Pawelec G. 2007. *Aging Cell* 6: 155-63
52. Cao JN, Gollapudi S, Sharman EH, Jia ZY, Gupta S. 2010. *Aging Cell* 9: 19-31
53. Rebrin I, Sohal RS. 2008. *Advanced Drug Delivery Reviews* 60: 1545-52
54. Pinzani P, Petrucci E, Orlando C, Stefanescu A, Antonini MF, et al. 1997. *Clinical Chemistry* 43: 855-6
55. Beckerman P, Yehuda A. 2009. In *Handbook on Immunosenescence*, ed. T Fulop, C Franceschi, K Hirokawa, G Pawelec, pp. 713-26: Springer Netherlands
56. Lesnfsky EJ, Hoppel CL. 2006. *Ageing Research Reviews* 5: 402-33
57. Lener B, Koziel R, Pircher H, Hutter E, Greussing R, et al. 2009. *Biochemical Journal* 423: 363-74
58. McCrann DJ, Yang D, Chen HJ, Carroll S, Ravid K. 2009. *Cell Cycle* 8: 902-8
59. Passos JF, Nelson G, Wang CF, Richter T, Simillion C, et al. 2010. *Mol Syst Biol* 6: -
60. Nelson G, Wordsworth J, Wang C, Jurk D, Lawless C, et al. 2012. *Aging Cell* 11: 345-9
61. Pahlavani MA, Harris MD. 1998. *Free Radical Biology and Medicine* 25: 903-13
62. Poggioli S, Mary J, Bakala H, Friguet B. 2004. *Strategies for Engineered Negligible Senescence: Why Genuine Control of Aging May Be Foreseeable* 1019: 211-4
63. Chevanne M, Calia C, Zampieri M, Cecchinelli B, Caldini R, et al. 2007. *Rejuvenation Research* 10: 191-203
64. Mutlu-Turkoglu U, Ilhan E, Oztezcan S, Kuru A, Aykac-Toker G, Uysal M. 2003. *Clinical Biochemistry* 36: 397-400

65. Friguet B. 2009. In *Handbook on Immunosenescence*, ed. T Fulop, C Franceschi, K Hirokawa, G Pawelec, pp. 729-49: Springer Netherlands
66. Petropoulos I, Friguet B. 2005. *Biochimica Et Biophysica Acta-Proteins and Proteomics* 1703: 261-6
67. Weindruch RH, Cheung MK, Verity MA, Walford RL. 1980. *Mechanisms of Ageing and Development* 12: 375-92
68. Witkowski J, Micklem HS. 1985. *Immunology* 56: 307-13
69. Tsai K, Hsu TG, Lu FJ, Hsu CF, Liu TY, Kong CW. 2001. *Free Radical Research* 35: 395-403
70. Ross OA, Hyland P, Curran MD, McIlhatton BP, Wikby A, et al. 2002. *Experimental Gerontology* 37: 329-40
71. Schriner SE, Linford NJ, Martin GM, Treuting P, Ogburn CE, et al. 2005. *Science* 308: 1909-11
72. Mitsui A, Hamuro J, Nakamura H, Kondo N, Hirabayashi Y, et al. 2002. *Antioxidants & Redox Signaling* 4: 693-6
73. De la Fuente M, Ferrandez MD, Del Rio M, Sol Burgos M, Miquel J. 1998. *Mech Ageing Dev* 104: 213-25
74. Duthie SJ, Ma AG, Ross MA, Collins AR. 1996. *Cancer Research* 56: 1291-5
75. Panayiotidis M, Collins AR. 1997. *Free Radical Research* 27: 533-7
76. Douziech N, Seres L, Larbi A, Szikszay E, Roy PM, et al. 2002. *Experimental Gerontology* 37: 369-87
77. Kaminski M, Kiessling M, Suss D, Krammer PH, Gulow K. 2007. *Molecular and Cellular Biology* 27: 3625-39
78. Jackson SH, Devadas S, Kwon J, Pinto LA, Williams MS. 2004. *Nature Immunology* 5: 818-27
79. Kwon J, Shatynski KE, Chen H, Morand S, de Deken X, et al. 2010. *Science Signaling* 3: -
80. Kwon J, Devadas S, Williams MS. 2003. *Free Radical Biology and Medicine* 35: 406-17
81. Salmeen A, Barford D. 2005. *Antioxidants & Redox Signaling* 7: 560-77
82. Droge W, Breitkreutz R. 2000. *Proceedings of the Nutrition Society* 59: 595-600
83. Adimora NJ, Jones DP, Kemp ML. 2010. *Antioxidants & Redox Signaling* 13: 731-43
84. Hogan PG, Lewis RS, Rao A. 2010. *Annual Review of Immunology* 28: 491-533
85. Quintana A, Schwindling C, Wenning AS, Becherer U, Rettig J, et al. 2007. *Proceedings of the National Academy of Sciences of the United States of America* 104: 14418-23
86. Skupin A, Kettenmann H, Winkler U, Wartenberg M, Sauer H, et al. 2008. *Biophysical Journal* 94: 2404-11
87. Skupin A, Kettenmann H, Falcke M. 2010. *Plos Computational Biology* 6: -
88. Dolmetsch RE, Lewis RS. 1994. *Journal of General Physiology* 103: 365-88
89. Dolmetsch RE, Xu KL, Lewis RS. 1998. *Nature* 392: 933-6
90. Lewis RS. 2003. *Biochemical Society Transactions* 31: 925-9
91. Galan C, Jardin I, Dionisio N, Salido G, Rosado JA. 2010. *Molecules* 15: 7167-87
92. Csordas G, Hajnoczky G. 2009. *Biochim Biophys Acta* 1787: 1352-62
93. Trebak M, Ginnan R, Singer HA, Jourdain H. 2010. *Antioxid Redox Signal* 12: 657-74
94. Hidalgo C, Donoso P. 2008. *Antioxid Redox Signal* 10: 1275-312
95. Singh DK, Kumar D, Siddiqui Z, Basu SK, Kumar V, Rao KVS. 2005. *Cell* 121: 281-93
96. Brookes PS, Yoon YS, Robotham JL, Anders MW, Sheu SS. 2004. *American Journal of Physiology-Cell Physiology* 287: C817-C33
97. Yan Y, Wei CL, Zhang WR, Cheng HP, Liu J. 2006. *Acta Pharmacologica Sinica* 27: 821-6
98. Kowaltowski AJ, Naia-da-Silva ES, Castilho RF, Vercesi AE. 1998. *Archives of Biochemistry and Biophysics* 359: 77-81

99. Bootman MD, Taylor CW, Berridge MJ. 1992. *Journal of Biological Chemistry* 267: 25113-9
100. Abramson JJ, Zable AC, Favero TG, Salama G. 1995. *Journal of Biological Chemistry* 270: 29644-7
101. Feng W, Liu GH, Allen PD, Pessah IN. 2000. *Journal of Biological Chemistry* 275: 35902-7
102. Bogeski I, Kilch T, Niemeyer BA. 2012. *The Journal of Physiology*: no-no
103. Hawkins BJ, Irrinki KM, Mallilankaraman K, Lien YC, Wang Y, et al. 2010. *Journal of Cell Biology* 190: 391-405
104. Prins D, Groenendyk J, Touret N, Michalak M. 2011. *EMBO Rep* 12: 1182-8
105. Grupe M, Myers G, Penner R, Fleig A. 2010. *Cell Calcium* 48: 1-9
106. Bogeski I, Kummerow C, Al-Ansary D, Schwarz EC, Koehler R, et al. 2010. *Sci Signal* 3: ra24
107. Tong X, Evangelista A, Cohen RA. 2010. *Current Opinion in Pharmacology* 10: 133-8
108. Barnes KA, Samson SE, Grover AK. 2000. *Mol Cell Biochem* 203: 17-21
109. Xu KY, Zweier JL, Becker LC. 1997. *Circ Res* 80: 76-81
110. Grover AK, Samson SE. 1997. *Am J Physiol* 273: C1250-8
111. Waring P. 2005. *Archives of Biochemistry and Biophysics* 434: 33-42
112. Cartwright EJ, Oceandy D, Neyses L. 2007. *Annals of the New York Academy of Sciences* 1099: 247-53
113. Whitesides GM. 2006. *Nature* 442: 368-73
114. Squires TM, Quake SR. 2005. *Reviews of Modern Physics* 77: 977-1026
115. Hatakeyama T, Chen DLL, Ismagilov RF. 2006. *Journal of the American Chemical Society* 128: 2518-9
116. Kastrup CJ, Runyon MK, Shen F, Ismagilov RF. 2007. *Blood* 110: 51B-B
117. Kastrup CJ, Runyon MK, Lucchetta EM, Price JM, Ismagilov RF. 2008. *Accounts of Chemical Research* 41: 549-58
118. Kastrup CJ, Runyon MK, Shen F, Ismagilov RF. 2006. *Proceedings of the National Academy of Sciences of the United States of America* 103: 15747-52
119. Kastrup CJ, Shen F, Ismagilov RF. 2007. *Angewandte Chemie-International Edition* 46: 3660-2
120. Lucchetta EM, Lee JH, Fu LA, Patel NH, Ismagilov RF. 2005. *Nature* 434: 1134-8
121. Lucchetta EM, Munson MS, Ismagilov RF. 2006. *Lab on a Chip* 6: 185-90
122. Sims CE, Allbritton NL. 2007. *Lab on a Chip* 7: 423-40
123. Salieb-Beugelaar GB, Simone G, Arora A, Philippi A, Manz A. 2010. *Analytical Chemistry* 82: 4848-64
124. Cheong R, Wang CJ, Levchenko A. 2009. *Molecular & Cellular Proteomics* 8: 433-42
125. King KR, Wang S, Jayaraman A, Yarmush ML, Toner M. 2008. *Lab on a Chip* 8: 107-16
126. Leslie DC, Easley CJ, Seker E, Karlinsey JM, Utz M, et al. 2009. *Nature Physics* 5: 231-5
127. Azizi F, Mastrangelo CH. 2008. *Lab on a Chip* 8: 907-12
128. Di Carlo D, Wu LY, Lee LP. 2006. *Lab on a Chip* 6: 1445-9
129. Skelley AM, Kirak O, Suh H, Jaenisch R, Voldman J. 2009. *Nature Methods* 6: 147-52
130. Gaudet S, Janes KA, Albeck JG, Pace EA, Lauffenburger DA, Sorger PK. 2005. *Molecular & Cellular Proteomics* 4: 1569-90
131. Miller-Jensen K, Janes KA, Brugge JS, Lauffenburger DA. 2007. *Nature* 448: 604-U11
132. Kemp ML, Wille L, Lewis CL, Nicholson LB, Lauffenburger DA. 2007. *Journal of Immunology* 178: 4984-92
133. Janes KA, Albeck JG, Gaudet S, Sorger PK, Lauffenburger DA, Yaffe MB. 2005. *Science* 310: 1646-53

134. Janes KA, Kelly JR, Gaudet S, Albeck JG, Sorger PK, Lauffenburger DA. 2004. *Journal of Computational Biology* 11: 544-61
135. Mettetal JT, Muzzey D, Gomez-Urbe C, van Oudenaarden A. 2008. *Science* 319: 482-4
136. Bennett MR, Pang WL, Ostroff NA, Baumgartner BL, Nayak S, et al. 2008. *Nature* 454: 1119-22
137. Shimizu TS, Tu YH, Berg HC. 2010. *Mol Syst Biol* 6: -
138. Jovic A, Howell B, Takayama S. 2009. *Microfluidics and Nanofluidics* 6: 717-29
139. Geva-Zatorsky N, Dekel E, Batchelor E, Lahav G, Alon U. 2010. *Proceedings of the National Academy of Sciences of the United States of America* 107: 13550-5
140. Fujita KA, Toyoshima Y, Uda S, Ozaki Y, Kubota H, Kuroda S. 2010. *Science Signaling* 3: -
141. Gattinoni L, Powell DJ, Rosenberg SA, Restifo NP. 2006. *Nature Reviews Immunology* 6: 383-93
142. Rosenberg SA, Restifo NP, Yang JC, Morgan RA, Dudley ME. 2008. *Nature Reviews Cancer* 8: 299-308
143. Mackensen A, Meidenbauer N, Vogl S, Laumer M, Berger J, Andreessen R. 2006. *Journal of Clinical Oncology* 24: 5060-9
144. Porter DL, Levine BL, Bunin N, Stadtmauer EA, Luger SM, et al. 2006. *Blood* 107: 1325-31
145. Park JR, DiGiusto DL, Slovak M, Wright C, Naranjo A, et al. 2007. *Molecular Therapy* 15: 825-33
146. Perillo NL, Walford RL, Newman MA, Effros RB. 1989. *Experimental Gerontology* 24: 177-87
147. Yee C, Thompson JA, Byrd D, Riddell SR, Roche P, et al. 2002. *Proceedings of the National Academy of Sciences of the United States of America* 99: 16168-73
148. Shen XL, Zhou JH, Hathcock KS, Robbins P, Powell DJ, et al. 2007. *Journal of Immunotherapy* 30: 123-9
149. Gattinoni L, Klebanoff CA, Palmer DC, Wrzesinski C, Kerstann K, et al. 2005. *Journal of Clinical Investigation* 115: 1616-26
150. Pawelec G, Akbar A, Caruso C, Solana R, Grubeck-Loebenstien B, Wikby A. 2005. *Immunological Reviews* 205: 257-68
151. Hamann D, Kostense S, Wolthers KC, Otto SA, Baars PA, et al. 1999. *International Immunology* 11: 1027-33
152. Mazzatti DJ, Pawelec G, Longdin R, Powell JR, Forsey RJ. 2007. *Proteome Sci* 5: 7
153. Stroock AD, Dertinger SKW, Ajdari A, Mezić I, Stone HA, Whitesides GM. 2002. *Science* 295: 647-51
154. Partanen S. 2001. *Histochemical Journal* 33: 387-95
155. Röth A, Schneider L, Himmelreich H, Baerlocher G, Dührsen U. 2007. *Cytotherapy* 9: 91-8
156. Laux I, Khoshnan A, Tindell C, Bae D, Zhu XM, et al. 2000. *Clinical Immunology* 96: 187-97
157. Perillo NL, Naeim F, Walford RL, Effros RB. 1993. *Mechanisms of Ageing and Development* 67: 173-85
158. Jaruga E, Skierski J, Radziszewska E, Sikora E. 2000. *Acta Biochimica Polonica* 47: 293-300
159. Jaruga E, Skierski J, Radziszewska E, Sikora E. 2000. *Acta Biochimica Polonica* 47: 293-300
160. Erickson S, Sangfelt O, Heyman M, Castro J, Einhorn S, Grandt D. 1998. *Oncogene* 17: 595-602
161. Vallejo AN, Weyand CM, Goronzy JJ. 2004. *Trends in Molecular Medicine* 10: 119-24

162. Brenchley JM, Karandikar NJ, Betts MR, Ambrozak DR, Hill BJ, et al. 2003. *Blood* 101: 2711-20
163. Koch S, Larbi A, Derhovanessian E, Ozcelik D, Naumova E, Pawelec G. 2008. *Immun Ageing* 5: 6
164. Effros RB, Schachter F, Boucher N, Spaulding C, Zhu XM, Porter V. 1995. *Journal of Cellular Biochemistry*: 92-
165. Fulop T, Larbi A, Dupuis G, Pawelec G. 2003. *Arthritis Research & Therapy* 5: 290-302
166. Berg NN, Puente LG, Dawicki W, Ostergaard HL. 1998. *Journal of Immunology* 161: 2919-24
167. Fauce SR, Jamieson BD, Chin AC, Mitsuyasy RT, Parish ST, et al. 2008. *Journal of Immunology* 181: 7400-6
168. Altan-Bonnet G, Germain RN. 2005. *Plos Biology* 3: 1925-38
169. Singh K, Deshpande P, Pryshchep S, Colmegna I, Liarski V, et al. 2009. *Journal of Immunology* 183: 8258-67
170. Lin J, Harding A, Giurisato E, Shaw AS. 2009. *Molecular and Cellular Biology* 29: 2082-91
171. Eisen MB, Spellman PT, Brown PO, Botstein D. 1998. *Proceedings of the National Academy of Sciences of the United States of America* 95: 14863-8
172. Carr JM, Carrasco MJ, Thaventhiran JED, Bambrough PJ, Kraman M, et al. 2006. *Proceedings of the National Academy of Sciences of the United States of America* 103: 19454-9
173. Frauwirth KA, Riley JL, Harris MH, Parry RV, Rathmell JC, et al. 2002. *Immunity* 16: 769-77
174. Miller J, Baker C, Cook K, Graf B, Sanchez-Lockhart M, et al. 2009. *Immunologic Research* 45: 159-72
175. Carey KD, Dillon TJ, Schmitt JM, Baird AM, Holdorf AD, et al. 2000. *Molecular and Cellular Biology* 20: 8409-19
176. Melenhorst JJ. 2009. *Cytotherapy* 11: 813-4
177. Rasmussen AM, Borelli G, Hoel HJ, Lislerud K, Gaudernack G, et al. 2010. *Journal of Immunological Methods* 355: 52-60
178. Zhang H, Snyder KM, Suhoski MM, Maus MV, Kapoor V, et al. 2007. *Journal of Immunology* 179: 4910-8
179. Jeras M, Bricl I, Zorec R, Svajger U. 2010. *Journal of Biomedicine and Biotechnology*: -
180. Germenis AE, Karanikas V. 2010. *Journal of Reproductive Immunology* 85: 47-50
181. Dagarag M, Ng H, Lubong R, Effros RB, Yang OO. 2003. *J. Virol.* 77: 3077-83
182. Larbi A, Dupuis G, Khalil A, Douziech N, Fortin C, Fulop T. 2006. *Cellular Signalling* 18: 1017-30
183. Suni MA, Maino VC, Maecker HT. 2005. *Current Opinion in Immunology* 17: 434-40
184. Barber DL, Wherry EJ, Ahmed R. 2003. *Journal of Immunology* 171: 27-31
185. Djeu JY, Jiang K, Wei S. 2002. *Clinical Cancer Research* 8: 636-40
186. Lawless C, Wang C, Jurk D, Merz A, Zglinicki TV, Passos JF. 2010. *Experimental Gerontology*
187. Tsygankov D, Liu Y, Sanoff HK, Sharpless NE, Elston TC. 2009. *Proceedings of the National Academy of Sciences* 106: 16562-7
188. Huse M, Klein LO, Girvin AT, Faraj JM, Li QJ, et al. 2007. *Immunity* 27: 76-88
189. Janes KA, Albeck JG, Gaudet S, Sorger PK, Lauffenburger DA, Yaffe MB. 2005. *Science* 310: 1646-53
190. Janes KA, Kelly JR, Gaudet S, Albeck JG, Sorger PK, Lauffenburger DA. 2004. *J Comput Biol* 11: 544-61
191. Borthwick NJ, Lowdell M, Salmon M, Akbar AN. 2000. *International Immunology* 12: 1005-13

192. Miller RA, Garcia G, Kirk CJ, Witkowski JM. 1997. *Immunological Reviews* 160: 79-90
193. Larbi A, Douziech N, Dupuis G, Khalil A, Pelletier H, et al. 2004. *J Leukoc Biol* 75: 373-81
194. Tomoiu A, Larbi A, Fortin C, Dupuis G, Fulop T. 2007. *Biogerontology: Mechanisms and Interventions* 1100: 98-110
195. Weber GF. 2002. In *Advances in Cell Aging and Gerontology*, ed. PM Mark, pp. 127-45: Elsevier
196. Passos JF, Saretzki G, Ahmed S, Nelson G, Richter T, et al. 2007. *Plos Biology* 5: e110
197. Bahar R, Hartmann CH, Rodriguez KA, Denny AD, Busuttil RA, et al. 2006. *Nature* 441: 1011-4
198. Feinerman O, Veiga J, Dorfman JR, Germain RN, Altan-Bonnet G. 2008. *Science* 321: 1081-4
199. Pritchard JR, Cosgrove BD, Hemann MT, Griffith LG, Wands JR, Lauffenburger DA. 2009. *Molecular Cancer Therapeutics* 8: 2183-92
200. Thompson JA, Figlin RA, Sifri-Steele C, Berenson RJ, Frohlich MW. 2003. *Clinical Cancer Research* 9: 3562-70
201. Newrzela S, Gunda B, Laer Dv. 2008. pp. 71-82
202. McDonald JC, Duffy DC, Anderson JR, Chiu DT, Wu HK, et al. 2000. *Electrophoresis* 21: 27-40
203. Krutzik PO, Nolan GP. 2003. *Cytometry Part A* 55A: 61-70
204. Wold S, Sjostrom M, Eriksson L. 2001. *Chemometrics and Intelligent Laboratory Systems* 58: 109-30
205. Pawelec G, Wagner W, Adibzadeh M, Engel A. 1999. *Exp Gerontol* 34: 419-29
206. Kwon J, Shatynski KE, Chen H, Morand S, de Deken X, et al. 2010. *Sci Signal* 3: ra59
207. Kaminski M, Kiessling M, Suss D, Krammer PH, Gulow K. 2007. *Mol Cell Biol* 27: 3625-39
208. Jackson SH, Devadas S, Kwon J, Pinto LA, Williams MS. 2004. *Nat Immunol* 5: 818-27
209. Kwon J, Devadas S, Williams MS. 2003. *Free Radic Biol Med* 35: 406-17
210. Weindruch RH, Cheung MK, Verity MA, Walford RL. 1980. *Mech Ageing Dev* 12: 375-92
211. Tsai K, Hsu TG, Lu FJ, Hsu CF, Liu TY, Kong CW. 2001. *Free Radic Res* 35: 395-403
212. Ross OA, Hyland P, Curran MD, McIlhatton BP, Wikby A, et al. 2002. *Exp Gerontol* 37: 329-40
213. Chevanne M, Calia C, Zampieri M, Cecchinelli B, Caldini R, et al. 2007. *Rejuvenation Res* 10: 191-204
214. Mutlu-Turkoglu U, Ilhan E, Oztezcen S, Kuru A, Aykac-Toker G, Uysal M. 2003. *Clin Biochem* 36: 397-400
215. Das R, Ponnappan S, Ponnappan U. 2007. *Free Radic Biol Med* 42: 541-51
216. Friguet B. 2009. ed. T Fulop, C Franceschi, K Hirokawa, G Pawelec, pp. 729-49: Springer Netherlands
217. Petropoulos I, Friguet B. 2005. *Biochim Biophys Acta* 1703: 261-6
218. Pahlavani M, Harris M. 1998. *Free Radical Biology and Medicine* 25: 903-13
219. Poggioli S, Mary J, Bakala H, Friguet B. 2004. *Ann N Y Acad Sci* 1019: 211-4
220. Visala Rao D, Boyle GM, Parsons PG, Watson K, Jones GL. 2003. *Mech Ageing Dev* 124: 55-69
221. Cao JN, Gollapudi S, Sharman EH, Jia Z, Gupta S. 2010. *Aging Cell* 9: 19-31
222. Remondini D, Salvioli S, Francesconi M, Pierini M, Mazzatti DJ, et al. 2010. *Mol Biosyst* 6: 1983-92
223. Gautam N, Das S, Mahapatra SK, Chakraborty SP, Kundu PK, Roy S. 2010. *Oxidative Medicine and Cellular Longevity* 3: 275-82
224. Rivet CA, Hill AS, Lu H, Kemp ML. 2011. *Mol Cell Proteomics* 10: M110 003921



225. Comes N, Buie LK, Borrás T. 2011. *Genes Cells* 16: 243-59
226. Ruperez P, Gago-Martinez A, Burlingame AL, Osés-Prieto JA. 2012. *Mol Cell Proteomics* 11: 171-86
227. Fernandes AP, Holmgren A. 2004. *Antioxid Redox Signal* 6: 63-74
228. Wang W, Gou L, Xie G, Tong A, He F, et al. 2010. *J Proteome Res* 9: 3812-9
229. Anathy V, Aesif SW, Guala AS, Havermans M, Reynaert NL, et al. 2009. *Journal of Cell Biology* 184: 241-52
230. Spaulding C, Guo W, Effros RB. 1999. *Exp Gerontol* 34: 633-44
231. Chen X, Zhong Z, Xu Z, Chen L, Wang Y. 2010. *Free Radic Res* 44: 587-604
232. Kemp M, Go YM, Jones DP. 2008. *Free Radic Biol Med* 44: 921-37
233. Filomeni G, Rotilio G, Ciriolo MR. 2002. *Biochem Pharmacol* 64: 1057-64
234. Kwon YW, Masutani H, Nakamura H, Ishii Y, Yodoi J. 2003. *Biol Chem* 384: 991-6
235. Fratelli M, Goodwin LO, Orom UA, Lombardi S, Tonelli R, et al. 2005. *Proc Natl Acad Sci U S A* 102: 13998-4003
236. Castellani P, Angelini G, Delfino L, Matucci A, Rubartelli A. 2008. *Eur J Immunol* 38: 2419-25
237. Wu C, Parrott AM, Fu C, Liu T, Marino SM, et al. 2011. *Antioxid Redox Signal* 15: 2565-604
238. Pawelec G, Effros RB, Caruso C, Remarque E, Barnett Y, Solana R. 1999. *Front Biosci* 4: D216-69
239. Fulop T, Jr., Larbi A, Dupuis G, Pawelec G. 2003. *Arthritis Research & Therapy* 5: 290-302
240. Rink L, Cakman I, Kirchner H. 1998. *Mech Ageing Dev* 102: 199-209
241. Griffiths HR, Dunston CR, Bennett SJ, Grant MM, Phillips DC, Kitas GD. 2011. *Biochem Soc Trans* 39: 1273-8
242. Staal FJ, Anderson MT, Staal GE, Herzenberg LA, Gitler C, Herzenberg LA. 1994. *Proc Natl Acad Sci U S A* 91: 3619-22
243. Kregel KC, Zhang HJ. 2007. *Am J Physiol Regul Integr Comp Physiol* 292: R18-36
244. Rider DA, Sinclair AJ, Young SP. 2003. *Mech Ageing Dev* 124: 191-8
245. Kippner LE, Finn NA, Shukla S, Kemp ML. 2011. *BMC Syst Biol* 5: 164
246. Margis R, Dunand C, Teixeira FK, Margis-Pinheiro M. 2008. *FEBS J* 275: 3959-70
247. Gladyshev VN, Stadtman TC, Hatfield DL, Jeang KT. 1999. *Proc Natl Acad Sci U S A* 96: 835-9
248. Hofmann B, Hecht HJ, Flohe L. 2002. *Biol Chem* 383: 347-64
249. Ishii T, Warabi E, Yanagawa T. 2012. *J Clin Biochem Nutr* 50: 91-105
250. Smart-Halajko MC, Robciuc MR, Cooper JA, Jauhiainen M, Kumari M, et al. 2010. *Arterioscler Thromb Vasc Biol* 30: 2277-82
251. Tskhovrebova L, Trinick J. 2003. *Nat Rev Mol Cell Biol* 4: 679-89
252. Thieblemont C, Nasser V, Felman P, Leroy K, Gazzo S, et al. 2004. *Blood* 103: 2727-37
253. Salles N, Szanto I, Herrmann F, Armenian B, Stumm M, et al. 2005. *Exp Gerontol* 40: 353-7
254. Rueckschloss U, Villmow M, Klockner U. 2010. *Exp Gerontol* 45: 788-96
255. Swindell WR. 2011. *Ageing Research Reviews* 10: 132-45
256. Malavolta M, Cipriano C, Costarelli L, Giacconi R, Tesi S, et al. 2008. *Rejuvenation Res* 11: 455-9
257. Storz P. 2006. *Sci STKE* 2006: re3
258. Rohrbach S, Gruenler S, Teschner M, Holtz J. 2006. *Am J Physiol Regul Integr Comp Physiol* 291: R927-35
259. Cho CG, Kim HJ, Chung SW, Jung KJ, Shim KH, et al. 2003. *Exp Gerontol* 38: 539-48
260. Adimora NJ, Jones DP, Kemp ML. 2010. *Antioxid Redox Signal* 13: 731-43

261. Lenton KJ, Therriault H, Cantin AM, Fulop T, Payette H, Wagner JR. 2000. *Am J Clin Nutr* 71: 1194-200
262. Boraldi F, Annovi G, Tiozzo R, Sommer P, Quagliano D. 2010. *Mech Ageing Dev* 131: 625-35
263. Schmittgen TD, Lee EJ, Jiang J, Sarkar A, Yang L, et al. 2008. *Methods* 44: 31-8
264. Watson WH, Jones DP. 2003. *FEBS Lett* 543: 144-7
265. Jones DP. 2002. *Methods Enzymol* 348: 93-112
266. Schafer FQ, Buettner GR. 2001. *Free Radic Biol Med* 30: 1191-212
267. Rost J, Rapoport S. 1964. *Nature* 201: 185-
268. Watson WH, Pohl J, Montfort WR, Stuchlik O, Reed MS, et al. 2003. *J Biol Chem* 278: 33408-15
269. Oh-hora M, Rao A. 2008. *Curr Opin Immunol* 20: 250-8
270. Oh-Hora M, Yamashita M, Hogan PG, Sharma S, Lamperti E, et al. 2008. *Nature Immunology* 9: 432-43
271. Hogan PG, Lewis RS, Rao A. 2010. *Annu Rev Immunol* 28: 491-533
272. Ritchie MF, Samakai E, Soboloff J. 2012. *EMBO J* 31: 1123-33
273. Quintana A, Hoth M. 2012. *Cell Calcium*
274. Feske S. 2007. *Nat Rev Immunol* 7: 690-702
275. Grossmann A, Maggio-Price L, Jinneman JC, Rabinovitch PS. 1991. *Cell Immunol* 135: 118-31
276. Miller RA. 1996. *Life Sci* 59: 469-75
277. Gupta S. 1989. *Ann N Y Acad Sci* 568: 277-82
278. Sulger J, Dumais-Huber C, Zerfass R, Henn FA, Aldenhoff JB. 1999. *Biological psychiatry* 45: 737-42
279. Grossmann A, Ledbetter JA, Rabinovitch PS. 1989. *Experimental Cell Research* 180: 367-82
280. Chay TR. 1996. *Neural Computation* 8: 951-78
281. Holcman D, Schuss Z. 2005. *Siam Journal on Applied Mathematics* 65: 1006-26
282. Roussel C, Erneux T, Schiffmann SN, Gall D. 2006. *Cell Calcium* 39: 455-66
283. Rice JJ, Jafri MS. 2001. *Philosophical Transactions of the Royal Society of London. Series A: Mathematical, Physical and Engineering Sciences* 359: 1143-57
284. Hake J, Edwards AG, Yu Z, Kekenos-Huskey PM, Michailova AP, et al. 2012. *J Physiol*
285. Cui JJ, Kaandorp JA, Sloot PMA, Lloyd CM, Filatov MV. 2009. *Fems Yeast Research* 9: 1137-47
286. Swietach P, Spitzer KW, Vaughan-Jones RD. 2010. *Frontiers in Bioscience-Landmark* 15: 661-80
287. Groenendaal W, Jeneson JAL, Verhoog PJ, van Riel NAW, Ten Eikelder HMM, et al. 2008. *Iet Systems Biology* 2: 411-22
288. Wong AYK, Klassen GA. 1993. *Cell Calcium* 14: 227-43
289. Ahnadi CE, Payet MD, Dupuis G. 1996. *Cell Calcium* 19: 509-20
290. Kim S, Patrick SM, Braunstein NS, Thomas JL, Leonard EF. 2001. *Ann Biomed Eng* 29: 373-83
291. Maurya MR, Subramaniam S. 2007. *Biophysical Journal* 93: 709-28
292. Maurya MR, Subramaniam S. 2007. *Biophysical Journal* 93: 729-40
293. Pawelec G, Kempf J, Larbi A. 2009. ed. T Fulop, C Franceschi, K Hirokawa, G Pawelec, pp. 107-15: Springer Netherlands
294. Abell E, Ahrends R, Bandara S, Park BO, Teruel MN. 2011. *Proceedings of the National Academy of Sciences* 108: 14485-90
295. Liu W, Tang F, Chen J. 2010. *Math Biosci* 228: 110-8
296. Marhl M, Haberichter T, Brumen M, Heinrich R. 2000. *Biosystems* 57: 75-86

297. Zhang SL, Yu Y, Roos J, Kozak JA, Deerinck TJ, et al. 2005. *Nature* 437: 902-5
298. Prakriya M, Feske S, Gwack Y, Srikanth S, Rao A, Hogan PG. 2006. *Nature* 443: 230-3
299. Quintana A, Pasche M, Junker C, Al-Ansary D, Rieger H, et al. 2011. *EMBO J* 30: 3895-912
300. Bezprozvanny I, Watras J, Ehrlich BE. 1991. *Nature* 351: 751-4
301. De Young GW, Keizer J. 1992. *Proceedings of the National Academy of Sciences* 89: 9895-9
302. Atri A, Amundson J, Clapham D, Sneyd J. 1993. *Biophysical Journal* 65: 1727-39
303. Li YX, Rinzel J. 1994. *J Theor Biol* 166: 461-73
304. Sneyd J, Dufour JF. 2002. *Proc Natl Acad Sci U S A* 99: 2398-403
305. Politi A, Gaspers LD, Thomas AP, Höfer T. 2006. *Biophysical Journal* 90: 3120-33
306. Kowalewski JM, Uhlén P, Kitano H, Brismar H. 2006. *Math Biosci* 204: 232-49
307. Chen X-f, Li C-x, Wang P-y, Li M, Wang W-c. 2008. *Biophysical Chemistry* 136: 87-95
308. Luik RM, Wang B, Prakriya M, Wu MM, Lewis RS. 2008. *Nature* 454: 538-42
309. Guse AH, Roth E, Emmrich F. 1993. *Biochem J* 291 ( Pt 2): 447-51
310. Lewis RS. 2001. *Annu Rev Immunol* 19: 497-521
311. Hoth M, Fanger CM, Lewis RS. 1997. *Journal of Cell Biology* 137: 633-48
312. Petrzilka GE, Schroeder HE. 1979. *Cell Tissue Res* 201: 101-27
313. Mirza N, Pollock K, Hoelzinger DB, Dominguez AL, Lustgarten J. 2011. *Aging Cell* 10: 853-67
314. Esser MT, Haverstick DM, Fuller CL, Gullo CA, Braciale VL. 1998. *J Exp Med* 187: 1057-67
315. Maul-Pavicic A, Chiang SC, Rensing-Ehl A, Jessen B, Fauriat C, et al. 2011. *Proc Natl Acad Sci U S A* 108: 3324-9
316. Philosophe B, Miller RA. 1989. *Eur J Immunol* 19: 695-9
317. Kennes B, Hubert C, Neve P. 1981. *Immunology Letters* 2: 231-8
318. Zaidi A, Gao J, Squier TC, Michaelis ML. 1998. *Neurobiol Aging* 19: 487-95
319. Zhao X, Weisleder N, Thornton A, Oppong Y, Campbell R, et al. 2008. *Aging Cell* 7: 561-8
320. Le Jemtel T, Lambert F, Levitsky D, Clergue M, Anger M, et al. 1993. *Circulation Research* 72: 341-8
321. Pottorf WJ, De Leon DD, Hessinger DA, Buchholz JN. 2001. *Brain Res* 914: 57-65
322. Kaplan P, Jurkovicova D, Babusikova E, Hudecova S, Racay P, et al. 2007. *Molecular and Cellular Biochemistry* 301: 219-26
323. Chung K, Rivet CA, Kemp ML, Lu H. 2011. *Anal Chem* 83: 7044-52
324. Thakur P, Fomina AF. 2012. *Biophysical Journal* 102: 315a
325. Dadsetan S, Zakharova L, Molinski TF, Fomina AF. 2008. *J Biol Chem* 283: 12512-9
326. Redondo PC, Salido GM, Rosado JA, Pariente JA. 2004. *Biochem Pharmacol* 67: 491-502
327. Bootman MD, Taylor CW, Berridge MJ. 1992. *J Biol Chem* 267: 25113-9
328. Kang S, Kang J, Kwon H, Frueh D, Yoo SH, et al. 2008. *Journal of Biological Chemistry* 283: 25567-75
329. Arrol HP, Church LD, Bacon PA, Young SP. 2008. *Clin Exp Immunol* 153: 86-95
330. Schmittgen TD, Livak KJ. 2008. *Nat Protoc* 3: 1101-8
331. Raj A, Peskin CS, Tranchina D, Vargas DY, Tyagi S. 2006. *Plos Biology* 4: 1707-19
332. Elowitz MB, Levine AJ, Siggia ED, Swain PS. 2002. *Science* 297: 1183-6
333. Chang HH, Hemberg M, Barahona M, Ingber DE, Huang S. 2008. *Nature* 453: 544-U10
334. Singh DK, Ku CJ, Wichaidit C, Steininger RJ, Wu LF, Altschuler SJ. 2010. *Mol Syst Biol* 6: -
335. Cohen AA, Geva-Zatorsky N, Eden E, Frenkel-Morgenstern M, Issaeva I, et al. 2008. *Science* 322: 1511-6

336. Spencer SL, Gaudet S, Albeck JG, Burke JM, Sorger PK. 2009. *Nature* 459: 428-U144
337. Eldar A, Elowitz MB. 2010. *Nature* 467: 167-73
338. Rivet CA, Hill AS, Lu H, Kemp ML. 2011. *Molecular & Cellular Proteomics* 10: M110003921
339. Irimia D, Toner M. 2006. *Lab on a Chip* 6: 345-52
340. Wheeler AR, Throdset WR, Whelan RJ, Leach AM, Zare RN, et al. 2003. *Analytical Chemistry* 75: 3581-6
341. Taff BM, Voldman J. 2005. *Analytical Chemistry* 77: 7976-83
342. Voldman J, Gray ML, Toner M, Schmidt MA. 2002. *Analytical Chemistry* 74: 3984-90
343. Enger J, Goksor M, Ramser K, Hagberg P, Hanstorp D. 2004. *Lab on a Chip* 4: 196-200
344. Rettig JR, Folch A. 2005. *Analytical Chemistry* 77: 5628-34
345. Yamamura S, Kishi H, Tokimitsu Y, Kondo S, Honda R, et al. 2005. *Analytical Chemistry* 77: 8050-6
346. Figueroa XA, Cooksey GA, Votaw SV, Horowitz LF, Folch A. 2010. *Lab on a Chip* 10: 1120-7
347. Park JY, Morgan M, Sachs AN, Samorezov J, Teller R, et al. 2010. *Microfluidics and Nanofluidics* 8: 263-8
348. Di Carlo D, Aghdam N, Lee LP. 2006. *Analytical Chemistry* 78: 4925-30
349. Tan WH, Takeuchi S. 2007. *Proceedings of the National Academy of Sciences of the United States of America* 104: 1146-51
350. Faley S, Seale K, Hughey J, Schaffer DK, VanCornpernelle S, et al. 2008. *Lab on a Chip* 8: 1700-12
351. Kobel S, Valero A, Latt J, Renaud P, Lutolf M. 2010. *Lab on a Chip* 10: 857-63
352. Kim MC, Wang ZH, Lam RHW, Thorsen T. 2008. *Journal of Applied Physics* 103: -
353. Chung K, Kim Y, Kanodia JS, Gong E, Shvartsman SY, Lu H. 2011. *Nature Methods* 8: 171-U03
354. Jeon NL, Dertinger SKW, Chiu DT, Choi IS, Stroock AD, Whitesides GM. 2000. *Langmuir* 16: 8311-6
355. Imboden JB, Weiss A. 1987. *Biochemical Journal* 247: 695-700
356. Dalerba P, Kalisky T, Sahoo D, Rajendran PS, Rothenberg ME, et al. 2011. *Nature Biotechnology* 29: 1120-U11
357. Nakamura N, Yamazawa T, Okubo Y, Iino M. 2009. *Molecular Systems Biology* 5: -
358. Williams MS, Kwon J. 2004. *Free Radic Biol Med* 37: 1144-51
359. Yan Y, Wei CL, Zhang WR, Cheng HP, Liu J. 2006. *Acta Pharmacol Sin* 27: 821-6
360. Decuypere JP, Monaco G, Missiaen L, De Smedt H, Parys JB, Bultynck G. 2011. *J Aging Res* 2011: 920178
361. Block SM, Segall JE, Berg HC. 1983. *J Bacteriol* 154: 312-23
362. Shimizu TS, Tu Y, Berg HC. 2010. *Mol Syst Biol* 6: 382
363. Taylor RJ, Falconnet D, Niemisto A, Ramsey SA, Prinz S, et al. 2009. *Proc Natl Acad Sci U S A* 106: 3758-63
364. Geva-Zatorsky N, Dekel E, Batchelor E, Lahav G, Alon U. 2010. *Proc Natl Acad Sci U S A* 107: 13550-5
365. Fujita KA, Toyoshima Y, Uda S, Ozaki Y, Kubota H, Kuroda S. 2010. *Sci Signal* 3: ra56
366. Garstecki P, Fuerstman MJ, Whitesides GM. 2005. *Nat Phys* 1: 168-71
367. Mosadegh B, Kuo C-H, Tung Y-C, Torisawa Y-s, Bersano-Begey T, et al. 2010. *Nat Phys* 6: 433-7
368. Olofsson J, Bridle H, Sinclair J, Granfeldt D, Sahlin E, Orwar O. 2005. *Proc Natl Acad Sci U S A* 102: 8097-102
369. Kim SJ, Yokokawa R, Leshner-Perez SC, Takayama S. 2012. *Anal Chem* 84: 1152-6
370. Kuczenski B, Ruder WC, Messner WC, Leduc PR. 2009. *PLoS One* 4: e4847
371. Zhang X, Grimley A, Bertram R, Roper MG. 2010. *Anal Chem* 82: 6704-11

372. Jackson SH, Devadas S, Kwon J, Pinto LA, Williams MS. 2004. *Nat Immunol* 5: 818-27
373. Kwon J, Shatynski KE, Chen H, Morand S, de Deken X, et al. 2010. *Sci. Signal.* 3: ra59-
374. Camello-Almaraz C, Gomez-Pinilla PJ, Pozo MJ, Camello PJ. 2006. *Am J Physiol Cell Physiol* 291: C1082-8
375. Brookes PS, Yoon Y, Robotham JL, Anders MW, Sheu S-S. 2004. *American Journal of Physiology - Cell Physiology* 287: C817-C33
376. Bedard K, Krause K-H. 2007. *Physiological Reviews* 87: 245-313
377. Raad H, Paclet M-H, Boussetta T, Kroviarski Y, Morel F, et al. 2009. *The FASEB Journal* 23: 1011-22
378. Yin W, Jo H, Voit EO. 2010. *Ann Biomed Eng* 38: 291-307
379. Fontayne A, Dang PM-C, Gougerot-Pocidallo M-A, El Benna J. 2002. *Biochemistry* 41: 7743-50
380. Roose JP, Mollenauer M, Gupta VA, Stone J, Weiss A. 2005. *Molecular and Cellular Biology* 25: 4426-41
381. Rigutto S, Hoste C, Grasberger H, Milenkovic M, Communi D, et al. 2009. *Journal of Biological Chemistry* 284: 6725-34
382. Enyedi B, Varnai P, Geiszt M. 2010. *Antioxid Redox Signal* 13: 721-9
383. Csala M, Margittai E, Banhegyi G. 2010. *Antioxid Redox Signal* 13: 77-108
384. Pollard MG, Travers KJ, Weissman JS. 1998. *Mol Cell* 1: 171-82
385. Frand AR, Kaiser CA. 1998. *Mol Cell* 1: 161-70
386. Sevier CS, Qu H, Heldman N, Gross E, Fass D, Kaiser CA. 2007. *Cell* 129: 333-44
387. Rao RV, Ellerby HM, Bredesen DE. 2004. *Cell Death and Differentiation* 11: 372-80
388. Joseph SK, Nakao SK, Sukumvanich S. 2006. *Biochem J* 393: 575-82
389. Kaplin AI, Ferris CD, Voglmaier SM, Snyder SH. 1994. *J Biol Chem* 269: 28972-8
390. Renard-Rooney DC, Joseph SK, Seitz MB, Thomas AP. 1995. *Biochem J* 310 ( Pt 1): 185-92
391. Higo T, Hattori M, Nakamura T, Natsume T, Michikawa T, Mikoshiba K. 2005. *Cell* 120: 85-98
392. Kang S, Kang J, Kwon H, Frueh D, Yoo SH, et al. 2008. *J Biol Chem* 283: 25567-75
393. Li G, Mongillo M, Chin KT, Harding H, Ron D, et al. 2009. *J Cell Biol* 186: 783-92
394. Zaidi A, Barron L, Sharov VS, Schoneich C, Michaelis EK, Michaelis ML. 2003. *Biochemistry* 42: 12001-10
395. Zaidi A, Michaelis ML. 1999. *Free Radic Biol Med* 27: 810-21
396. Jones DP, Go YM. 2010. *Diabetes Obes Metab* 12 Suppl 2: 116-25
397. Blais JD, Chin KT, Zito E, Zhang Y, Heldman N, et al. 2010. *J Biol Chem* 285: 20993-1003
398. Hersen P, McClean MN, Mahadevan L, Ramanathan S. 2008. *Proc Natl Acad Sci U S A* 105: 7165-70
399. VanDersarl JJ, Xu AM, Melosh NA. 2011. *Lab Chip* 11: 3057-63
400. Xie Y, Wang Y, Chen L, Mastrangelo CH. 2008. *Lab Chip* 8: 779-85
401. Raj A, Peskin CS, Tranchina D, Vargas DY, Tyagi S. 2006. *PLoS Biol* 4: e309
402. Cohen RA, Weisbrod RM, Gericke M, Yaghoubi M, Bierl C, Bolotina VM. 1999. *Circ Res* 84: 210-9
403. Uhlen P. 2004. *Sci. STKE* 2004: pl15-
404. Rasmussen AM, Borelli G, Hoel HJ, Lislerud K, Gaudernack G, et al. 2010. *J Immunol Methods* 355: 52-60
405. Teschner D, Wenzel G, Distler E, Schnürer E, Theobald M, et al. 2011. *Scandinavian Journal of Immunology* 74: 155-64
406. Brimnes M, Gang A, Donia M, thor Straten P, Svane I, Hadrup S. *Cancer Immunology, Immunotherapy*: 1-11

407. Gribben JG, Stephenson JJ, Bartlett NL, Milder MS, Boccia RV, et al. 2005. *Journal of Clinical Oncology* 23: 168S-S
408. Kipps TJ, Wierda WG, Castro JE, Keating MJ, Boccia RV, et al. 2005. *Journal of Clinical Oncology* 23: 168S-S
409. Perillo NL, Naeim F, Walford RL, Effros RB. 1993. *Experimental Cell Research* 207: 131-5
410. Wikby A, Ferguson F, Forsey R, Thompson J, Strindhall J, et al. 2005. *Journals of Gerontology Series A-Biological Sciences and Medical Sciences* 60: 556-65
411. Hadrup SR, Strindhall J, Kollgaard T, Seremet T, Johansson B, et al. 2006. *Journal of Immunology* 176: 2645-53
412. Berlett BS, Stadtman ER. 1997. *Journal of Biological Chemistry* 272: 20313-6
413. Gaudet S, Janes KA, Albeck JG, Pace EA, Lauffenburger DA, Sorger PK. 2005. *Mol Cell Proteomics* 4: 1569-90
414. Kemp ML, Wille L, Lewis CL, Nicholson LB, Lauffenburger DA. 2007. *J Immunol* 178: 4984-92
415. Faure P, Korn H. 2001. *Comptes Rendus De L Academie Des Sciences Serie Iii-Sciences De La Vie-Life Sciences* 324: 773-93
416. Wagner CD, Persson PB. 1996. *Cardiovasc Res* 31: 380-7
417. Kay BA, Saltzman EL, Kelso JAS. 1991. *Journal of Experimental Psychology-Human Perception and Performance* 17: 183-97
418. Eichwald C, Kaiser F. 1995. *Bioelectromagnetics* 16: 75-85
419. Deeks SG. 2011. *Annual Review of Medicine* 62: 141-55
420. Dock JN, Effros RB. 2011. *Aging Dis* 2: 382-97
421. Chen WH, Kozlovsky BF, Effros RB, Grubeck-Loebenstein B, Edelman R, Sztein MB. 2009. *Trends Immunol* 30: 351-9
422. Skupin A, Kettenmann H, Winkler U, Wartenberg M, Sauer H, et al. 2008. *Biophys J* 94: 2404-11
423. Dolmetsch RE, Xu K, Lewis RS. 1998. *Nature* 392: 933-6
424. Dupont G, Goldbeter A. 1992. *Biophysical Chemistry* 42: 257-70
425. Salazar C, Politi AZ, Hofer T. 2008. *Biophys J* 94: 1203-15